Behrmann, J.H., Lewis, S.D., Musgrave, R.J., et al., 1992
Proceedings of the Ocean Drilling Program, Initial Reports, Vol. 141

6. SITE 859[1]

Shipboard Scientific Party[2]

HOLE 859A

Date occupied: 28 November 1991

Date departed: 1 December 1991

Time on hole: 3 days, 5 hr, 15 min

Position: 45°53.761′S, 75°51.165′W

Bottom felt (rig floor; m, drill-pipe measurement): 2753.3

Distance between rig floor and sea level (m): 11.07

Water depth (drill-pipe measurement from sea level, m): 2741.2

Total depth (rig floor; m): 2899.8

Penetration (m): 146.5

Number of cores (including cores with no recovery): 21

Total length of cored section (m): 145.0

Total core recovered (m): 53.56

Core recovery (%): 37

Oldest sediment cored:
Depth (mbsf): 146.5
Nature: Silty clay
Earliest age: late Pliocene

HOLE 859B

Date occupied: 1 December 1991

Date departed: 8 December 1991

Time on hole: 6 days, 18 hr

Position: 45°53.72′S, 75°51.33′W

Bottom felt (rig floor; m, drill-pipe measurement): 2760.0

Distance between rig floor and sea level (m): 11.07

Water depth (drill-pipe measurement from sea level, m): 2748.9

Total depth (rig floor; m): 3236.1

Penetration (m): 476.10

Number of cores (including cores with no recovery): 38

Total length of cored section (m): 365.0

Total core recovered (m): 169.67

Core recovery (%): 46

Oldest sediment cored:
Depth (mbsf): 476.1
Nature: Sandy silty claystone
Earliest age: late Pliocene

Principal results: Drilling at Site 859 sampled deformed rocks of a small accretionary wedge and its slope sediment cover at the leading edge of the South American forearc basement. The accretionary wedge is composed of a uniform suite of fine-grained terrigenous clastic sediments of Pliocene age and is overlain by a thin, lower-trench-slope cover sequence of Pleistocene and late Pliocene age. The main source area of the sediment is the nearby Andean volcanic arc and crystalline basement. Glacial rock flour composes a significant fraction of the sediment in the wedge. Microfauna suggest a middle to lower bathyal depositional realm. A cold-water marine paleoenvironment existed during the Pliocene, followed by temperate to subtropical conditions during the late Pleistocene. The cold-water dominated paleoenvironment during the late Pliocene was interrupted by three short periods of temperate water conditions. The Matuyama/Gauss reversal of magnetic polarity was tentatively identified near 300 mbsf and the Gauss/Gilbert reversal at about 400 mbsf. The Pleistocene cover sediments are folded and have axial orientations perpendicular to the direction of plate convergence. Below 200 mbsf, the Pliocene sediments show signs of pervasive shearing and stratal disruption. Physical properties were measured on structurally intact subspecimens of the core or on firm, but nonrigid, mud or clay interbeds. The most important discoveries here are high average grain densities (2.8 g/cm^3) and low porosities: an average 55% near the mud line, decreasing to an average 15% at 470 mbsf, and consequently wet-water contents as low as 5% at this shallow subsurface depth. These circumstances do not reflect cementation, but an unusually consolidated sediment. Anomalously high porosities were found in the intervals of 200 to 240 mbsf (up to 55%, 20% above local background) and 380 to 420 mbsf (up to 37%, 15% above local background).

Chemical analyses of interstitial water samples and water sampler temperature probe (WSTP) samples show a pronounced chlorinity and salinity minimum between 30 and 70 mbsf. This may represent a dilution of pore fluids with freshwater liberated by the decomposition of gas hydrate. The chlorinity profile does not exhibit a diffusion gradient, suggesting that gas hydrate decomposition was triggered by drilling and that the gas hydrate is stable in situ. In this case, it can be estimated that approximately 25% of the pore volume is filled with disseminated gas hydrate. A second chemical discontinuity was intersected at around 240 mbsf. This is a zone of marked increase in Ca, a matching decrease in Mg, and a minimum in alkalinity of interstitial water. With no dolomitization present, this chemical signature is characteristic of a fluid resulting from the alteration of oceanic basement. A corresponding low K content corroborates this interpretation.

Headspace and vacutainer analyses of gases trapped in the core liner indicate a microbial, biogenic gas source in the upper part of Site 859. A significant component of thermogenic gas is evident from analyses of the cores in the lower part of Hole 859B. The content of solid organic matter is mostly lower than 0.5%, and generally, its degree of maturity is low. Thus, the thermogenic gas component must have migrated to its present location, probably from deeper parts of the accretionary prism downdip in the subduction zone.

Downhole temperature measurements using the WSTP revealed an approximate geothermal gradient of 200°C/km for the upper 50 mbsf. Below this depth, an extremely irregular temperature profile was recorded that included a zone of downward decrease in temperature between 130 and 220 mbsf. At 240 mbsf, a downhole temperature of 62°C was recorded, which may relate to an ambient rock temperature of 42°C and hot fluids entering the borehole nearby through a closely defined aquifer. Wireline logs in Hole 859B show disturbances in the temperature profile of the downhole mud column at positions that roughly correspond to the WSTP measurements. The temperature of the mud at terminal depth was approximately 50°C, constraining an overall thermal gradient of 100°C/km for the drilled interval. Sonic velocities in the upper part of the hole are 1.8 to 2.2 km/s, with a smooth downward increase. A low velocity zone is seen between 180 and 250 mbsf having variations between 1.6 and 2.2 km/s. Below 250 mbsf, variations exist between 2.3 and 2.8 km/s, with a smooth downhole increase. In most of the profile, velocities are anomalously high for sediments so near the surface.

[1] Behrmann, J.H., Lewis, S.D., Musgrave, R.J., et al., 1992. *Proc. ODP, Init. Repts.,* 141: College Station, TX (Ocean Drilling Program).
[2] Shipboard Scientific Party is as given in list of participants preceding the contents.

BACKGROUND AND OBJECTIVES

The Chile Triple Junction (Fig. 1) represents the only presently active zone of ridge-trench collision where the overriding plate is composed of continental lithosphere. The north-south trending Chile Trench lies at the western margin of the South American continent. Here, the Nazca and Antarctic plates and the oceanic spreading ridge separating them (the Chile Ridge) are underthrusted in a shallowly dipping subduction zone. Regional plate tectonic reconstructions are well constrained by marine magnetic anomaly studies (Cande et al., 1987), so that the detailed relationships between plate kinematics and continental margin geology can be effectively studied here. The Chile Ridge first collided with the South American continent at 14 Ma in the region of Tierra del Fuego, and other ridge segments were later subducted between there and the Taitao Peninsula. Prior to ridge collision, the Nazca Plate was subducted at a rapid rate in a direction slightly north of east. Subduction rates were roughly 80 mm/yr for the past 3 Ma and were as fast as 130 mm/yr during the late Miocene (Chase, 1978). South of the triple junction, the Antarctic Plate is subducted at a much slower rate, roughly 20 mm/yr for the past 15 Ma in a direction slightly south of east (Chase, 1978).

Currently, the section of the Chile Ridge between the Darwin and the Taitao fracture zones is gradually being subducted beneath the landward trench slope (Fig. 1). SeaBeam bathymetric data acquired during the *Conrad* cruise C-2901 show that the southern part of the ridge segment is already partly covered by the leading edge of the advancing South American forearc. At the latitude of seismic Line 745 (Figs. 1 and 2), the lower trench slope has reached the eastern rift shoulder. Site 859 is located on seismic Line 745 near the western end of the lowermost trench slope. From the seismic section (Fig. 2), it is evident that the toe of a small accretionary wedge sits on the eastern rift shoulder. A bottom-simulating reflector (BSR) at a depth of approximately 0.2 s two-way traveltime probably marks a lower boundary of gas hydrate stability (e.g., Kuustraa et al., 1983) within the accretionary wedge. A strong, shallowly east-dipping seismic reflector at 0.7 s two-way traveltime below Site 859 images the top of the subducting oceanic crust. Not much can be inferred from the seismic section about the internal structure of the accretionary wedge. However, comparison with previously studied accretionary wedges (e.g., Mascle, Moore, et al., 1988; Taira, Hill, Firth, et al., 1991) suggests that internal deformation is pronounced and that it is floored by a basal décollement zone.

Site 859, and indeed all of Leg 141, was primarily designed to solve problems of the geometry and dynamics of forearc evolution in a collision zone of a continent and an oceanic spreading ridge. An important secondary goal of investigation was provided by the opportunity to penetrate a zone of gas hydrate stability, its base, and the underlying sequence of rocks. To ensure safe drilling and to reduce the probability of finding hydrocarbons trapped at high pressures beneath a potentially impermeable seal, Site 859 was located in the small topographic depression on the lowermost trench slope (Fig. 2). Here, the BSR forms a structural low and thus cannot act as a trap for significant hydrocarbon accumulations.

Accordingly, the specific objectives of drilling at Site 859 were as follows:

1. To define the lithology, depositional environment, and age of the accreted and underthrusted sediment sequences. This and the nature of the contact between oceanic basalts and the sediments help to distinguish periods of accretion from periods of subduction erosion at the lower trench slope.
2. To analyze the deformation and structural fabrics of the lower trench slope sediments and to investigate their relationship to the plate kinematic framework.
3. To penetrate the BSR, to sample the gas hydrate, and to determine downhole temperatures for improving understanding of the physics and chemistry of gas hydrate formation.
4. To determine the chemical composition of rocks, interstitial fluids, and gases. This is to identify patterns of fluid and gas flow within the forearc and between the subducting oceanic slab and the forearc.

OPERATIONS

Panama to Site 859

The *JOIDES Resolution* departed Port Balboa, Panama, at 1600 hr Panama time (= 2100 Universal Time Coordinated or UTC) on 15 November 1991. A transit was made to Valparaiso Harbor, where the ship arrived at anchor on 25 November at 0700 hr Chilean time (Chilean time = UTC – 3 hr, and is used throughout the rest of this section). This transit of 2628 nmi was made through seas that ranged from fair to moderately rough in roughly 10.5 days at an average speed of 10.4 kt. After exchanging part of the technical crew, embarking the remaining scientists, and completing formalities, the ship departed Valparaiso Harbor at 1400 hr on the same day and arrived at the way-point for the pre-site survey for proposed Sites SC-1, SC-2, and SC-3 at 1500 hr on 28 November 1991. The 803-nmi transit from Valparaiso Harbor was completed in 73 hr at an average speed of 11.0 kt.

Site 859 (Proposed Site SC-3)

The vessel then ran an east-to-west confirming seismic line over the three proposed sites along survey Line 745, and a 14-kHz Datasonics commandable/releasable beacon was dropped at each site as it was passed. Each of the sites was accurately located, and beacons were dropped at SC-1, -2 and -3 at 1657, 1727, and 1819 hr, respectively.

Hole 859A

The seismic gear was retrieved and the ship returned to the SC-3 beacon (S/N 756) to begin Site 859 (Table 1). The vessel was steadied over the beacon at 2030 hr, and the process of making up the bottom-hole assembly (BHA) began. A conventional advanced piston corer/extended core barrel (APC/XCB) BHA was assembled that had a standard 11 7/16-in. roller cone bit.

The precision depth recorder (PDR) depth estimate for Hole 859A was 2743 m below sea level (mbsl), but the depth recorder signal was not sharp. Hence, the driller felt for bottom before picking up the top drive and deploying the first APC core barrel. Bottom was tagged and then confirmed in the first mud-line APC shot at 2741.2 mbsl. A second APC core was taken routinely. The third, fourth, and fifth APC attempts resulted in partial strokes and shattered liners because the formation became stiff at an unexpectedly shallow depth. Despite this, the four APC cores after the mud line were relatively intact and averaged more than 6 m long.

Orientation of the last three APC cores was done using both the normal Eastman multishot camera tool and a new, electronic Tensor orientation tool. Later, while recovering Core 141-859A-16X, the two tools were deployed together once more for final calibration after making mechanical adjustments to the sinker bar housing system and the old, camera-based units. Comparison of the results of these tandem measurements demonstrated that they

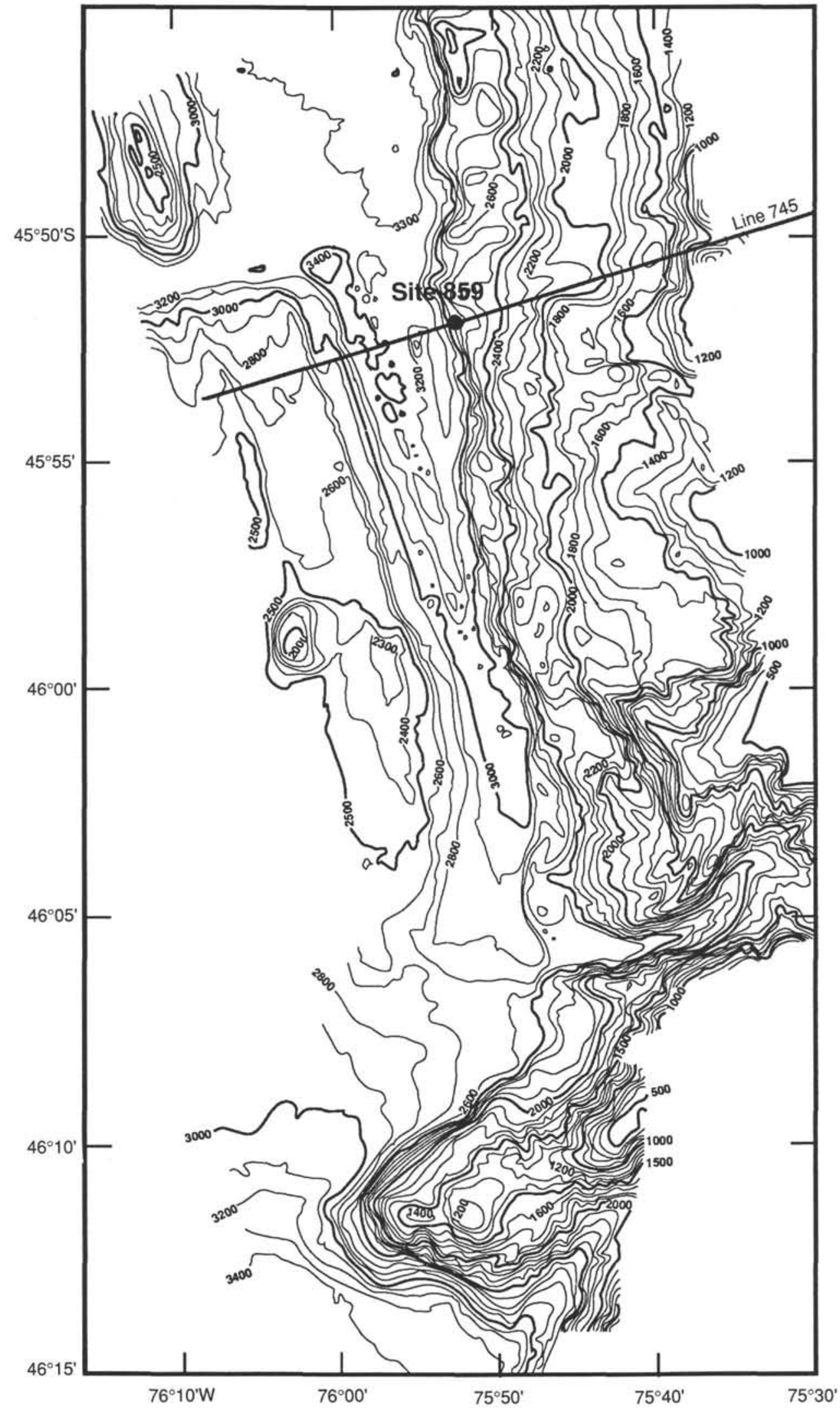

Figure 1. Detailed SeaBeam bathymetric map of the collision zone of the Chile Ridge and Chile Trench. Locations of seismic Line 745 and Site 859 are marked. Contour interval = 50 m.

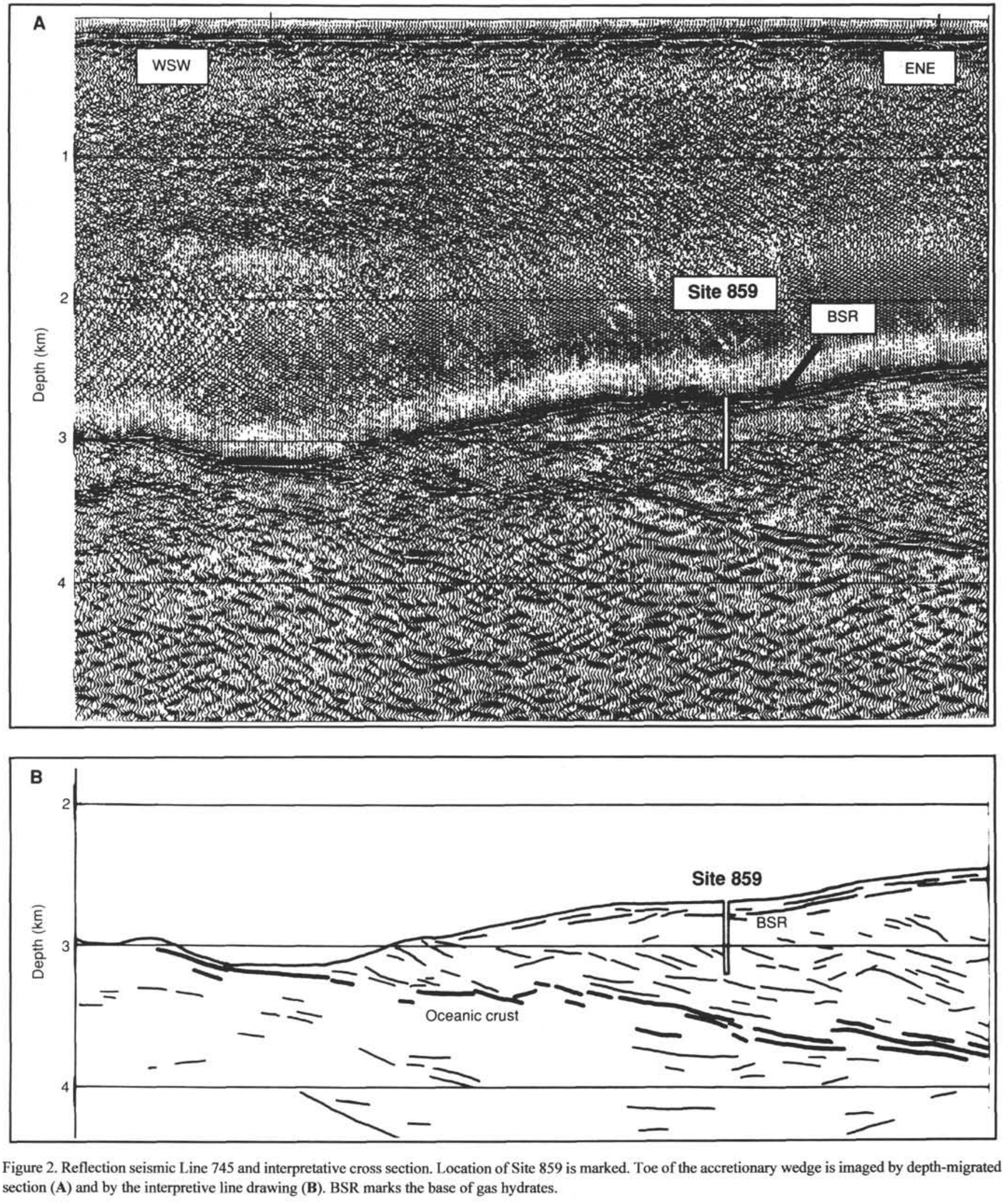

Figure 2. Reflection seismic Line 745 and interpretative cross section. Location of Site 859 is marked. Toe of the accretionary wedge is imaged by depth-migrated section (**A**) and by the interpretive line drawing (**B**). BSR marks the base of gas hydrates.

Table 1. Coring summary for Holes 859A and 859B.

Core	Date (1991)	Time (UTC)	Depth (mbsf)	Length cored (m)	Length recovered (m)	Recovery (%)	Age
141-859A-							
1H	29 Nov	0915	0.0–1.2	1.2	1.20	100.0	upper Pleistocene
2H	29 Nov	1045	1.2–10.7	9.5	9.81	103.0	upper Pleistocene
3H	29 Nov	1200	10.7–16.7	6.0	6.47	108.0	upper Pliocene
4H	29 Nov	1300	16.7–25.2	8.5	8.71	102.0	upper Pliocene
5H	29 Nov	1600	25.2–34.7	9.5	5.81	61.1	upper Pliocene
6X	29 Nov	2200	34.7–41.0	6.3	2.70	42.8	upper Pliocene
7X	29 Nov	0105	41.0–49.0	8.0	0.82	10.2	upper Pliocene
8X	29 Nov	0605	49.0–57.4	8.4	1.73	20.6	upper Pliocene
9P	30 Nov	0720	57.4–58.4	1.0	0.03	3.0	[a]upper Pleistocene
10X	30 Nov	1025	58.4–68.3	9.9	0.17	1.7	upper Pliocene
11X	30 Nov	1445	68.3–77.0	8.7	5.58	64.1	upper Pliocene
12P	30 Nov	1645	77.0–78.0	1.0	0.24	24.0	upper Pliocene
13X	30 Nov	1945	78.0–87.6	9.6	1.83	19.0	upper Pliocene
14X	30 Nov	2300	87.6–97.3	9.7	4.54	46.8	upper Pliocene
15P	1 Dec	0300	98.8–100.2	1.4	0.37	26.4	upper Pliocene
16X	1 Dec	0700	100.2–106.9	6.7	0.71	10.6	upper Pliocene
17X	1 Dec	0940	106.9–116.5	9.6	0.30	3.1	upper Pliocene
18X	1 Dec	1230	116.5–126.2	9.7	1.02	10.5	upper Pliocene
19X	1 Dec	1630	126.2–135.9	9.7	0.63	6.5	upper Pliocene
20X	1 Dec	1900	135.9–145.5	9.6	0.61	6.4	upper Pliocene
21P	1 Dec	2015	145.5–146.5	1.0	0.28	28.0	B
Coring totals				145.0	53.56	36.9	
141-859B-							
	Drilled		0.0–52.0				
1R	2 Dec	1745	52.0–61.6	9.6	3.86	40.2	upper Pliocene
2R	2 Dec	1900	61.6–71.3	9.7	5.84	60.2	upper Pliocene
3R	2 Dec	2130	71.3–80.9	9.6	9.67	101.0	upper Pliocene
	Drilled		80.9–148.5				
4R	3 Dec	0330	140.0–148.5	8.5	2.53	29.7	upper Pliocene
5R	3 Dec	0440	148.5–158.1	9.6	0.05	0.5	upper Pliocene
6R	3 Dec	0620	158.1–167.8	9.7	0.00	0.0	upper Pliocene
7R	3 Dec	0740	167.8–177.4	9.6	0.00	0.0	upper Pliocene
8R	3 Dec	0945	177.4–187.1	9.7	0.00	0.0	upper Pliocene
9R	3 Dec	1315	187.1–196.7	9.6	0.12	1.3	upper Pliocene
10R	3 Dec	1500	196.7–206.4	9.7	7.00	72.1	upper Pliocene
11R	3 Dec	1715	206.4–216.0	9.6	1.58	16.4	upper Pliocene
12R	3 Dec	2000	216.0–225.6	9.6	5.69	59.3	upper Pliocene
13R	3 Dec	2115	225.6–235.3	9.7	9.26	95.4	upper Pliocene
14R	3 Dec	2240	235.3–245.0	9.7	8.30	85.5	upper Pliocene
15R	4 Dec	0155	245.0–254.6	9.6	6.15	64.0	upper Pliocene
16R	4 Dec	0535	254.6–264.3	9.7	6.37	65.7	upper Pliocene
17R	4 Dec	0740	264.3–274.0	9.7	9.33	96.2	upper Pliocene
18R	4 Dec	1215	274.0–283.5	9.5	7.43	78.2	upper Pliocene
19R	4 Dec	1415	283.5–293.2	9.7	6.58	67.8	upper Pliocene
20R	4 Dec	1900	293.2–302.8	9.6	7.75	80.7	upper Pliocene
21R	4 Dec	2100	302.8–312.2	9.4	5.88	62.5	upper Pliocene
22R	4 Dec	2305	312.2–321.9	9.7	1.44	14.8	upper Pliocene
23R	5 Dec	0105	321.9–331.5	9.6	3.87	40.3	upper Pliocene
24R	5 Dec	0310	331.5–341.2	9.7	0.00	0.0	upper Pliocene
25R	5 Dec	0645	341.2–350.8	9.6	6.97	72.6	upper Pliocene
26R	5 Dec	0930	350.8–360.4	9.6	3.38	35.2	upper Pliocene
27R	5 Dec	1250	360.4–370.1	9.7	5.72	58.9	upper Pliocene
28R	5 Dec	1500	370.1–379.5	9.4	6.92	73.6	upper Pliocene
29R	5 Dec	1715	379.5–389.2	9.7	6.94	71.5	upper Pliocene
30R	5 Dec	2000	389.2–398.9	9.7	8.22	84.7	upper Pliocene
31R	5 Dec	2220	398.9–408.6	9.7	0.00	0.0	upper Pliocene
32R	6 Dec	0230	408.6–418.3	9.7	1.73	17.8	upper Pliocene
33R	6 Dec	0530	418.3–427.9	9.6	2.65	27.6	upper Pliocene
34R	6 Dec	0845	427.9–437.6	9.7	5.52	56.9	upper Pliocene
35R	6 Dec	1115	437.6–447.1	9.5	5.50	57.9	upper Pliocene
36R	6 Dec	1330	447.1–456.7	9.6	2.39	24.9	upper Pliocene
37R	6 Dec	1615	456.7–466.4	9.7	2.46	25.3	upper Pliocene
38R	6 Dec	2000	466.4–476.1	9.7	2.57	26.5	upper Pliocene
Coring totals				365.0	169.67	46.5	

[a] Downhole contamination.

were identical between the tools to within 1° of arc. Also included in the APC coring deployments were ADARA heat-flow cutting shoes. The ADARA instrumentation worked well, but the measurements were not valid because of the apparent movement of the cutting shoe within the sediment during the equilibrium waiting period.

A WSTP water sampler deployment was attempted after Core 141-859A-5H, but this failed as a result of a depth error that apparently left the tool inside the drill collars. All WSTP runs were conducted with the old Uyeda temperature electronic package because the new WSTP deck electronic interface box could not be made to work.

Drilling switched to the XCB system for Core 141-859A-6X onward. In general, the sticky clay-silt formation was difficult to core using the XCB system. Recovery was poor, and the rate of penetration was as low as 5 to 6 m/hr at times. Bit-balling was suspected, but could not be proved. The WSTP was deployed after Cores 141-859A-7X, -10X, -14X, and -18X. A valid water sample was recovered during two of the runs, and three valid in-situ temperatures were recorded.

The pressure core sampler (PCS) was deployed for Cores 141-859A-9P, -12P, -15P, and -21P. The PCS was being operated for the first time by operators other than the PCS project engineer, and a steep learning curve had to be followed. The first two core attempts did not recover in-situ (hydrostatic) pressure because of operator error. Cores 141-859A-15P and -21P most likely did collect samples at hydrostatic pressure, although the technique used to measure the trapped pressure on deck was not suitable for confirming this. No significant gases or evidence of methane hydrates were discovered in either of the two "successful" PCS cores, although the scientific staff made an attempt by placing the PCS sample container in a temperature-controlled, chilled bath and attaching it to a special gas/liquid sampling manifold.

The rate of penetration was so poor using the 11 7/16-in.-diameter roller cone bit that the XCB mode of coring was abandoned as soon as the last desired PCS deployment was completed at 146.5 m below the seafloor (mbsf). The hole was abandoned after being filled with barite-weighted mud, and the pipe was tripped to the deck. The bit cleared the rotary table at 2330 hr, 1 December 1991, ending operations at Hole 859A.

Hole 859B

The ship was offset 20 m to the northwest while the rotary core barrel (RCB) BHA was made up and the pipe was run into the hole. The hole was spudded at 0800 hr, 2 December 1991, because the driller detected bottom at a depth of 2749 mbsl. Later confirmation from logging in the Hole 859B suggested that the tag depth was low, the driller having failed to detect soft sediments at about 2743 mbsl, essentially identical to the depth assigned to Hole 859A.

The hole was drilled with a center bit to 52 mbsf, and three spot cores were taken with the RCB in an attempt to recover material missed by coring in a Hole 859A. The attempt was mostly successful, with cores of 3.86, 5.84, and 9.67 m in length. A WSTP run at 71.3 mbsf yielded a valid temperature measurement but no water sample because of filter clogging. The center bit again was used as the hole was deepened to 140.0 mbsf to begin continuous coring. Again, the sticky, firm formation allowed only slow penetration rates, and the 60-m drilling job required 5.5 hr to complete, including wireline and connection time. The WSTP was deployed in temperature-only mode five additional times deeper in the hole, but apparently was successful in measuring in-situ temperature only twice.

Routine RCB coring began at 140.0 mbsf and ended at total depth (TD) of 476.1 mbsf. Coring operations were terminated after exhaustion of allowable time at the site. The bit deplugger was dropped three times over the deeper sections of the hole and successfully deplugged the throat of the core bit when mud in the throat inhibited core recovery.

In neither Hole 859A nor Hole 859B did any solid methane hydrate appear, although seismic evidence and secondary, inferential geochemical evidence suggest that some clathrates were present in the formation. Gas contents of the cores were continuously monitored in those cores (the majority) that exhibited trapped gas pockets. Some gas expansion of the cores on deck was observed, but no violently gassy cores were brought up. Gas chromatograph analysis of the vacutainer samples revealed large percentages of methane, but also had significant portions of C_2 and C_3 (as high as 163 and 65 ppm, respectively) plus small concentrations of hydrocarbon gas species up to 7 ppm C_6 and above. Microscopic globules were detected in Core 141-859B-27R that would fluoresce when placed under ultraviolet light, indicating hydrocarbons. These were examined by extract techniques and were determined to be condensed, low-molecular-weight hydrocarbons. The presence of these indications of hydrocarbons was sufficient to require further clarification from ODP headquarters about the acceptability of continued drilling at this site. Authorization was received via MariSat and operations continued without interruption.

Drilling conditions were good with no hole problems. Virtually no sweep mud was used because the hole seemed to make its own mud readily. A few cobbles appeared in some cores, but these did not present drilling or hole stability difficulties. The few cobbles and a general lack of sweep mud used made a wiper trip prior to logging seem prudent. No ledges or bridges were detected during the downward portion of the wiper trip.

The pipe was positioned about 10 m off TD, and the bit was released through routine activation of the mechanical bit release (MBR). A second wireline trip was made to shift the MBR back down over the top connector windows. The pipe then was pulled to the selected logging depth (40.6 mbsf) while the hole was displaced with combination logging and abandonment mud composed of freshwater gel, barite, and 1% KCl.

Logging operations (Table 2) in Hole 859B made use of the logging heave compensator for all runs. Heave compensation was turned on and off at 75 mbsf. Rig-up of the geophysical tool string and Lamont-Doherty temperature tool began at 2330 hr on 6 December 1991. The sonic tool had to be turned off because the tool string appeared to contain too many tools for the telemetry capability. Uphole logs (minus the sonic data) were recorded from a total depth of 463.6 mbsf to the base of pipe (42.3 mbsf). The Lamont-Doherty temperature tool appeared to have flooded, and only 12 min of data was recovered from the first run.

A sonic tool string that consisted of the sonic, caliper, and natural gamma-ray tools was rigged up to retrieve downhole velocity data in Hole 859B. At 200 m below the rig floor, the sonic tool malfunctioned. The tool string was run back to the rig floor, the sonic tool changed out, and the tool string run back into the hole. Logs were recorded from 469.7 mbsf to the base of pipe (43.6 mbsf).

The formation microscanner (FMS) tool string was rigged up and lowered. During the first pass, the hole was logged over the interval from 460.5 to 38.7 mbsf. The tool string was lowered again, and a second pass was made from 460.5 to 28.0 mbsf.

To take advantage of the excellent weather conditions, the well seismic tool (WST) was run next instead of the geochemical tool string. The seismic source was a 400-in.^{3} water gun that hung from the side of the ship. The WST was rigged up with the Lamont-Doherty temperature tool and lowered to 461.1 mbsf. On the trip down, the tool string encountered a constriction at 33.2 mbsf, but managed to break through. Eight seismic stations were attempted, but because of enlarged hole conditions, clamping of the tool was successful at only four stations. Eleven additional stations were taken during this run for temperature measurements.

The last run was with the geochemical tool string and Lamont-Doherty temperature tool. On the first pass, the hole was logged from near the bottom (455.6 mbsf) to the base of pipe (30.1 mbsf)

Table 2. Hole 859B well log data.

Log type	Depth (mbsf)
Resistivity	41.6–456.5
Bulk density	41.6–457.9
Sonic velocity	40.9–459.7
Gamma ray/U-Th-K	15.1–455.6
Aluminum	15.1–451.4
Geochemistry	15.1–451.4
Caliper	43.6–459.7
Formation microscanner	28.0–460.5
LDGO temperature	0.0–463.6

Note: Values based on seafloor at 2749.0 mbsl and with all logs correlated and depth shifted to the gamma-ray log from the geophysical tool string.

in open hole and 15 m into pipe. The second pass was recorded from 202.7 to 30.1 mbsf in open hole, and 11 m into pipe. The tool string was run up to the rig floor and rigged down at 1115 hr on 8 December 1991, which ended logging at Hole 859B.

An additional 100 bbl of barite-weighted mud was spotted in the top 200 m of the hole following logging to account for the extra volume caused by hole elongation. After the pipe cleared the mud line, the ship was moved with thrusters and hydrophones toward proposed Site SC-2 while the drill string was pulled. The end of pipe was on deck at 1730 hr on 8 December 1991, ending operations at Hole 859B.

LITHOSTRATIGRAPHY

Hole 859A was drilled using the APC/XCB technique to a sub-bottom depth of 146.5 mbsf. Spot RCB coring in Hole 859B through geochemical and paleontological zones of interest (52.0–80.9 mbsf) has provided some stratigraphic overlapping between the two holes. Continuous RCB coring in Hole 859B began with Core 141-859B-4R at 140 mbsf.

The stratigraphic succession at Site 859 (Fig. 72 and Table 3) consists of two sedimentary lithologic units that have been primarily differentiated by their microfossil content. The contact between lithologic Units I and II has been placed at approximately 10.2 mbsf, at the base of Section 6 in Core 141-859A-2H. The subdivision of lithologic Unit II at 235.3 mbsf (Fig. 72 and Table 3) reflects a gradational change in induration within what appears to be a compositionally monotonous sequence of muddy sediments. Exact determination of compositional change within lithologic Unit II was hampered by drilling disturbance and the fine grain-size of the sediments.

There was 100% recovery of lithologic Unit I in Hole 859A, but recoveries for lithologic Unit II were highly variable in Holes 859A and 859B. Recovery may be a function of the various coring techniques used, variable induration of the sediments, and/or perhaps the presence of gas hydrate zones. Drilling disturbance increased downhole: whereas lithologic Unit I was largely undisturbed, much of lithologic Unit II recovery ranged in form from severely disturbed sediment to drilling breccia.

Lithologic Units

Unit I (Core 141-859A-1H and Sections 141-859A-2H-1 through -6; age: late Pleistocene; depth: 0—10.2 mbsf)

Lithologic Unit I is entirely restricted to Hole 859A (Fig. 72 and Table 3). This unit consists of grayish olive-green (5GY 3/2) to dusky yellow-green (5GY 5/2) clayey silt to silty clay with various proportions of siliceous microfossils (0%–20%; average 13%) and calcareous microfossils (0%–25%; average 7%). These microfossils include radiolarians, diatoms, sponge spicules, silicoflagellates, foraminifers, and nannofossils. Calcareous microfauna typically constitute a much smaller percentage, except in one bed of nannofossil silty clay (Section 141-859A-2H-5, 102 cm, to Section 141-859A-2H-6, 26 cm).

The terrigenous fraction of these sediments is poorly sorted mud. The total sand-sized component ranges from 0% to 5%. Only rough compositional percentages could be determined from smear slide analysis because of the fine-grained nature of these sediments, but mineral grains and rock fragments could be easily identified in the medium-to-coarse silt- and sand-sized fractions. The proportion of true clay minerals in the clay-sized fraction is thought to be minor (see discussion of Unit II below). Silt- and sand-sized grains consist predominantly of quartz and feldspar, with minor amounts of glassy volcanic fragments, amphibole, opaque minerals, and biotite.

Unit I lithologies are commonly mottled, but few distinct burrow traces are present. Color changes within the sequence are gradational and may roughly correlate to bedding, but in only one instance was a sharp bedding plane identified (at 26 cm in Section 141-859A-2H-6). Bedding orientations and recumbent isoclinal folds present in Sections 141-859A-2H-2, -3, and -4 (Fig. 19) are discussed in the Structural Geology section, this chapter. This bedding is defined by faint to discontinuous, black (N1) silty laminae.

The base of Unit I is defined by microfossil content ≤10%. Isolated zones rich in microfossils also occur in Unit II below this boundary, and zones having negligible microfossil content occur above this boundary (e.g., Section 141-859A-2H-2, 48–123 cm), suggesting that it is gradational.

Unit II (Section 141-859A-2H-7 through Core 141-859A-21P and Cores 141-859B-1R through -38R; age: late Pleistocene to late Pliocene; depth: 10.2—469 mbsf)

Although lithologic Unit II was recovered in both holes, detailed correlation between holes is unreliable because of variations in recovery rate, coring/drilling deformation, gas expansion (Fig. 3), and cutting methods (wire vs. saw), in conjunction with the semi-uniform sediment composition. For an example of cutting effects, see complete core photograph of Core 141-859B-10R in the Visual Core Descriptions section (this volume); Sections 141-859B-10R-1 to -4 were cut with saw and Sections 141-859B-10R-5 and the core catcher were cut with wire. The sub-bottom depth ranges for Cores 141-859A-8X and -859B-1R

Table 3. Site 859 lithostratigraphy summary.

Units	Age	Interval and depth	Lithology
Unit I	late Pleistocene	Core 141-859A-1H, and Core 141-859A-2H, Sections 1–6 (0–10.2 mbsf)	Clayey silt to silty clay with various proportions of siliceous (0% to 20%) and calcareous (0% to 25%) microfossils, commonly mottled; some soft-sediment deformation.
Subunit IIA	Pleistocene to late Pliocene	Core 141-859A-2H, Section 7 through Core 141-859A-21P, and Cores 141-859B-1R to –13R* (10.2–235.3 mbsf)	Silty clay to clayey silt; low microfossil content, some lamination, thin bedding, bioturbation and soft-sediment deformation, minor normal and inverse grading, rare pyrite concretions.
Subunit IIB	late Pliocene	Cores 141-859B-14R to –38R (235.3–469 mbsf)	Silty claystone, claystone, and clayey siltstone, barren to very low microfossil content; minor soft-sediment deformation, lamination, and bioturbation.

*Boundary between Subunits IIA and IIB is transitional across Cores 141-859B-12R and -13R.

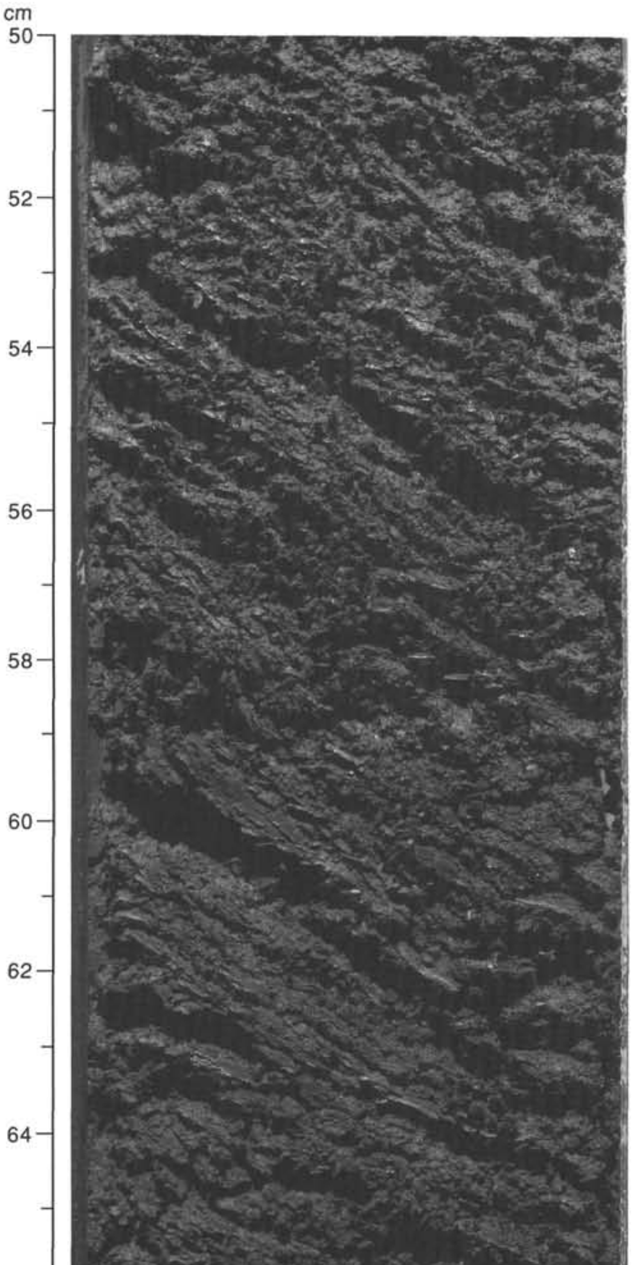

Figure 3. Fine-scale gas expansion fractures in semi-consolidated clayey silt to silty clay, Section 141-859B-11R-1, 50 to 70 cm. Larger features appear as voids in whole-core photographs.

overlap; these two cores can be roughly correlated in that each is dominantly composed of clayey silt, and subsequent cores in each hole contain silty clay to clayey silt. The estimated distance between the two holes is relatively small (20 m); thus, major stratigraphic changes are unlikely.

The sedimentary sequence included in lithologic Unit II is roughly subdivided according to sediment induration (Fig. 72 and Table 3). From Cores 141-859A-3H through -20X and from Core 141-859B-1R to the top of Core 141-859B-14R (235.3 mbsf), the sediments are unconsolidated to semiconsolidated and are termed "clays" and "silts." This interval constitutes Subunit IIA. Below the top of Core 141-859B-14R (235.3 mbsf), the sediments are sufficiently consolidated so that the suffix "stone" has been added to the name; these sediments make up Subunit IIB. The low recovery rate of "undisturbed" sections within Unit II cores, due to pervasive drilling disturbance and/or structural deformation, in part masks this change in hardness. However, changes in the relative hardness of core and drill cuttings can be seen just above this boundary in Cores 141-859B-12R and -13R (see complete core photographs in the Visual Core Description section, this volume).

Muddy lithologies in Unit II range from clay/claystone to silt/siltstone, with the majority being silty clay to clayey silt within Subunit IIA, and silty claystone to claystone in Subunit IIB. Thus, Subunit IIB is somewhat finer-grained than Subunit IIA. Sediment color does not markedly change across the Subunit IIA/IIB boundary, and unlithified and lithified sediments exhibit the same range of colors, including shades of black, gray, and green (dominantly Munsell colors 5Y 2/1, 5GY 2/1, N2, N3, and N4). Because of the compositional similarities of the two subunits, their grain size and mineralogy are discussed collectively.

In general, Unit II is composed of a poorly sorted mixture of clay- and silt-sized terrigenous and volcaniclastic materials. The texture and mineralogy of the clay- and silt-sized fraction at the top of Unit II is similar to that of Unit I, with an apparent downhole increase in the percentage of clay minerals in the clay-sized fraction (defined in a preliminary manner by smear-slide observations). Preliminary shipboard estimates of bulk and clay mineralogy using X-ray diffraction techniques are given in Tables 4 and 5 (see discussion below). X-ray diffraction data are consistent with the smear-slide analyses, which indicate that quartz and feldspar are the major silt-sized components, with lesser amounts of biotite, muscovite, chlorite, volcanic glassy fragments, other lithic fragments, amphibole, epidote, zircon, pyroxene, opaque minerals, organic matter (including rare plant fragments), micrite, siliceous and calcareous microfossils, and rare macrofossil fragments (e.g., shell fragments, echinoid spines). Some downhole trends in composition are illustrated in Figure 4. Microfossil content significantly decreases down through Unit II. Minor amounts of sponge spicules, nannofossils, foraminifers, silicoflagellates, and radiolarians are present in Subunit IIA, whereas Subunit IIB is essentially barren, with rare occurrences of diatoms in Core 141-859B-16R, foraminifer fragments in Core 141-859B-25R, and nannofossils in Cores 141-859B-25R and -28R. The shapes of silt grains are generally angular to subrounded, and a small percentage range up to moderately well-rounded. Some correlation of composition to rounding is seen in that the rare grains that exhibit better rounding tend to be quartz and altered feldspar.

The total proportion of sand-rich sediments in Unit II is significantly less than 1%. True sands and sandstones are rare (e.g., Core 141-859B-16R; Fig. 5), with approximately half of the cores in Unit II exhibiting no trace of sand-sized material. Cores having higher, but still minor sand contents are found within the upper part of Subunit IIA and the lower part of Subunit IIB. This can be seen in plots of maximum grain-size ranges for these subunits

Table 4. XRD mineralogy of nonclay fraction of sediments for Site 859.

Core, section, interval, (cm)	Depth mbsf	Nonclay mineral phases [a, b]				Phyllosilicates		
		Quartz	Feldspar	Hornblende	Calcite	Amorph.	Chlorite	Illite
141-859A-								
2H-7, 23–25	10.43	4	3	1	2	2	4	4
6X-1, 14–142	34.84	4	3	1	0	2	4	3
11X-3, 46–48	71.76	4	3	1	0	2	4	4
13X-1, 56–58	78.56	4	3	1	0	2	4	4
14X-2, 55–56	89.65	4	3	1	0	2	4	4
14X-3, 32–33	90.92	4	3	1	0	2	4	4
[c]17X-CC, 21–23	119.11	4	3	1	0	2	4	4
20X-CC, 23–25	148.13	4	3	1	0	2	4	4
141-859B-								
1R-2, 32–34	53.82	4	3	1	0	2	4	4
2R-2, 46–48	63.56	4	3	1	0	2	4	4
3R-1, 64–66	71.94	4	3	1	0	2	4	3
4R-1, 86–88	140.86	4	3	2	1	2	4	3
10R-5, 61–63	203.31	4	3	2	0	2	4	4
11R-1, 70–72	207.10	4	3	1	1	2	4	4
12R-3, 64–66	219.64	4	3	1	0	2	4	4
13R-7, 123–127	235.83	3	4	2	0	2	4	2
14R-3, 72–74	239.02	4	4	2	0	2	4	2
15R-2, 81–82	247.31	4	3	2	0	2	4	3
16R-4, 105–107	260.15	4	3	2	0	2	4	2
19R-4, 123–125	289.23	4	3	2	0	2	4	2
20R-3, 44–46	296.64	4	3	2	0	2	4	2
21R-2, 65–67	304.95	4	3	2	1	2	4	4
22R-1, 64–66	312.84	4	3	2	0	2	4	3
23R-2, 48–50	323.88	4	4	2	0	2	4	2
25R-3, 102–106	345.22	4	3	1	0	1	4	4
26R-1, 123–125	352.03	4	2	2	0	1	4	3
27R-3, 76–78	364.16	4	3	2	0	2	4	4
28R-4, 82–84	375.42	4	3	2	0	2	4	3
29R-2, 62–64	381.62	4	4	2	0	2	4	2
30R-3, 60–62	392.80	4	2	2	0	2	4	3
32R-2, 40–42	410.00	4	2	0	0	2	4	3
33R-1, 72–74	419.02	4	3	1	0	2	4	3
34R-2, 48–50	429.88	4	2	1	0	2	4	3
35R-1, 100–102	438.60	4	2	2	0	2	4	3
36R-1, 114–116	448.24	4	3	1	0	2	4	3
37R-2, 53–55	458.73	4	2	1	0	2	4	3
38R-1, 90–92	467.30	4	2	1	0	1	4	3

[a]Numbers indicate: 4. dominant, 3. secondary, 2. minor, and 1. trace phases; *0 indicates none present.*
[b]All diffractograms have a phase with a small peak at 2.71Å; possibly from trace amounts of pyrite.
[c]Possible trace amounts of ilmenite (peaks at 1.72 and 1.71Å).

(Fig. 6). The maximum grain size indicates the relative amounts of energy required to emplace the grains. In general, the maximum grain-size range appears to show some cyclicity downhole. Subunit IIA coarsens upward slightly, and grain sizes generally vary over a wider range in the upper part of this subunit than in its lower part. Subunit IIB fines upward over two distinct cycles from slightly coarser to fine-grained material: these cycles correspond approximately to Cores 141-859B-38R through -26R and 141-859B-25R through -14R.

Diagenetic features within the muddy sediments of Unit II include small, isolated in-situ pyrite and carbonate concretions in Subunit IIA (e.g., Cores 141-859A-4H, -6X; Fig. 20) and local zones pervasively cemented by carbonate (e.g., Core 141-859B-17R), or incipiently cemented by clay minerals (Cores 141-859B-37R and -38R). The incipient clay-mineral cements occur as thin, discontinuous birefringent rims (illite?) on some silt and sand grains in poorly consolidated units.

Enigmatic tabular to subrounded fragments of foraminifer-bearing, impure micritic limestone are present in the uppermost section of many Hole 859B cores (141-859B-1R, -2R, -13R, -19R, -26R, -27R, -29R, -32R, -34R, -37R, -38R). These fragments are suspect because they consistently occur in thoroughly disrupted zones, typically at the top of the recovered interval. This pattern of occurrence suggests that they are not in-situ, and probably have been dislodged from a lithified or concretion-bearing zone(s) located within the uncored intervals above Core 141-859B-1R (52 mbsf). Similar fragments were not recovered at Hole 859A. However, small carbonate concretion zones were observed in Cores 141-859A-4H and -6X. A round cobble of diorite (Fig. 7) located at the top of Core 141-859B-12R may have been similarly dislodged from unconsolidated sediments at the top of the hole. This cobble is similar to Mesozoic basement plutons of coastal Chile and has been interpreted as glacially transported and possibly ice-rafted.

Sedimentary structures are not common in Unit II cores. Decimeter-scale zones of soft-sediment deformation (e.g., folds and rare injection features, Fig. 19) occur in the upper part of Subunit IIA (Cores 141-859A-3H, -5H, and -859B-3R). Isolated pods of sponge spicules (Core 141-859A-5H), calcareous silt (Core 141-859A-6X), and silty sand (Cores 141-859A-6X and -11X) are probable burrow fillings. Bioturbation is indicated by mottling in other cores (e.g., Cores 141-859B-6R and -17R). Some rhythmically bedded zones are probably drilling disturbance features (see discussion in the Visual Core Description section for Core 141-859A-16X, this volume). Some undisturbed to moderately disturbed sections are laminated to thinly bedded, where beds/laminae consist of alternating clayey silt and silty clay or silty claystones and claystones. Bedding contacts vary from abrupt to gradational. Reverse (Fig. 8) and normal grading within laminae and beds is present in a few sandy intervals. Some beds are massive: for example, in Section 141-859B-16R-4, massive, very fine sandstone grades into silty claystone (Fig. 5). Brecciated

Table 5. XRD mineralogy of fine-grained (μm) fraction of Site 859 sediment.

Core, section, interval (cm)	Depth (mbsf)	Smectite (%)	Illite (%)	Chlorite (%)	Opal (%)	Amphibole (%)	Quartz (%)	Feldspar (%)	Amorphous (%)
141-859B-									
11R-1, 72–74	207.12	23	45	32	[b]TR	TR	cM	M	M
12R-3, 64–66	218.94	12	54	34	TR	TR	M	M	M
13R-7, 121–123	233.74	23	42	35	TR	TR	M	M	M
15R-2, 78–81	247.28	22	36	42	TR	TR	M	M	M
16R-4, 103–105	260.13	34	32	34	TR	TR	M	M	M
20R-3, 47–49	296.67	18	39	43	TR	TR	M	M	M
23R-2, 46–48	323.80	26	36	38	TR	TR	M	M	M
25R-3, 100–102	345.20	18	52	30	TR	TR	M	M	M
28R-4, 75–77	375.35	8	44	48	TR	TR	M	M	M
30R-3, 63–65	392.83	15	50	35	TR	TR	M	M	M
33R-1, 69–71	418.99	6	58	36	TR	0	M	M	M
36R-1, 103–108	448.13	9	57	34	TR	0	M	M	M
38R-1, 94–96	467.34	10	57	33	TR	0	M	M	M

TR = trace amounts; M = minor amounts.

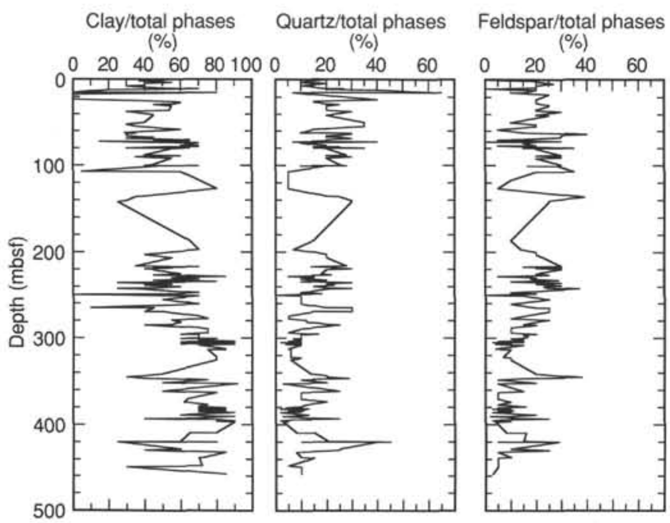

Figure 4. Graphs of percentages of mineral phases for Site 859, based on smear-slide analysis.

zones and deformation features are discussed in the Structural Geology section (this chapter).

X-ray Diffraction Analysis of Sediments

Fifty samples were selected from Unit II cores for X-ray diffraction analysis to better characterize the silt- and clay-size mineral phases. Bulk powders (37 samples) and clay-size separates (13 samples) were prepared and then analyzed using the shipboard Philips ADP 3520 X-ray diffractometer.

Based on mineral compositions of sediments analyzed from Unit II, the dominant phase present in the bulk samples is quartz (Table 4). In Sample 141-859B-13R-7, 123–127 cm, feldspar is the most abundant phase, and in a few samples, feldspar and quartz are approximately equal in abundance (Samples 141-859B-14R-3, 72–74 cm, -23R-2, 48–50 cm, and -859B-29R-2, 62-64 cm). The remaining samples have feldspar as the second most abundant phase. Most cores have a minor to trace amount of hornblende. Calcite is present only in a few samples: Samples 141-859A-2H-7, 23-25 cm, -4R-1, 86-88 cm, and as a trace amount in Samples 141-859B-11R-1, 70-72 cm, and -21R-2, 65-67 cm. An unidentified amorphous phase is present in all samples. Overall, the samples are very similar in the presence and relative abundance of mineral phases. The clay and phyllosilicate minerals identified in the bulk samples are chlorite and illite. These minerals are present in roughly equal amounts, except in a few samples (Samples 141-859B-3R-1, 64-66 cm, -4R-1, 86-88 cm, -13R-7, 123–127 cm, -14R-3, 72–74 cm, and -19R-4, 123–125 cm), where illite is less abundant than chlorite.

A separate study of the fine fraction removed from the sediments indicates that the main clay-mineral components are illite and chlorite (together forming from 66% to 94% of the fine fraction), with lesser amounts of smectite (Table 5). Traces of opal and amphibole (hornblende) were found in the clay fraction of all but a few samples (i.e., Samples 141-859B-33R-1, 69–71 cm; -36R-1, 103–108 cm; and -38R-1, 94–96 cm). Quartz, feldspar, and an amorphous phase are distributed in the fine fraction of all samples in minor amounts.

Illite is easily recognized by a series of reflections based on its 10-Å periodicity. The intensity ratio of the first three basal reflections (at 10, 5, and 3.33 Å) identifies the illite as a dioctahedral Fe-Al variety. It may be a polytype modification of illite 2M1 (of muscovitic type).

Chlorite is identified by a series of basal reflections based on 14.1-Å periodicity. Ratios of reflection peaks at 7.1 (002) and 3.5 (004) to those at 14.1 (001) and 4.7 (003) Å identify the chlorite in sediments recovered in Hole 859B as being of the Fe-Mg trioctahedral variety.

Smectites are characterized by a first-order basal reflection in the area of 14 Å, which shifts from 16.7 to 17.4 Å after saturation with ethylene glycol, and by weak reflections appearing at about 8.5 (002), 5.6 (003), and 3.33 (005) Å. After heating at 550°C, the reflection (001) is at 10 Å.

An unusual reflection peak from 13.6 to 13.9 Å appeared in all samples after they were heated for 1 hr at 550°C. This peak is unidentified at this time. It may represent mixed-layer clay minerals or chlorite having high concentrations of Fe atoms in silicate sheets.

The distribution of clay or phyllosilicate minerals in samples from Hole 859B (Fig. 9) shows a ubiquitous and relatively constant chlorite content throughout the lower 300 m of the hole. This contrasts with the distribution seen for illite and smectite. Smectite, in general, decreases from the upper to the lower analyzed section (200–500 mbsf). By contrast, illite is found to generally increase over the same depth range.

An important deviation from the general trend can be seen in the smectite concentrations for Sample 141-859B-16R-4, 103–105 cm. This sample has the highest abundances of smectite, and lowest of illite, in the section (smectite = 34%). This sample is located at 254.6 mbsf, near the high-temperature anomaly recorded by the WSTP and borehole logging run (see discussion in the WSTP—ADARA Measurements and Wireline Measurements sections, this chapter); this suggests that the smectite/illite anom-

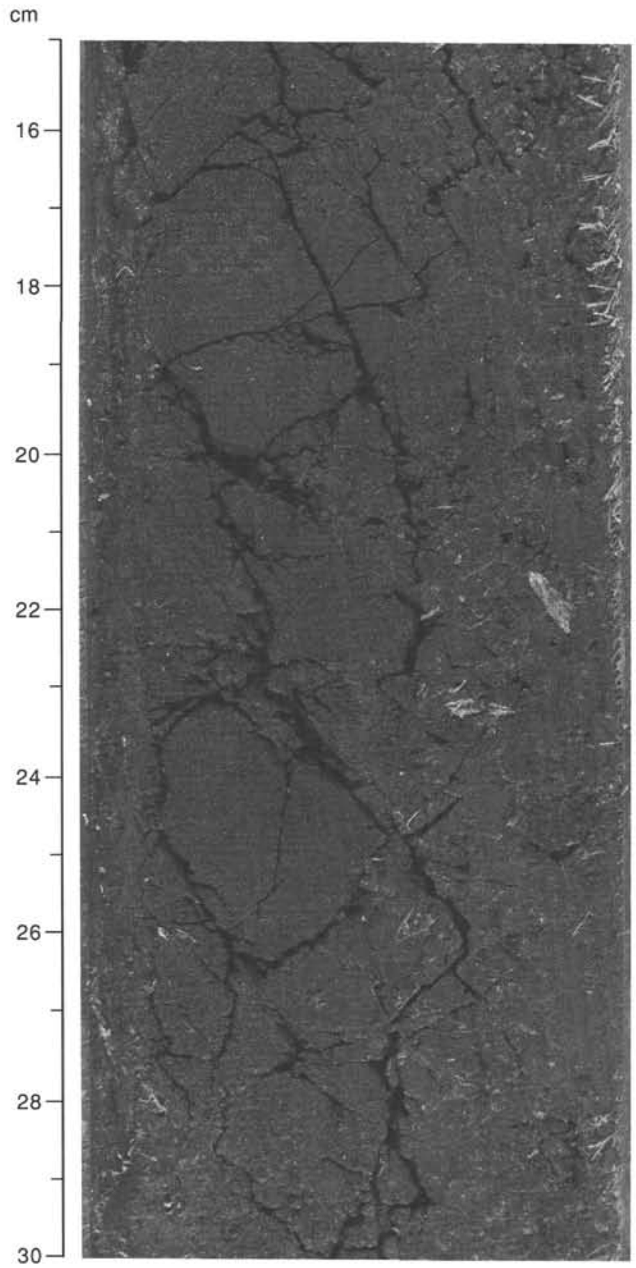

Figure 5. Fractured bed of massive, very fine sandstone, Section 141-859B-16R-4, 15 to 30 cm.

aly at this level may be related to hydrothermal circulation in this zone.

Diagenetic processes have not apparently affected illites or chlorites with stable crystalline structure. Distribution of these minerals in Hole 859B is thought primarily to reflect the processes of sedimentation and the primary composition of terrigenous clay minerals. The crystalline structure of smectite is more yielding under shallow burial and diagenesis. A general decrease of smectite is apparent in the lower part of the hole. However, the details of the smectite to illite transitions that are likely occurring at these levels require more detailed laboratory work.

Sediment Accumulation Rates

Estimates of Site 859 sediment accumulation rates (uncorrected for compaction) have been plotted in Figure 10. Only a few age constraints were provided by the biostratigraphic analysis of Site 859 cores (Fig. 72). The upper 10.2 m is latest Pleistocene in age (NN21) and thus not older than ~250,000 yr. The minimum accumulation rate for this section is 40.8 m/m.y. Below 10.2 m, a biostratigraphically defined hiatus and a structural change occur that may reflect an unconformity. The minimum time represented by this discontinuity is approximately 1.35 m.y. Sediments below this zone are 1.6 m.y. old or older (NN16-18). Nannofossils recovered in Core 141-859B-38R indicate that the section at that point (469 mbsf) is still younger than early Pliocene (see discussion in Biostratigraphy section, this chapter). The late Pliocene section has a minimum sedimentary accumulation rate of 287 m/m.y. This is a minimum for two reasons. First, nannofossil biostratigraphy at 469 mbsf only constrains the age to younger than early Pliocene. The actual boundary between the early and late Pliocene is found beneath this level; thus, rates of accumulation will be correspondingly higher. Second, porosities diminish to 10% to 15% (or lower) at the bottom of Hole 859B. If this reduction reflects compaction, then sedimentation rates may be underestimated by a factor of two or more, substantially magnifying the contrast seen in the apparent accumulation rates in the top and bottom of the holes.

The apparent accumulation rate over the interval from 10.2 to 469 mbsf is roughly seven times that of the estimated rate for 0 to 10.2 mbsf. This may reflect some degree of tectonic thickening within Subunit IIB. Alternatively, it may be the result of an actually higher sedimentation rate in Subunit IIB.

Discussion/Interpretation

Many factors, related both to the geology and the drilling process, contribute to the overall homogeneity and featureless nature of lithologic Unit II, and these hamper attempts at environmental interpretation. First and foremost, the section is underrepresented because of large gaps in recovery and/or low recovery over many intervals. Even when recovery rates increased in Subunit IIB, recovered core often consisted entirely of drilling biscuits, with biscuited sections ranging from wholly to partially coherent. Successive sedimentary intervals may be differentially indurated within Subunit IIB, and thus they may be preferentially cored, brecciated, or totally disaggregated as a function of their mechanical strength. Drilling evidently served to exaggerate structural deformation of the sediments by disrupting material with preexisting fractures and shears.

Paleontological evidence for depositional environment is also poor in that microfossil content decreases markedly down through Unit II, with many barren intervals. This change in microfossil content might be explained by post-Pliocene uplift above the carbonate and silica compensation depths (CCD/SCD) (present water depth is approximately 2750 m), or an increase in productivity during the Pleistocene (upwelling?) that culminated with the deposition of Unit I. The overall concentration of microfossils is also a function of terrigenous accumulation rates, which apparently increase downhole. A more likely scenario, given the elevated geothermal gradient in this region, is that microfossils have been progressively removed by dissolution during burial, and that their original distribution has now been lost.

The fine grain size of the sediments suggests either that Site 859 was distant from its source regions, structurally isolated from sediment influx, or alternatively, the source region may have simply supplied only muddy sediments. The source of these materials was almost certainly associated with glacial processes along this high-latitude, volcanically active margin. Continental ice sheets extended out over the modern Chonos and Taitao Archipelago during the Pleistocene; the extent of Pliocene glaciation is not known and may have been restricted to alpine glaciers along the main Andean front. The poorly sorted nature of the

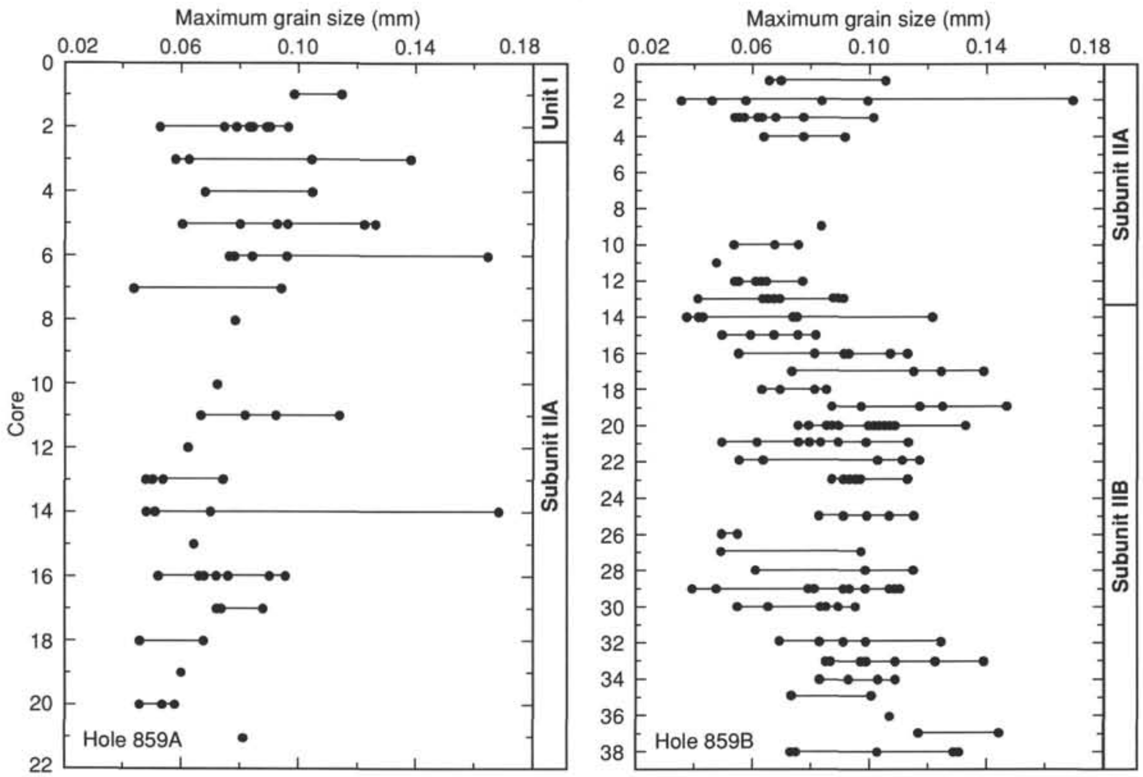

Figure 6. Maximum grain-size ranges of silty clays to clayey silts in Holes 859A and 859B. Each dot represents the average diameter of the five largest grains within a smear slide. Lines connect data for cores having more than one smear slide.

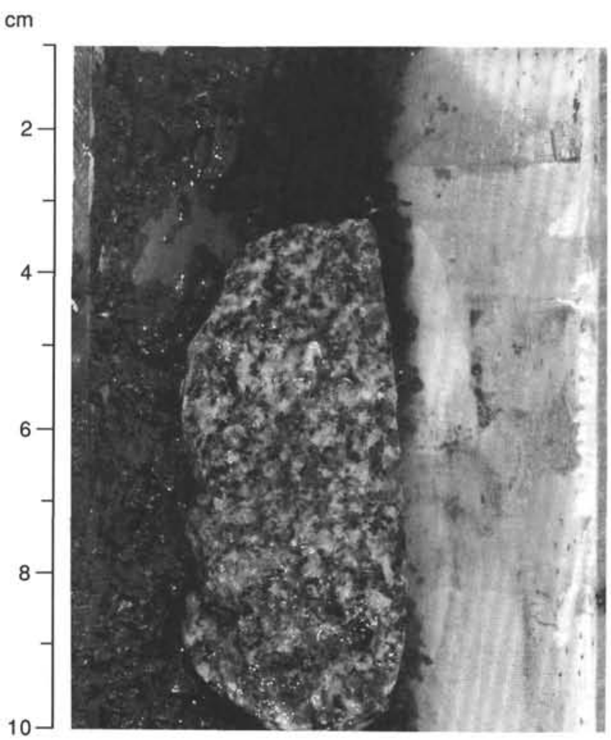

Figure 7. Cobble of diorite from Section 141-859B-21R-1, 1 to 10 cm. See text for discussion.

terrigenous muds in both Units I and II, specifically the wide range of silt-sized material, is probably a function of glacial melt-water influx of rock flour and minimal onshore chemical weathering during the Pleistocene and back to the late Pliocene. The apparent increase of clay minerals downhole may represent changes in provenance. Sand and coarse silt compositions are consistent with a mixed provenance of predominantly pyroclastic materials (glassy volcanic fragments, fresh plagioclase, and fresh hornblende) from the Andean arc, and lesser quantities of grains derived from the Patagonian batholith, Paleozoic metamorphic complexes, and Tertiary marine sedimentary rocks that crop out west of the arc. The grain-size variations and cycles in Subunits IIA and IIB (Fig. 6) may be partly related to changes in sea level, influx of glacial sediments, or, if valid, the tectonic thickening model (Fig. 11).

The paucity of diagnostic sedimentary structures preserved in recovered sections does not closely constrain environmental interpretation. Grain size, preserved lamination, and grading trends are consistent with deposition by relatively low-density turbidity currents (induced by slope processes) and hemipelagic sedimentation, rather than distal, submarine-fan sedimentation. Laminations preserved in some parts of Unit II indicate transport by weak traction currents, whereas reverse grading may indicate partial reworking by bottom currents. Perhaps these sediments were deposited as suspension fallout from sediment-charged glacial meltwater plumes extending off the shelf. Downslope redistribution of materials may then have resulted from earthquake-induced submarine mass movement, or oversteepening of the upper slope because of glacial dumping. Slumping would produce semi-coherent to deformed units (proximal: observed in Unit I and Subunit IIA), fine-grained turbidites (distal), and suspension fallout lamination (even more distal).

The apparent increase in sedimentary accumulation rate seen below the Pliocene/Pleistocene boundary (Fig. 10) does not correlate with any observable change in lithofacies, other than that

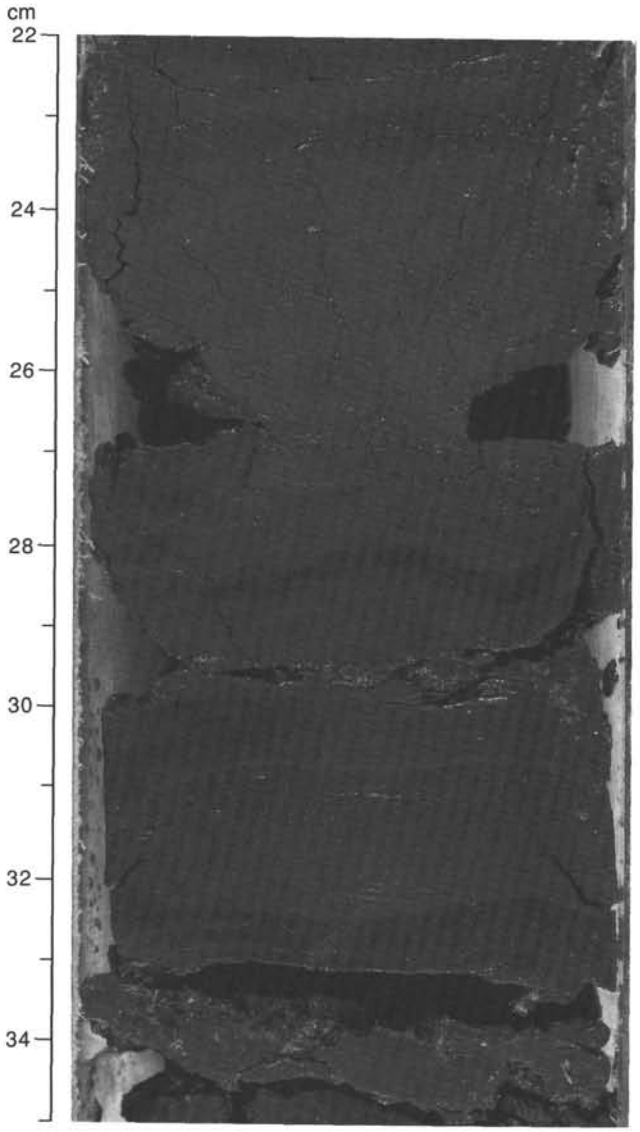

Figure 8. Interlaminated/bedded clayey silt and silty clay. Two laminations show reverse grading (at Sections 141-859A-16X-CC at 30–31 cm, and 31–33 cm) from silty clay to clayey silt with some sand.

of a gradual trend to more fine-grained sediments (discussed above). If anything, the lithofacies would suggest slower rates of accumulation for the lower part of the hole. The proportions of mineral phases in the silts and clays (identified by smear slide and XRD analysis) are remarkably uniform throughout the transition from low to high sedimentation rates below 70 mbsf. This argues for a reasonably stable depositional framework, at least with regard to basin provenance attributes. While tectonic as well as climatic mechanisms are available to explain the changes in apparent rates, a structural imbrication model for the lower part of the basin is seen as the simplest interpretation (Fig. 11). If so, a major phase of structural thickening is likely to have operated prior to deposition of the upper part of Unit II, at about 2 Ma.

Finally, a range of possible Pliocene-Pleistocene basin configurations are plausible because of the uncertain plate tectonic history of this portion of the Chile margin. Possible tectonic scenarios include accumulation of these sediments within the trench and subsequent accretion through underplating or obduction, or accumulation in a slope basin and then tectonic erosion

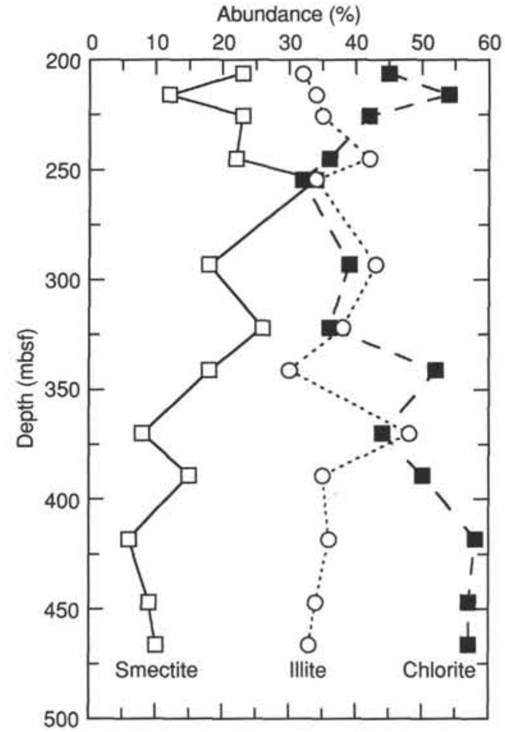

Figure 9. Graph showing relative abundances of clay mineral phases in samples from Site 859, as determined by X-ray diffraction techniques (see text for further discussion).

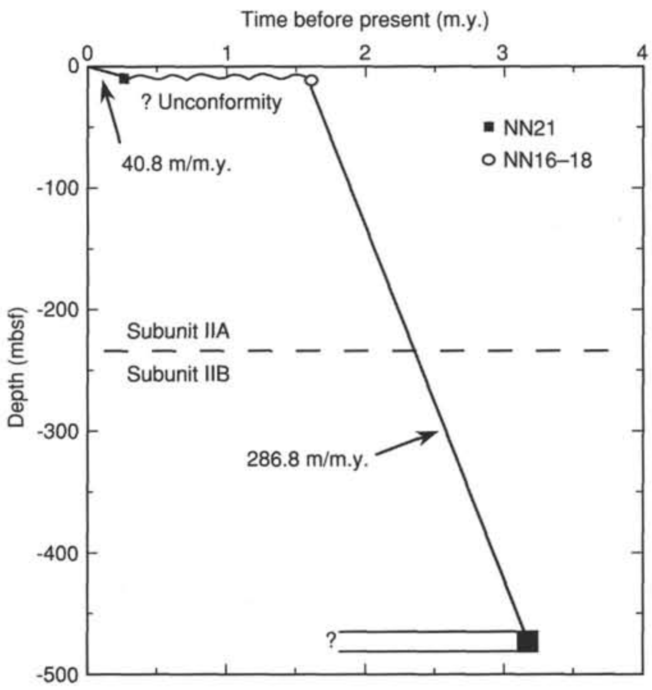

Figure 10. Estimates of sediment accumulation rates at Site 859. Open lines at bottom show uncertainty in paleontologic data.

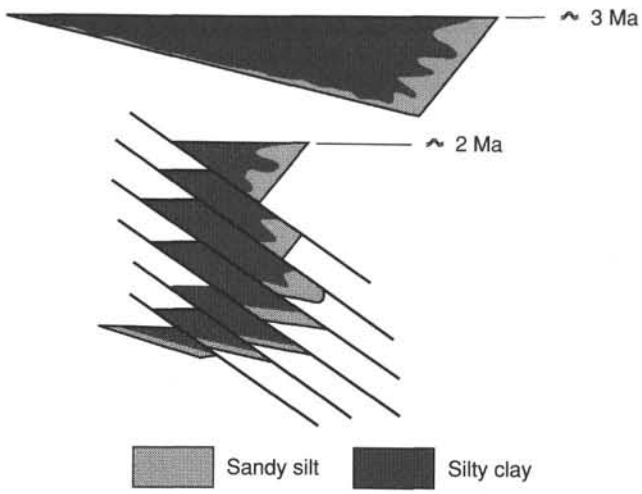

Figure 11. Model to explain apparent increase in sedimentation rate within Unit II by a process of subduction-related tectonic thickening.

of the accretionary prism. The sedimentary sequence recovered at Site 859 might be attributed to either depositional scenario.

BIOSTRATIGRAPHY

Introduction

Quaternary through upper Pliocene sediments were recovered at Site 859. Eighteen core-catcher samples from Hole 859A and 31 core-catcher samples from Hole 859B were examined on board the ship for diatoms, radiolarians, and planktonic and benthic foraminifers (Fig. 12). Selected additional samples within cores were examined to follow more accurately the sequence of warm/temperate and cold climatic fluctuations. We also examined five calcareous micrite-cemented fragments found near the tops of Cores 141-859B-18R, -27R, -29R, -37R, and -38R to determine the origin of the micrite-cements. Additional age determinations based on calcareous nannofossils were obtained by shore-based studies (C. Müller).

The biostratigraphic resolution is low because of the scarcity of all different fossil groups and low diversified assemblages. Climatic intervals indicating warm, temperate, and cold-water environments were recognized primarily on the basis of planktonic foraminifers.

The Pleistocene warm-water assemblage of PCS Core 141-859A-9P (recovery only 3 cm) is considered downhole contamination. This implies a hiatus within Core 141-859A-3H.

Diatoms

Diatoms were encountered in Samples 141-859A-1H-CC and 141-859A-2H-CC, whereas Samples 141-859A-3H-CC through -20X-CC and 141-859B-1R-CC through -38R-CC were barren. The abundance level of diatoms within these two uppermost samples from Hole 859A can be characterized as few to common, and preservation as moderate. These samples were assigned to the upper Pleistocene *Pseudoeunotia doliolus* Zone (NTD 17) on the basis of the observed occurrence of *P. doliolus* (although this species was rare) and the absence of *Nitzschia reinholdii*. The observed assemblages are dominated by *Paralia sulcata* and by species belonging to the genus *Thalassiosira*, especially by species within the *T. eccentrica* Group (i.e., *Thalassiosira* species showing an eccentric areolae pattern). Large-sized specimens of *Coscinodiscus* are less frequent but significant portions of the assemblages. The rare occurrences of *Nitzschia kerguelensis* and *Thalassiosira lentiginosus* (only a few specimens observed) concurrently with the rare occurrences of *P. doliolus* indicate that the

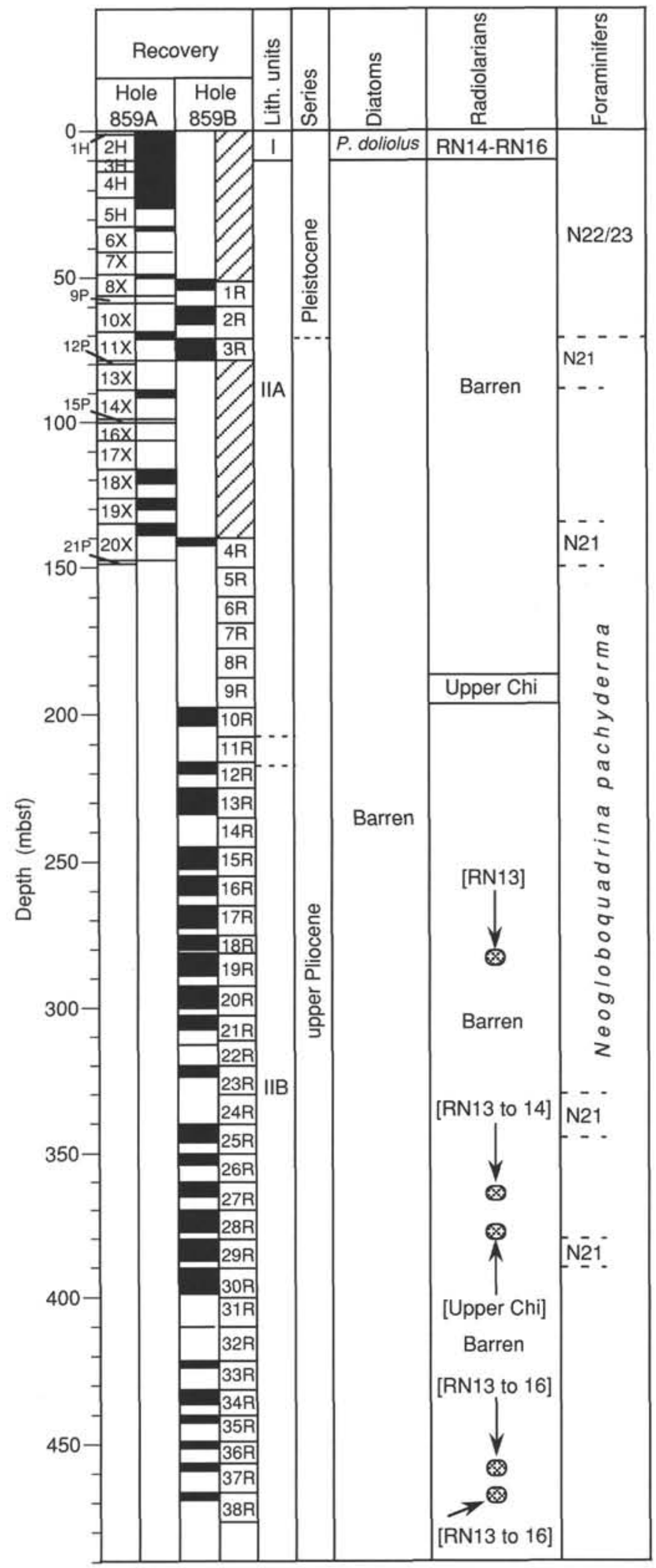

Figure 12. Summary of biostratigraphic age for the sediments recovered at Site 859.

region was influenced both by warm/temperate waters from the north as well as cold waters from the south.

In addition to the core-catcher samples, five clasts of fine-grained calcite recovered in Hole 859B were examined for their diatom content. These clasts are located in the uppermost portions of Cores 141-859B-18R, -27R, -29R, -37R, and -38R (see Visual Core Descriptions section, this volume). Analysis of all five samples yielded occurrences of rare to few diatoms having poor to moderate preservation. The observed assemblages are similar in their composition and are dominated by *Coscinodiscus* and *Thalassiosira* species (e.g., *C. oculus iridis, T. oestrupii, T. praeoestrupii,* and species within the *T. eccentrica* Group. The rare, but consistent, occurrences of *N. kerguelensis* indicate that these clasts are younger than this species, which has a reported first occurrence at 2.7 Ma in the Southern Ocean (McCollum, 1975; Barron, 1985). However, these calcite clasts are not thought to represent the stratigraphic levels where they have been found; instead, they are interpreted to be displaced from a level above Core 141-859B-1R because of downhole contamination (see Lithostratigraphy section, this chapter). This interpretation is justified by the occurrence of these clasts within sediments of a completely different lithology. Moreover, Ruddiman et al. (1987) showed that disturbances and downhole contamination often are located in the top of cores. Thus, the occurrence of these calcite clasts in the top of the cores further strengthens the interpretation that they were dislocated by downhole contamination.

Radiolarians

A total of 52 core-catcher samples and an additional 13 samples within cores were examined at Site 859 for radiolarians. Age-diagnostic radiolarians were found in only three core-catcher samples from both Holes 859A and 859B combined and in five samples of the micrite-cements of Hole 859B. Radiolarians have been consistently preserved in warm-water intervals, which are conformable among diatom, radiolarian, and planktonic foraminifer assemblages. On the other hand, samples from temperate or cold intervals, indicated by planktonic foraminifers, were consistently barren for radiolarians, with exceptions of trace numbers of radiolarians (1–3 specimens) found in the following samples: 141-859A-4H-2, 142–144 cm; -10X-CC; and 141-859B-2R-CC; -3R-CC; and -25R-CC.

Samples 141-859A-1H-CC and 141-859A-2H-CC contain moderately preserved common radiolarians of the following stratigraphically important taxa: *Lamprocyrtis nigriniae, Eucyrtidium erythromystax, Theocorythium trachelium dianae, Cycladophora bicornis, C. davisiana davisiana,* and *Pterocanium trilobum*(?). These two samples can be placed in the *Amphirhopalum ypsilon* to *Buccinosphaera invaginata* Zone of the Pleistocene of the tropical zonation (Sanfilippo et al., 1985) or the Upper Chi to Omega Zone of the Antarctic zonation (Lazarus, 1992) that falls in the middle Pleistocene to Holocene. The latter assignment was based on the presence of *E. erythromystax* (Nigrini and Caulet, in press). Certainly, these samples are younger than the *Anthocyrtidium angulare* Zone of the early Pleistocene because of the unambiguous presence of *L. nigriniae.* The presence of *Pterocanium trilobum*(?) presents a conflict because its last appearance datum (LAD) is at 0.8 Ma (Lazarus, 1992). Thus, the observed specimens are either reworked or are not *P. trilobum.*

Several specimens of Eucyrtidium calvertense, a form thought to range from the late Miocene to Pliocene (e.g., Lazarus, 1990), were recognized in each of these two samples. Although a possibility exists that they have been reworked, it may be that the LAD of E. calvertense in this region is much later than that in the Weddell Sea region (Lazarus, 1990). Note also that this species has been found in Samples 141-859A-9P-CC and 141-859B-38R-1, 0–1 cm, mentioned below.

Samples 141-859A-3H-CC to -8X-CC are barren of radiolarians. Sample 141-859A-9P-CC contains a few moderate to poorly preserved radiolarians, including P. trilobum, C. bicornis, and C. davisiana davisiana. This material is considered to be downhole contamination. Sample 141-859A-10X-CC contains only three poorly preserved nonage-diagnostic radiolarians. Samples 141-859A-11X-CC through -20X-CC, which represent the remainder of the sequence down to the bottom of Hole 859A, are all barren of radiolarians.

Sample 141-859B-1R-CC, the first sample from Hole 859B, is barren of radiolarians. Sample 141-859B-2R-CC contains one broken specimen of *Didymocyrtis laticonus*(?) (or possibly *D. mammifera*), a middle Miocene species, clearly indicating reworking. Next, Sample 141-859B-3R-CC has only one nassellarian (gen. et sp. undet.) species in it and thus no age can be given. Samples 141-859B-4R-CC through -38R-CC yielded no radiolarians from radiolarian slides. Foraminifer preparation of Samples 141-859B-3R-CC and 141-859B-25R-CC yielded two specimens and seven specimens, respectively, of spongodiscids, but no age information can be provided. Prompted by a shipboard sedimentologist who found some siliceous microfossil fragments, the following three samples from Core 141-859B-16R were examined: 141-859B-16R-1, 86–88 cm; 141-859B-16R-1, 98–100 cm; and 141-859B-16R-2, 40–42 cm. These were all barren of radiolarians.

Calcareous Micrite-cemented Sediments

Pebble-sized calcareous micrite-cemented sediments were found in Cores 141-859B-1R, -2R, -13R, -18R, -27R, -29R, -37R, and -38R. Their colors range from olive gray (5Y 4/1) to dark greenish-gray (5GY 4/1). Lithologically, these sediments are markedly different from the background core materials of relatively unconsolidated gray sediments within which the calcareous cements were located at the time of the core recovery (for details see Lithostratigraphy section, this chapter). They contain few to common radiolarians of a moderate to poor preservation state as well as some diatoms (see above). The following micrite samples were examined: 141-859B-18R-1, 0–1 cm; -27R-1, 43–45 cm; -29R-1, 14–15 cm; -37R, 0–2 cm; and -38R, 0–1 cm. Note that they are always located at or near the top of cores, suggesting the possibility that they may have fallen from the upper part of the hole during times when the core-barrel was being retrieved and the bit was raised above the bottom of the hole.

All five calcareous pebbles showed similar early Pleistocene ages. Sample 141-859B-18R-1, 0–1 cm, contains two specimens each of *Lamprocyrtis neoheteroporos* and *L. nigriniae,* among two dozen or more specimens of stratigraphically less significant taxa (e.g., *C. davisiana davisiana, C. bicornis, Botryostrobus acquilonaris, Phormosticoartus corbula,* and a transition form between *Antarctissa strelkovi* and *A. deflandrei*). The presence of the above two species of *Lamprocyrtis* indicates that, with a high degree of confidence, the sample can be placed in the upper part of the *Anthocyrtidium angulare* Zone (early Pleistocene) of the tropical zonation, in the vicinity of 1.07 to 1.09 Ma. Sample 141-859B-27R-1, 0–1 cm, contains one specimen each of *L. nigriniae* and *Axoprunum angelinum,* among a dozen other taxa. This places it in the *Anthocyrtidium angulare* Zone to the *Amphirhopalum ypsilon* Zone of the tropical zonation (early Pleistocene). Sample 141-859B-29R-1, 14–15 cm, contains three specimens of *P. trilobum* and more than a dozen specimens of *C. bicornis,* among a dozen other taxa, which places it between 1.4 to 0.8 Ma in the Upper Chi Zone, the early Pleistocene of the Antarctic zonation. Sample 141-859B-37R-1, 0–2 cm, has three specimens of *L. nigriniae,* among a dozen or more other taxa. This sample belongs to the *A. angulare* to *Buccinosphaera invaginata* Zone of the Quaternary. The next sample, 141-859B-38R-1, 0–1 cm, contains six specimens of *L. nigriniae.* Thus, it also belongs to the *A. angulare* Zone to the *Buccinosphaera invaginata* Zone of the Quaternary. The last sample (Sample 141-859B-38R-1, 0–1 cm) contains one specimen of *E. calvertense* and two specimens of *Prunopyre trypopyrena,* indicating reworking. The circumstantial evidence (e.g., the same lithology, placement in the core tops) and similar taxonomic compositions of the assemblages indicate that these last two samples are probably of early Pleistocene age as well. It is likely that these micrite-cemented stones derived from the same formation somewhere above Core 141-859B-1R, in which the first micrite-cemented stone appeared, thus suggesting a strong possibility that they were reworked downhole.

Paleotemperature

Climatic fluctuations in this region appear to be reflected in the planktonic faunal and floral assemblages. Radiolarian assemblages observed at Site 859 (Samples 141-859A-1H-CC, -2H-CC, -9P-CC, and five samples of calcareous micrite-cements) generally consist predominantly of taxa presently found in the temperate to tropical oceans (Lombari and Boden, 1985). For instance, warm-water taxa include *Lamprocyrtis hannai, L. nigriniae, Saturnalis circularis, Dictyocoryne profunda/Hymeniastrum euclidis* Group, and *Spongocore puella* (Lombari and Boden, 1985). On the other hand, a small proportion (<10%) of the radiolarian assemblages in the above three samples is represented by typical Antarctic forms (e.g., *Antarctissa denticulata*) and sub-boreal taxa (*Pterocanium diplotriaena* and *Pterocanium korotonevi* (Takahashi, 1987). Note that relatively high percentages (e.g., 25% for Sample 141-859B-38R-1, 0–1 cm) of the sum of *Cyclndophora bicornis, C. davisiana davisiana,* and *C. davisiana cornutoides* were observed in the total radiolarian assemblages, indicating that paleoclimates were certainly colder than tropical environments because the proportions are higher than several percent (Morley, 1980). In addition, although many tropical taxa are present, not all typical tropical taxa are included in the assemblages. For example, the missing taxa are Collosphaeridae, *Euchitonia elegans, Spongodiscus tetras, Amphirhopalum ypsilon, Didymocyrtis tetrathalamus tetrathalamus, Anthocyrtidium zanguebaricum, Pterocanium praetextum praetextum,* and Carpocaniidae (except for *Carpocanarium papillosum,* which is consistently present in all of the radiolarian assemblages). Therefore, the "warm" climate defined here, at least in the radiolarian section, is warmer than the conditions presented by typical subpolar assemblages (e.g., Nigrini, 1970; Takahashi, 1987), but does not necessarily represent subtropical or tropical conditions. Detailed percentage analysis of the radiolarian assemblages is one of the subject matters of the shore-based post-cruise analysis.

Coastal Upwelling

Several radiolarian species indicating upwelling (Nigrini and Caulet, in press) have been observed in the above radiolarian-bearing samples, including *L. nigriniae, C. davisiana davisiana, Tetrapyle octacantha, Eucyrtidium erythromystax, Lithostrobus* sp. cf. *L. haxagonalis, Pterocanium minythorax,* and *Pterocanium auritum* (and *E. calvertense,* if not reworked). In particular, *L. nigriniae* is present in six of eight radiolarian-bearing assemblages (excluding samples containing trace amounts of radiolarians): these are from Samples 141-859A-1H-CC; -2H-CC; 141-859B-18R-1, 0–1 cm; -27R-1, 43–45 cm; -37R, 0–2 cm; and -38R, 0–1 cm. In the equatorial upwelling region of the Ontong Java Plateau (Kroenke, Berger, Janacek, et al., 1991), *L. nigriniae* is almost always present in the samples of well-preserved radiolarian assemblages belonging to the *A. ypsilon* Zone and younger. However, it is rare and generally only one to three specimens per slide of well-preserved radiolarian assemblages can be found out of a normal total of about 5000 specimens/slide using 22 × 50 mm cover slips. Lombari and Boden (1985) noted up to 1% of this species in modern assemblages off South America. Considering the rarity of this species, the occurrence of up to six specimens of this taxon having moderate to poor preservation (out of a total of <200 specimens/slide) by itself indicates an upwelling regime. Furthermore, the modern biogeographic map of Lombari and Boden (1985) clearly illustrated higher populations of this species along the equatorial upwelling as well as coastal upwelling regions along North and South America. According to the literature, this species has been found so far only at latitudes of less than 45° (Sanfilippo et al., 1985). Therefore, the recognition of the high percentage of this species at this site is significant, not only for biostratigraphy, but also for paleoceanography. The findings of upwelling planktonic foraminifers *Globigerina bulloides* and *Neogloboquadrina dutertrei* (e.g., Caulet et al., in press) in Samples 141-859A-1H-CC (both taxa), -2H-CC, and -9P-CC (*G. bulloides* only) further corroborate the upwelling hypothesis. The low observed population density of diatom, radiolarian, planktonic, and benthic foraminifer thanatocoenoses is considered to be due to dilution by terrigenous sediments that effectively enhanced dissolution because of low dissolved silicon concentrations in the interstitial waters (see the argument regarding the CCD in the foraminifer section). Nevertheless, the rare occurrence of diatoms and the taxonomic composition of the assemblages in the uppermost part of Hole 859A do not appear to indicate upwelling environments.

Planktonic Foraminifers

Foraminifers occurred in small numbers with low diversities in 78% of the observed samples from Hole 859A and in 45% of the samples from Hole 859B. No specimens of foraminifers were obtained from the micrite-cemented stones in Cores 141-859B-18R, -27R, -29R, -37R, and -38R.

In Holes 859A and 859B (Tables 6 and 7), analysis of planktonic foraminifers permits the division of the cored sequence into a succession of warm/temperate- and cold-water-influenced assemblages, reflecting marked changes in paleoenvironments. Planktonic foraminifers are common and well preserved in the "warm" sequence, but in the "temperate" and "cold" sequences, they are small-sized, occur in few to rare abundances, and preservation is only moderate or poor. To acquire enough specimens, the entire residue was usually picked out. Downhole of Sample 141-859B-22R-CC, the specimens are decalcified and deformed, indicating the upper boundary of the lysocline. Below Sample 141-859B-32R-CC, no foraminifers were found, indicating the probable increase of the CCD in this area.

The drilled sequence of Site 859 can be generally described as an assemblage represented by the cold-adapted sinistral coiling forms of *Neogloboquadrina pachyderma* with warm/temperate interruptions, represented by *Truncorotalia truncatulinoides, Globigerina bulloides, Neogloboquadrina dutertrei, Globoconella inflata,* and *Neogloboquadrina pachyderma* (both dextral and sinistral coiling forms) in the Pleistocene, and *Globorotalia crassaformis, G. crassula, G. puncticulata, G. inflata, N. pachyderma* (dextral and also small amounts of the sinistral form) in the Pliocene.

In Samples 141-859A-1H-CC and -2H-CC, the planktonic foraminifers represent warm-water conditions and belong to the *Truncorotalia truncatulinoides* Zone of the upper Pleistocene. Sample 141-859A-9P-CC at 58.40 mbsf also contains *T. truncatulinoides,* but this is considered to represent downhole contamination. Temperate-influenced taxa are documented in the following intervals: between Sample 141-859A-11X-2, 69–74 cm, and 141-859A-13X-CC (70.54–87.60 mbsf); in Samples 141-859B-3R-CC at 80.90 mbsf and 141-859B-4R-CC at 148.50 mbsf; in the interval between Samples 141-859B-25R-2, 27–32 cm, and

Table 6. Occurrence, preservation, and estimated relative abundances of planktonic foraminifers in samples from Hole 859A.

Sample	Depth (mbsf)	Abundance	Preservation	*G. bulloides*	*N. dutertrei*	*T. truncatulinoides*	*G. inflata*	*G. crassaformis*	*G. crassula*	*N. pachyderma* D	*N. pachyderma* S	Paleotemperatures	Zones
141-859A													
-1H-CC	1.20	C	G	A	C	R	R			C	R	Warm	*T. trunc.*
-2H-CC	10.70	A	G	C		R	C						
-3H-2, 67–70 cm	12.90	R	M					F			R	Temperate	
-3H-3, 40–50 cm	14.20	B											
-3H-4, 56–60 cm	15.30	B											
-3H-CC	17.20	R	M								R		
-4H-CC	25.20	F	M								F	Cold	*Neogloboquadrina pachyderma* sin.
-5H-CC	34.70	F	M								F		
-6X-CC	41.00	R	M								R		
-7X-CC	49.00	R	M							R	R		
-8X-CC	57.40	B											
-9P-CC*	58.40	F	M	C		R	F			R	R	Warm	*T. tr.*
-10X-CC	68.30	C	M							R	C	Cold	
-11X-2, 42–47 cm	70.27	R	P								R		
-11X-2, 69–74 cm	70.54	R	P					R		R	F		
-11X-CC	77.00	R	P						R	R	F	Temperate	
-13X-CC	87.60	F	P					R	R	R	F		
-14X-CC	97.30	R	M								R		
-16X-CC	106.90	R	P								R		
-17X-CC	116.50	R	M								R	Cold	
-18X-CC	126.20	R	M							R	F		
-19X-CC	135.90	B											
-20X-CC	145.50	B											

*Downhole contamination.

Table 7. Occurrence, preservation and estimated relative abundance of planktonic foraminifers in samples from Hole 859B.

Sample	Depth (mbsf)	Abundance	Preservation	*G. inflata*	*G. crassaformis*	*G. crassula*	*G. puncticulata*	*G. ruber*	*N. pachyderma* D	*N. pachyderma* S	Paleotemperatures	Zones
141-859B												
-1R-CC	61.60	B										
-2R-CC	71.30	R	M							R	Cold	
-3R-CC	80.90	F	M		R		R		R	R	Temperate	
-4R-CC	148.50	F	P	R	R				R	F	Temperate	
-5R-CC	158.10	R	M							R	Cold	
-9R-CC	196.70	R	P							R		
-10R-CC	206.40	B										
-11R-CC	216.00	B										
-12R-CC	225.60	B										
-13R-CC	235.30	B										
-14R-CC	245.00	B										*Neogloboquadrina pachyderma*
-15R-CC	254.60	B										
-16R-1, 70–72 cm	255.32	B										
-16R-2, 20–22 cm	256.32	R	G					(R)			?	
-16R-CC	264.30	B										
-17R-CC	274.00	B										
-18R-4, 28–30 cm	278.80	B										
-18R-CC	283.50	R	M							R		
-19R-CC	293.20	B										
-20R-CC	302.80	R	P							R	Cold	
-22R-CC	321.90	R	P							R		
-23R-CC	331.50	R	P							R		
-25R-2, 27–32 cm	343.02	R	P	R	R				R	R	Temperate	
-25R-CC	350.80	R	P		R				R	R		
-26R-CC	360.45	R	P							R		*G. inflata*
-27R-CC	370.10	B									Cold	
-28R-CC	379.50	R	P							R		
-29R-5, 18–22 cm	385.72	B										
-29R-CC	389.20	R	P	R	R	R			R	R	Temperate	
-30R-CC	398.90	R	P							R	Cold	
-32R-CC	418.30	R	P							R		
-33R-CC	424.40	B										
-34R-CC	437.60	B										*G. inflata*
-36R-2,,74–77 cm	449.37	B										
-36R-CC	456.70	B										
-37R-CC	466.80	B										
-38R-CC	476.10	B										

141-859B-25-CC (343.02–350.80 mbsf); and in Sample 141-859B-29R-CC at 389.20 mbsf.

At Site 859, a sequence of two bioevents must be considered: the real first occurrence (FO) of *T. truncatulinoides* in Sample 141-859A-2H-CC, and the FO of *Globoconella inflata* in Sample 141-859B-29-CC. Unfortunately, both events are followed downhole by "cold" assemblages documented only by *N. pachyderma*. Consequently, these FOs are not thought to correlate with the general first appearance datum (FAD) of the taxa, but they are not older than the generally mentioned FAD. According to Srinivasan and Kennett (1981), the FAD of *T. truncatulinoides* is younger than 2.0 Ma and the FAD of *G. inflata* lies just below the NN15/NN16 nannofossil zone boundary at 3.2 Ma. Consequently, Sample 141-859A-2H-CC must be younger in age than 2 Ma, and Sample 141-859B-29R-CC can be dated as younger than 3.2 Ma.

Benthic Foraminifers

Benthic foraminifers occur in small amounts in most of the core-catcher samples of Hole 859A. *Melonis pompilioides, Cassidulina crassa, Ehrenbergina pupa, Bulimina mexicana,* and *Uvigerina* sp. indicate a middle to lower bathyal environment. *Uvigerina peregrina* occurs in Samples 141-859A-1H-CC, and -9P-CC, whereas *Uvigerina mantanensis* is present in Samples 141-859A-11X-2, 69–72 cm, through -16X-CC. Abundances of benthic foraminifers in Hole 859B are even less than those in Hole 859A. Samples 141-859B-1R-CC through -5R-CC contain *Pullenia bulloides, Ehrenbergina pupa,* and *Bulimina mexicana,* typically from a middle to lower bathyal environment. Downhole, *Uvigerina mantanensis* and *Nonion pompilioides* are scattered. Below Sample 141-859B-20-CC, the specimens are decalcified and broken off; below Sample 141-859B-32X-CC, no benthic foraminifers occur. The "warm/cold" successions, documented in the assemblages of planktonic foraminifers, are not recognizable in the benthic associations.

Calcareous Nannofossils

Calcareous nannofossils are few to common in Cores 141-859A-1H and -2H. The following species have been found: *Helicosphaera carteri, Coccolithus pelagicus, Cyclococcolithus leptoporus, Gephyrocapsa ericsonii, G. oceanica, Syracosphaera pulchra,* and *Emiliania huxleyi.* This sequence belongs to the upper Pleistocene and most probably to nannoplankton Zone NN21.

A significant decrease in nannoplankton can be observed from Cores 141-859A-3H to 141-859A-10X. Nannoplankton are only rare to few because of dilution and dissolution. A precise age determination was difficult. The observed species would indicate at least a late Pliocene age, based on the presence of *Helicosphaera carteri, H. sellii, Coccolithus pelagicus, Pseudoemiliania lacunosa, Cyclococcolithus macintyrei,* and small *Gephyrocapsa* sp. The rare specimens of *Reticulofenestra pseudoumbilica* and *Sphenolithus abies* are considered to be reworked. No typical Pleistocene species were observed.

Nannofossils are only scattered in the sediments from Cores 141-859A-11X to 141-859A-20X. No precise age assignment was possible. However, these fossils are not older than latest early Pliocene (NN15), as indicated by the presence of small *Gephyrocapsa* sp.

Hole 859B was washed down to 52.0 mbsf. Nannofossils are absent or extremely rare. The entire sequence is probably of late Pliocene age. As in Hole 859A, species indicating an early Pliocene age (NN15) are considered to be reworked. Definite reworkings from the lower to middle Miocene were observed. Otherwise, the assemblages observed are comparable with those from Hole 859A.

PALEOMAGNETISM

Introduction

Magnetic remanence measurements using the pass-through cryogenic magnetometer were performed on archive-half sections from Holes 859A and 859B. Some sections were not measured because of excessive drilling disturbance. The resulting magnetostratigraphy is illustrated in Figure 72. No magnetostratigraphic correlation was attempted in Hole 859A below about 30 mbsf (in Core 141-859A-5H) because of poor recovery. Coring and recovery in Hole 859B above Core 141-859B-12R was also limited, which restricted magnetostratigraphic correlation in Hole 859B to sub-bottom depths below 216 mbsf. Alternating field (AF) demagnetization in archive-half sections was conducted at 10 mT and 15 mT, and sections were measured at intervals of 10 cm. APC Cores 141-859A-3H, -4H, and -5H were oriented with the Whipstock multishot tool. Discrete specimens were also measured; stepwise AF demagnetization in these specimens was continued up to 60 mT. Magnetic susceptibility measurements on the multisensor track (MST) were performed routinely on whole-round sections.

Remanence and Susceptibility (Continuous Sections)

Figure 13 records the variation with sub-bottom depth of natural remanent magnetization (NRM) inclination before demagnetization, inclination, and intensity after 15-mT demagnetization, and bulk magnetic susceptibility, measured along continuous sections in the two holes at Site 859. Although the record down to 200 mbsf is patchy, average intensity appears to increase steadily from about 50 mAm^{-1} near the surface to about 100 mAm^{-1} at 10 mbsf, and then to remain roughly constant down to at least 90 mbsf. Intensity below the poorly recovered interval from about 100 to 200 mbsf is again lower and averages about 50 mAm^{-1}. Susceptibility also increases over the first 10 to 15 mbsf, then averages a roughly constant value of about 700 to 800 $\times 10^{-6}$ (SI). In contrast to the intensity, susceptibility does not decline below 200 mbsf, but initially increases slightly to about 1000 $\times 10^{-6}$ (SI) between about 230 and 270 mbsf. Below 270 mbsf, susceptibility follows a cyclic series of increases and decreases, with a wavelength of about 50 to 80 m.

The intensity and remanence patterns define three intervals, which equate with the units and subunits defined on sedimentological and structural grounds (see Lithostratigraphy and Structural Geology sections, this chapter). Both intensity and susceptibility increase within lithologic Unit I, reach constant levels within Subunit IIA, then diverge from each other in Subunit IIB. The increase in both intensity and susceptibility through Unit I may reflect either a changing sedimentary provenance or progressive magnetic diagenesis involving the production of magnetite by bacterial action (Mann et al., 1984; Karlin et al., 1987). Variation in the demagnetized intensity between Subunits IIA and IIB cannot simply be ascribed to differences in the total ferromagnetic mineral content, as this would require a parallel variation in the susceptibility. Demagnetized intensity also reflects the coercivity spectrum of the material; lower coercivity (magnetically "softer") sediments will preserve a smaller proportion of the NRM, and so have a lower intensity:remanence ratio after demagnetization. Variations in the coercivity spectrum between Subunits IIA and IIB might arise from differences in the magnetic mineralogy (principally the Ti content of the magnetite) or magnetic grain size.

Cyclicity in the susceptibility through Subunit IIB is not reflected in the demagnetized intensity, and so presumably is an expression of variation in the amount of low-coercivity magnetite (either paramagnetic grains less than about 0.03 µm in diameter, or multidomain grains greater than about 10 µm (McElhinny, 1973). The period of this variation is too long (50 m represents roughly 0.2 m.y. over this stratigraphic interval) to result from Milankovitch forcing, which has been shown to control susceptibility variation in other studies (e.g., Tarduno et al., 1991). Glacial-interglacial variations in sediment grain size or provenance during the Pliocene are the likely cause.

Prior to demagnetization, the NRM was plainly biased to negative (Southern Hemisphere normal polarity) inclinations. After 15-mT cleaning of the archive-half sections, the inclination record below 215 mbsf broke up into a fairly well defined (albeit discontinuous) pattern of alternating polarity. Above 40 mbsf in Hole 859A, inclination is predominantly negative, although a short reversed polarity interval occurs from 25 to 28 mbsf, inconclusive, "mixed" polarity from 29.5 mbsf to the bottom of recovery in Core 141-859A-6X at about 38.5 mbsf, and a number of shorter intervals of apparently reversed polarity at about 5.5, 9.0, and 20.0 mbsf.

Demagnetization of Discrete Specimens

Progressive AF demagnetization was conducted on discrete samples. Examples of demagnetization behavior of samples from the folded domain (see Structural Geology section, this chapter) are illustrated in Figure 14. Demagnetization vectors in Samples 141-859A-5H-1, 52–54 cm, and 141-859B-3R-2, 119–121 cm, are typical of samples from this structural interval; they display a low coercivity overprint, removed by between 5 and 25 mT, with a characteristic remanence (ChRM) indicated by demagnetization converging on the origin of the Zijderveld plot through steps above 25 mT. The overprint has an inclination similar to that of the normal dipole field and is likely to be dominantly VRM with a long relaxation time. The ChRM also has an inclination near that expected for a normal-polarity primary magnetization at this latitude. Closely spaced demagnetization intervals applied to Sample 141-859A-4H-5, 71–73 cm, suggest a slightly more complex development of overprints, but little evidence of a severe "drill-string remanence" of the type frequently reported in ODP studies (e.g., Kroenke et al., 1991) was seen in any of these specimens. Sample 141-859B-3R-4, 38–40 cm, illustrates a more complex overprinting history, with an additional, reversely polarized overprint partially isolated between 15 and 30 mT.

Samples from below the folded domain behave distinctly differently (Fig. 15). Demagnetization usually suggests the presence of extensive overprinting. Demagnetized directions do not stabilize even at the maximum AF fields applied (50 mT), implying that the ChRM in these samples has not been isolated. The overprint inclination is near that of the present field, suggesting that the overprint may be a VRM, although the high coercivity of the overprint leaves open to question whether other magnetization processes may have been involved.

The contrast between the behavior of samples from the folded domain and from below this domain implies that different magnetization processes may apply to these two parts of the sequence. Folding in the folded domain (which is recumbent in Core 141-859A-2H) should have widely dispersed the direction of any primary magnetization, contrary to the relatively uniform inclination seen in the discrete samples and in most of the demagnetized continuous core record. In effect, this part of the sequence fails the fold test, implying that the ChRM was mostly acquired synfolding or post-folding. Short intervals of reversed polarity visible in the cryogenic magnetometer record for Cores 141-859A-1H to -4H may represent localized survival of some of the primary magnetization. Reversed polarity is more prominent in Cores 141-859A-5H and -6X. Increased survival of the primary magnetization in these two cores may mark the change from recumbent folding to upright folding, which presumably indicates less deformation. Depositional magnetization was probably destroyed during soft-sediment deformation of the folded domain, and the ChRM presumably reflects resettling of magnetite grains during or after folding, perhaps accompanying dewatering. No magnetostratigraphic correlation is possible, therefore, over the folded domain.

Magnetostratigraphy and Accumulation Rates

A magnetostratigraphy can be interpreted for the sequence below the folded domain, which is best represented in Hole 859B over the interval from 216 to 291 mbsf. The behavior of discrete samples indicates that the 15-mT demagnetization available on the cryogenic magnetometer is insufficient to completely isolate the primary magnetization. However, partial demagnetization does indicate the presence of intervals of reversed polarity by the shift of inclinations to positive or low negative values. The complex series of polarity alternations over this interval can be tentatively tied to the Matuyama and Gauss chrons (Figs. 72 and 16). Distinct changes in the dominant polarity that occur at about 280 and 390 mbsf are consistent with the Gauss/Matuyama and Gilbert/Gauss chron boundaries, respectively; individual polarity intervals within the Gauss and Matuyama chrons (the Olduvai, Reunion 1 and 2, Kaena and Mammoth subchrons) can also be tentatively identified.

Attempts to fit accumulation rates to the dipping, folded, and possibly faulted sequences at Site 859 are of dubious value. Nevertheless, the sub-bottom depths of the subchron boundaries over the Gauss and Matuyama chrons are nearly linear with depth, giving a mean apparent accumulation rate over this interval (which is restricted to lithostratigraphic Subunit IIB) of about 75 to 80 m/m.y. (Fig. 17). This is significantly lower than the overall rate for lithologic Unit II (see Lithostratigraphy section, this chapter). The interval from 280 to 390 mbsf may represent one of a series of repetitions of the upper Pliocene Unit II sequence, which cumulatively result in the apparent accumulation rate of more than 280 m/m.y. for Unit II.

Structural Orientation

Multishot orientation is not available for XCB and RCB cores. Paleomagnetism was used at Site 859 for orienting both XCB and RCB cores, and the structures they contained, in geographic coordinates (see Structural Geology section, this chapter) and to determine the strike and dip of the bedding directly from the orientation of the ChRM. Orientation of the XCB and RCB cores in geographic coordinates was achieved by rotating the core around a vertical axis to bring the VRM direction into the closest possible agreement with the geocentric axial dipole field direction (declination = 000°, inclination = –65°). Where multiple components were present, the VRM was assumed to be the second lowest coercivity component in the specimens (the lowest coercivity component presumably being drill-string remanence or another similar overprint), and was fitted by Hoffman-Day analysis of the components removed at each step (the "difference vectors") (Hoffman and Day, 1978). In this method, two planes in remanence-direction space, one representing overlapping demagnetization of the ChRM and VRM, the other of VRM and the "softer" component, are defined; their intersection is taken to be the VRM direction (Fig. 18).

After orientation to geographic coordinates by this method ("Step A"), the characteristic magnetization in samples from five cores (141-859B-3R, -22R, -32R, -33R, and -34R) was rotated back around a horizontal axis to as close to the dipole direction as possible ("Step B"). The rotation defines the strike and dip of the bedding, on the assumption that fold axes are horizontal. In Table 8, strikes calculated by this method are compared with observed bedding strikes oriented in geographic coordinates us-

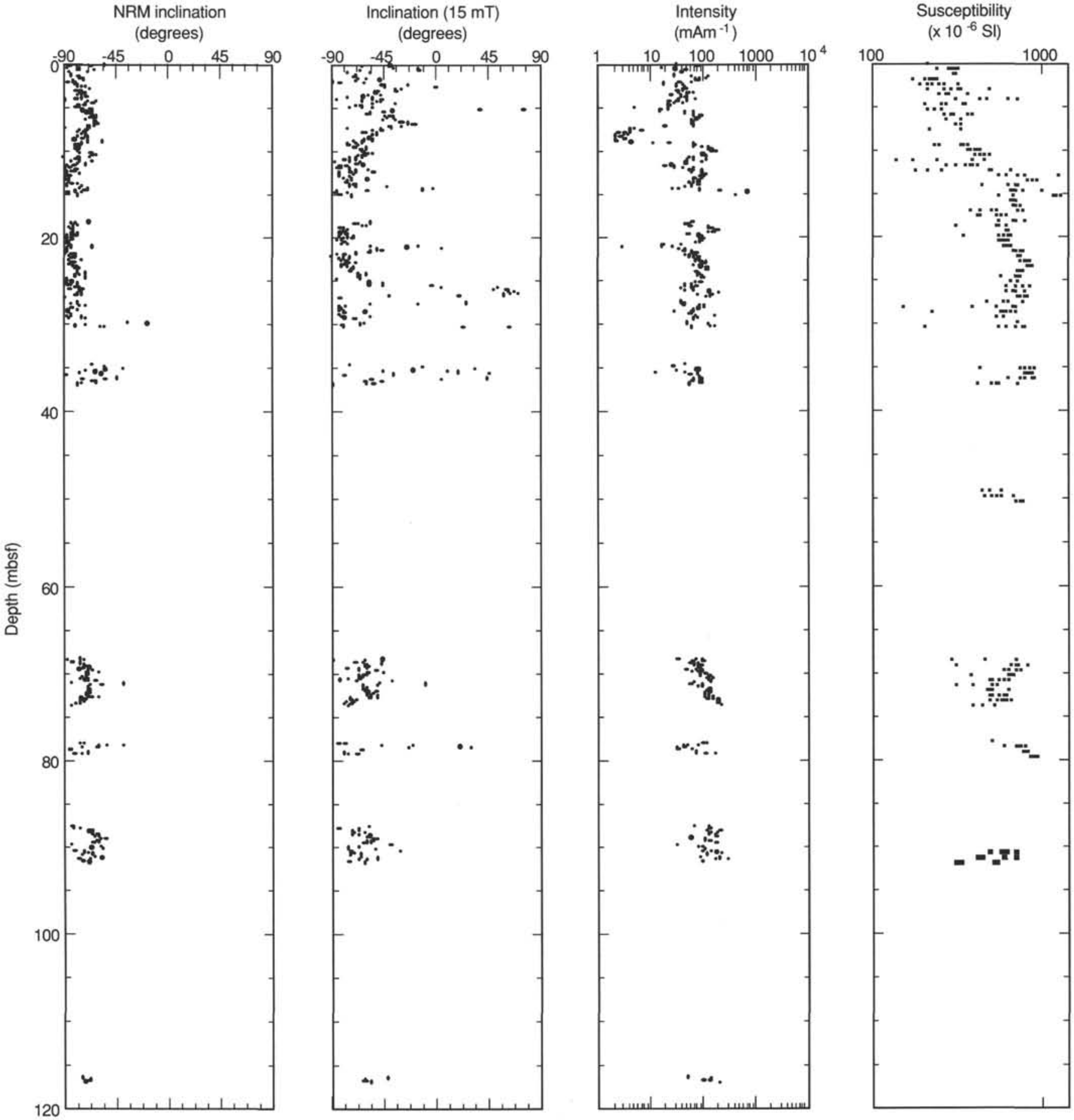

Figure 13. NRM inclination, demagnetized inclination, demagnetized intensity, and susceptibility at Hole 859A.

ing Step A. Core 141-859B-3R lies near the base of the folded domain, and one may expect that at least some samples from this core will have a ChRM acquired synfolding or post-folding, producing a poor match between observed and calculated strikes. This appears to be the case for Samples 141-859B-3R-1, 123–125 cm, 141-859A-3R-2, 119–121 cm, and possibly 141-859B-3R-2, 77–79 cm. Calculated strikes from other samples from this core, and from samples deeper in the sequence below the folded domain, agree well with observed bedding.

STRUCTURAL GEOLOGY

Summary

Three distinct structural styles can be recognized at Site 859: an upper folded domain, a central domain of flat-bedded sediments, and a lower domain comprising predominantly broken formation. The domains and their postulated boundaries are shown schematically in Figure 19, together with information

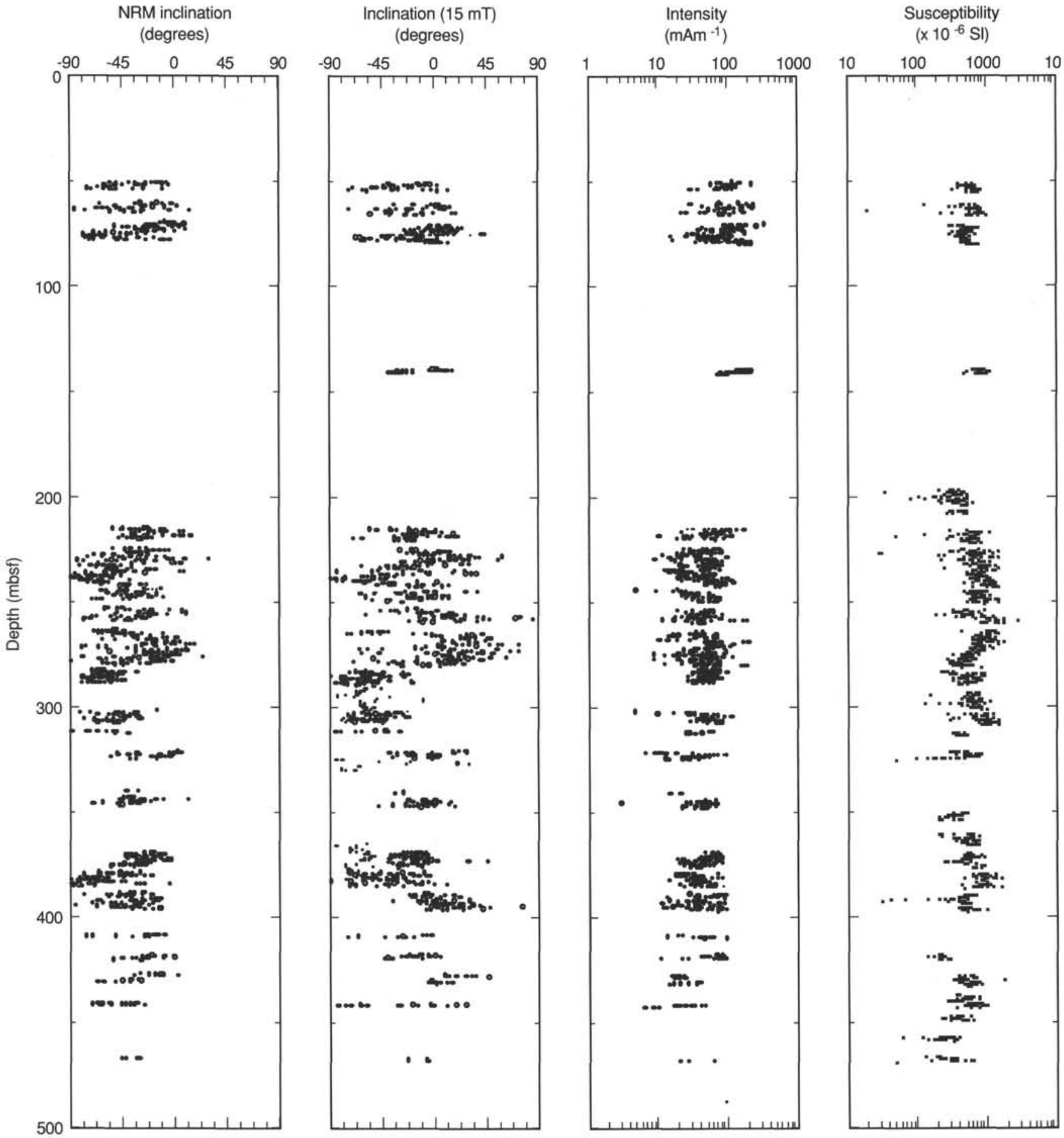

Figure 13. (Continued).

about recovery and the amount of recovered material that was coherent enough to make useful structural observations. Detailed documentation of the distribution, geometry, and nature of structures was severely hindered by poor recovery and by severe drilling and cutting disturbances. As a result, the nature and position of the contacts of the three structural domains have been estimated with much reference to the more continuous observations provided by physical properties and wireline logging (see Physical Properties and Logging sections, this chapter). The folded domain (0–80 mbsf) corresponds to lithologic Unit I and the upper part of Subunit IIA (see Lithostratigraphy section, this chapter). The flat-bedded domain (80–200 mbsf) corresponds approximately with the lower part of lithologic Subunit IIA, and the broken formation (>200 mbsf) corresponds approximately to Subunit IIB. The boundary between the flat-bedded domain and the broken formation corresponds to a transition from seismically transparent material to a region having considerable seismic noise (see Seismic Stratigraphy chapter, this volume).

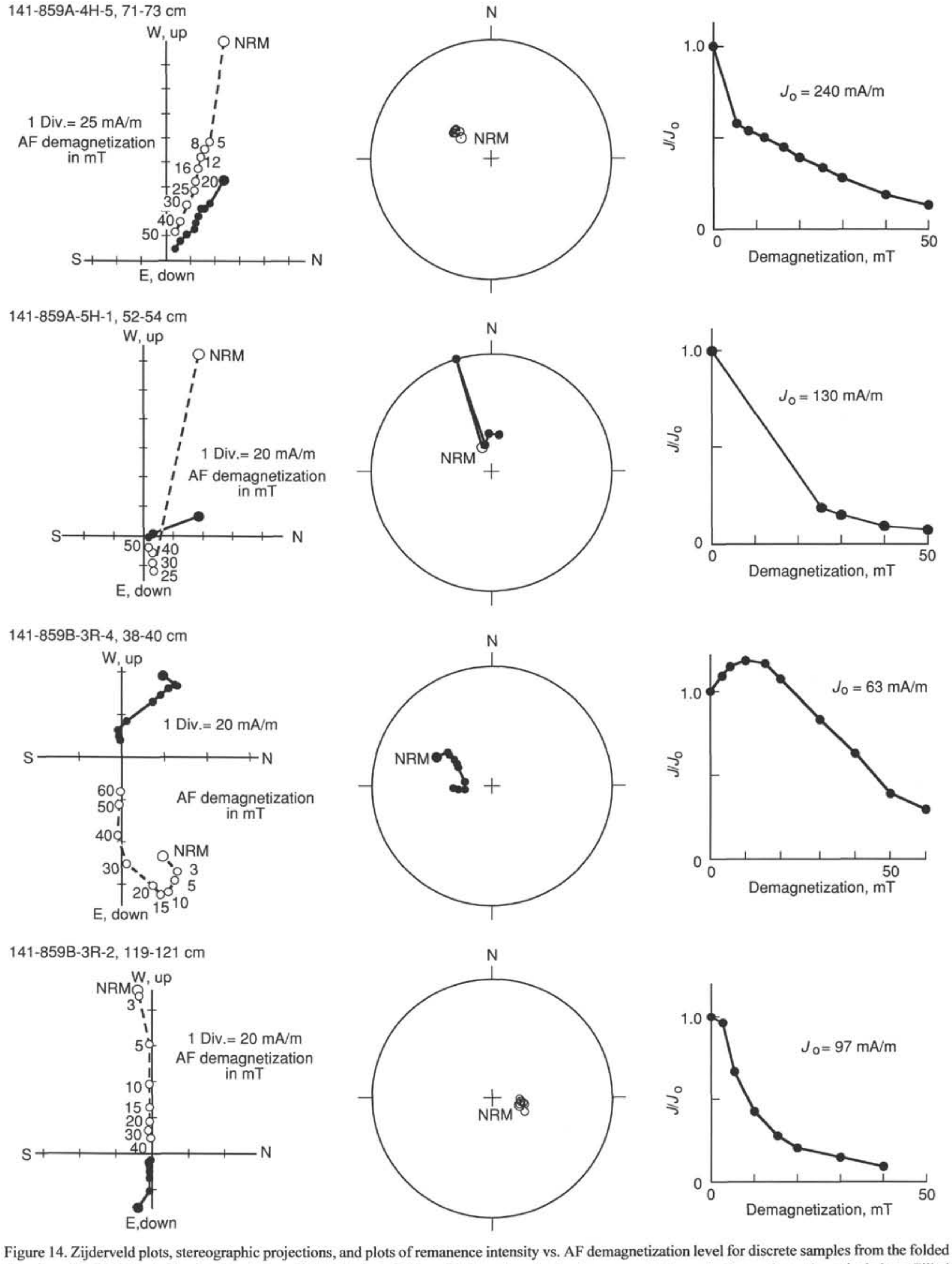

Figure 14. Zijderveld plots, stereographic projections, and plots of remanence intensity vs. AF demagnetization level for discrete samples from the folded domain at Site 859. North direction is arbitrary. Filled circles in Zijderveld plots show declination; open circles are in the north-south vertical plane. Filled (open) circles in stereographic projections are in the lower (upper) hemisphere.

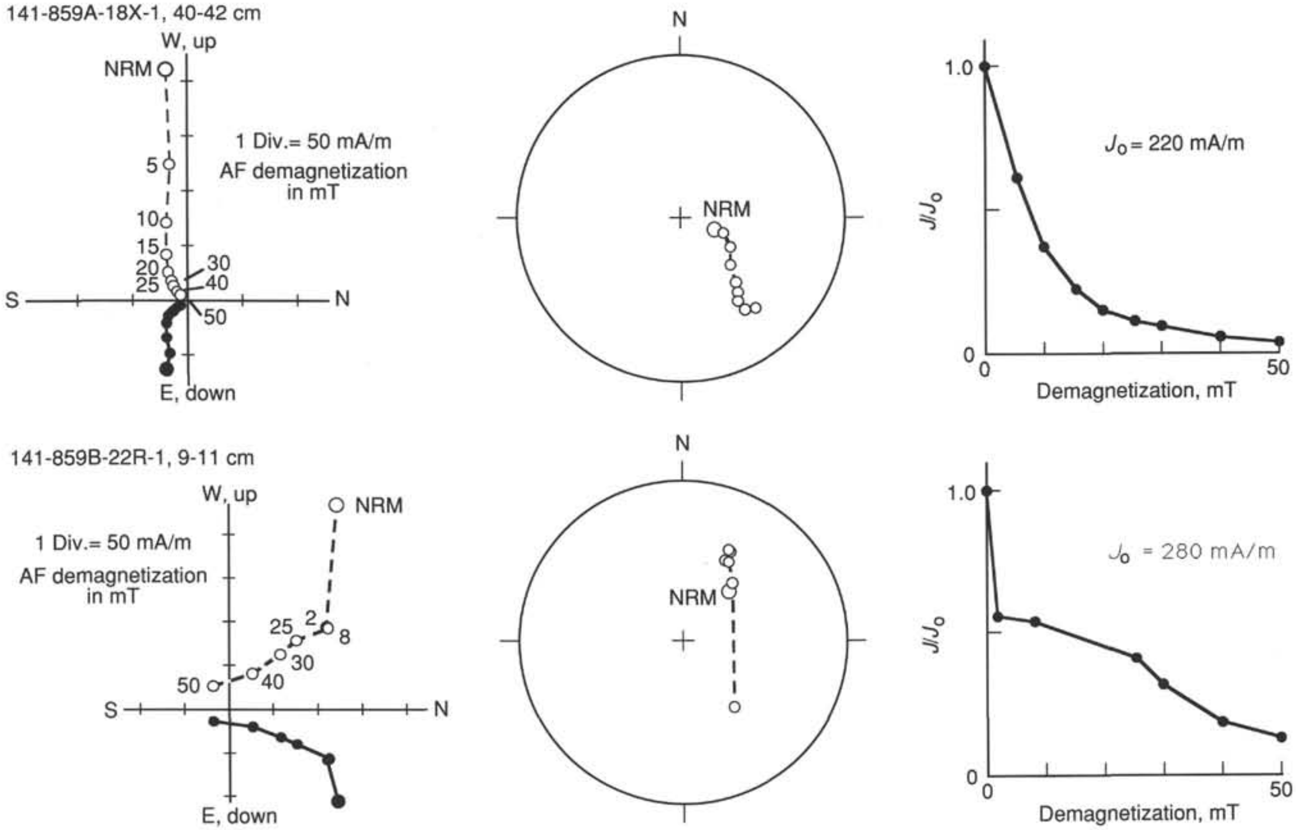

Figure 15. Zijderveld plot, stereographic projection, and plot of remanence intensity vs. AF demagnetization level, for discrete samples from below the folded domain at Site 859. Sample 141-859A-18X-1, 40–42 cm, is from the flat-bedded domain; Sample 141-859B-22R-1, 9–11 cm, is from the broken formation.

Detailed structural data recorded on spreadsheets for Holes 859A and 859B are presented in Table 9. Wherever possible, structural measurements were reoriented into a geographical reference frame. Sections where reorientation was possible are shown in Figure 19.

Folded Domain

Structures characteristic of the folded domain were observed in cores between 1.5 and about 80 mbsf. The data set is based almost entirely on Cores 141-859A-2H, -3H, -5H, and 141-859B-3R. The position of the contact with the flat-bedded domain is reasonably well constrained by structural data alone. Structural style within the folded domain varies. For instance, the top of the domain contains recumbent folds, whereas upright folds are prevalent lower down. However, most of the structures in this domain can be related to each other, and the heterogeneities in structural style can be explained in a single model.

Recumbent Folds

Recumbent fold closures were observed in Core 141-859A-2H (between 1.2 and 6.7 mbsf). Three fold closures can be seen; another one can be postulated at a change in bedding dip. Faint color bands representing bedding laminations can be traced around the folds and are highlighted by surface fractures that developed preferentially along bedding surfaces during splitting of the core (Fig. 20). Two of the observed folds are cut at sufficiently high angles to the fold axis to show that they are tight to isoclinal recumbent folds. Dip isogon analysis (Ramsay, 1967) indicates that the hinge regions of the folds have Ramsay class 2 geometries, whereas the limbs have Ramsay class 1c or more complex geometries. Traces of axial surfaces dip at about 10° relative to the core axis. The fold axis at 6.69 mbsf (Section 141-859A-2H-4 at 109–112 cm) plunges at 14° and the axial surface at this point has a true dip of 33°. The third observed fold is an eye structure (Section 141-859A-2H-3, 73–74 cm), indicative of a curvilinear fold axis.

Upright Folds

Folds having steep axial surfaces can be observed in Cores 141-859A-5H and -3R.

At 26.94 mbsf, a single upright antiform was dentified (Section 141-859A-5H-2, 25–35 cm). The fold profile is defined by a bed of silty material. The fold axis plunges at 28° and the axial surface has a true dip of about 80°.

In Core 141-859B-3R, between 74.0 and 79.7 mbsf, three fold closures were identified. The traces of bedding around these folds are defined by narrow zones of clay alignment and by color banding. The traces of these folds suggest that they are open and moderately dipping to recumbent. However, the core face cuts fold axes and axial surfaces obliquely, so that these profiles may be misleading. One measurement of a fold axis indicates a plunge of 76°. The corresponding axial surface is nearly vertical. The folds are probably much tighter than suggested by the observed profiles.

Faults

A contact with a true dip of 14° (Fig. 21) at 14.84 mbsf (interval 141-859A-3H-3, 134–136 cm) juxtaposes steeply dip-

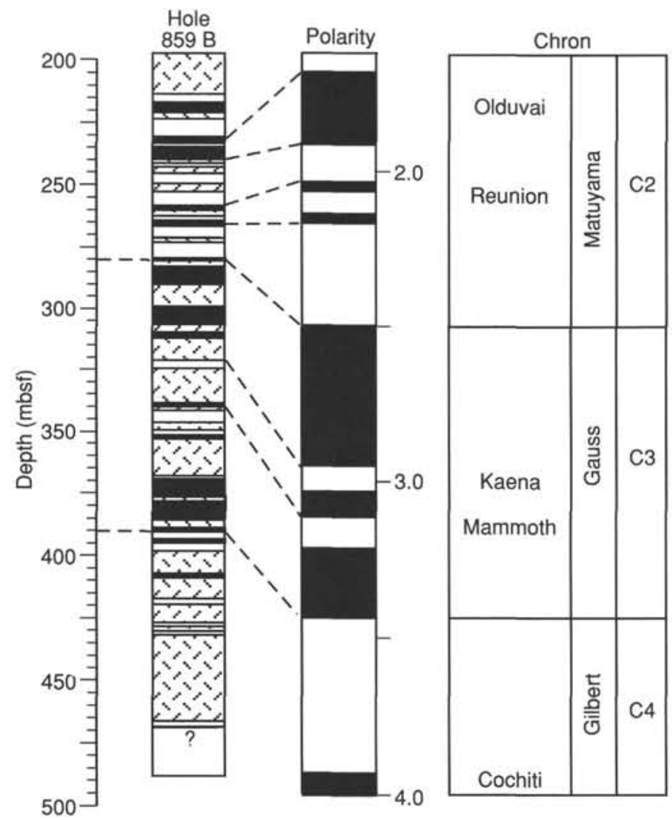

Figure 16. Magnetostratigraphic correlation of part of the sequence in Hole 859B with the standard magnetostratigraphy of Berggren et al. (1985a, 1985b). Black = normal polarity, white = reversed polarity, cross-hatched = unknown or mixed polarity.

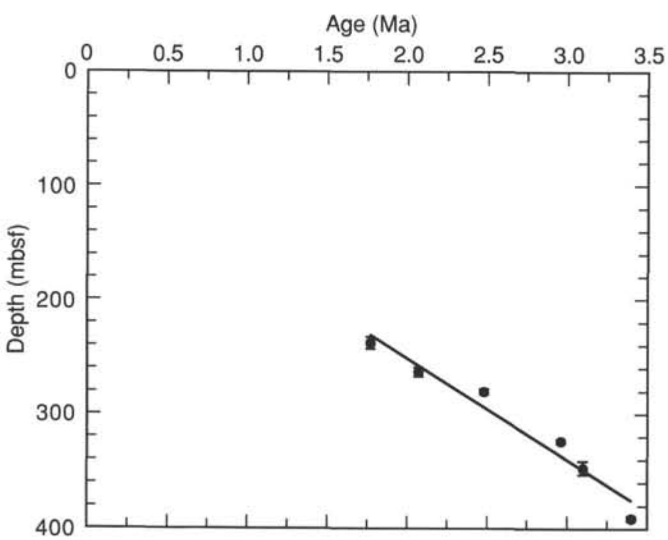

Figure 17. Age vs. depth for the magnetostratigraphic interval represented in Figure 16.

ping bedding (55°–75°), such as that characteristic of Core 141-859A-3H-2, above flat-bedded sediments. It is unlikely that this represents an original sedimentary contact. The fault is discrete and shows no development of fault rock. No slickenlines were observed. This was the only observed fault, but it is possible that others exist in this domain.

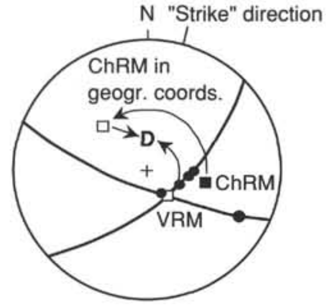

Figure 18. Orientation method for rotary drilled cores. A stereographic projection of results from Sample 141-859B-22R-1, 9–11 cm, is shown. Dots indicate difference vectors, including a VRM component; great circles fitted to these intersect to define the VRM direction. This is rotated around a vertical axis to bring it close to the dipole direction ("D"); the mean ChRM is rotated through the same angle to bring it into "geographic" coordinates. Further rotation of the corrected ChRM direction around a horizontal axis to bring it as close as possible to the dipole direction defines the strike and dip of bedding.

Table 8. Bedding orientations determined directly from paleomagnetic data, and comparison with observed beds oriented by VRM, Hole 859B.

Sample number	Dip (from paleomagnetics)	Strike[a] (from paleomagnetics)	Strike[a] (from beds oriented by VRM)
141-859B-			
3R-1, 123–125	89	122	214
3R-2, 77–79	45	061	091
3R-2, 119–121	44	249	157
3R-4, 38–40	50	068	053
3R-5, 52–54	68	257	274
22R-1, 4–6	41	018	No data
32R-2, 28–30	12	216	237
33R-2, 50–52	25	256	252
34R-4, 43–45	79	018	No data

[a] Strike is quoted clockwise from dip azimuth.

Isolated near-vertical veins (or dismembered beds[?]) of sand and silty sand were observed in Sections 141-859A-5H-4, 45 cm, through -5H-6, 72 cm. Although these features occur below a zone of inclined bedding and fold closures, they are less continuous than the bedding and more likely represent some kind of clastic vein.

A complex clastic vein occurs at the base of the folded section in interval 141-859A-3H-3, 113–135 cm. In this case, lighter-colored silty material appears to have been injected upward into darker, more clayey material (Fig. 21). Although irregular in outline, the boundaries of the silty zone are sharply defined. The lower termination of this structure corresponds to the fault described in the previous section.

True Orientation of Structures

It was possible to rotate Cores 141-859A-2H, -3H, -4H, -5H, and 141-859B-3R into geographical coordinates. All rotations were done around vertical axes, and the magnitude of rotations for each core are shown in Table 10. The rotations for each core are justified below. In Core 141-859A-2H, the vector mean of the directions of remanent magnetization after demagnetization at 15 mT has an orientation −61° to 278° in the core reference frame with a 95% confidence cone of 10°. These data were used for reorientation of Core 141-859A-2H. In Core 141-859A-3H, multishot data indicate that 0° in the core reference frame lies 223° clockwise (looking downcore) of magnetic north. In the Chile Triple Junction margin area, the magnetic declination is 14° east.

For comparison, the vector mean of the directions of remanent magnetization in this core after demagnetization at 15 mT has an orientation −76° to 326° in the core reference frame, with a 95% confidence cone of 8°. The paleomagnetic information and multishot data agree to within 20°. In Core 141-859A-5H, multishot data indicate that 0° in the core reference frame lies 86° clockwise (looking downcore) of magnetic north. For comparison, the vector mean of the directions of remanent magnetization after demagnetization at 15 mT, for sections having normal polarity only, has an orientation −84° to 035° in the core reference frame with a 95% confidence cone of 11°. The paleomagnetic information and multishot data agree to within 40°. Because the paleomagnetic inclinations are very steep, the multishot data are thought to be more reliable, and multishot rotations were used for Cores 141-859A-3H and 141-859A-5H. Paleomagnetic data used to orient Core 141-859A-2H should be reliable as the direction of remanent magnetization after demagnetization at 15 mT is likely to have been acquired after deformation (see Paleomagnetism section, this chapter). The reasonable agreement of paleomagnetic with multishot data in Cores 141-859A-3H and -5H also supports the use of paleomagnetic data for orienting Core 141-859A-2H.

In rotary drilled cores, reorientation is more problematic. In Core 141-859B-3R, a more complicated reorientation procedure was applied by the paleomagnetists. These studies (see Paleomagnetism section, this chapter) suggest that Sections 141-859B-3R-2, -4, and -5 have not been significantly rotated with respect to each other. These sections were oriented in the geographical reference frame using the viscous remanence component of magnetization. This reorientation is not as well constrained as those in the piston cores.

Structural data in the core reference and geographical reference frames are shown in Figure 22.

Model for Formation of the Folded Domain

A schematic illustration of the structures observed in the folded domain and their relative orientations is shown in Figure 23. The upper recumbent fold structures are consistent with development by simple shear. The types 2 to 1c fold geometries are most easily developed by shearing parallel to the axial surface, and curvilinear fold hinges are generally indicative of shear origin (Cobbold and Quinquis, 1980). Were the dominant fold axis orientation perpendicular to shear, as should be the case for mildly curvilinear folds, then these folds should indicate east-northeast or west-southwest shearing. This is consistent with the observation of the eye structure in the core face, which is oriented at about 170° in the geographical reference frame. Whether the shearing relates to downslope motion driven by gravity or to thrusting in response to plate tectonic convergence cannot be assessed; at this locality, the shear directions are consistent with both possibilities. Clastic veins indicate a small amount of extension perpendicular to transport. Upright folds also indicate shortening subparallel to transport. These may be an indication that the structures were developed in response to thrusting, rather than gravity-driven processes, although extension perpendicular to transport has been recorded in slump sheets at the bottom of a glide slope (Fitches et al., 1986). The structures are consistent with east-northeast or west-southwest transport, with shearing higher up in the sequence and transport-parallel shortening deeper down.

Flat-bedded Domain

Apart from flat bedding, often difficult to distinguish from drilling biscuits, the only structure observed in this domain was a breccia at 81.1 mbsf. The base of this unit is not clearly defined because of the absence of recovery between about 150 and 200 mbsf. Other major changes, such as in velocity (see Wireline Measurements section, this chapter) and in porosity (see Physical Properties section, this chapter) occur from 200 to 240 mbsf, suggesting that this is the likely depth for the change in structural style. The contact between the flat-bedded domain and the broken formation may be an unconformity or a fault.

Breccia

A zone of breccia has been preserved in Section 141-859A-13X-CC at 17–23 cm (Fig. 24). The breccia consists of semiconsolidated clayey silt, silty clay, and clay. The more competent silt beds thicken and thin along their length and have been offset by normal microfaults that pass into the clay beds and then disappear. The ductility contrasts and style suggest that brecciation occurred by layer-parallel extension, necking, and faulting in semilithified beds of differing degrees of consolidation. Deformation may have been triggered by any one of several mechanisms: slumping and sliding, faulting of soft sediments, or drilling disturbance.

Broken Formation

Much of the core recovered below about 200 mbsf was too dismembered to permit useful structural observations. However, where coherent sections exist, they contain one or more of the suite of structures described here that together indicate broken formation; that is, originally layered sediments that have undergone significant stratal disruption (Raymond, 1984). Broken formation continues to the base of Hole 859B and, presumably, to the basal décollement of the accretionary prism.

Deformation Bands

A series of structures that appear as narrow, dark, or pale seams was identified in the broken formation. Similar structures observed in accretionary sediments sampled through ocean drilling have been termed shear bands (Taira, Hill, Firth, et al., 1991; Byrne et al., in press; Maltman et al., in press), kinks (Lundberg and Moore, 1986), and deformation bands (Karig and Lundberg, 1990). Mesoscopically, the deformation bands are similar to web structures described from onshore and offshore accretionary complexes (Cowan, 1982, 1985; Byrne, 1984; Lundberg and Moore, 1986). The structures observed during Leg 141 (see also Structural Geology section, Site 860 chapter, this volume) form a continuum with subtle differences in geometry, displacement, internal strain, and microstructure. Because most accommodate deformation, we have chosen the term deformation band to refer to this family of structures.

At Site 859, deformation bands in claystones and siltstones are distinctly different and have been described separately.

Deformation Bands in Claystones

In claystones, deformation bands comprise finite dark layers 0.5 to 4 mm thick, either within clayey silt horizons (Fig. 25) or along discrete lithological contacts (Fig. 26). Deformation bands are variable in orientation (Fig. 27). Some anastomose on the 10-cm scale to produce isolated pods of a different lithology than that outside the pod (Fig. 25). Deformation bands in claystones in Sections 141-859B-32R-2 and -33R-2 have been reoriented using the viscous component of remanent magnetism (see Paleomagnetism section, this chapter). The poles to deformation bands from Section 141-859B-33R-2 fall on a great circle, with a pole oriented at 03° to 076°. This distribution reflects the anastomosing nature of the deformation bands. The rotations used to reorient these data are shown in Table 11.

In rare instances, the surfaces of these deformation bands can be exposed by excavation in the working half of the core. Two such surfaces were observed (intervals 141-859B-18R-5, 95–110 cm, and -26R-2, 63–65 cm). In both cases, the surfaces are polished and contain submillimeter-spaced slickenlines (Fig. 28)

Table 9. Tabulation of detailed structural data on a section-by-section basis for holes 859A and 859B.

Core, section, interval (cm)	Depth (mbsf)	X-ref hand sheets	Photo(?)	ID	Identifier	Thickness (cm)	Care Face Orientation		Corrected core reference frame			Reorient Method	Corrected geographical reference frame			Comments
							App. dip	Direction	Strike	Dip	Dir.		Strike	Dip	Dir.	
Hole 859A																
141A-859A-																
1H-1	0.00	NIL														
1H-CC	1.00	NIL														
2H-1, 97–99	2.17	1		B	Bedding		18	270	135	25	W	Palaomag	217	25	W	Remanent magnetism after 15 mT.
2H-2, 23–26	2.93	1		Fo	Fold	2										
2H-2, 24–25	2.94	1		Fap	Axial plane		16	270								
2H-2, 37–50	3.07	2		B	Bedding		0	0								
2H-2, 78–83	3.48	3		B	Bedding		16	270								
2H-2, 122–126	3.92	4		B	Bedding		30	27	203	32	W	Paleomag	285	32	N	
2H-2, 146–149	4.16	5		B	Bedding		50	270								
2H-3, 10–12.5	4.30	1		B	Bedding		25	270	180	25	W	Paleomag	262	25	N	
2H-3, 30–36	4.50	2		B	Bedding		24	270	180	24	W	Paleomag	262	24	N	
2H-3, 72–72	4.92	3		B	Bedding		0	90	90	6	S	Paleomag	172	6	W	
2H-3, 74–74	4.94	4		Fo	Fold	0.5										
2H-3, 96–102	5.16	5		B	Bedding		34	270	202	36	W	Paleomag	284	36	N	
2H-3, 111–116	5.31	6		B	Bedding		48	270								
2H-4, 8–12	5.68	1		B	Bedding		0	0	0	0		Paleomag	82	0		
2H-4, 109–112	6.69	2	Yes	F	Fold	2										
2H-4, 109–112	6.69	2	Yes	Fax	Fold axis											14/235 Fold axis reorients to 14/317.
2H-4, 109–112	6.69	2	Yes	Fap	Axial plane		8	90	78	33	S	Paleomag	160	33	W	
2H-4, 111–115	6.71	3		B	Bedding		18	90	320	23	E	Paleomag	222	23	E	
2H-5, 9–9	7.19	1		B	Bedding		3	270	103	13	S	Paleomag	185	13	W	
2H-5, 26–27	7.36	2		B	Bedding		9	90	59	17	S	Paleomag	141	17	W	
2H-5, 102–103	8.12	3		B	Bedding		5	270								
2H-6, 16–17	8.76	1		B	Bedding		4	90	84	34	S	Paleomag	166	34	W	
2H-6, 26–27	8.86	2		B	Bedding		7	270	125	12	S	Paleomag	207	12	W	
2H-6, 104–105	9.64	3		B	Bedding		2	270	117	4	S	Paleomag	199	4	W	
2H-7	10.10	NIL														
2H-CC	10.60	NIL														
3H-1, 21–23	10.91	1		B	Bedding		7	90	325	9	E	Multishot	202	9	N	Double line towards 043° magnetic.
3H-1, 21–23	10.91	1		B	Bedding		30	90								
3H-1, 121–128	11.91	2		B	Bedding		50	90	358	50	E	Multishot	235	50	N	
3H-1, 124–125	11.94	3		B	Bedding		19	96	27	21	E	Multishot	258	21	N	
3H-2, 24–25	12.34	1		B	Bedding		10	270	169	10	W	Multishot	46	10	S	
3H-2, 55–62	12.65	2		B	Bedding		53	270	156	55	W	Multishot	33	55	S	
3H-2, 94–107	13.04	3		B	Bedding		85	270								
3H-2, 108–117	13.18	4		B	Bedding		73	270	174	73	W	Multishot	51	73	S	
3H-3, 110–135	14.60	1	Yes	CV	Clastic vein?	4	84	90	0	84	E	Multishot	321	84	N	Some concern over origin.
3H-3, 134–136	14.84	2	Yes	F	Fault		12	270	150	14	W	Multishot	27	14	S	Must be tectonic, perhaps gravity glide.
3H-4, 60–150	15.60	1	Yes	CV	Clastic vein?	2.5	90	90	0	90	W	Multishot	327	90	S	En echelon. Possibly drill related?
3H-CC, 0–24	16.50			CV	Clastic vein?	2.5										Continuation of Section 4.
4H-1	16.70	NIL														
4H-2	18.20	NIL														
4H-3	19.70	NIL														
4H-4	21.10	NIL														
4H-5	22.60	NIL														
4H-6	24.10	NIL														
4H-CC	24.70	NIL														
5H-1, 33–43	25.20	1		B	Bedding		47	90	41	55	E	Multishot	141	55	N	
5H-2, 0–14	26.70	2		B	Bedding		72	90								
5H-2, 24–57	26.94	3		Fax	Fold axis											28/180 Estimate only.
5H-3, 27–41	28.47	6		B	Bedding		72	90	57	80	S	Multishot	157	80	E	
5H-4, 45–92	30.15	4		CV	Clastic vein	0.2–1.0	78	270	144	80	W	Multishot	244	80	S	

5H-5	31.20	NIL														
5H-6, 55–170	33.25	5		B	Bedding	0.5	88	270	175	88	W	Multishot	275	88	S	
6X-1	34.70	NIL														
6X-2	36.20	NIL														
6X-CC	37.70	NIL														
7X-1	41.00	NIL														
7X-CC	42.50	NIL														
8X-1	49.00	NIL														
8X-CC	50.50	NIL														
9P-1	57.40	NIL														
10-CC	58.40	NIL														
11X-1	68.30	NIL														
11X-2	69.80	NIL														
11X-3	71.30	NIL														
11X-4	72.80	NIL														
11X-CC	74.30	NIL														
12P-1	77.00	NIL														
13X-1	78.00	NIL														
13X-2	79.50	NIL														
13X-CC, 15–24	81.15	1	yes	SBr	Sedimentary breccia	9										
13X-CC, 15–24	81.15	2	yes	FBr	Fracture in breccia	64	270	22	66	W						
13X-CC, 15–24	81.15	3	yes	FBr	Fracture in breccia	50	90	5	50	E						
14X-1	87.60	NIL														
14X-2	89.10	NIL														
14X-3	90.60	NIL														
14X-4	92.10	NIL														
14X-CC	93.60	NIL														
15P-1	98.80	NIL														
16X-CC, 30–32	100.50	1	Yes	B	Bedding		0	0	0	0						
17X-CC	106.90	NIL														
18X-1	116.50	NIL														
18X-CC	118.00	NIL														
19X-CC	126.20	NIL														
20X-CC	135.90	NIL														
21P-1	145.50	NIL														
Hole 859B																
1R-1	52.00	NIL														
1R-2	53.50	NIL														
1R-3	55.00	NIL														
1R-CC	56.50	NIL														
2R--1	61.60	NIL														
2R--2	63.10	NIL														
2R--3	64.60	NIL														
2R--4	66.10	NIL														
2R--CC	67.60	NIL														
3R-1, 26–27	71.56	1		B	Bedding		5	90	22	5	E					
3R-2, 14–17	72.94	2		B	Bedding		29	270	117	51	S	Paleomag	149	51	N	Complex rotation.
3R-2, 14–17	72.94	2		B	Bedding		37	90								Viscous remenanence at 1480.
3R-2, 52–56	73.32	3		B	Bedding		48	90	40	55	E	Paleomag	72	55	N	
3R-2, 120–140	74.00	4		B	Bedding		46	270	123	62	S	Paleomag	155	62	E	Three parts of a fold structure.
3R-2, 120–140	74.00	4		B	Bedding		43	90								Three parts of a fold structure.
3R-2, 120–140	74.00	4		B	Bedding		84	90								Three parts of a fold structure.
3R-3	74.30	NIL														
3R-4, 52–59	75.02	5		B	Bedding		50	90	33	55	E	Paleomag	65	55	N	
3R-5, 15–33	75.85	6		Fax	Fold axis											76/029 Reorients to 77/241.
3R-5, 15–33	75.85	6		Fap	Fold axial surface				259	89	N	Paleomag	291	89	S	
3R-5, 15–33	75.85	6		B	Bedding		71	90	9	71	E	Paleomag	41	71	N	Above fold.
3R-5, 15–33	75.85	6		B	Bedding		60	270	166	61	W	Paleomag	198	61	E	Below fold.
3R-5, 38–44	76.08	7		B	Bedding		54	90	35	61	E	Paleomag	67	61	N	
3R-5, 60–65	76.30	8		B	Bedding		42	90	53	56	S	Paleomag	85	56	N	

Table 9 (continued).

Core, section, interval (cm)	Depth (mbsf)	X-ref hand sheets	Photo(?)	ID	Identifier	Thickness (cm)	Care Face Orientation		Corrected core reference frame			Reorient Method	Corrected geographical reference frame			Comments
							App. dip	Direction	Strike	Dip	Dir.		Strike	Dip	Dir.	
Hole 859B (cont.)																
3R-5, 100–110	76.70	9		B	Bedding		53	90	30	57	E	Paleomag	62	57	N	
3R-6, 80–83	78.00	10		B	Bedding		48	270	154	51	W					
3R-6, 80–83	78.00	10		B	Bedding		24	90	11	24	E					
3R-7, 15–18	78.85	11		B	Bedding		54	270	149	58	W					
3R-7, 20–25	78.95	12		B	Bedding		20	270								
3R-7, 45–50	79.15	13		B	Bedding		32	90	61	52	S					
3R-7, 101–103	79.71	14		B	Bedding		22	90	52	33	S					Above fold.
3R-7, 101–103	79.71	14		B	Bedding		10	270	111	26	S					Below fold.
3R-8, 24–32	80.44	15		B	Bedding		42	270	158	44	W					
3R-CC	80.70	NIL														
4R-1	140.00	NIL														
4R-2	141.50	NIL														
4R-CC	143.00	NIL														
9R-CC	187.10	NIL														
10R-1	196.70	NIL														
10R-2	198.20	NIL														
10R-3	199.70	NIL														
10R-4	201.20	NIL														
10R-5	202.70	NIL														
10R-CC	204.20	NIL														
11R-1	206.40	NIL														
11R-CC	207.90	NIL														
12R-1	216.00	NIL														
12R-2	217.50	NIL														
12R-3	219.00	NIL														
12R-4	220.50	NIL														
12R-5	222.50	NIL														
12R-CC	223.50	NIL														
13R-1	225.60	NIL														
13R-2	225.90	NIL														
13R-3	227.40	NIL														
13R-4	228.70	NIL														
13R-5	229.30	NIL														
13R-6	230.60	NIL														
13R-7	232.00	NIL														
13R-CC	233.50	NIL														
14R-1	235.30	NIL														
14R-2	236.80	NIL														
14R-3	238.30	NIL														
14R-4	239.80	NIL														
14R-5	241.30	NIL														
14R-6	242.80	NIL														
15R-1	245.00	NIL														
15R-2	246.50	NIL														
15R-3	248.00	NIL														
15R-4	249.50	NIL														
15R-5	251.00	NIL														
16R-1	254.60	NIL														
16R-2	256.10	NIL														
16R-3	257.60	NIL														
16R-4, 10–30	259.20	1	Yes	J	Joint		57	90	5	57	E					
16R-4, 10–30	259.20	2	Yes	J	Joint		63	90	25	65	E					
16R-4, 10–30	259.20	3	Yes	J	Joint		50	270	20	52	W					
16R-4, 10–30	259.20	4	Yes	J	Joint		55	90	4	55	E					

16R-4, 10–30	259.20	5	Yes	J	Joint		58	90	32	62	E	
16R-4, 10–30	259.20	6	Yes	J	Joint		55	90	6	55	E	
16R-4, 10–30	259.20	7	Yes	J	Joint		88	270	12	87	W	
16R-4, 10–30	259.20	8	Yes	J	Joint		28	270	33	32	W	
16R-4, 10–30	259.20	9	Yes	J	Joint		16	270	26	17	W	
16R-4, 10–30	259.20	10	Yes	J	Joint		62	90	3	62	E	
16R-4, 10–30	259.20	11	Yes	J	Joint		30	90	12	31	E	
16R-4, 10–0	259.20	12	Yes	J	Joint		68	90	12	68	E	
16R-CC	260.60	NIL										
17R-1, 53–54	264.83	1		Br	Breccis							
17R-1, 53–54	264.83	1		McV	Mineral vein, calcite		58	270	0	62	W	
17R-1, 53–54	264.83	1		McV	Mineral vein, calcite		55	270	48	56	W	
17R-1, 53–54	264.83	1		FBr	Fault in breccia		58	90	332	61	E	
17R-1, 53–54	264.83	1		FBr	Fault in breccia		85	270	170	85	W	
17R-1, 53–54	264.83	1		FBr	Fault in breccia		68	90	9	21	E	
17R-2, 130–135	267.10	2		S	Seams							
17R-3	267.30	NIL										
17R-4	268.80	NIL										
17R-5	270.30	NIL										
17R-6	271.80	NIL										
17R-7	273.30	NIL										
18R-1	274.00	NIL										
18R-2	275.50	NIL										
18R-3	277.00	NIL										
18R-4	278.50	NIL										
18R-5, 28–30	280.28	1	Yes	SP	Shear plane		24	90	312	33	N	
18R-5, 30–30	280.30	2		SP	Shear plane		11	270	258	43	N	
18R-5, 50–65	280.50	3		SP	Shear plane		43	270				
18R-5, 70–90	280.70	4	Yes	W	Web strand		72	270	16	72	W	
18R-5, 70–90	280.70	4	Yes	W	Web strand		45	270	21	48	W	
18R-5, 70–90	280.70	4	Yes	W	Web strand		42	90	33	47	E	
18R-5, 70–90	280.70	4	Yes	W	Web strand		60	90	73	80	S	
18R-5, 95–110	280.95	5	Yes	SP	Shear plane		55	270	20	57	W	
18R-5, 95–110	280.95	5	Yes	SL	Slickenline							57/290 Slick direction.
18R-CC	281.50	NIL										
19R-1	283.50	NIL										
19R-2	285.00	NIL										
19R-3, 80–120	287.30	1		FC	Fracture cleavage	40	24	270	206	26	W	
19R-4, 74–140	288.74	2		FC	Fracture cleavage	65	3	90	272	54	N	
19R-4, 74–140	288.74	2		FC	Fracture cleavage	65	10	90	76	37	S	
19R-CC	289.50	NIL										
20R-1	293.20	NIL										
20R-2	294.70	NIL										
20R-3	296.20	NIL										
20R-4	297.70	NIL										
20R-5	299.20	NIL										
20R-6	300.70	NIL										
20R-CC	302.20	NIL										
21R-1, 135–150	304.15	1		FC	Fracture Cleavage		12	270	264	63	N	
21R-2, 15–80	304.45	2		FC	Fracture Cleavage		27	270	211	31	W	
21R-2, 15–80	304.45	2		FC	Fracture Cleavage		37	90	357	37	E	
21R-3, 15–30	305.95	3		FC	Fracture Cleavage		34	90	336	37	E	
21R-3, 15–30	305.95	3		FC	Fracture Cleavage		64	270	194	65	W	
21R-4, 50–70	307.80	4		FC	Fracture Cleavage		32	90	281	72	N	
21R-4, 50–70	307.80	4		FC	Fracture Cleavage		72	270	191	72	W	
22R-1	312.20	NIL										
22R-CC	313.70	NIL										
23R-1	321.90	NIL										
23R-2	323.40	NIL										
23R-3, 30–40	325.20	1		Fr	Fracture		46	270	190	46	W	
23R-3, 30–40	325.20	1		Fr	Fracture		48	90	333	51	E	
23R-3, 30–40	325.20	1		Fr	Fracture		82	90	359	82	E	

Table 9 (continued).

Core, section, interval (cm)	Depth (mbsf)	X-ref hand sheets	Photo(?)	ID	Identifier	Thickness (cm)	Care Face Orientation		Corrected core reference frame			Reorient Method	Corrected geographical reference frame			Comments
							App. dip	Direction	Strike	Dip	Dir.		Strike	Dip	Dir.	
Hole 859B (cont)																
23R-CC	326.40	NIL														
25R-1	341.20	NIL														
25R-2	342.70	NIL														
25R-3	344.20	NIL														
25R-4	345.70	NIL														
25R-5	347.20	NIL														
26R-1, 125–150	352.05	1		BF	Broken formation		25									
26R-1, 131–132	352.11	2		B	Bedding		15	270	208	17	W					
26R-1, 134–136	352.14	3		SP	Shear plane	1	33	90	11	33	E					
26R-1, 137–138	352.17	4		SP	Shear plane	3	36	90	24	39	E					
26R-1, 139–139	352.19	5		SP	Shear plane	2	7	90	344	7	E					
26R-1, 140–140	352.195	6		SP	Shear plane		7	90	305	12	N					
26R-1, 141–142	352.205	7		SP	Shear plane	1.5	11	90	286	36	N					
26R-1, 141–143	352.21	8		SP	Shear plane	1	2	270	256	8	N					
26R-2, 0–65	352.30	1		BF	Broken formation		65									
26R-2, 31–32	352.61	2		SP	Shear plane		20	90	334	22	E					
26R-2, 32–33	352.62	3		SP	Shear plane		0	90	90	10	S					
26R-2, 33.5–34	352.635	4	Yes	SP	Shear plane	2	19	90	27	21	E					
26R-2, 63–65	352.93	5	Yes	SP	Shear plane		22	90	74	56	S					
26R-2, 63–65	352.93	5		SL	Slickenline											56/064 Slick direction.
26R-2, 92–150	353.23	6		FC	Fracture cleavage				0	0						
27R-1	360.40	NIL														
27R-2	361.90	NIL														
27R-3	363.40	NIL														
27R-4	364.90	NIL														
27R-CC	366.40	NIL														
28R-1	370.10	NIL														
28R-2	371.60	NIL														
28R-3	373.10	NIL														
28R-4	374.60	NIL														
28R-5	376.10	NIL														
28R-CC	377.60	NIL														
29R-1, 45–55	379.95			Fr	Fracture		52	90	327	57	E					
29R-1, 45–55	379.95			Fr	Fracture		38	270	149	42	W					
29R-2, 55–88	381.55			Fr	fracture		25	90	46	34	S					
29R-2, 55–88	381.55			Fr	Fracture		38	270	211	42	W					
29R-3, 75–100	383.25			Fr	Fracture											
29R-4	384.00	NIL														
29R-5	385.50	NIL														
29R-CC	387.00	NIL														
30R-1	389.20	NIL														
30R-2	390.70	NIL														
30R-3	392.20	NIL														
30R-4	393.70	NIL														
30R-5, 90–150	396.10			Fr	Fracture		25	90	17	26	E					
30R-5, 90–150	396.10			Fr	Fracture		80	90	309	84	N					
30R-6	396.70	NIL														
30R-CC, 5–5	398.70			B	Bedding		40	0	247	42	N					
32R-1	408.60	NIL														
32R-2, 0–18	410.10	1		FC	Fracture cleavage				273	86	N	Paleomag	273	86	N	
32R-2, 0–18	410.10	1		FC	Fracture cleavage				183	56	W	Paleomag	183	56	W	
32R-2, 10–18	410.30	2		SP	Shear planes				199	33	W	Paleomag	199	33	W	
32R-2, 23–24	410.30	3		SP	Shear planes				152	25	W	Paleomag	152	25	W	
32R-2, 50–52	410.30	4		SP	Shear planes				202	26	W	Paleomag	202	26	W	

Core, section, interval (cm)	Depth (mbsf)	X-ref hand sheets	Photo(?)	ID	Identifier	Thickness (cm)	Care Face Orientation App. dip	Care Face Orientation Direction	Corrected core reference frame Strike	Corrected core reference frame Dip	Corrected core reference frame Dir.	Reorient Method	Corrected geographical reference frame Strike	Corrected geographical reference frame Dip	Corrected geographical reference frame Dir.	Comments
Hole 859B (cont)																
33R-1	418.30	NIL														
33R-2, 55–70	420.40	1		SP	Shear planes				240	25	N	Paleomag	259	25	N	
33R-2, 55–70	420.40	1		SP	Shear planes				213	18	W	Paleomag	232	18	W	
33R-2, 55–70	420.40	1		SP	Shear planes				247	15	W	Paleomag	266	15	W	
33R-2, 55–70	420.40	1		SP	Shear planes				24	24	E	Paleomag	43	24	E	
33R-2, 55–70	420.40	1		SP	Shear planes				61	44	S	Paleomag	80	44	S	
34R-1	427.90	NIL														
34R-2	429.40	NIL														
34R-3	430.90	NIL														
34R-4, 25–40	432.65			W	Web strand											
35R-1	437.60	NIL														
35R-2	439.10	NIL														
35R-3	440.60	NIL														
35R-4	442.35	NIL														
36R-1	447.10	NIL														
36R-2	448.60	NIL														
36R-CC	450.10	NIL														
37R-1	456.70	NIL														
37R-2	458.20	NIL														
37R-CC	459.70	NIL														
38R-1	466.40	NIL														
38R-2	467.90	NIL														
38R-CC	469.40	NIL														

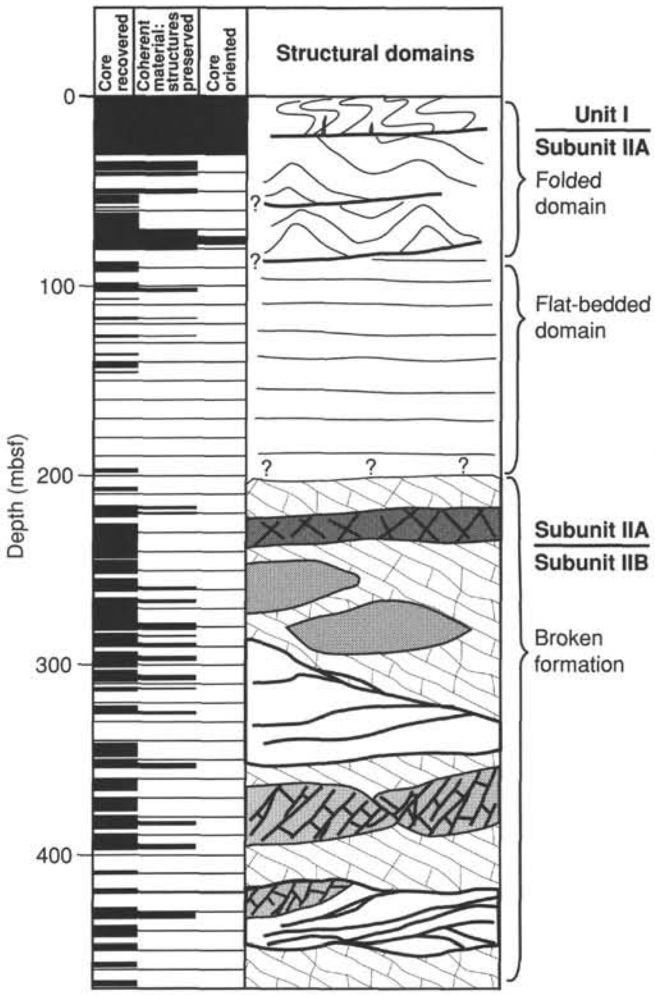

Figure 19. Schematic illustration of structural domains at Site 859 plotted vs. depth in borehole. First three columns show distribution of sediment recovery, the distribution of material sufficiently coherent to make structural observations, and the distribution of material in which structural measurements could be reoriented into a geographical reference frame. Approximate boundaries of lithologic Unit I and Subunits IIA and IIB are shown for reference.

indicative of dip-slip motion (Fig. 27). In neither case is there any consistent stepping at slickenline terminations that may be used to assess whether motion is normal or reversed. Thin-section data for deformation bands within claystones are not yet available.

Deformation Bands in Siltstones

In siltstones, deformation bands typically appear on the core surface as conjugate sets of relatively straight pale lines (Fig. 29). They vary in thickness from submillimeter to about 2 mm and generally stand above surrounding material (Fig. 30). On a 1- to 10-cm scale, the deformation bands bifurcate and vary in orientation in three dimensions (Fig. 31) while maintaining a generally conjugate pattern. One of the conjugate sets is dominant. The subdominant deformation bands terminate at their intersection with a deformation band of the dominant set. It is not clear whether the dominant set offsets the subdominant one or whether individual subdominant deformation bands stop for another reason.

In thin section, deformation bands in siltstones are seen to comprise discrete planes bounded by thin layers of phyllosilicate alignment and to contain grains of the host siltstone, supported in

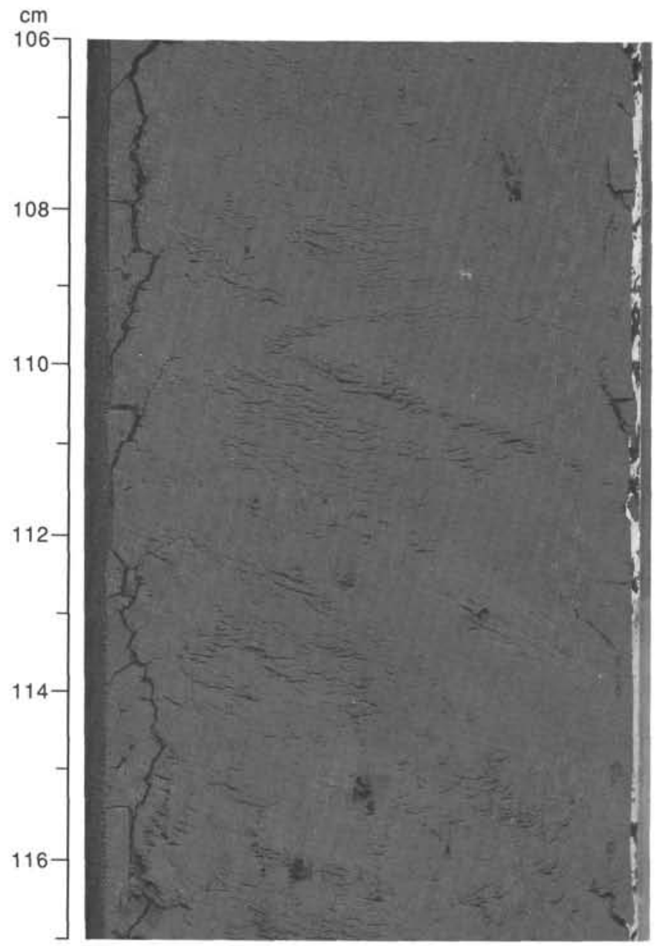

Figure 20. Recumbent fold of light and dark bedding laminations in interval 141-859A-2H-4, 106–117 cm, at 6.69 mbsf. The fold axis is best displayed at 109.5 cm. Note that the fold geometry is highlighted by fractures (caused by cutting with wire) that concentrate along the bedding surfaces.

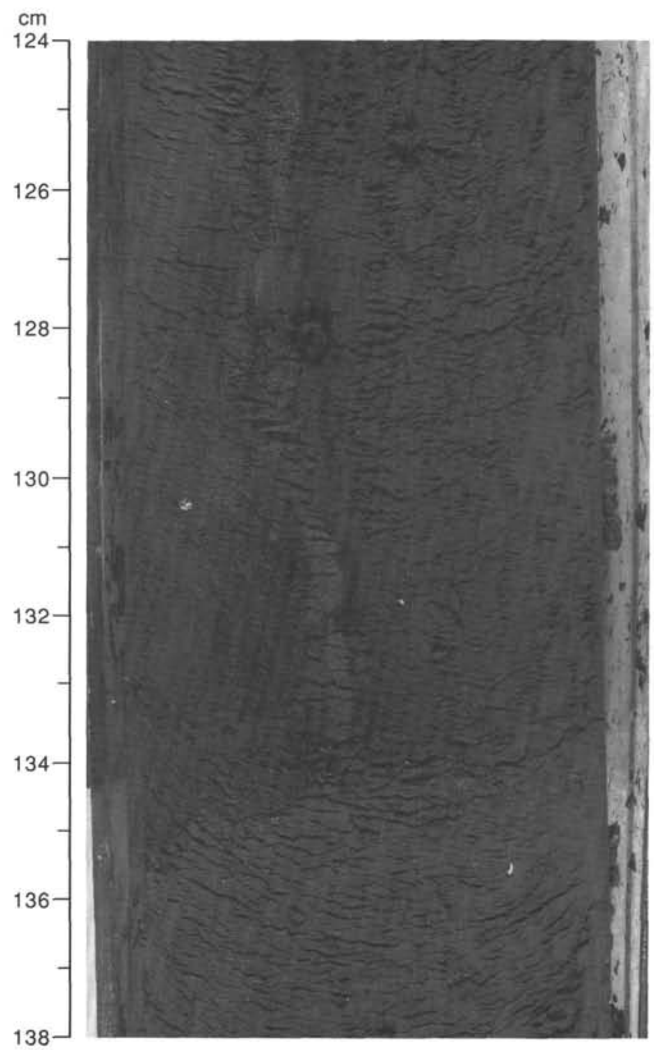

Figure 21. Fault at 14.84 mbsf in interval 141-859A-3H-3, 124–138 cm. The fault juxtaposes dark over light material. The fault appears at 135 cm on the left and at 133.5 cm on the right. Smeared subvertical pale and dark layers above the fault are clastic veins of pale muddy material and dark silt, respectively. Small, isolated carbonate concretions are also present.

a fine-grained matrix (Fig. 32). The degree of phyllosilicate alignment within deformation bands is variable and typically relates to variations in deformation band thickness. A wide deformation band that narrows along its length contains more aligned material where it is narrower. Deformation bands are parallel to and cross-cut foliations within the host siltstone, indicating that deformation bands, at least locally, post-date this foliation, while their orientation has been influenced by the foliation.

In some sandstones, anastomosing networks of dark irregular and planar zones between 0.5 and 2 mm thick have a matrix different from the surrounding host sandstone, but no other petrographic differences. These networks were observed in sandstones of Core 141-859B-17R and are mesoscopically similar to vein structures described by Lundberg and Moore (1986).

Table 10. Rotations used to reorient structural data from the core reference frame into the geographic reference frame in the folded domain.

Core	Rotation (°)	Method
141-859A		
-2H	82°	Paleomagnetism
-3H	237°	Multishot
-5H	100°	Multishot
141-859B		
-3R-2, 4-5 cm	212°	Paleomagnetism

Note: All rotations are around vertical axes and are quoted as clockwise rotations looking down-axis.

Breccia

A zone of breccia and associated carbonate veining was identified at 264.8 mbsf in interval 141-859B-17R, 53–54 cm. The breccia comprises angular fragments of pale siltstone within a darker siltstone (Fig. 33). Thin section studies reveal that the grain fabric and composition of the two siltstones are similar. The major difference is in the fine-grained matrix. The pale siltstone has an early cement of clear carbonate that rims most grains, but rarely joins grains together. A later phase of pore-filling matrix comprises mixed clays and carbonate. The dark siltstone has only one matrix phase, which consists of mixed clays and carbonate. Variation in matrix occurs within both lithologies, so that a continuum exists between the end members described. Where the early carbonate cement is well developed, the contacts of the pale and dark siltstones are angular. Where the early cement is less well developed, the contacts are more irregular. Carbonate veins cut both siltstones and commonly mark the contacts of the two (Fig. 33).

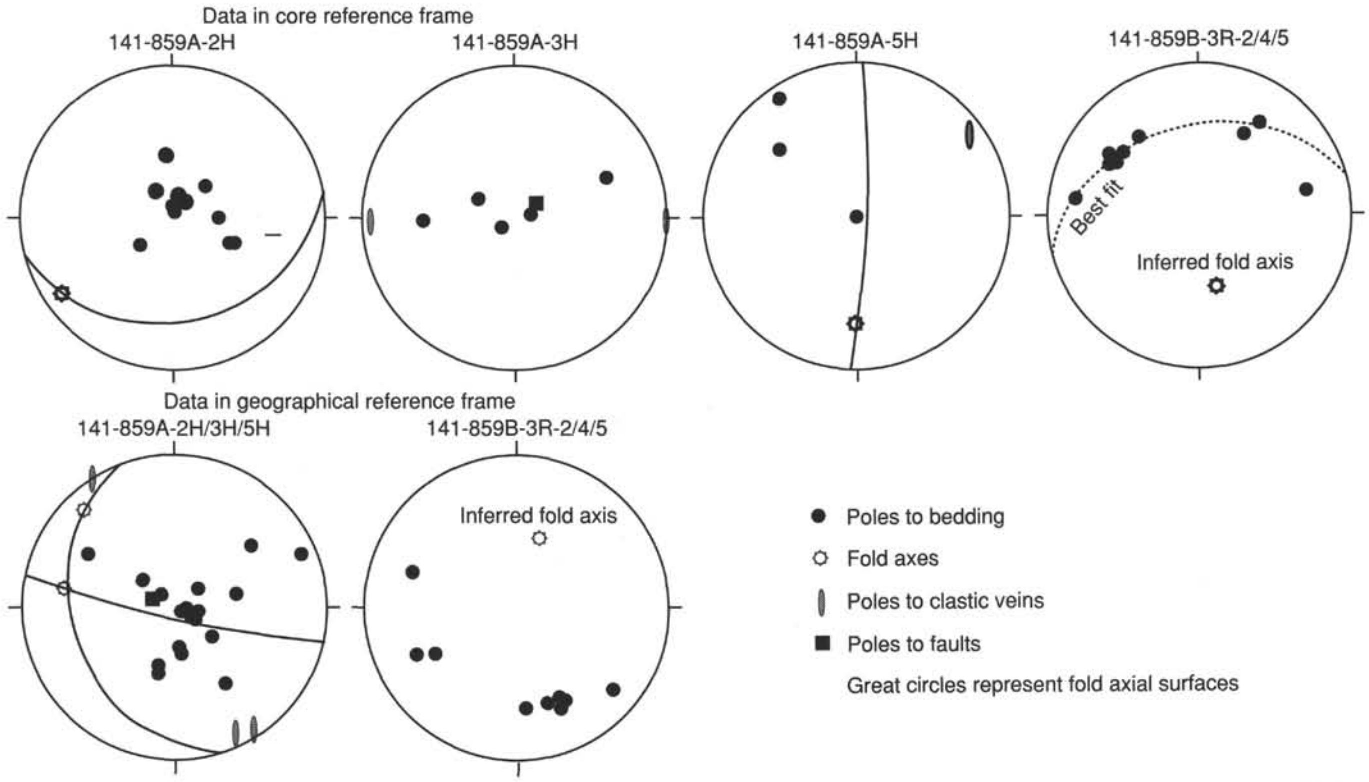

Figure 22. Structural data for the folded domain plotted in both core and geographical reference frames. Data from piston Cores 141-859A-2H through -5H have been plotted together because good agreement between rotations was predicted by multishot and paleomagnetic techniques and the results give a coherent structural data set. The rotation required for rotary Core 141-859B-3R is not as well constrained, so these data were plotted separately.

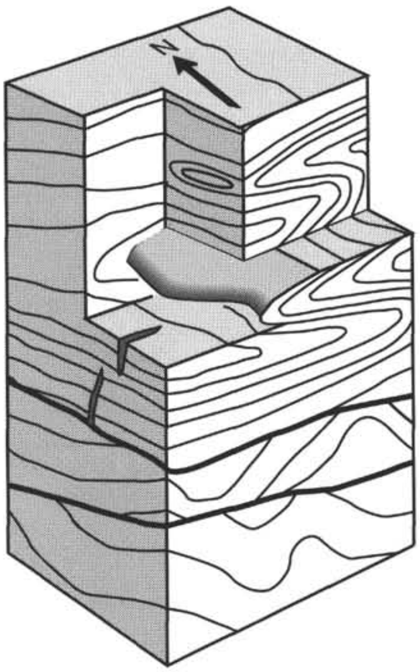

Figure 23. Schematic model to illustrate the structure of the folded domain. In the model, the domain comprises thrust (heavy lines) bound packages. The uppermost package is characterized by curvilinear recumbent folds formed by shearing toward approximately 070° or 250°. Lower packages contain more upright folds with axes consistent with east-northeast to west-southwest shortening. Clastic veins are oriented in a vertical plane with strike 070° and are consistent with east-northeast to west-southwest shortening.

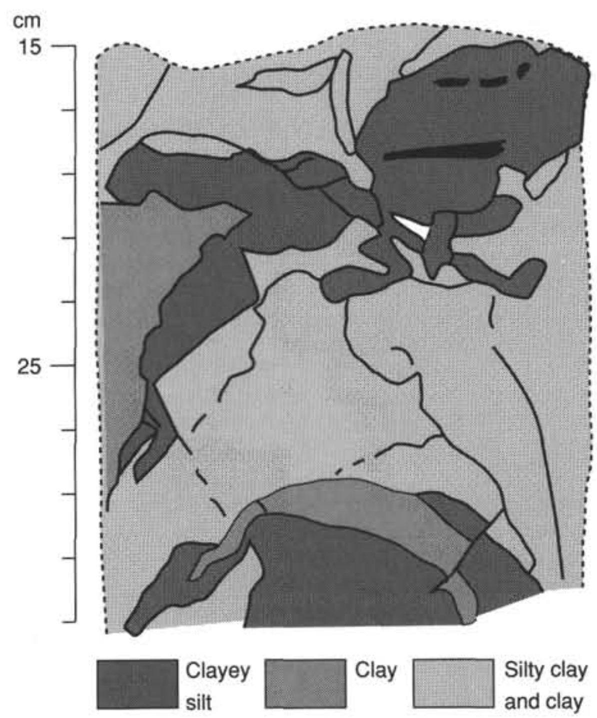

Figure 24. Sketch of breccia composed of fragments of clayey siltstone, silty clay/claystone, and clay at interval 141-859A-13X-CC, 17–23 cm. The siltstone and claystone clasts appear to have been pulled apart by layer-parallel extension, with the clay squeezing plastically around them. The more competent lithologies have been cross cut by normal-to-vertical microfaults that die out in the softer clay areas.

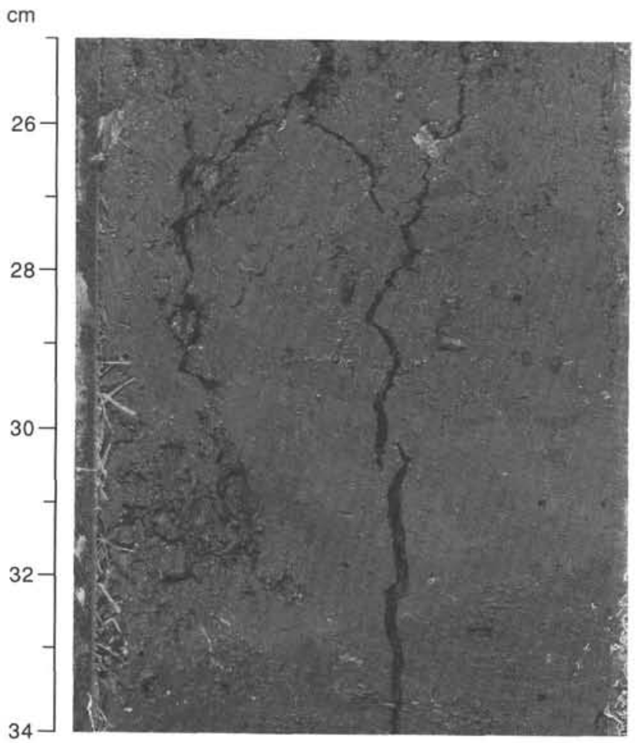

Figure 25. Lithologic contacts in broken formation in interval 141-859B-18R-5, 25–34 cm. The contact between 32 and 33 cm may be an original sedimentary contact. The darker pod on the right of the core between 27 and 30 cm is bounded by dark 1- to 2-mm deformation bands (well developed at 30 cm). Steep deformation bands splay off the upper contact of the pod.

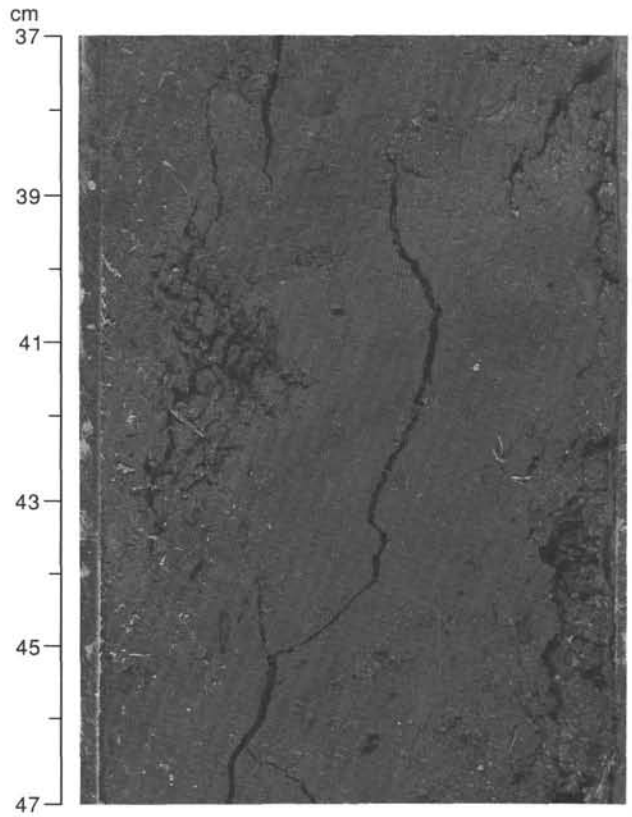

Figure 26. Deformation band in broken formation in interval 141-859B-18R-5, 37–47 cm, best seen in the center of the core between 40 and 43 cm. In this section, the dark shear plane anastomoses on the millimeter scale, bifurcating several times to the right.

Carbonate veins generally form discrete planes up to 2 cm long and 2 mm wide. Measured orientations (Fig. 34) indicate that veins lie in two conjugate orientations. Some conjugate pairs of carbonate veins were observed (Fig. 35). Where carbonate veins cut siltstone with little of the early cement, they have irregular contacts (Fig. 36).

Fracture Cleavage

Fracture cleavage is well developed in clayey siltstones and silty claystones in a number of sections deeper than 200 mbsf. Two subperpendicular fracture orientations have been developed (Fig. 37), with one, usually the steeper cleavage, dominant. The dominant cleavage is spaced 1 to 5 mm, with the subdominant spacing two to three times this. Cleavage surfaces are typically polished, but are not striated. In strongly drilling-disturbed material below 200 mbsf, many of the drilling breccias comprise millimeter-sized angular pieces with polished subperpendicular sides that suggest that fracture cleavage was an important structure through much of this section.

One is tempted to call the fracture cleavage a scaly fabric (Lundberg and Moore, 1986), but one must be careful, given the connotations of shear that have become associated with this term. Whether the fracture cleavage relates to shearing or other processes, such as stress release fracture (cf. Prior and Behrmann, 1990), cannot be assessed without detailed microstructural studies (Agar et al., 1989). Thin sections of fracture-cleaved material are not yet obtainable. However, thin section observations of siltstones containing deformation bands (Fig. 32) show that inequant detrital grains such as micas have aligned to form a foliation, and some quartz-quartz grain boundaries are indented into each other parallel to this foliation. The foliation, although heterogenous in intensity, is present throughout the thin section. It is possible that the fracture cleavage relates to a similar microscopic grain alignment. This comparison seems reasonable as structures similar to deformation bands were observed in dried fragments of pervasively fractured material that were used in physical property investigations.

Sand units are jointed. The joints form a conjugate pattern. It is not clear how these joint patterns relate to other structures in the broken formation.

Environment and Nature of Deformation

Broken formation is typical of deformation within accretionary complexes (Cowan, 1974, 1982, 1985) and has been accredited to near-surface slope processes (e.g., Raymond, 1984), development in shear zones (e.g., Cowan, 1982; Byrne, 1984; Agar, 1990), and diapirism (Pickering et al., 1988). The coherent sections observed show geometries typical of bulk simple shear, such as anastomosing shear planes.

Deformation bands contain isolated grains similar to the grains in the host siltstone. This is good evidence that deformation involves intergranular fracture, breaking the weak cement but not the siltstone grains themselves. The fabric present in the host siltstone involves grain indentation and has been interpreted as the result of pressure solution. Deformation bands post-date the fabrics related to pressure solution. A deformation mechanism path involving the change from pressure solution to intergranular fracture is likely to result from increased shear strain rates or pore

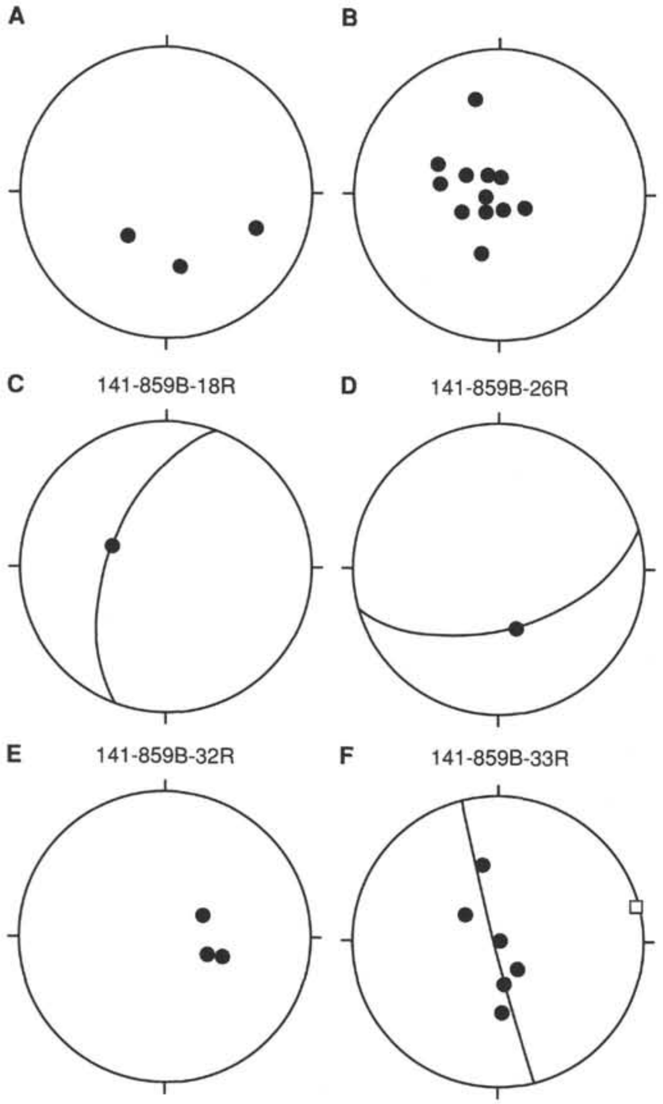

Figure 27. Stereoplots **A** and **B** show the orientations of poles to deformation bands in clayey lithologies in Cores 141-859B-18R and -26R, respectively. Data are oriented in the core reference frame. In each of Cores 141-859B-18R and -26R, slickenline measurements were possible on one surface. The surfaces containing slickenlines have been plotted as great circles in **C** and **D** for data from Cores 141-859B-18R and -26R, respectively. In each case, the slickenline orientation has been plotted as a point. Cores 141-859B-32R and -33R were reoriented using the viscous component of remanent magnetism. Poles to deformation bands in clayey lithologies in Cores 141-859B-32R and -33R are shown in **E** and **F**, respectively. The poles to deformation bands in Core 141-859B-33R fall on a great circle (marked) and indicate the intersection of anastomosing deformation bands at 03° toward 076°, marked as a square.

Table 11. Rotations used to reorient structural data from the core reference frame into the geographic reference frame in the broken formation.

Core	Rotation (°)	Method
141-859B-		
32R-2	0	Paleomagnetism
33R-2	19	Paleomagnetism

Note: All rotations are around vertical axes and are quoted as clockwise rotations looking down-axis.

Figure 28. Polished deformation band surface at 352.93 mbsf in interval 141-859B-26R-2, 63–65 cm (archive half). The surface dips out of the page. Dip-slip slickenlines are clear.

pressures (Knipe, 1986a). Evidence from the breccia and the deformation bands observed here suggests that deformation was ongoing during cementation and lithification and that quantification of these processes may provide better constraints on the depths, temperatures, and fluid conditions during deformation. It is likely that the deformation structures recorded probably acted as pathways for cementing fluids. More detailed microstructural studies of these specimens (cf. Agar et al., 1989; Knipe, 1986b, 1986c) are likely to lead to a better understanding of the changing conditions during deformation.

Deformation style varies from one lithology to the next. It is important to note that, although deformation bands in different lithologies have distinct geometries, they affect a similar bulk geometrical change: shearing. The geometrical contrasts reflect different mechanical responses to deformation. The magnitude of shear accommodated by each of these structures cannot be assessed quantitatively. Deformation bands in claystones were observed along lithological boundaries and within clayey lithologies. These observations suggest that these structures may be responsible for major dismemberment of the original strata, whereas deformation bands within siltstones are small displacement structures accommodating minor shape changes. If fracture cleavage is also a shear-related structure (the necessary microstructural observations to confirm this have not been made), then it is possible that fracture cleavage represents a third material response to shear. If shear in anastomosing deformation bands is perpendicular to their intersection, then the limited paleomagnetically reoriented data (Fig. 27) suggest that transport associated with their formation was west-northwest to east-southeast.

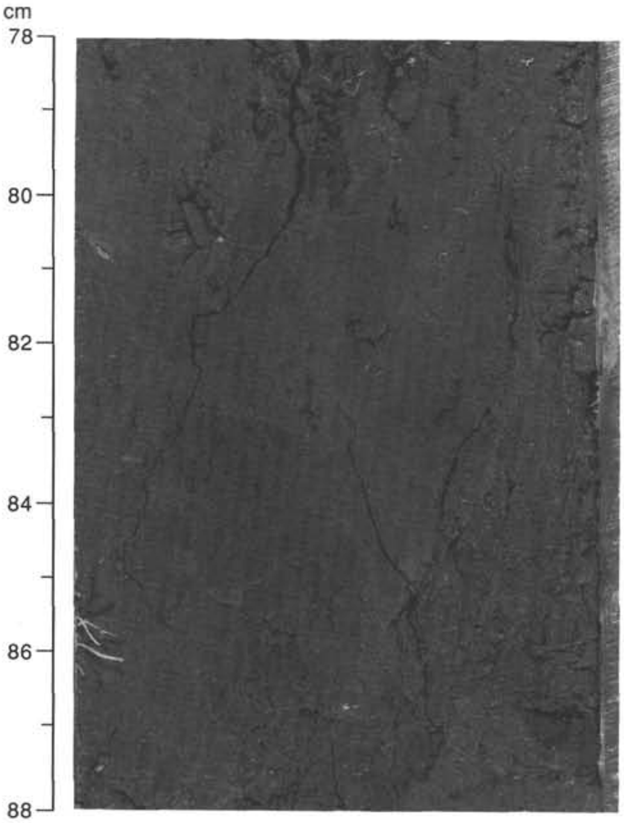

Figure 29. Deformation bands within a silty layer in interval 141-859B-18R-5, 78–88 cm. The dominant set dips steeply from right to left. A subdominant set dips more shallowly from left to right, and each of these terminates against one of the dominant set. The upper left contact of dark siltstone with paler silty claystone (intersects core-liner at about 85 cm) is marked by a complex shear plane.

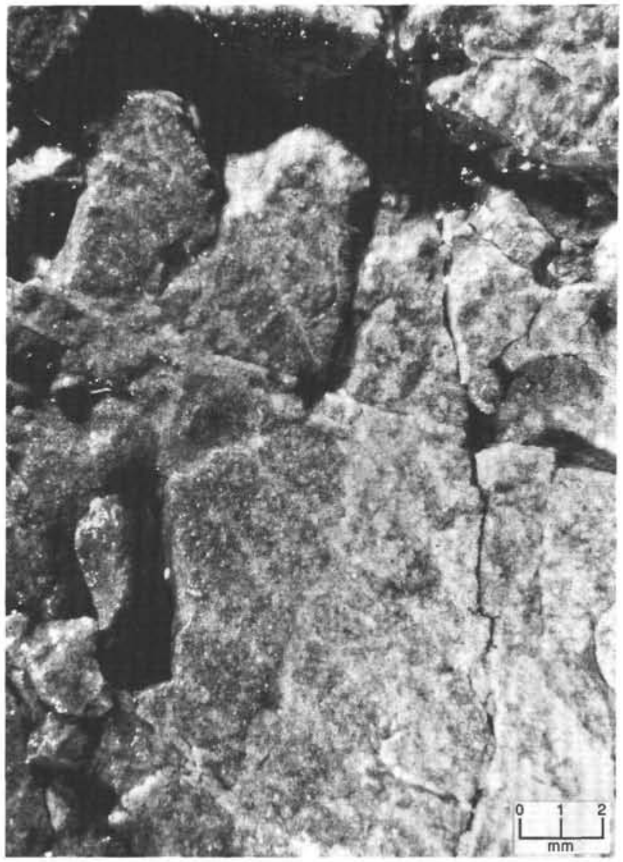

Figure 30. Close-up of deformation bands in siltstone in Section 141-859B-26R-2, 51 cm. Deformation bands stand above the surface and are paler than surrounding material.

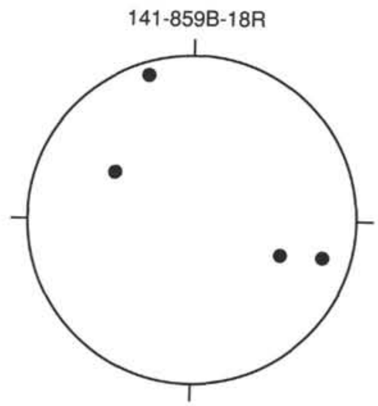

Figure 31. Poles to deformation bands in siltstone in Core 141-859B-18R.

ORGANIC GEOCHEMISTRY

Shipboard organic geochemical analyses of sediments from Holes 859A and 859B included volatile hydrocarbon and nonhydrocarbon gases, organic matter fluorescence estimation, total hexane soluble lipid/bitumen analysis, and Rock-Eval analysis. The instrumentation, operating conditions, and procedures are summarized in the Explanatory Notes chapter (this volume).

Volatile Gases from Sediments

Volatile gases (hydrocarbons, CO_2, H_2S, N_2, CS_2, O_2) released by the sediments recovered at Sites 859 were continuously measured by gas chromatography as part of the shipboard safety and pollution monitoring program. We used the headspace technique, in which a sediment plug is heated in a sealed vial to drive off gases (Emeis and Kvenvolden, 1986). The results are listed in Table 12 and Figure 38. The methane concentrations in the headspace volumes range between 527 and 12,278 ppm (vol/vol) and are significantly greater than the laboratory background level of 2 to 3 ppm. Ethane and higher hydrocarbons up to C_7 (heptane) were also detected and presented a nonuniform distribution with depth. No H_2S was detected in the samples collected at this site. The overall gas contents of these sediments, as determined by headspace analysis, were found to range from 0.004 to 0.082 cm^3 of methane per cubic centimeter of sediment, with the predominant gas being methane.

Two general gas zones were observed: an upper zone (5.7 to about 220 mbsf), where the gases consist predominantly of methane with small amounts of ethane and a general composition consistent with a biogenic origin; and a lower zone where, in addition to methane and ethane, small amounts of heavier hydrocarbons (C_3–C_7) were observed that suggest a contribution of thermogenic hydrocarbons.

Methanogenic bacteria are generally active after complete sulfate depletion by sulfate-reducing bacteria (Claypool and Kaplan, 1974). The sulfate content in interstitial waters at Site 859

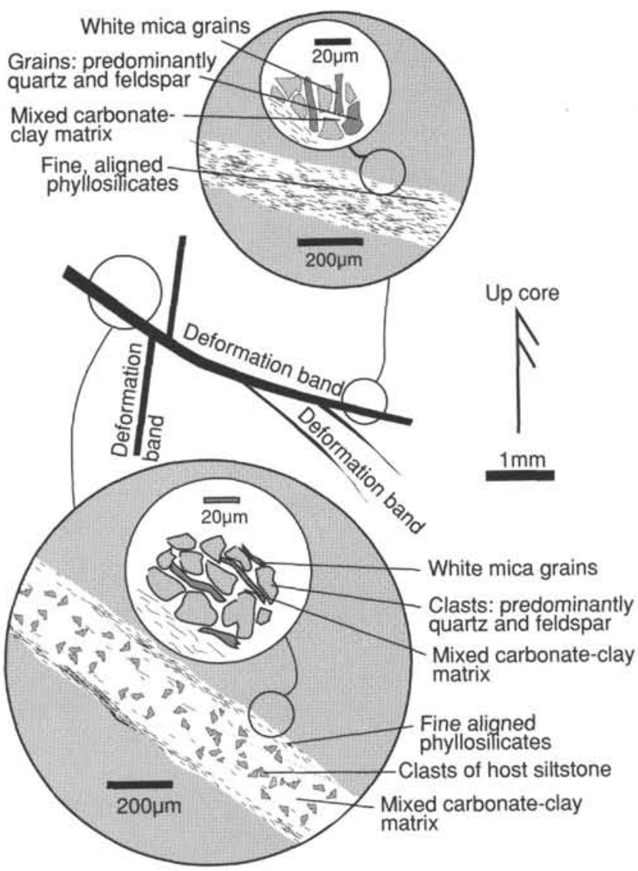

Figure 32. Composite sketch of characteristics of deformation bands in a thin section from interval 141-859B-18R-5, 72–76 cm. The deformation bands are developed in a siltstone with tightly packed structure, predominantly of quartz, feldspar, and white mica clasts. Carbonate and clay cement fill fine pores. Inequant grains, particularly the white micas, are aligned to form a pervasive but heterogenous foliation. In the deformation bands, fine phyllosilicates align to define discrete planar boundaries (lower close-up). Within the deformation band, isolated clasts of the host siltstone are supported in a fine cement of carbonate and clays. Where deformation bands narrow, the entire width of the band may be made up of aligned phyllosilicates (upper sketch). No evidence of fracturing or dissolution of grains is seen at the edges of deformation bands. The deformation bands are often parallel to foliation in the host siltstone (lower close-up). Where they are not parallel, they cross cut the foliation.

is relatively low in the upper section from 5.7 to about 140 mbsf, with total sulfate depletion observed around the 15- to 22-mbsf interval (see Inorganic Geochemistry section, this chapter). Therefore, environmental conditions for methanogenesis through CO_2 reduction, the major process by which microbial methane is produced in deep-sea sediments, were probably favorable for biogenic methane generation in the upper portion of the sedimentary column.

Organic matter maturation indicates that local thermal maturity in the lower zone would have been too low to generate the observed thermogenic hydrocarbons. These hydrocarbons are most likely of migrational origin from deeper sources in the accretionary prism (see below).

Carbon dioxide was present at concentrations up to 1002 ppm in gases desorbed from the sediments by the headspace method (Table 12). Even higher amounts of free CO_2 may have been present in the sediments and pore waters prior to the depressurization that occurs during core retrieval. Large fluctuations in concentrations of CO_2 were observed throughout the sequence of recovered sediments, suggesting possible alterations caused by (1) drilling fluid contamination (seawater); (2) degassing during depressurization and core sectioning; and (3) air contamination at sample introduction in headspace containers.

Fluorescence and Bitumen Particles

The extract colors progressed from pale yellow-green to pale yellow and, finally, to colorless, with increasing depth in the hole. The concentrations of extractable organic matter are low on the basis of their color, fluorescence intensities, and relative chromatogram intensities (see below). Nevertheless, two disseminated, diffuse, and weak white-blue fluorescent spots were observed in intervals 141-859B-27R-1, 97–98 cm, and -29R-3, 80–81 cm, at 361.4 and 383.3 mbsf, respectively. Chromatographic analysis of the extracts of the fluorescent areas indicates that the overall organic matter isolated had a generally immature character, with the exception of the presence of gasoline-range hydrocarbons up to the C_{12} carbon atom range (Fig. 39D). Yellow fluorescence has been interpreted as incipient thermal maturation of bitumen to the mature stage and white (or white-blue fluorescence) has been associated with mature and overmature bitumen enriched in polynuclear aromatic hydrocarbons (PAH) (Shipboard Scientific Party, 1982).

During isolation of foraminifers (Sample 141-859A-9P-CC) by water washing, several soft, black, bitumen particles were detected. After hand selection, isolation, hexane extraction, and chromatographic analysis, we confirmed that the particles were composed of well-matured bitumen (Fig. 39A), with a bimodal distribution (C_{max} at C_{22} and C_{33}), a large unresolved complex mixture (UCM) and low C_{max}/UCM ratios (0.38 and 0.68, respectively), suggesting environmental exposure and/or water-washing. The low degree of maturation of the sediments in which the bitumen was found suggests that its origin is allochthonous and that it has been emplaced in its present position by migration from areas of higher geothermal maturation.

Gas in Core Expansion Voids

After core retrieval on deck, gas expansion voids were observed in the core liner-contained core. The gas was sampled directly from the gas voids by piercing the core liner with a sampling needle and collecting the gases in pre-evacuated vacutainers. Upon chromatographic analysis, the expansion void gases (EVG) were found to contain hydrocarbons in the C_1 to C_7 range and to have a composition somewhat different from the gases isolated by headspace analysis (Table 13 and Fig. 40).

EVG hydrocarbon contents were found to be significantly higher (up to 953,850 ppm; 95.3% by vol.) than headspace gas and presented different gas ratios for equivalent depths. Due to higher gas concentrations, EVG gas allows for better detection of heavier hydrocarbons (C_4 plus), but headspace analysis gives lower C_1/C_2 ratios. Thus, for Site 859, gas analyses for an equivalent depth range gave C_1/C_2 ratios from 5198 to 2347 for the EVG gas, whereas C_1/C_2 levels of only 2984 to 406 were obtained for the same interval by the headspace analyses. This difference is most likely the result of different gas fugacities and degassing processes that occurred during core retrieval and the inevitable air exposure of headspace samples that results in a preferential loss of methane, which will lead to a decrease of the C_1/C_2 ratio in the headspace gases. Simultaneously, the gas released in the core is enriched in methane and will give consistently higher C_1/C_2 ratios. These differences have importance in the drilling safety criteria as C_1/C_2 or C_1/C_3 ratios (as analyzed on board the ship) are method-dependent, and therefore different safety limits should be established for data based on headspace and core liner gas analyses.

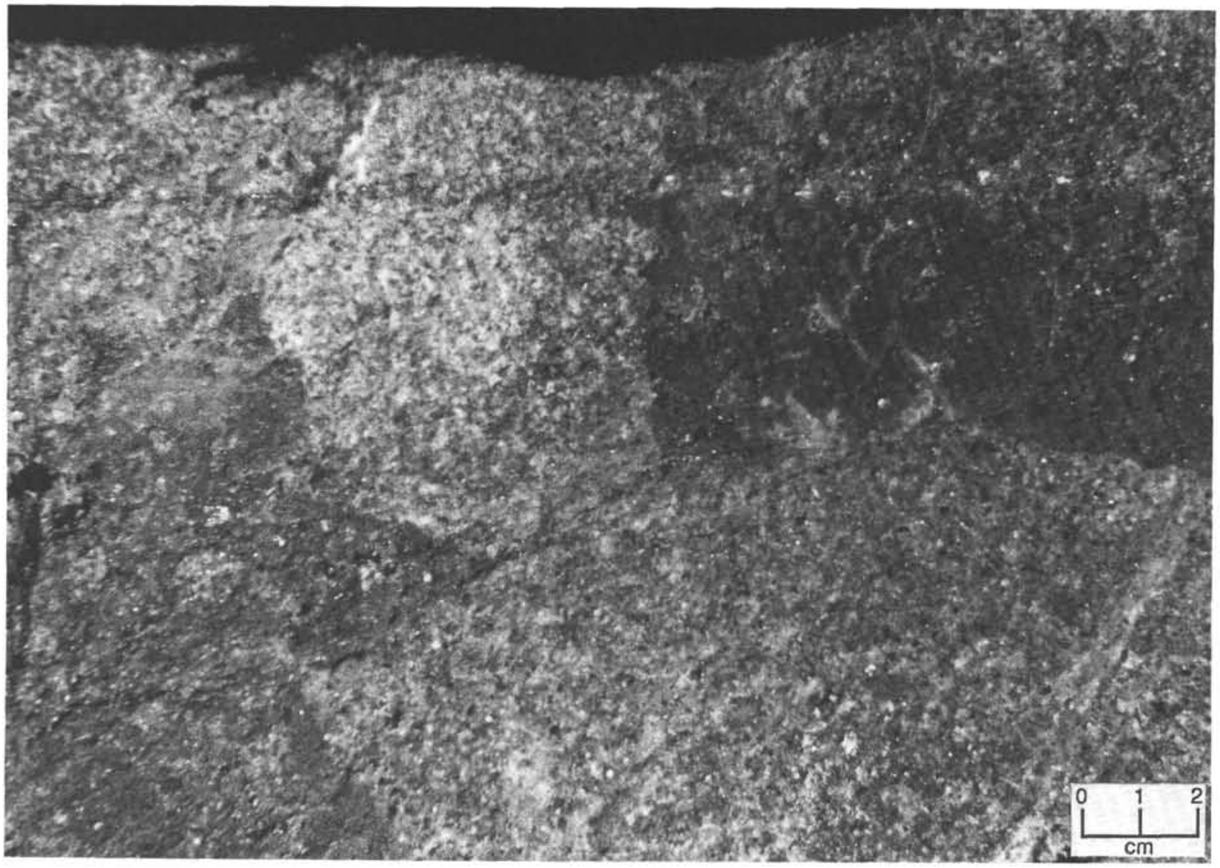

Figure 33. Angular breccia fragments of pale siltstone in dark siltstone (interval 141-859B-17R-1, 53–54 cm). Carbonate veins follow the fragment boundaries (e.g., top left contact of upper fragment) and cut through fragments (e.g., right side of lower fragment).

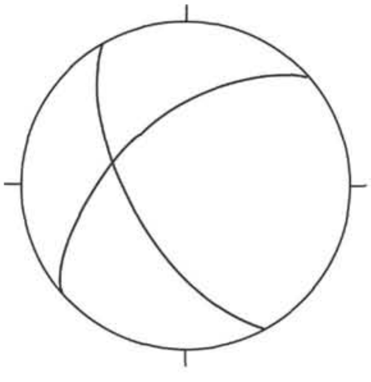

Figure 34. Orientations of carbonate veins in the breccia zone at interval 141-859B-17R-1, 53–54 cm, plotted as great circles.

Consistently, and in spite of these compositional differences, two distinct gas zones can also be observed: an upper layer down to about 200 mbsf of predominantly biogenic gas composed almost exclusively of methane having high C_1/C_2 ratios (6,066 to 26,765), and a deeper layer from 220 mbsf downward containing a gas with somewhat higher ethane content and small but significant amounts of C_{4+} compounds (up to 254 ppm). Heavier hydrocarbons in the deeper layer extend up to C_7 (heptane), well within the natural gasoline range. In both cases, either headspace or expansion void gas analyses, the carbon range cutoff is at C_7 and was determined by the chromatographic conditions and the volatility of the heavier hydrocarbons under sampling and handling conditions. The presence of heavier hydrocarbons was confirmed by organic extraction analysis (see below).

Bitumen Analyses and Organic Matter Characterization

The hexane extracts of the samples from the fluorescence assessment were concentrated under a stream of helium to about 10 to 40 μL. These concentrates were analyzed by high-resolution gas chromatography, and examples of traces are shown in Figures 39B and 39C. The dominant compound series in the total extracts are hydrocarbons ranging from n-C_{15} to n-C_{36}, with pristane ($C_{19}H_{40}$) and phytane ($C_{20}H_{42}$) as the major isoprenoid alkanes. As a general trend, the n-alkanes $>C_{26}$ have a significant predominance of odd carbon numbers (carbon preference index, CPI, >1.0; Table 14), typical for immature hydrocarbons that originate from terrestrial higher plants (Simoneit, 1977, 1978). The value of the carbon preference index decreases with geothermal maturation, approaching values of CPI = 1 for crude oils and mature organic matter. The CPI has to be calculated for the range C_{26}–C_{35}, because in some samples n-C_{25} co-elutes with a contaminant. This contaminant is more abundant in samples taken from split cores and is most likely associated with core-liner fragments incorporated during core splitting.

For Site 859, some significant anomalies in the characteristics of the extractable organic matter were observed: for the upper layers (15.2–199.8 mbsf) the CPI increases with increasing sub-bottom depth, suggesting a maturational inversion in which more mature sediments overlie a less mature sequence. In addition, at 78.9 and 313.7 mbsf, relatively lower values of CPI were ob-

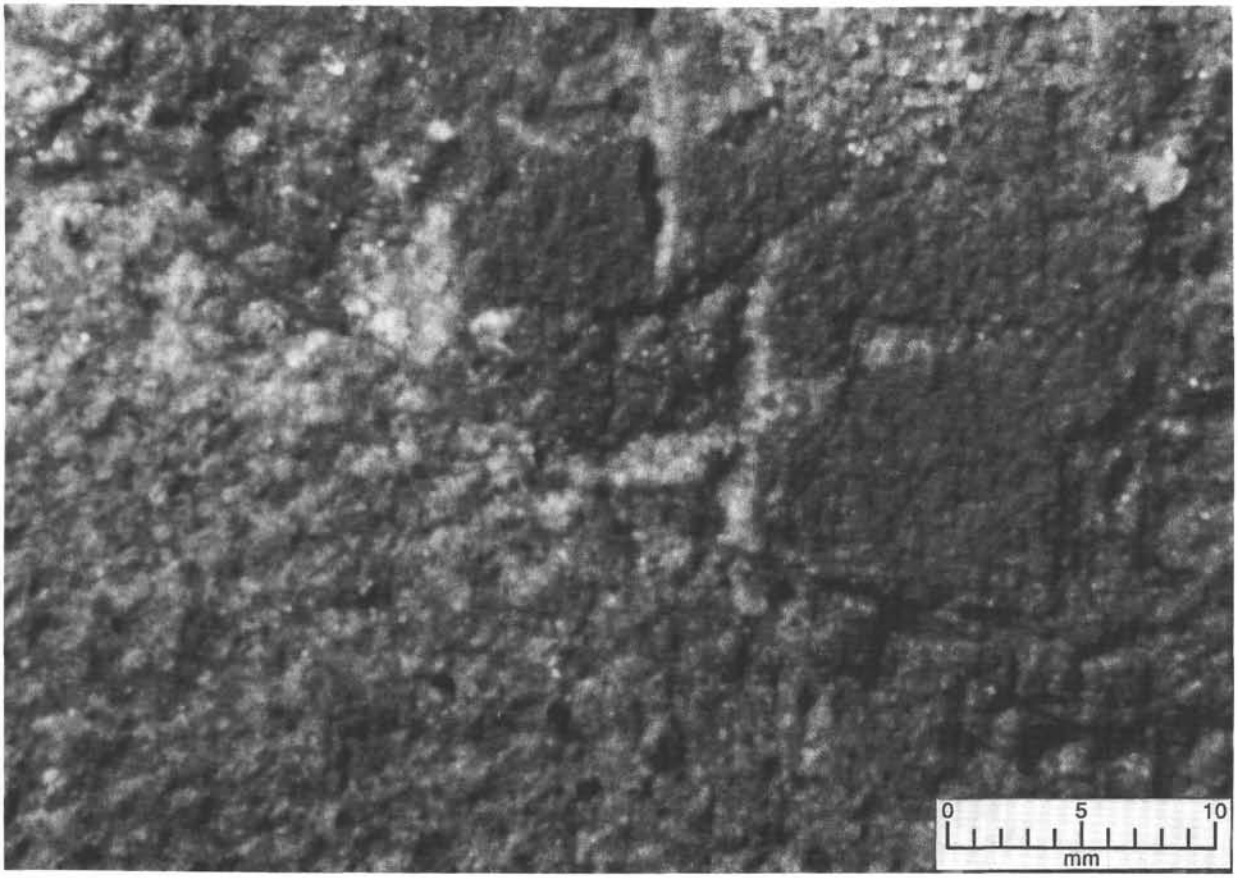

Figure 35. Conjugate carbonate veins in dark siltstone adjacent to contact with pale siltstone (interval 141-859B-17R-1, 53–53.5 cm).

served: 1.14 and 1.9, respectively, which suggests localized increases in maturation superimposed over a generally low maturational trend.

The detection of well-matured bitumen particles (58.4 mbsf; CPI = 1.02) and fluorescent spotting in the split core (361.4 mbsf; CPI = 1.87), both emplaced in an immature sedimentary sequence, suggest a migrational origin.

The presence of two sedimentary units is also evident from the difference in the isoprenoid-to-normal hydrocarbon ratios (Pr/n-C_{17} and Ph/n-C_{18}; Table 14), with the upper layer having ratios of <1 and the lower layer having ratios of >1. A similar indication was provided by the pristane-to-phytane ratios (Pr/Ph), which increase slightly, from 1.00 to 1.29, with depth for the upper layer, and range from 0.24 to 0.73 in the lower layer, with no evident depth-related variations, and a low of 0.24 near 246.4 mbsf. Although pristane-to-phytane ratios are highly formation-dependent (Farrington et al., 1988), they have been reported to be an indicator responding to maturation (Simoneit el al., 1981), as well as an indicator of anoxic conditions of sedimentation (Didyk et al. 1978).

The n-alkane patterns <C_{24} with the unresolved complex mixture (UCM) of branched and cyclic compounds are typical of autochthonous marine bitumen derived from alteration of microbial lipids (Simoneit, 1977, 1978). The n-alkanes range extends from C_{10} to C_{36} (carbon number maxima at C_{18} and C_{21}; Table 14). The marine components are in the range of <n-C_{22} and the terrestrial plant wax influx is represented by the homologs >n-C_{23}.

Analysis of gases released in the core liner as well as gases released from sediments during headspace analysis indicated the presence of gasoline-range hydrocarbons up to C_7, the upper limit of detection of the chromatographic conditions and calibration of the natural gas analyzer. The presence of gasoline-range hydrocarbons was also corroborated by the extraction analyses, which show that hydrocarbons up to C_{12}, well in the natural gasoline carbon atom range, can be observed on the solvent elution peak when contrasted with the solvent extraction blank. The relative amount of gasoline-range hydrocarbons increases with depth and is indicative of an increased thermal stress and/or the existence of a deeper source of thermogenic hydrocarbons.

The actual nature of this deeper source of thermogenic hydrocarbons might be related to a conventional, slowly matured hydrocarbon source, or alternatively, the thermogenic hydrocarbons may be generated by a high-temperature energy source (Simoneit et al., 1981) and/or by petroleum hydrocarbon generation by action of hydrothermal fluids upon immature sedimentary organic matter (Didyk and Simoneit, 1989).

Organic Content and Type of Organic Matter

Total organic carbon contents (TOC) were found to be relatively low, with the uppermost part of the sediments (0–30 mbsf) having slightly higher values (0.34–1.13), whereas the deeper section has lower TOC levels (0.07–0.47) (Table 15 and Fig. 41).

Rock-Eval pyrolysis of the organic matter indicated the presence of an immature kerogen having values of T_{max} ranging from 401° to 422°C that can be tentatively associated with vitrinite reflectance levels of not higher than about 0.5. Pyrolyzable organic matter content (S_2) is also low, and because T_{max} values for samples having S_2 contents of less than 0.5 mg hydrocarbons per gram of sediment often are inaccurate, and most T_{max} values were rejected.

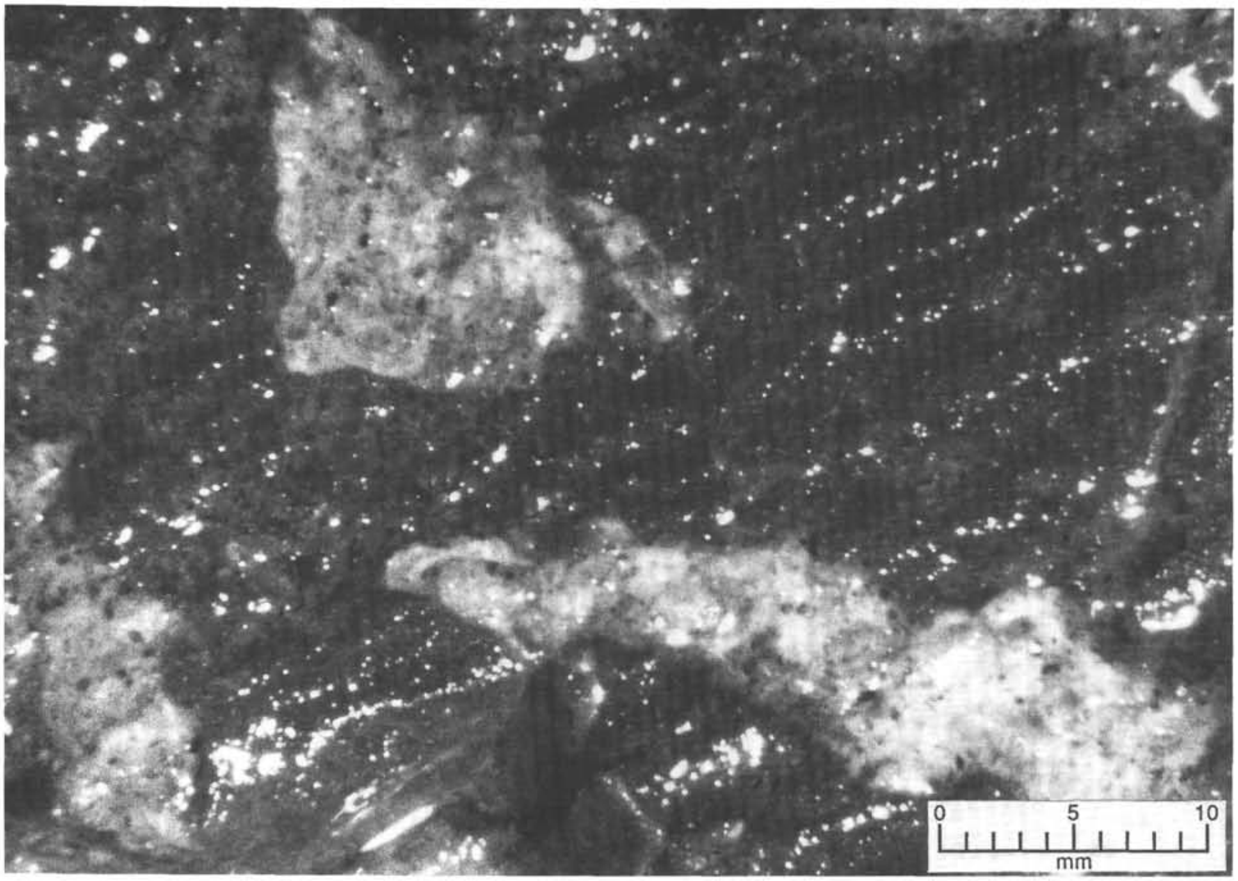

Figure 36. Carbonate veins in dark siltstone showing very irregular margins and geometry (interval 141-859B-17R-1, 53.5–54 cm).

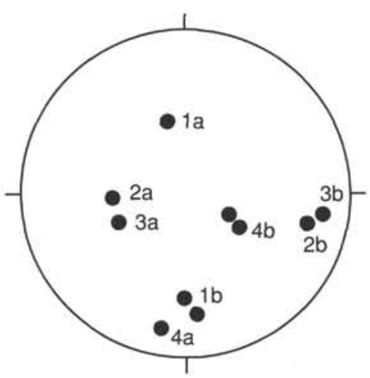

Figure 37. Composite plot of poles to fracture cleavage in Cores 141-859B-19R, -21R, and -26R. All but two measurements are paired. For paired cleavages, the poles to the two pairs have been numbered the same, with the dominant cleavage labeled *a* and the sub-dominant *b*.

The kerogen for Site 859 is relatively homogeneous, shows no trends related to depth, and has low hydrogen indexes (HI <200 mg HC/g TOC), together with high oxygen indexes (OI >100 mg CO_2/g TOC) characteristic of Type III, gas-prone kerogen of terrigenous origin (Fig. 42). However, for clay-rich sediments containing less than 0.5% of TOC, the measured HIs are likely too low because of adsorption of pyrolytic organic compounds onto the mineral matrix, which suggests that the actual HI values can be higher but well within the Type III, gas-prone kerogen zone (Fig. 42). Significantly high levels of OI are suggestive of oxidative alteration of the organic matter during sedimentation and early diagenesis and/or long-range transport processes that contributed to the oxidation of the organic matter.

Conclusions

Biogenic gas composed mainly of methane and ethane was detected in the upper zone of the sedimentary section of Site 859, with an increasing amount of migrational thermogenic hydrocarbons extending into the gasoline range present in the lower section. The organic matter of the sediments corresponds to a Type III, gas prone kerogen having a low degree of maturation. Localized maturational and organic anomalies suggest the occurrence of migrational processes and a deeper source of thermogenic hydrocarbons.

INORGANIC GEOCHEMISTRY

The primary purposes of the pore-water program at this site were (1) to determine if methane hydrates were present above a prominent bottom-simulating reflector (BSR) at ~80 mbsf where hydrates might be stable and (2) to evaluate whether pore-fluid compositions provide information about fluid sources and migration pathways through the toe of the accretionary prism. The site also was chosen to study the possibility that hydrothermal circulation from the underthrusted young oceanic crust might induce fluid migration through faults cutting this wedge to basement. Pore waters obtained from squeezing whole-round cores were analyzed for salinity, chloride, calcium, magnesium, pH, alkalinity, sulfate, sodium, potassium, silica, strontium, ammonia, lithium, fluoride, and boron. These data are presented in Table 16 and Figure 43.

Table 12. Composition of headspace gases for sediments from Holes 859A and 859B.

Core, section, interval (cm)	Depth (mbsf)	Hydrocarbon concentration (ppm) C_1	C_2	C_3	i-C_4	n-C_4	i-C_5	n-C_5	C_{6+}	CO_2	C_1 (cm^3/cm^3)	C_1/C_2
141-859A-												
2H-4, 0–3	5.7	7660	0	0	0	0	0	0	0	138	0.051	-
3H-4, 0–3	15.2	5268	0	0	0	0	0	0	0	439	0.035	-
4H-3, 137–140	21.1	3896	0	0	0	0	0	0	0	454	0.026	-
5H-6, 0–3	32.7	929	0	0	0	0	0	0	0	545	0.006	-
6X-2, 10–13	36.3	2514	0	0	0	0	0	0	0	877	0.017	-
10X-CC, 0–3	58.7	3505	0	0	0	0	0	0	0	441	0.023	-
11X-3, 0–3	71.3	5784	0	0	0	0	0	0	0	303	0.039	-
13X-1, 90–95	78.9	4517	0	0	0	0	0	0	0	218	0.030	-
14X-2, 135–140	90.5	9576	0	0	0	0	0	0	0	385	0.064	-
16X-CC, 10–13	100.8	1191	0	0	0	0	0	0	0	702	0.008	-
17X-CC, 10–13	107.3	1750	0	0	0	0	0	0	0	822	0.012	-
18X-CC, 10–13	117.6	2250	0	0	0	0	0	0	0	144	0.015	-
19X-CC, 10–13	126.9	2846	2	0	0	0	0	0	0	915	0.019	1423
20X-CC, 10–13	136.6	3753	2	0	0	0	0	0	0	760	0.025	1877
141A-859B-												
1R, 2, 140–145	54.9	11655	0	0	0	0	0	0	0	373	0.078	-
2R-2, 140–145	64.5	2195	0	0	0	0	0	0	0	171	0.015	-
3R-4, 113–118	78.4	2906	0	0	0	0	0	0	0	402	0.019	-
4R-1, 135–140	141.4	527	0	0	0	0	0	0	0	774	0.004	-
9R-CC, 10–13	187.2	1651	0	0	0	0	0	0	0	919	0.011	-
10R-3, 10–13	199.8	5215	3	0	0	0	0	0	0	895	0.035	1738
12R-3, 90–96	219.9	4669	2	0	0	1	0	0	0	934	0.031	2335
13R-5, 140–145	233.0	7094	11	11	4	tr	3	0	2	935	0.047	645
14R-4, 130–135	241.1	3197	4	4	2	0	1	0	0	596	0.021	799
15R-1, 145–150	246.5	2032	3	6	3	0	1	0	1	918	0.014	677
16R-2, 130–135	257.4	2952	2	2	2	0	0	0	0	209	0.020	1476
17R-3, 145–150	268.8	8953	3	5	2	0	1	0	0	1001	0.060	2984
18R-2, 137–140	276.9	3018	4	9	2	0	2	0	0	994	0.020	755
19R-3, 142–145	287.9	1856	4	7	3	0	0	0	0	209	0.012	464
20R-1, 115–120	294.2	8369	13	24	8	2	6	2	tr	951	0.056	644
21R-2, 145–150	305.2	8366	8	13	5	tr	4	0	tr	185	0.056	1046
22R-1, 145–150	313.7	3245	8	17	6	tr	4	0	0	440	0.022	406
23R-3, 0–5	324.9	4790	8	11	3	tr	1	0	0	246	0.032	599
25R-3, 135–140	345.5	2848	2	4	2	0	1	0	0	636	0.019	1424
26R-1, 147–150	352.3	2628	3	3	2	0	0	0	0	261	0.018	876
27R-1, 132–135	361.7	3730	3	7	3	0	1	0	0	953	0.025	1243
28R-4, 142–145	376.0	2698	5	7	3	0	0	0	0	946	0.018	540
29R-3, 137–140	384.0	1370	2	4	4	0	2	0	0	390	0.009	685
30R-3, 147–150	393.7	2606	3	7	3	0	0	0	0	1006	0.017	869
32R-1, 80–85	409.4	5665	7	14	6	0	2	0	8	562	0.038	809
33R-1, 145–150	419.8	2417	3	6	2	0	5	0	5	702	0.016	806
34R-3, 135–140	432.3	3817	4	8	5	0	1	0	2	316	0.025	954
35R-1, 142–145	439.0	1753	2	5	3	0	0	0	0	902	0.012	877
36R-2, 147–150	450.0	2627	3	4	2	0	2	3	10	180	0.018	876
38R-2, 15–18	468.1	12278	15	22	12	2	4	0	12	nd	0.082	819

The water-sampler-temperature probe (WSTP) was deployed in two configurations, one for collection of temperature data and fluids, the other for measurement of temperature only. At Site 859, the WSTP was deployed five times in the water-plus-temperature configuration. During the second and third runs, interstitial formation fluids were recovered successfully (Table 17 and Fig. 44). The first attempt did not penetrate the formation and recovered only drill fluids, while the fourth and fifth deployments failed because of misfunction of a valve and clogging of the sampling coils with sediment.

The pressure core sampler (PCS) was run four times in Hole 859A. Core 141-859A-9P (PCS #1: 57.4–58.4 mbsf) did not retain pressure and only 3 cm of sediment was recovered. Core 141-859A-12P (PCS #2: 77.0–78.0 mbsf) also did not retain hydrostatic pressure on deck, but 24 cm of sediment was recovered. Core 141-859A-15P (PCS #3: 98.8–100.2 mbsf) recovered 37 cm of sediment from the interval interpreted case to contain free gas at the bottom of the hydrate zone (by correlation with the lithodensity logs: see Wireline Measurements section, this chapter). This PCS retained about 700 kPa pressure on deck, but had leaked to 0 psi pressure after transfer to a thermostated water bath (8°C) in the laboratory. Attempts to recover gas or fluid were unsuccessful. Core 141-859A-21P (PCS #4: 145.5–146.5 mbsf) was deployed at the bottom of Hole 859A near XCB refusal. It retained ~2600 kPa pressure on deck and was transferred to the water bath, where it stabilized at ~1400 kPa (4.1°C). Manipulation of the pressure decrease on opening the PCS to a gas manifold suggested that only a small fraction of the initial hydrostatic pressure was retained, and no gases or fluids were recovered.

Reevaluation of shipboard sonic velocity data suggests that the BSR observed on the *Conrad* MCS Line 745 occurred somewhat deeper than initially predicted, at about 100 mbsf, rather than 80 mbsf, which is consistent with an observed low-velocity, high-porosity, high-resistivity interval at 100 mbsf in the lithodensity logs (see Wireline Measurements section, this chapter). The presence of methane hydrates in the interval above 100 mbsf is suggested by the distinct and sharp salinity and chloride minima in the interval between 27 and 70 mbsf (Figs. 43 and 44). Salinities as low as 25 mM and chloride concentrations as low as 438 mM measured in this interval are about 25% fresher than seawater. The sharp chloride gradients, which would be erased by diffusion within several thousand years, argue against a steady-state process and seem to require that the freshening be caused either by hydrate dissociation during the drilling and recovery process, or to a very recent dissociation of the hydrate layer (if interpreted as a contemporary in-situ feature).

WSTP results from this interval (Fig. 44) are consistent with those obtained by squeezing, suggesting that core decompression upon recovery is not the sole reason for low chlorides, but rather that hydrate dissociation occurs ahead of the bottom of the drill

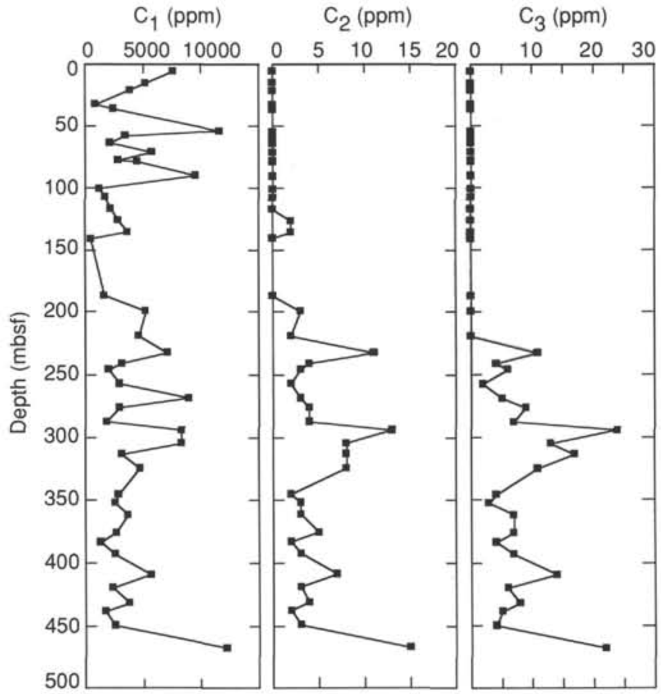

Figure 38. Composition of headspace gases vs. depth (mbsf) for sediments from Holes 859A and 859B.

bit induced by temperature and pressure changes during drilling. If the minimum chloride values observed reflect decomposition of in-situ methane hydrates with composition $CH_4 \bullet 5.75\ H_2O$ in sediments of about 50% porosity, then about 25% of the pore volume is occupied by solid hydrate. Unfortunately, no solid hydrates were recovered in cores from this interval where core recovery was poor. However, other major cations and anions show evidence of freshwater dilution similar to chloride in this depth interval (Fig. 43: fluoride, potassium, and strontium). This pattern is consistent with dilution of in-situ profiles by freshwater derived from drilling-induced hydrate dissociation.

Above and below the hydrate layer, chloride values are generally >560 mM, saltier than seawater, with a maximum value (titrated four times) at 220 mbsf of almost 650 mM. This is probably salt enrichment of the entire column caused by long-term extraction of freshwater into hydrates in the uppermost part of the section or lateral downward migration and diffusion of fluids similarly enriched elsewhere (perhaps regionally) at some time in the past. The integrated "excess salt" in the entire interval (0–30 and 70–450 mbsf) is approximately equal to the "missing salt" in the 40-m-thick hydrate layer (30–70 mbsf), suggesting a local salt balance.

The pore fluid profiles at Site 859 are consistent with a number of processes. Decreasing-downward Na and increasing-downward Ca, Sr, and Li probably reflect chemical exchange with basement basalts (plagioclase albitization), and the downward-increasing sulfate profile may suggest dissolution of anhydrite from previously-active, but now cooled, hydrothermal plumbing in the

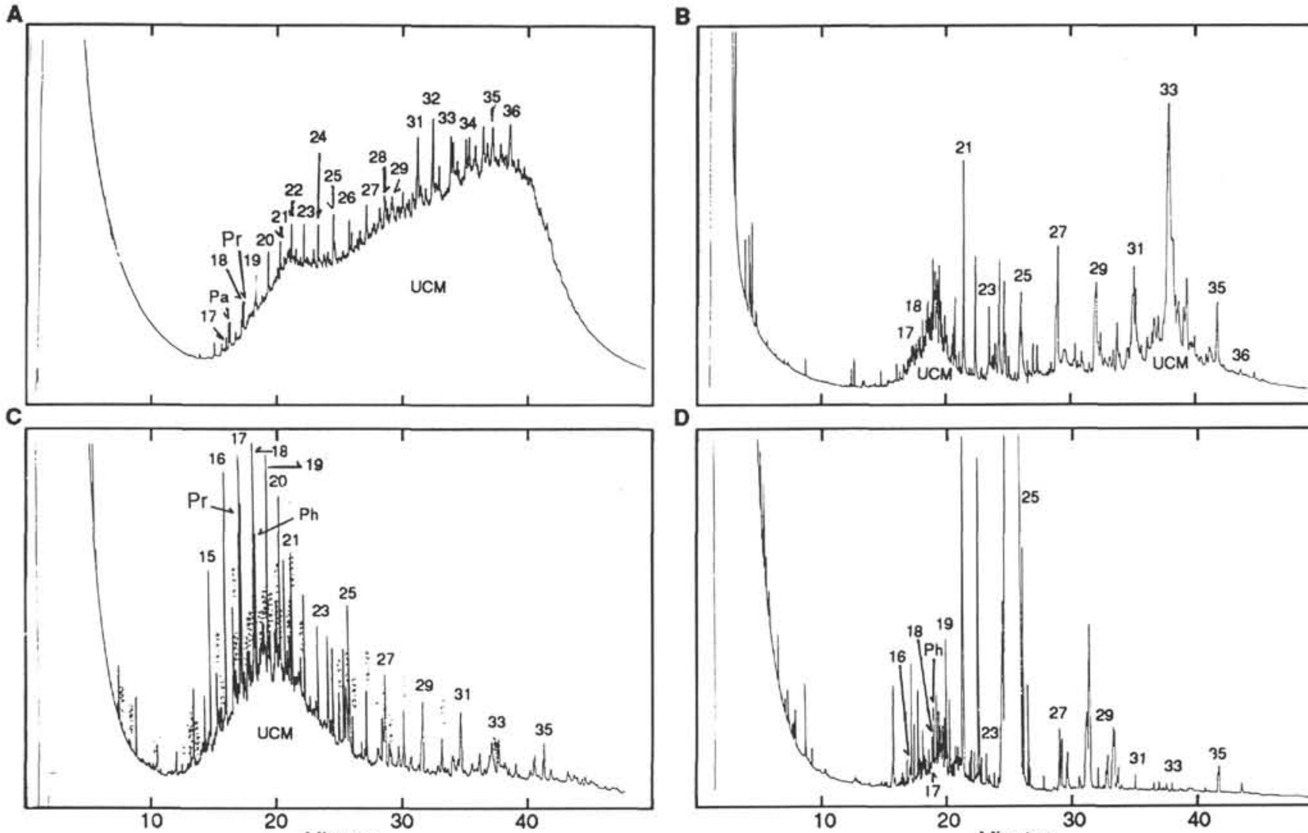

Figure 39. Gas chromatographic traces of the bitumen (hexane soluble matter) of sediments from Holes 859A and 859B. **A.** Sample 141-859A-9P-CC. **B.** Sample 141-859B-10R-3, 10–13 cm. **C.** Sample 141-859A-13X-1, 90–95 cm. **D.** Sample 141-859B-27R-1, 97 cm. Numbers on peaks refer to carbon chain length of *n*-alkanes, Pr = pristane, Ph = phytane, UCM = unresolved complex mixture of branched and cyclic compounds.

Table 13. Composition of gases from core expansion voids of sediments from Holes 859A and 859B.

Core, section, interval (cm)	Depth (mbsf)	Hydrocarbon concentration (ppm)								CO_2	C_1/C_2	C_1/C_3	$C_1/n\text{-}C_4$
		C_1	C_2	C_3	$i\text{-}C_4$	$n\text{-}C_4$	$i\text{-}C_5$	$n\text{-}C_5$	C_{6+}				
141-859A-													
4H-1	17.5	862231	56	0	0	0	0	0	0	992	15397	–	–
5H-6	33.5	916452	58	0	0	0	0	0	0	984	15801	–	–
6X-1	35.5	636960	105	0	0	0	0	0	0	756	6066	–	–
11X-2	70	204601	32	0	0	0	0	0	0	966	6394	–	–
13X-1	80	140145	tr	0	0	0	0	0	0	700	–	–	–
14X-3	90	521106	44	0	0	0	0	0	0	617	1184	–	–
141-859B-													
1R-2	54	562072	21	0	0	0	0	1	1	999	26765	–	–
2R-3	65	700872	75	0	0	0	0	0	0	nd	9345	–	
3R-5	78	880897	72	tr	2	0	0	0	0	984	12235	–	–
10R-3	200	742056	156	7	2	0	0	0	0	411	4757	106008	–
12R-3	220	922939	275	39	10	3	3	0	0	nd	3356	23665	307646
13R-4	231	944456	282	53	16	56	5	3	6	961	3349	17820	16865
14R-5	241	785153	277	86	19	64	8	2	6	998	2834	9130	12268
15R-1	246	882433	290	85	17	2	6	tr	2	356	3043	10382	441217
16R-3	259	953223	373	152	37	41	14	3	7	702	2556	6271	23249
17R-2	266.8	817246	254	89	18	2	7	2	0	344	3218	9183	408623
18R-3	278	140350	27	11	2	0	0	0	0	618	5198	12759	–
20R-1	294	925201	367	127	29	3	11	3	4	967	2521	7285	308400
21R-2	305	831895	302	109	21	3	9	tr	tr	985	2755	7632	277298
23R-3	325	131681	38	12	4	2	0	0	0	nd	3465	10973	65841
25R-4	346.5	19339	5	1	0	0	0	0	0	698	3868	19339	–
27R-2	362.2	78759	19	8	3	0	0	0	0	976	4145	9845	–
29R-4	385	2201	0	0	0	0	0	0	0	1004	–	–	–
34R-2	430	750898	320	163	65	4	11	2	3	725	2347	4607	187725

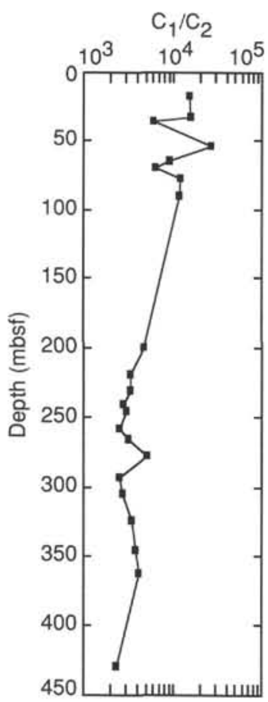

Figure 40. C_1/C_2 ratio of gases from core expansion voids of sediments from Holes 859A and 859B.

Table 14. Extractable bitumen of sediments from Holes 859A and 859B.

Core-section	Depth (mbsf)	C_{max}	C_{range}	Pr/Ph	Pr/nC_{17}	Ph/nC_{18}	CPI
141-859A-							
3H-4	15.2	21	17–36	1.00	0.43	0.21	1.21
6X-5	36.3	21	14–36	1.00	0.55	0.50	2.47
10X-CC	62.8	18	12–36	1.17	0.60	0.50	3.29
13X-1	78.9	18	10–36	1.29	0.72	0.55	1.14
141-859B-							
10R-3	199.8	21	10–36	0.67	1.14	1.33	3.66
15R-1	246.4	21	14–36	0.24	1.33	1.21	2.33
22R-1	313.7	21	10–36	0.56	5.00	12.00	1.90
27R-1	361.7	21	10–36	0.73	2.57	4.11	3.67
36R-2	450.7	18	10–36	0.54	9.60	2.54	2.41
38R-2	468	18	10–36	0.67	1.91	5.94	2.22
Bitumen particles							
859A-9P-CC		20	15–37	0.83	0.83	0.75	1.02
Extract of fluorescent spot							
859B-27R-1	361.4	21	10–36	0.66	1.91	5.94	1.87

oceanic crust. The K and Si profiles suggest a diagenetic front at the depth of the "thermal jet" (~240 mbsf; see WSTP-ADARA Temperature Measurements section, this chapter) involving smectite to illite conversion. Vertical advection of fluids through this section seems unlikely, based on the very low porosities, high compaction, and inferred low permeabilities (see Physical Properties section, this chapter). Between 0 and 50 mbsf, the dramatic downward-decreasing magnesium gradient probably reflects volcanic glass alteration and/or Mg-smectite formation with Mg-uptake in the interval between 50 and 75 mbsf. No evidence from petrographic description of the sediment supports the presence of dolomites (see discussion of XRD results in Lithostratigraphy section, this chapter). However, the lithostratigraphy logs do suggest the presence of a hard layer at 67 mbsf (low porosity, with high density, sonic velocity, and resistivity) that may be a carbonate stringer not recovered in Core 141-859A-10X. Drilling records for Core 141-859A-10X also support the presence of a "hard layer." This might represent a "floor" to the hydrated interval.

Below about 80 mbsf, magnesium concentrations are low but fairly constant (~15 mM), with the exception of a magnesium-depleted interval between about 220 and 280 mbsf. This interval also coincides with a Ca-enriched interval (above the Ca-trend) that is described as containing fractured (brecciated) material (see Lithostratigraphy section, this chapter) that might provide a migration pathway for lateral fluid flow. If these Mg and Ca offsets reflect contemporary flow, the sourcing of the water must be from lithologic units deeper than recovery because the offsets are toward a more "basaltic" component (higher Ca and lower Mg). Both borehole temperature logs and in-situ temperature measure-

Table 15. Rock-Eval and total organic carbon (TOC) of sediments from Holes 859A and 859B.

Core, section, interval (cm)	Depth (mbsf)	T_{max} (°C)	S_1 (mg/g)	S_2 (mg/g)	S_3 (mg/g)	TOC (%)	HI	OI	PI	S_2/S_3
141-859A-										
1H-1, 54–56	0.5	422	0.37	1.74	2.39	1.13	154	212	0.18	0.73
2H-1, 102–105	2.2	408	0.18	0.69	1.14	0.64	108	178	0.21	0.61
2H-2, 102–104	3.7	–	0.05	0.20	0.97	0.34	59	285	0.20	0.21
2H-3, 103–105	5.2	–	0.10	0.37	0.88	0.52	71	169	0.21	0.42
2H-4, 101–103	6.7	401	0.12	0.50	0.92	0.53	94	174	0.19	0.54
2H-5, 101–104	8.2	–	0.10	0.31	1.15	0.40	78	288	0.24	0.27
2H-6, 96–98	9.7	414	0.17	0.74	1.71	0.71	104	241	0.19	0.43
2H-7, 32–34	10.5	–	0.13	0.45	1.50	0.46	98	326	0.22	0.30
3H-3, 32–34	14.0	–	0.05	0.43	2.30	0.39	110	590	0.10	0.19
4H-1, 98–100	17.7	–	0.08	0.40	1.93	0.49	82	394	0.17	0.21
4H-3, 9–11	19.8	403	0.10	0.61	0.62	0.56	109	111	0.14	0.98
4H-3, 137–140	21.1	–	0.07	0.49	0.71	0.44	111	161	0.13	0.69
4H-5, 87–89	23.6	–	0.06	0.37	1.19	0.42	88	283	0.14	0.31
5H-4, 22–24	29.9	412	0.09	0.62	0.96	0.60	103	160	0.13	0.65
6X-1, 102–104	35.7	–	0.05	0.27	0.95	0.36	75	264	0.16	0.28
11X-2, 13–15	69.9	–	0.03	0.19	1.67	0.29	66	576	0.14	0.11
13X-1, 77–79	78.8	–	0.06	0.36	0.49	0.39	92	126	0.14	0.73
13X-1, 83–85	78.8	–	0.08	0.43	0.48	0.33	130	145	0.16	0.90
14X-2, 131–133	90.4	–	0.05	0.30	0.46	0.33	91	139	0.14	0.65
17X-CC, 25–27	107.2	–	0.01	0.09	0.35	0.13	69	269	0.10	0.26
18X-CC, 28–30	117.4	–	0.03	0.07	1.13	0.23	30	491	0.30	0.06
20X-CC, 46–48	136.4	–	0.10	0.32	1.54	0.47	68	328	0.24	0.21
141-859B-										
1R-2, 73–75	54.2	–	0.03	0.24	1.05	0.32	75	328	0.11	0.23
2R-2, 96–98	64.1	–	0.04	0.28	1.10	0.26	108	423	0.13	0.25
3R-4, 97–99	75.8	–	0.02	0.22	1.83	0.26	85	704	0.08	0.12
4R-2, 73–75	142.2	–	0.02	0.16	0.96	0.25	64	384	0.11	0.17
10R-3, 114–116	200.8	–	0.01	0.13	0.72	0.25	52	288	0.07	0.18
11R-1, 85–87	207.3	–	0.01	0.10	0.33	0.27	37	122	0.09	0.30
12R-1, 54–56	216.5	–	0.00	0.12	0.34	0.12	100	283	0.00	0.35
13R-3, 70–72	229.3	–	0.00	0.09	0.45	0.09	100	500	0.00	0.20
14R-3, 98–100	239.3	–	0.00	0.09	0.48	0.13	69	369	0.00	0.19
14R-4, 135–140	241.2	–	0.01	0.13	0.20	0.24	54	83	0.07	0.65
15R-3, 103–105	249.0	–	0.08	0.49	0.87	0.36	136	242	0.14	0.56
16R-1, 80–82	255.4	–	0.00	0.16	0.71	0.21	76	338	0.00	0.23
17R-7, 15–17	273.5	–	0.02	0.12	0.44	0.28	43	157	0.14	0.27
19R-3, 54–56	287.0	408	0.08	0.52	0.80	0.27	193	296	0.13	0.65
20R-4, 22–24	297.9	–	0.03	0.26	0.41	0.21	124	195	0.10	0.63
21R-3, 25–27	306.1	–	0.04	0.23	0.41	0.07	329	586	0.15	0.56
22R-1, 46–48	312.7	–	0.02	0.16	0.59	0.28	57	211	0.11	0.27
23R-1, 8–10	322.0	–	0.02	0.27	0.56	0.33	82	170	0.07	0.48
25R-3, 80–82	344.0	–	0.04	0.22	0.44	0.20	110	220	0.15	0.50
26R-2, 14–16	352.4	–	0.01	0.13	0.27	0.23	57	117	0.07	0.48
27R-2, 71–73	362.6	419	0.09	0.67	0.79	0.41	163	193	0.12	0.85
30R-3, 90–92	393.1	–	0.02	0.21	0.44	0.25	84	176	0.09	0.48
33R-3, 33–35	421.6	–	0.00	0.10	0.21	0.22	45	95	0.00	0.48
34R-2, 129–131	430.7	–	0.04	0.33	0.47	0.30	110	157	0.11	0.70
38R-2, 0–10	467.9	–	0.00	0.21	0.23	0.19	111	121	0.00	0.91

ments (WSTP) in this interval revealed hot and cold temperature anomalies over short vertical distances, which suggests recent and complex fluid and temperature histories in this fracture (fault?) zone. This zone also coincides with an alkalinity minimum and with the tops of sharp breaks in the profiles of potassium and silica.

These profiles may reflect in-situ reactions, temperature artifacts, or in the case of K and Si, differences in clay equilibration reactions between two different lithologic units bounded at ~240 mbsf. The dramatic offset in the strontium profile between 200 and 240 mbsf suggests fairly recent and large lateral displacement or emplacement of upper and lower thrust sheets bounded by the brecciated zone.

PHYSICAL PROPERTIES

Physical properties were measured at Site 859 by continuous scanning of whole-round cores with the multisensor track apparatus (MST) or by gathering data at routine or selected intervals along either whole-round or split cores. Expanded information concerning procedures for data collecting, processing, and measuring is provided in the Explanatory Notes (this volume).

APC cores were suitably coherent for MST scanning and digital sonic velocimeter (DSV) measurements of V_p values. However, except for the uppermost sediment, gas disrupted the cores to such an extent that V_p readings with the *P*-wave logger (PWL) were not reliable and the accuracy of gamma-ray attenuation estimator (GRAPE) readings was degraded. Below a depth of 35 mbsf, the combination of gas expansion and XCB coring disturbed the cores to such an extent that no V_p readings were possible and the GRAPE measurements of bulk density were unrepresentative of in-situ properties. However, by judicious selection of discrete samples and measuring points, useful index properties and thermal conductivity (TC) readings were collected to the base of Hole 859A.

During RCB coring at Hole 859B, disrupted as well as reasonably intact material was recovered from the beginning of coring at 52 mbsf to the bottom of the hole at 476.1 mbsf. Although mostly inappropriate for V_p (PWL) and GRAPE data via MST scanning, careful selection of coherent material from the disrupted RCB core sections provided useful index properties. We note in particular, as did the Shipboard Scientific Party of Leg 112 (Suess, von Huene, et al., 1988), that the upper part of core-catcher (CC) sediment of RCB cores was commonly much less

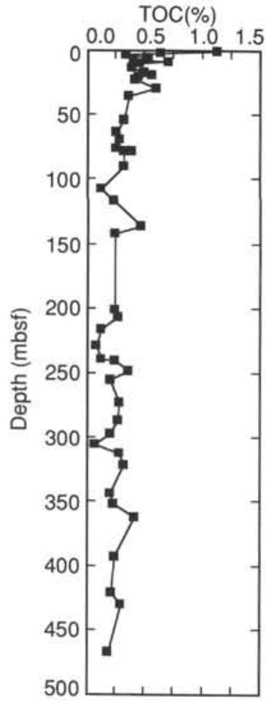

Figure 41. Total organic carbon content (Rock-Eval) vs. depth of sediments from Holes 859A and 859B.

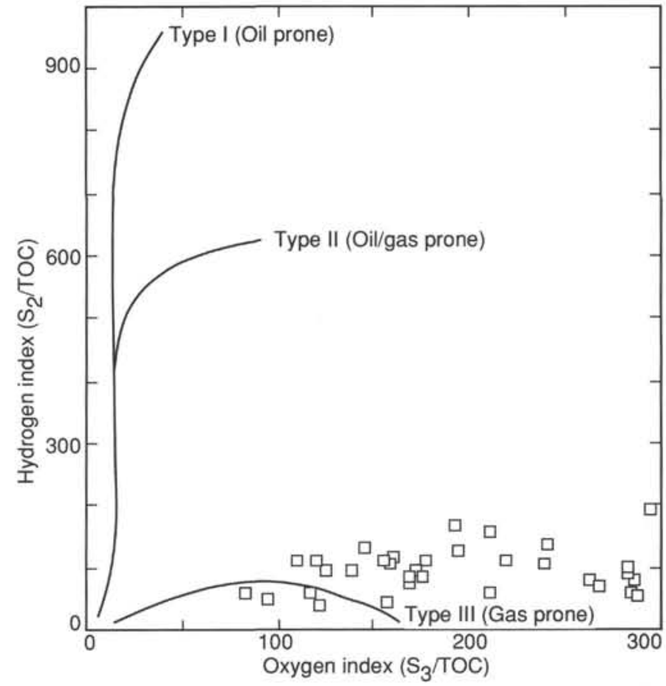

Figure 42. Diagram of hydrogen index vs. oxygen index (Rock-Eval) of organic matter of sediments from Site 859.

disturbed than higher core sections. However, care had to be exercised to avoid sampling structurally damaged and overly compacted material at the leading end of the CC section, where robust core extraction was used.

The most outstanding physical characteristics of the sedimentary section penetrated at Site 859 are, for any particular depth, low porosity and water content and, correspondingly, high bulk density. These dense sedimentary deposits crumble and fragment easily.

Descriptions of the physical properties of the sediments recovered at Site 859 are presented under three subheadings that group data by type rather than measuring technique: (1) the index properties of grain density, porosity, water content, and bulk density; (2) thermal conductivity; and (3) sonic or V_p velocity. Reference is made to three physical property units, which are recognized based on the physical characteristics of core sediments, in particular the index properties of porosity and bulk density. The distinguishing characteristics and stratigraphic positions of these units (and subunits) are described below; lithologic terms are derived from the Lithostratigraphy section (this chapter).

Unit A; 0–10.7 mbsf, clayey silt to silty clay exhibiting a relatively steep downward decrease in porosity. Equivalent to lithologic Unit I.

Unit B; 10.7–200 mbsf, clayey silt to silty clay displaying an overall gentle (5%/100 m) downsection decrease in pore space volume. Equivalent to all but the lower 35 m of lithologic Subunit IIA.

Table 16. Interstitial water data obtained from titanium squeezers for Site 859.

Core, section, interval (cm)	Depth (mbsf)	IW vol. (mL)	pH	Alk (mM) (Gran)	Sal (Refr)	Cl (mM) (Tit'n)	SO_4 (mM) ($BaSO_4$)	SO_4 (mM) (IC)	NH_4 (M) (Spec)	Si (µM) (Spec)	Mg (mM) (Tit'n)	Mg (mM) (AAS)	Ca (mM) (Tit'n)	K (mM) (AES)	Sr (µM) (AAS)	F (µM) (ISE)	B (mM) (Spec)	Na (mM) (AES)	Li (µM) (AES)
141-859A-																			
2H-3, 140–145	5.60	28	7.75	13.22	34.00	558	0.20	0.00	1370	666	38.92	47.20	2.78	12.1	67	62	0.67	500	25.0
3H-3, 145–150	15.15	30	8.29	10.50	33.00	568	0.00	0.00	1480	672	30.35	37.20	2.20	11.9	44	34	0.36	505	25.0
4H-3, 140–145	21.10	15	8.26	10.41	34.00	571	0.00	0.00	2060	640	27.12	30.94	3.12	11.1	49	29	0.41	516	24.0
5H-3, 40–50	27.44	8			33.50	567	0.20	0.00	2640	521	23.72	25.80	3.83	11		29	0.36	520	25.0
6X-2, 0–5	36.20	8	8.08		26.00	438	4.10	4.65	2550		18.37	18.50	3.92	7.4	50	30	0.23	416	
11X-2, 140–150	71.20	18	8.22	9.15	34.00	603	0.40	0.42	3100	528	16.24	17.40	5.61	9.4	77	27	0.23	567	30.6
13X-1, 100–110	79.00	32	8.11	6.93	34.00	591	0.50	0.76	3030	653	14.34	15.10	5.78	9.7	77	26	0.31	563	49.2
14X-2, 140–150	90.42	36	8.15	7.32	34.50	587	5.57	5.78	2920	546	18.16	17.41	6.53	10.2	85	27	0.23	550	62.0
141-859B-																			
1R-2, 145–150	54.95	9			26.50	474	2.90	3.44	3330		16.58	15.59	3.04	7.3	52	32	0.32	433	22.9
2R-2, 145–150	64.55	8			30.00	539	3.20	3.76	3260		20.13	16.08	4.78	7.9	61	31	0.32	490	24.4
3R-4, 118–128	75.70	42	8.23	8.90	34.00	602	2.60	3.19	3260	540	17.06	16.70	5.67	8.6	74	29	0.36	548	26.8
4R-1, 140–150	141.40	16	8.29		36.50	604	2.90	3.65	2860	558	13.64	12.68	7.13	9.2	96	29	0.33	576	33.0
10R-3, 0–10	199.70	22	8.05	4.26	35.00	606	8.10	8.69	2130	513	13.15	16.66	17.78	7.8	121	36	0.35	549	33.7
12R-3, 96–106	219.26	9			36.00	649	3.10	3.86	1970		7.75	6.80	26.95	4.9		40	0.25	586	29.1
14R-4, 140–145	241.20	6			36.00	619	7.30	8.31	1600	232	7.39	6.31	41.88	1.8		39	0.23	548	
16R-2, 140–150	257.50	24	8.31	1.66	36.00	595	10.80	11.38	1190	287	8.36	9.44	41.75	1.3	63	43	0.31	523	37.0
18R-2, 140–150	276.90	20	8.14	1.60	36.00	617	7.81	9.85	1090	159	9.96	8.05	44.84	1.2	64	43	0.28	580	51.5
20R-1, 140–150	294.60	12	8.41	2.33	36.00	593	13.12	17.17	880	185	15.81	15.11	40.24	1.6		47	0.33	514	
25R-3, 140–150	345.60	30	8.25	3.16	36.00	603	10.22	13.08	850	175	14.07	14.08	51.28	1.3	73	44	0.31	502	
27R-1, 135–150	361.75	22	8.37	2.89	35.50	590	12.44	16.26	820	139	16.42	16.74	49.09	1.4	81	46	0.33	490	72.0
29R-3, 140–150	384.90	15	8.15	3.74	36.00	586	10.37	12.93	700	138	14.99	14.12	59.86	1.5		48	0.31	483	
32R-1, 90–100	409.50	18	8.14	5.33	37.00	596	9.59			131	15.85		65.37	2.5	122	53	0.37	466	80.9
34R-3, 140–150	432.30	3			38.50	596	12.08			122	8.85		87.11	1.4	141	50	0.27	435	102.0

Note: Magnesium was determined by both titration and by atomic absorption spectrophotometry. Sulfate was determined by both barium sulfate turbidimetry and by ion chromotography.

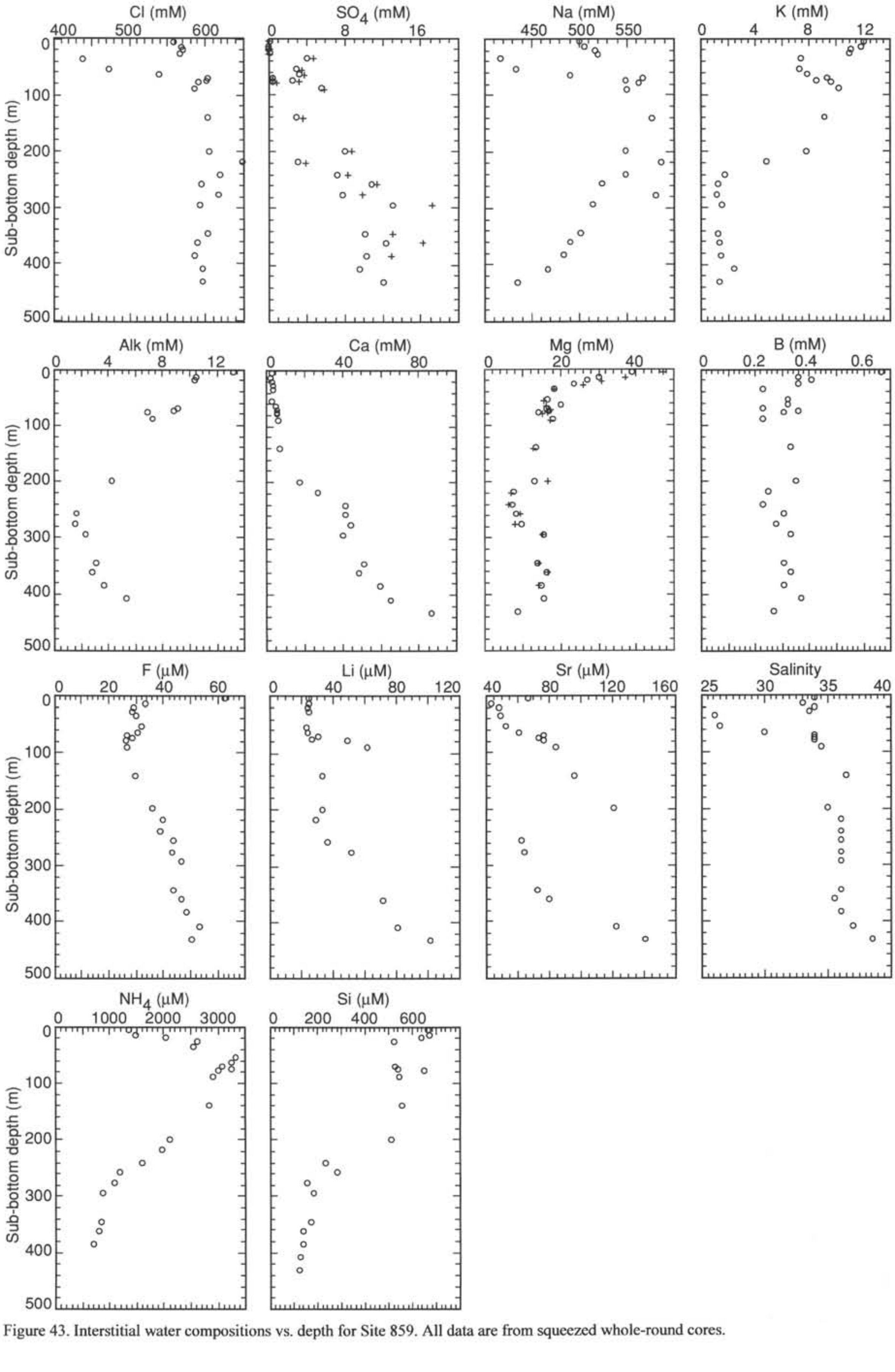

Figure 43. Interstitial water compositions vs. depth for Site 859. All data are from squeezed whole-round cores.

Table 17. Interstitial water data obtained from successful WSTP runs for Site 859.

Core	Depth (mbsf)	Designation	Vol. (mL)	Sal. (Refr)	Cl (mM)	SO_4 (mM)	Mg (mM)	Ca (mM)	F (μM)	K (mM)
141-										
859A-4H	16.7	No sample								
859A-8X	49.0	WT2T	6	33.5	406	0.4	22.10	5.26	131.0	
		WO2T	153	24.0	403	5.3	20.30	4.27	40.3	
859A-11X	68.3	WT3T	6	35.0	609	1.1	21.61	5.96	92.5	8.9
		WO3T	600	30.0	490	23	42.59	8.27	45.2	
859A-15P		No sample								
859B-3R	71.3	No sample								

WT = titanium coil; WO = overflow chamber.

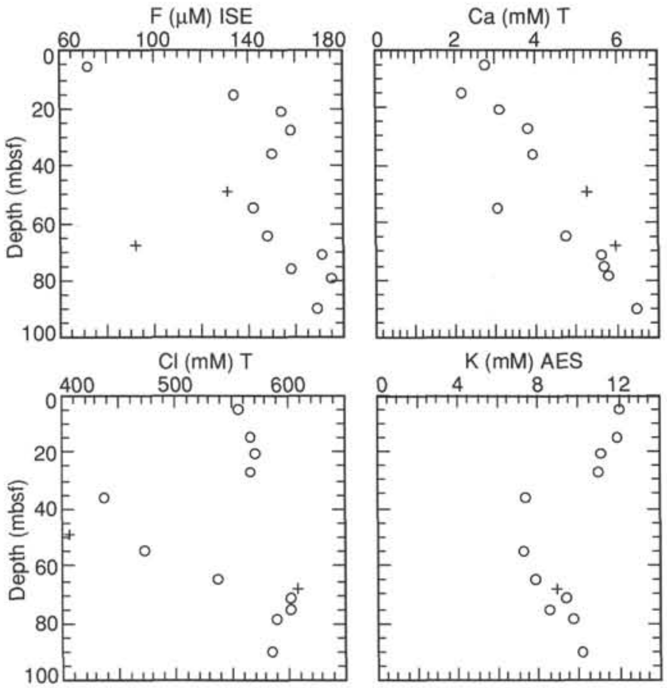

Figure 44. Comparison of interstitial water (IW) data from squeezed whole-round cores (open circles) and from the WSTP (crosses).

Unit C; 200–230 mbsf, clayey silt to silty clay characterized by a relatively high porosity and water content with respect to overlying and underlying deposits. Approximately equivalent to the lower 30 m of lithologic Subunit IIB.

Unit D; 230–476.1 mbsf (bottom of Hole 859B), mostly claystone and siltstone beds exhibiting an erratic but continuous overall trend of downward-decreasing porosity.

Subunit D1; 230–370 mbsf, silty claystone, claystone, and clayey siltstone displaying a gentle overall downward trend of decreasing porosity characterized by one or more breaks in gradient, apparently linked to an abrupt increase or regression in porosity. Equivalent to the upper 135 m of lithologic Subunit IIB.

Subunit D2; 370–476.1 mbsf, lithologically identical to Subunit D1 but distinguished by a prominent regression to a higher porosity value at the top of the subunit and a relatively steep gradient of decreasing porosity (25%/100 m) to the bottom of Hole 859B. Equivalent to the lower 100 m of lithologic Subunit IIB.

Index Properties

Separate listings, by depth and core number, of the index physical properties of sedimentary deposits recovered at Holes 859A and 859B are presented, respectively, in Tables 18 and 19. The downsection trends exhibited by these relatively large data sets are best discerned by examining the data plots of Figure 45.

Grain Density

For any particular core (generally cored over a length of 9.5 m, but typically recovering less than about 6–7 m), the measured variability in grain density is about 0.1 to 0.2 g/cm^3 (Fig. 45). The grain density for Site 859 sediment averages roughly 2.8 g/cm^3 in the upper 100 m and about 2.75 g/cm^3 near a depth of 470 mbsf. Grain density increases downsection through at least the first 150 mbsf (i.e., within Units A and B) and reaches an average value of about 2.9 g/cm^3 at this depth. This trend is reversed below a depth of about 200 mbsf, which marks the top of Unit B and the beginning of a gradual downward decrease in grain density sustained to the maximum depth of sampling at the base of Subunit D2. Poor core recovery between 150 and 200 mbsf (Cores 141-859B-5R to -8R) denied us an opportunity to map the shape or sharpness of the trend inversion.

Porosity

Wet sediment porosity measurements for suites of samples collected along any particular core differed by as little as 2% to as much as 18%. This variability reflects the contrasting properties of interbedded material recovered within one core. Intergranular porosity decreases rapidly with depth (Fig. 45), from near-surface values of 60% to 70% to about 12% near 470 mbsf. In particular, high porosity and a steep downward gradient of decreasing values characterize the thin surface sediment of Unit A (Fig. 46). These deposits are late Pleistocene in age; all underlying beds are upper Pliocene deposits. Beginning at a depth near 11 mbsf, a gentler profile of downward decreasing porosity is sustained from 45% to about 30% at the projected base of Unit B at 200 mbsf (poor core recovery between 150 and 200 mbsf does not allow the base of Unit B to be more closely defined). Distinctly higher porosity values (~40%–50%) define Unit C between 200 and 230 mbsf (Fig. 45). Underlying beds of Subunit D1 are much less porous and exhibit a gentle but erratic gradient of decreasing porosity, reaching a value of about 20% at the base of the subunit at 370 mbsf. This trend is abruptly offset to higher porosity values (~30%) coincident with the top of Subunit D2, below which a gradient of roughly 25%/100 m is established to the base of the hole (476.1 mbsf) where the porosity falls to only about 12%. Obviously, this trend cannot continue much farther downsection. One can only surmise that porosity at some short distance below the base of Hole 859B either increases or stabilizes between 5% and 10%.

The low-porosity sediment of Unit D is weakly cemented and crumbles and fragments easily. A qualitative assessment of the "connectability" or continuity of pore spaces in this weak material is provided by the data plot of Figure 47, in which is compared the volume measurement of the solid (i.e., mineral and rock grains) fraction of a small mass (5–8 cm^3) of oven-dried sediment

Table 18. Index physical properties for Hole 859A.

Depth (mbsf)	Core-section	Wet bulk density (g/cm^3)	Dry bulk density (g/cm^3)	Grain density (g/cm^3)	Wet porosity (%)	Dry porosity (%)	Wet water content (%)	Dry water content (%)	Wet void ratio	Dry void ratio
0.52	1H-1	1.60	0.85	2.69	72.60	69.90	46.60	87	2.65	2.29
2.19	2H-1	1.78	1.34	2.75	42.70	46.90	24.60	33	0.74	0.88
3.69	2H-2	1.99	1.47	2.78	51.20	49.50	26.30	36	1.05	0.97
5.20	2H-3	1.91	1.34	2.79	54.90	53.50	29.50	42	1.22	1.14
6.70	2H-4	1.91	1.36	2.74	53.70	52.30	28.80	40	1.16	1.08
8.19	2H-5	1.81	1.19	2.74	59.90	58.20	34.00	52	1.50	1.38
9.69	2H-6	1.82	1.22	2.68	58.40	56.40	32.90	49	1.40	1.28
10.4	2H-7	1.87	1.31	2.74	54.40	53.50	29.80	42	1.19	1.14
11.99	3H-1	2.08	1.62	2.70	44.20	42.60	21.80	28	0.79	0.74
13.49	3H-2	1.99	1.48	2.77	50.00	48.60	25.70	35	1.00	0.94
13.99	3H-3	2.03	1.53	2.78	49.10	47.40	24.80	33	0.97	0.89
15.43	3H-4	2.03	1.52	2.73	49.70	47.40	25.00	33	0.99	0.89
17.63	4H-1	2.04	1.59	2.75	44.60	43.80	22.40	29	0.80	0.77
19.20	4H-2	2.08	1.63	2.75	43.70	42.70	21.60	27	0.78	0.74
19.75	4H-3	1.99	1.50	2.87	48.30	48.30	24.80	33	0.94	0.93
22.04	4H-4	2.07	1.61	2.79	44.70	43.80	22.10	28	0.81	0.77
23.54	4H-5	2.08	1.64	2.81	42.40	42.30	20.90	26	0.74	0.73
24.25	4H-6	2.08	1.60	2.70	46.10	43.90	22.80	29	0.86	0.78
24.97	4H-CC	2.11	1.66	2.86	43.60	43.10	21.20	27	0.77	0.75
27.00	5H-2	2.04	1.53	2.90	49.10	48.50	24.70	33	0.97	0.93
28.54	5H-4	2.13	1.73	2.86	38.90	39.30	18.70	23	0.64	0.64
30.13	5H-5	2.16	1.74	2.86	41.50	40.80	19.70	25	0.71	0.68
30.66	5H-6	2.11	1.65	2.76	45.20	43.30	21.90	28	0.82	0.76
35.70	6X-1	2.10	1.66	2.79	43.40	42.40	21.10	27	0.77	0.73
37.17	6X-CC	2.16	1.77	2.73	37.60	36.90	17.80	22	0.60	0.58
41.64	7X-CC			2.83						3.22
50.30	8X-1	2.05	1.55	2.79	48.60	46.90	24.30	32	0.95	0.88
58.00	9P-CC	2.11	1.64	2.88	45.70	44.70	22.20	29	0.84	0.80
58.50	10X-CC									
69.12	11X-1	2.05	1.59	2.85	44.40	44.50	22.20	29	0.80	0.79
69.90	11X-2	2.07	1.61	2.84	45.10	44.60	22.30	29	0.82	0.80
70.62	11X-2	2.02	1.52	2.87	48.80	48.10	24.70	33	0.95	0.92
71.40	11X-3	2.05	1.57	2.89	46.80	46.50	23.40	30	0.88	0.86
72.12	11X-3	2.04	1.55	2.89	47.30	47.00	23.80	31	0.90	0.88
72.90	11X-4	2.15	1.70	2.84	44.00	42.60	21.00	26	0.79	0.74
73.59	11X-4	2.15	1.71	2.75	42.10	40.50	20.10	25	0.73	0.68
77.22	12P-1	2.10	1.63	2.88	45.50	44.70	22.20	29	0.84	0.80
77.22	12P-1	2.12	1.68	2.86	42.40	42.10	20.50	26	0.74	0.72
78.80	13X-1	2.10	1.62	2.78	46.70	44.70	22.80	30	0.88	0.80
91.86	14X-4									
100.69	16X-CC	2.12	1.71	2.78	39.60	39.40	19.20	24	0.66	0.64
100.76	16X-CC	2.18	1.79		38.50	255.20	18.10	22	0.63	
107.18	17X-CC	2.21	1.83	2.83	37.20	36.70	17.30	21	0.59	0.58
117.34	18X-CC	2.18	1.80	2.85	37.20	37.20	17.50	21	0.59	0.59
117.46	18X-CC	2.25			33.30		15.20	18	0.50	
136.36	20X-CC	2.26	1.87	2.87	38.30	37.20	17.40	21	0.62	0.59

determined separately as an intact lump or as a comminuted powder. The two measures (using a helium-displacement pentapycnometer) are effectively identical, thus implying that cementation has not importantly isolated or sealed off pore space, which evidently remains well interconnected even at a depth of nearly 500 mbsf in sediment retaining a porosity of as little as 10% to 12%.

Water Content

The downsection profile of wet-sediment water content mimics that of sediment porosity (Fig. 45). Regressions to higher values occur at 200 and 370 mbsf, corresponding to the tops of Unit C and Subunit D2. Continuing trends of downward decreasing intergranular moisture are reestablished a few meters below these discontinuities. Near 470 mbsf, moisture content decreases to as little as 5%, a seemingly low value for relatively shallowly buried and weakly cemented sediment of late Pliocene age.

Bulk Density

Consistent with the downward decrease in intergranular moisture and space, bulk density measured on selected and routine sediment samples increases from surface values of 1.6 to about 2.75 g/cm^3 at 470 mbsf (Fig. 45). Prominent discontinuities in this gradient occur at 200 (top of Unit C) and 370 (top of Subunit D2) mbsf, and lesser breaks within Subunit D1 (230–370 mbsf).

GRAPE scanning for bulk density did not determine in-situ values accurately and tracked details of subsurface trends poorly. Figure 48, in which we compare GRAPE and discrete sample bulk density, reveals both the great variability of GRAPE readings at specific stratigraphic levels and also their lower value relative to that of discrete samples. Inaccurate GRAPE results are the expected consequence of scanning disrupted XCB and RCB sediment cores replete with gaps and open fractures and insufficient in diameter to fill the core liner. However, GRAPE scanning of APC cores from the upper part of Hole 859A provided relatively accurate measures of sediment bulk density, in particular if the high range of scan readings was selected.

Thermal Conductivity

Thermal conductivity (TC) measurements were routinely conducted on sediment cores collected at both holes (Fig. 45), including the narrow diameter cores recovered with the pressure core barrel in Hole 859A, and core-catcher samples near the base of both Holes 859A and 859B (see Tables 20 and 21). Disrupted cores full of voids, gaps, and pieces of fragmented siltstone and

Table 19. Index physical properties for Hole 859B.

Depth (mbsf)	Core-section	Wet bulk density (g/cm^3)	Dry bulk density (g/cm^3)	Grain density (g/cm^3)	Wet porosity (%)	Dry porosity (%)	Wet water content (%)	Dry water content (%)	Wet void ratio	Dry void ratio
54.26	1R-2	2.04	1.57	2.90	45.70	45.90	22.90	29.70	0.84	0.84
55.51	1R-3	2.09	1.64	2.93	44.00	44.30	21.60	27.60	0.79	0.79
64.10	2R-2	2.10	1.67	2.92	41.90	42.50	20.50	25.70	0.72	0.73
67.10	2R-4	2.03	1.55	2.82	47.20	46.40	23.80	31.20	0.89	0.86
72.30	3R-1	1.97	1.43	2.98	53.00	52.70	27.60	38.10	1.13	1.11
75.52	3R-4	2.04	1.54	2.74	48.80	46.70	24.60	32.60	0.95	0.87
78.30	3R-6	2.00	1.46	2.78	52.70	50.30	26.90	36.90	1.12	1.00
142.20	4R-2	2.20	1.79	2.88	40.30	39.60	18.80	23.10	0.68	0.65
198.53	10R-2	1.95	1.42	2.86	52.10	51.40	27.30	37.60	1.09	1.05
203.03	10R-5	2.14	1.74	2.79	39.40	39.00	18.90	23.30	0.65	0.63
207.30	11R-1	2.12	1.69	2.81	41.70	41.10	20.20	25.20	0.71	0.69
216.50	12R-1	2.14	1.70	2.81	42.10	41.20	20.20	25.30	0.73	0.70
220.36	12R-4	1.87	1.31	2.72	53.90	53.00	29.60	42.00	1.17	1.12
231.75	13R-6	2.31	2.00	2.74	30.20	29.40	13.40	15.50	0.43	0.41
234.15	13R-8	2.26	1.90	2.82	34.20	33.80	15.60	18.40	0.52	0.51
239.30	14R-3	2.15	1.90	2.54	24.50	24.80	11.70	13.20	0.32	0.33
242.30	14R-5	2.26	1.97	2.69	27.70	27.60	12.60	14.40	0.38	0.38
249.00	15R-3	2.02	1.49	2.86	51.10	49.70	25.90	35.00	1.05	0.98
258.97	16R-3	2.51	2.22	2.91	28.60	27.50	11.70	13.20	0.40	0.38
259.12	16R-4	2.40	2.09	2.80	30.50	29.20	13.00	14.90	0.44	0.41
259.64	16R-4	2.31	1.94	2.85	35.40	34.40	15.70	18.70	0.55	0.52
265.63	17R-1	2.31	2.02	2.79	28.30	28.20	12.50	14.30	0.39	0.39
267.25	17R-2	2.41	2.12	2.80	28.30	27.40	12.00	13.70	0.39	0.37
269.84	17R-4	2.47	2.18	2.82	28.40	27.00	11.80	13.40	0.40	0.37
270.97	17R-5	2.37	2.04	2.86	32.50	31.60	14.10	16.40	0.48	0.46
280.38	18R-5	2.25	1.91	2.82	33.80	33.60	15.40	18.20	0.51	0.50
281.04	18R-5	2.40	2.14	2.73	24.80	24.20	10.60	11.90	0.33	0.32
281.30	18R-CC	2.29	1.95	2.77	32.90	32.00	14.70	17.30	0.49	0.47
284.57	19R-1	2.30	2.00	2.65	29.50	28.30	13.10	15.10	0.42	0.39
285.87	19R-2	2.46	2.22	2.83	24.00	23.50	10.00	11.10	0.31	0.31
286.99	19R-3	2.35	2.01	2.81	32.60	31.50	14.20	16.60	0.48	0.46
289.13	19R-4	2.42	2.16	2.80	25.40	24.90	10.70	12.00	0.34	0.33
289.85	19R-5	2.41	2.12	2.77	28.60	27.40	12.10	13.80	0.40	0.37
297.90	20R-4	2.44	2.16	2.81	27.00	26.10	11.40	12.80	0.37	0.35
300.69	20R-6	2.39	2.11	2.79	27.90	27.20	11.90	13.60	0.39	0.37
306.02	21R-3	2.39	2.12	2.75	25.80	25.20	11.10	12.40	0.35	0.33
312.68	22R-1	2.36	2.04	2.83	30.90	30.10	13.40	15.50	0.45	0.43
324.94	23R-3	2.42	2.14	2.78	27.30	26.40	11.60	13.10	0.38	0.36
341.28	25R-1	2.43	2.14	2.76	28.00	26.60	11.80	13.40	0.39	0.36
344.15	25R-2	2.61	2.36	2.87	24.00	22.70	9.40	10.40	0.32	0.29
346.14	25R-4	2.51	2.24	2.83	26.10	24.90	10.70	11.90	0.35	0.33
350.95	26R-1	2.48	2.20	2.80	27.40	26.00	11.30	12.80	0.38	0.35
353.96	26R-3	2.52	2.25	2.71	26.80	24.50	10.90	12.20	0.37	0.32
353.97	26R-3	2.47	2.19	2.78	27.40	26.00	11.40	12.80	0.38	0.35
362.68	27R-2	2.50	2.30	2.81	19.10	19.00	7.80	8.50	0.24	0.23
363.78	27R-3	2.52	2.31	2.84	20.80	20.50	8.50	9.20	0.26	0.26
365.92	27R-4	2.58	2.36	2.79	21.90	20.70	8.70	9.50	0.28	0.26
371.20	28R-1	2.49	2.26	2.78	22.90	22.10	9.40	10.40	0.30	0.28
373.38	28R-3	2.52	2.29	2.80	22.00	21.30	9.00	9.80	0.28	0.27
375.43	28R-4	2.51	2.32	2.85	19.30	19.30	7.90	8.50	0.24	0.24
376.92	28R-CC	2.49	2.21	2.81	27.20	25.80	11.20	12.60	0.37	0.35
383.24	29R-3	2.46	2.15	2.78	30.00	28.10	12.50	14.30	0.43	0.39
384.17	29R-4	2.52	2.19	2.74	32.30	29.00	13.20	15.20	0.48	0.41
385.81	29R-5	2.42	2.16	2.80	25.60	25.10	10.80	12.20	0.34	0.33
397.37	30R-CC	2.25	1.87	2.79	37.20	35.80	16.90	20.30	0.59	0.55
409.00	32R-1	2.46	2.19	2.84	26.50	26.70	11.00	12.40	0.36	0.36
410.06	32R-2	2.30	1.99	2.77	29.90	29.50	13.30	15.40	0.43	0.42
418.44	33R-1	2.38	2.09	2.74	28.40	32.80	12.20	13.90	0.40	0.48
420.10	33R-2	2.34	2.07	2.90	27.10	27.70	11.80	13.40	0.37	0.38
429.22	34R-1	2.59	2.44	2.76	15.10	14.70	6.00	6.30	0.18	0.17
430.74	34R-2	2.62	2.42	2.78	19.00	18.00	7.40	8.00	0.23	0.22
431.85	34R-3	2.67	2.51	2.77	15.10	14.40	5.80	6.20	0.18	0.17
432.62	34R-4	2.55	2.34	2.70	20.60	19.30	8.20	9.00	0.26	0.24
438.17	35R-1	2.55	2.38	2.77	16.40	16.10	6.60	7.10	0.20	0.19
439.68	35R-2	2.56	2.38	2.73	17.90	17.20	7.20	7.70	0.22	0.21
441.23	35R-3	2.52	2.32	2.75	19.10	18.60	7.80	8.40	0.24	0.23
442.18	35R-4	2.47	2.27	2.69	19.40	18.90	8.10	8.80	0.24	0.23
447.95	36R-1	2.60	2.45	2.79	14.80	14.50	5.80	6.20	0.17	0.17
448.94	36R-2	2.55	2.34	2.80	19.90	19.40	8.00	8.70	0.25	0.24
457.05	37R-1	2.66	2.53	2.80	12.60	12.30	4.90	5.10	0.14	0.14
458.55	37R-2	2.78	2.67	2.76	10.30	9.70	3.80	4.00	0.12	0.11
467.14	38R-1	2.49	2.28	2.80	20.80	20.50	8.50	9.30	0.26	0.26
468.33	38R-2	2.65	2.49	2.80	15.60	15.00	6.00	6.40	0.18	0.18

claystone affected the accuracy and significance (relative to in-situ values) of laboratory measurements. TC readings were most degraded by core disruption between 200 and 350 mbsf. The wide scatter of data exhibited within this depth range is reflective of the core-disruption problem.

In general, and despite the difficulties noted above, measurements at both holes imply an overall downward increase in thermal conductivity, from near-seafloor values of about 1.0 W/m·K to averaged readings approaching 1.75 W/m·K at 430 mbsf.

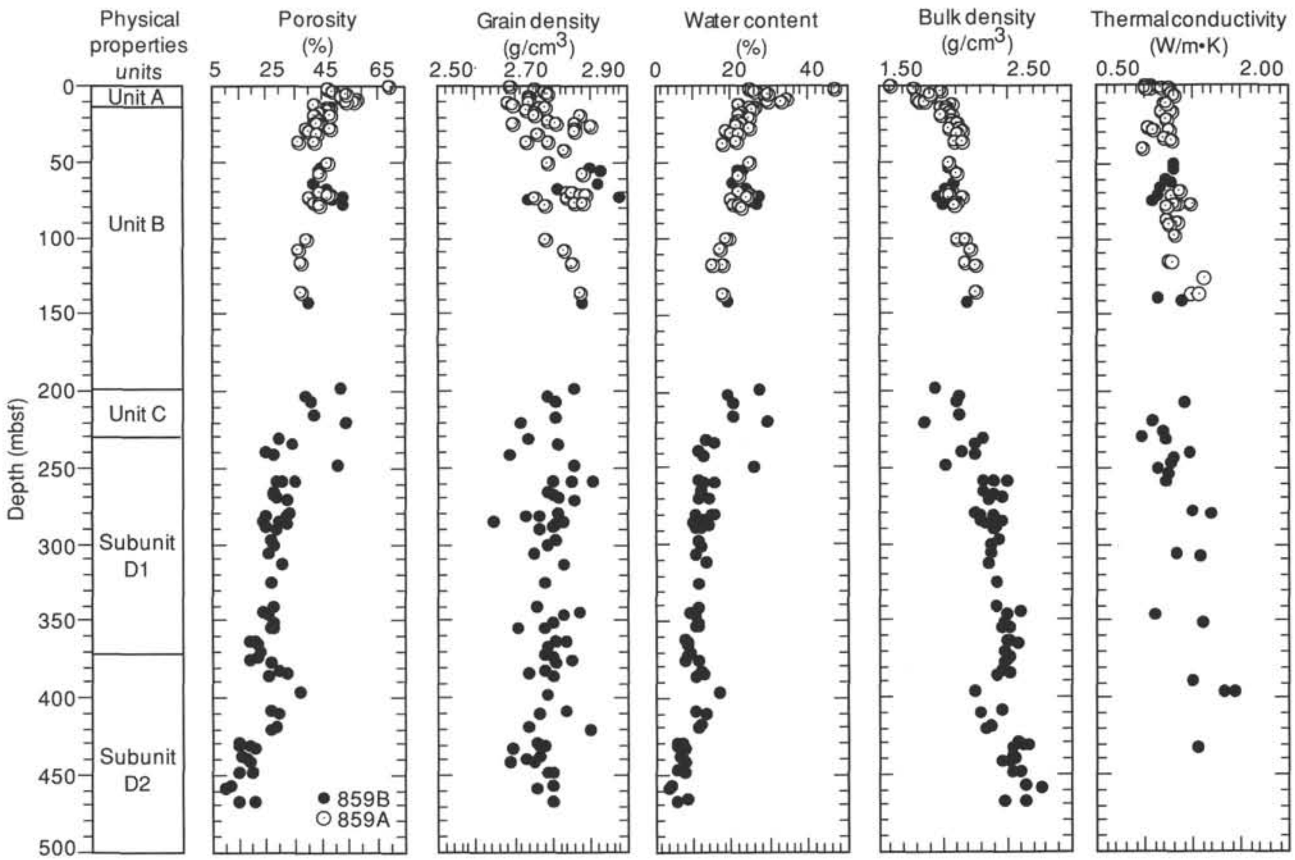

Figure 45. Plot of wet sediment index properties and thermal conductivity vs. depth for Holes 859A and 859B combined.

Sonic (V_p) Velocity

Except for the topmost core at Hole 859A, V_p could not be measured by either the PWL or the DSV apparatus. Cavities and voids linked to gas expansion and drilling-induced disruptions combined to acoustically blank the PWL sensors. Owing primarily to the dry and brittle nature of recovered sediments, the transducer blades of the DSV apparatus wedged apart and cracked the sediment to such a degree that V_p readings were not possible. Similarly, sediment samples that appeared rigid enough to be used on the Hamilton Frame velocimeter, crumbled or cracked under the slight pressure applied by the contacting transducers. Thus, no useful Hamilton Frame V_p measurements were collected.

Discussion and Overview

The high grain density recorded at Site 859 implies that the sedimentary section is poor in low density material; for example, clay minerals, volcanic ash, and siliceous microfossils. By implication, the deposits are dominantly an aggregation of fine-grained but little-weathered rock and mineral detritus. This interpretation supports the notion that the bulk of the section is constructed of relatively fresh rock flour contributed rapidly to the south Chile margin by late Cenozoic glaciation of Andean drainages and coastal lowlands (see Lithostratigraphy section, this chapter). In comparison to the downward increase in grain density within the upper 150 to 200 m of the section, the lower trend of decreasing grain density in Units C and D evidently reflects either downsection diagenesis or the contribution of increasing proportions of less dense detrital material (e.g., more weathered debris or glassy volcaniclastic detritus) from a source terrane.

Presuming that Unit D dominantly consists of accreted trench-floor deposits, one notices that the average porosity at the mean burial depth (350 mbsf) of this body is only about 25%, decreasing to about 12% near 500 mbsf. In comparison, the porosity of other accretionary deposits at the same burial depth is typically higher (~40%), and values as low as 12% are commonly not reached above a subsurface depth of 3000 to 4000 m (von Huene and Scholl, 1991).

The low porosity of the basal deposits of Unit D is evidently not ascribable to post-depositional cementation. Claystone and siltstone deposits recovered below a depth of about 230 mbsf are notably "dry" in appearance and crumble easily. Intergranular pore spaces are openly connected, implying that diagenetic cementation (e.g., carbonate or clay mineral deposition) may not have contributed importantly to pore-volume reduction. A major factor explaining the low porosity and water content of Site 859 deposits is implied by the thin (10–11 m) upper Pleistocene section of lithologic Unit I. Presumably, during Holocene time, a much thicker sequence of Pleistocene beds may have slid off the lower slope and depositionally unloaded the underlying upper Pliocene beds of Units A, C, and D. This hypothesis is strengthened by the observation that the surficial 80-mbsf section consists of folded clayey silt and silty clay beds of Units A and B. Low overall pore-space volume may also result from rapid deposition of glacial-marine debris of geochemically inactive mineral and rock grains of dominantly silt size. Relatively high geothermal temperatures, that may have favored sediment dewatering and compaction, may also have played a role.

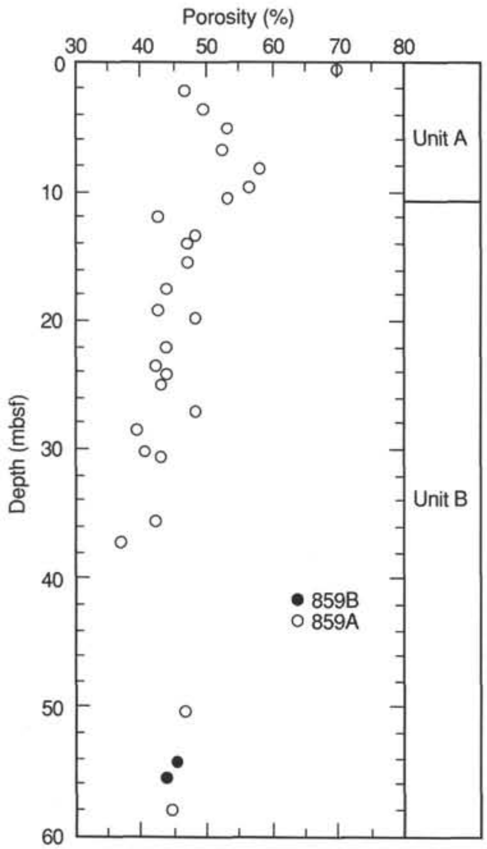

Figure 46. Plot of wet-sediment porosity vs. depth for upper 60 mbsf. Unit A is late Pleistocene in age, Unit B beds are late Pliocene deposits.

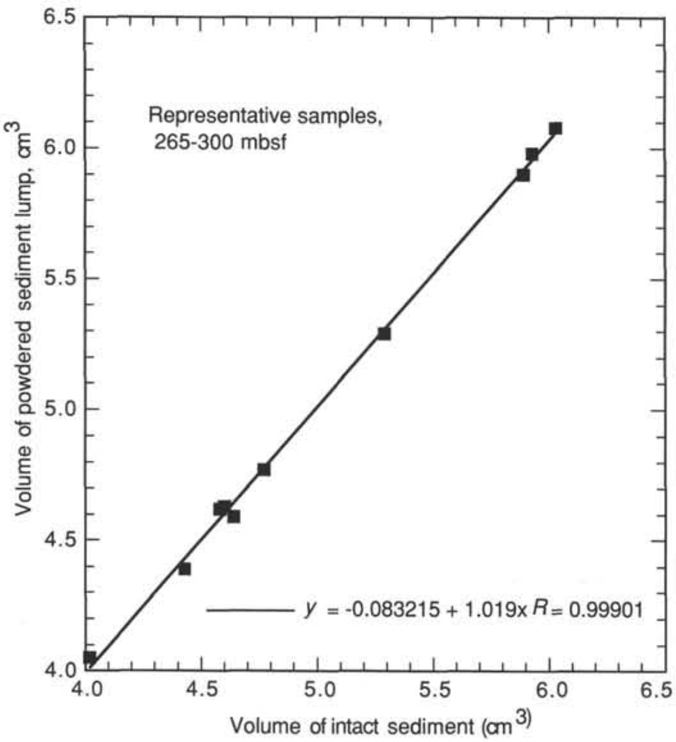

Figure 47. Comparison of volume of dried sediment mass measured as an intact lump or ground to a medium fine powder.

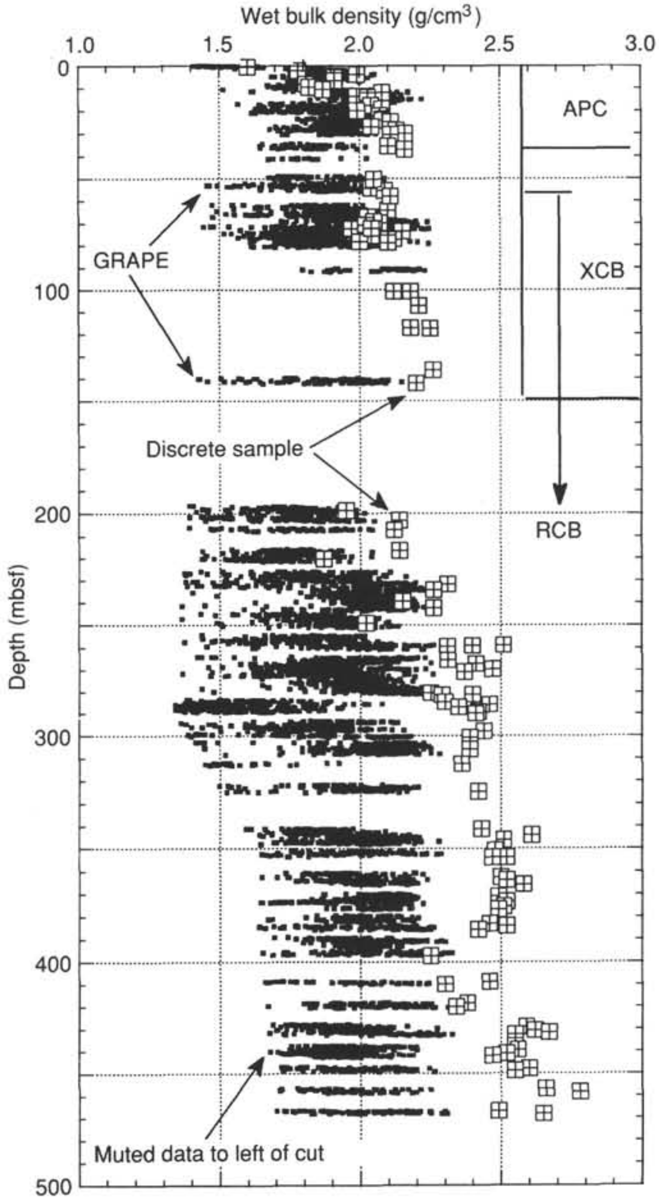

Figure 48. Comparison of wet-sediment bulk density determined by GRAPE scanner with gravimetric and volumetric measurements of discrete sediment samples.

The relatively sharp discontinuities in downward trends of decreasing sediment porosity, water content, and increasing bulk density (Fig. 45), can be reasonably ascribed to tectonic causes. All of the discontinuities occur below the base of Unit B at depths greater than about 200 mbsf. Each is associated with the abrupt downsection occurrence of more porous deposits that, presumably, had formerly been less deeply buried. We suggest that the discontinuities, in particular at the top of Subunit D2 at 370 mbsf, reflect the penetration of either landward- or seaward-dipping thrust or reverse faults.

The discontinuity and porosity regression coincident with the top of Unit C at 200 mbsf is so major that circumstances other than tectonic shortening may be involved. For example, a prominent geothermal anomaly is associated with this relatively high porosity zone (see WSTP-ADARA Temperature Measurements

Table 20. Thermal conductivity measurements for Hole 859A.

Depth (mbsf)	Core, section (cm)	Thermal conductivity (W/m·K)
0.50	1H-1, 50	1.06
0.90	1H-1, 90	1.05
0.50	1H-1, 50	1.01
0.80	1H-1, 80	0.99
2.20	2H-1, 100	1.17
2.20	2H-1, 100	1.25
5.25	2H-3, 105	1.26
6.75	2H-4, 105	1.29
11.70	3H-1, 100	1.22
11.70	3H-1, 100	1.18
16.25	3H-4, 105	1.15
5.25	2H-3, 105	1.26
6.75	2H-4, 105	1.29
11.70	3H-1, 100	1.22
11.70	3H-1, 100	1.18
16.25	3H-4, 105	1.15
17.70	4H-1, 100	1.27
22.20	4H-4, 100	1.21
27.78	5H-4, 24	1.01
28.42	5H-4, 88	1.07
29.99	5H-6, 10	1.24
34.98	6X-1, 28	1.19
35.80	6X-1, 110	1.28
41.24	7X-1, 24	0.97
77.10	12P-1, 10	1.32
77.05	12P-1, 5	1.48
69.33	11X-1, 103	1.34
72.54	11X-3, 124	1.27
78.27	13X-1, 27	1.31
78.76	13X-1, 76	1.22
88.61	14X-1, 101	1.22
89.36	14X-2, 34	1.32
90.82	14X-3, 30	1.25
98.87	15P-1, 7	1.31
116.65	18X-1, 15	1.25
116.60	18X-1, 10	1.27
126.61	19X-CC, 20	1.60
136.31	20X-CC, 41	1.47
136.30	20X-CC, 40	1.56

Table 21. Thermal conductivity measurements for Hole 859B.

Depth (mbsf)	Core, section (cm)	Thermal conductivity (W/m·K)
52.37	1R-1, 37	1.31
54.45	1R-2, 95	1.31
62.70	2R-1, 110	1.21
64.25	2R-2, 115	1.27
66.80	2R-4, 70	1.16
72.36	3R-1, 106	1.14
75.52	3R-4, 100	1.09
141.00	4R-1, 100	1.40
140.57	4R-1, 57	1.14
207.22	11R-1, 82	1.40
219.53	12R-4, 17	1.08
219.53	12R-4, 17	1.08
226.30	13R-2, 40	1.18
229.35	13R-4, 45	0.96
231.85	13R-6, 80	1.23
240.80	14R-4, 100	1.46
243.30	14R-6, 50	1.30
247.30	15R-2, 80	1.27
250.90	15R-5, 40	1.15
255.23	16R-1, 63	1.26
260.10	16R-4, 100	1.21
278.20	18R-3, 120	1.51
281.00	18R-5, 100	1.68
307.87	21R-4, 57	1.59
306.80	21R-3, 100	1.32
347.07	25R-4, 137	1.10
351.15	26R-1, 35	1.60
389.70	30R-1, 50	1.50
397.35	30R-CC, 5	1.83
397.35	30R-CC, 5	1.94
433.29	34R-CC, 8	1.56

section, this chapter), as is a distinct geochemical signature (see Inorganic Geochemistry section, this chapter). Some concern exists that drilling-fluidized core sections may have contributed to high porosity readings.

Thermal conductivity measurements, although affected by hydrate disassociation and core recovery problems, nonetheless display a downsection increase in conductivity that is consistent with increasing bulk density and decreasing moisture content. Although the most thoroughly disrupted cores were recovered between 200 and 350 mbsf, the downward gradient of increasing TC readings established in the overlying deposits of Units A and B noticeably increases below 230 mbsf (Fig. 45), coincident with the top of the more lithified claystone and siltstone beds of Unit D. These observations suggest that the TC data are geologically useful measurements.

WSTP-ADARA TEMPERATURE MEASUREMENTS

The principal aim of the temperature measurement at Site 859 was to determine the combined effects of both sediment accretion and oceanic ridge subduction on the geothermal regime in the wedge toe. Local surface heat-flow values in this region (Cande et al., 1987) indicate that heat flow may be in excess of 300 mW/m^2. Such high heat-flow values might reasonably be expected at this site because of its position within 4 to 6 km of the spreading-center axis, with the oceanic crust under the wedge probably being less than 200,000 yr old. In addition, hydrogeologic activity was also expected to cause measurable temperature perturbations as a result of both the tectonically driven consolidation processes occurring in the thickening wedge and the further influx of heat to the base of the wedge from the subducted oceanic spreading center.

This site was also chosen to examine the relationship between the local pressure/temperature conditions and the stability of methane hydrate in the surface sediments. A prominent BSR near the hole was thought to represent the base of the main methane hydrate layer and, thus, the base of the hydrate stability field. We hoped that our temperature determinations could be used to check whether the predicted upper temperature values for the stability field were correct.

Specific objectives of the temperature measurement program were as follows:

1. To determine the possible nature of the heat transfer processes in the wedge toe.
2. To identify any temperature anomalies associated with channelized fluid flow.
3. To provide a reference for the calibration of the upper temperature bound of the methane stability field.
4. To provide constraints for geochemical and other studies relating to the movement of fluids though the wedge and the thermal maturation of the sediments in the wedge.

To meet these objectives, 12 new water sampler temperature probe (new WSTP) and old WSTP (currently temperature probe only) runs (see Fig. 23 in the Explanatory Notes chapter, this volume) were made (divided between Holes 859A and 859B) in the top 293 mbsf of the sediment column. Nine of these runs were successful. In addition, several ADARA (see Explanatory Notes chapter, this volume) runs were made in the near surface of Hole 859A. Unfortunately, sea conditions were rough and this resulted in considerable disturbance of the ADARA tool, which limited the usefulness of these data. We confine the following discussion to the new and old WSTP temperature probe data that were of relatively good quality.

Temperature Measurements and Results

Hole 859A

Five WSTP tool deployments were attempted during Hole 859A, three of which obtained useful results. The two-channel logger was not operational, so we used the Uyeda recorder exclusively. Both the initial deployment at 25.2 mbsf and a deployment at 68 mbsf failed. The deployments at 49, 98.5, and 126.2 mbsf were successful, and results are displayed in Table 22. The initial two runs at 49 and 98.5 mbsf were performed with the new combined water sampler and temperature probe. Good water samples were taken in both cases and the curves show a characteristic probe-penetration heating pulse and subsequent decay (Figs. 49 and 50). In the third run at 126.2 mbsf, the signature is different (Fig. 51). This was taken with the older temperature probe but the probe gave a good bottom-water temperature and the driller reported that the tool was definitely firmly embedded as the drill string had to be used to pull the tool loose. Thus, as far as we can tell, the record is a good one. It appears that the sediment was sufficiently warm for the thermal pulse to have had a minimal effect so that it dissipated within the 60s recording interval of the tool. Then, as the main body of the probe was cooler than the surrounding sediment (having come down though the water column and cooler sediment section above), the temperature curve was inverted as the tool began to warm up to the local sediment temperatures.

Table 22. Temperature and error estimates for WSTP measurements in Holes 859A and 859B.

Depth (mbsf)	Temp (°C)	Error (±)	Approximate temp. (°C)
0.0	2.2		
49.0	16.65	0.08	15.2
71.3	16.48	0.06	16.3
98.5	19.63	0.05	19.4
126.2	19.81	0.07	20.8
187.1	17.3	0.1	16.4
216.0	10.29	0.04	11.5
245.0	43.6	0.1	61.1*
254.0	4.63	0.07	12.5
274.5	16.8	0.3	22.5

* Denotes anomalous records near hot jet.

Hole 859B

In Hole 859B, the newer WSTP tool was deployed once at 71.3 mbsf and the older temperature tool was deployed six times at deeper levels. At 71.3 mbsf, the WSTP profile shows an initial brief spike on penetration (P_1 in Fig. 52) that dissipates rapidly (<120 s). On extraction, the tool had to be pulled free with the main drill pipe. The main body of the probe tip was cooler than the surrounding sediments so the temperature subsequently increased to equilibrium. The tool was accidently withdrawn and pushed into the sediment again part way into the run (P_2 in Fig. 52). This enabled us to fit the data twice.

The second and subsequent deployments used the old temperature probe. At 187.1 mbsf, a good temperature spike and decay was achieved (Fig. 53). Similarly at 216.0 mbsf, the run appeared to proceed well, with a good temperature decay profile (Fig. 54). At the end of the decay curve, the temperatures appeared to equilibrate to about 10.6°C and then gently increased again to approximately 10.7°C. At 245.0 mbsf, however, the temperature record exhibits a remarkable form (Fig. 55). An initial fairly typical, if a little noisy, temperature decay to around 43°C can be seen from the temperature spike. After about 11 min in the decay sequence, the temperature rapidly, but smoothly, increases to about 55°C. As far as we can ascertain, this was not some peculiar disturbance of the electronics, because the bottom-water temperature was normal pre- and post-determination. Again, significantly, the subsequent deployment of the tool at 254.6 mbsf (Fig. 56) showed many of the same features as the deployment at 245.0 mbsf, but the temperatures had returned to generally lower values, with the spike dying away to approximately 5.2°C before increasing again to 7.8°C.

Some doubt exists about the reliability of the penultimate deployment at 274.0 mbsf. The tool did penetrate the formation as it took a considerable overpull to extract it. However, the temperature measurement did not behave as well as during the previous runs when plotted vs. l/t, and the formation may have been cracked on insertion (see below). The final deployment of the tool failed because the formation was becoming too hard for penetration.

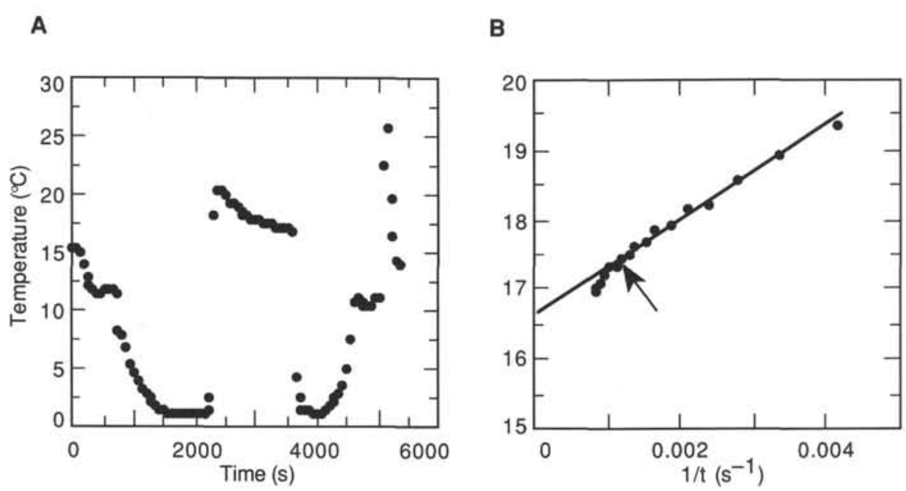

Figure 49. Temperature vs. time (**A**) and 1/t fit to data (**B**) at 49 mbsf in Hole 859A. Arrow marks departure (data "hook") from main trend at small 1/t time intervals (WSTP tool).

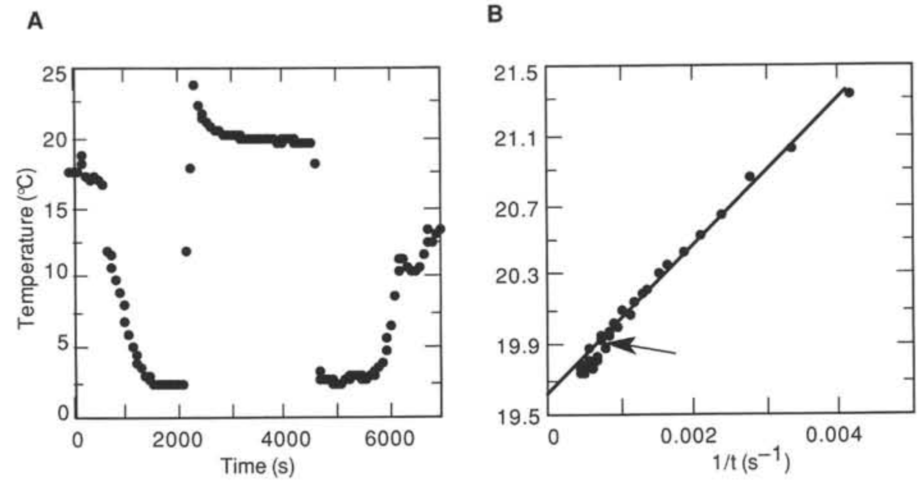

Figure 50. Temperature vs. time (**A**) and 1/t fit to data (**B**) at 98.5 mbsf in Hole 859A. Arrow marks departure (data "hook") from main trend at small 1/t time intervals (WSTP tool).

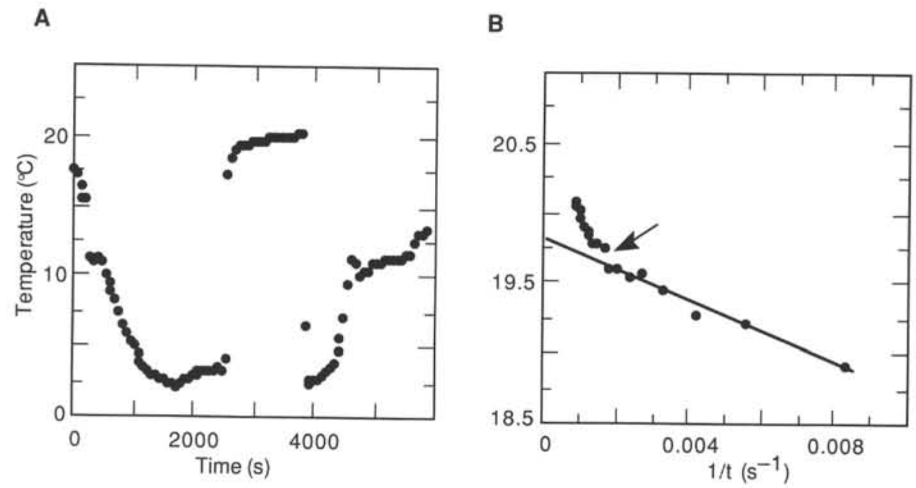

Figure 51. Temperature vs. time (**A**) and 1/t fit to data (**B**) at 126.2 mbsf in Hole 859A. Arrow marks departure (data "hook") from main trend at small 1/t time intervals (WSTP temperature probe only).

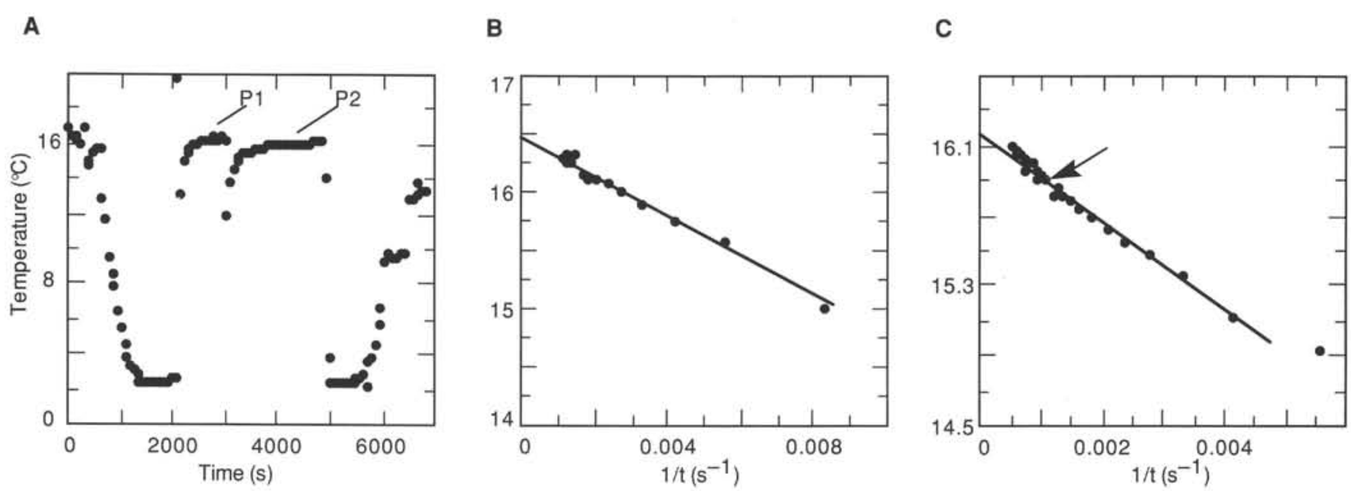

Figure 52. Temperature vs. time (**A**) and 1/t fit to data (**B** and **C**) at 71.3 mbsf in Hole 859B. Arrow marks departure (data "hook") from main trend at small 1/t time intervals (WSTP tool). P_1: first penetration, P_2: second penetration. **B** shows 1/t fit to P_1; **C** 1/t fit to P_2.

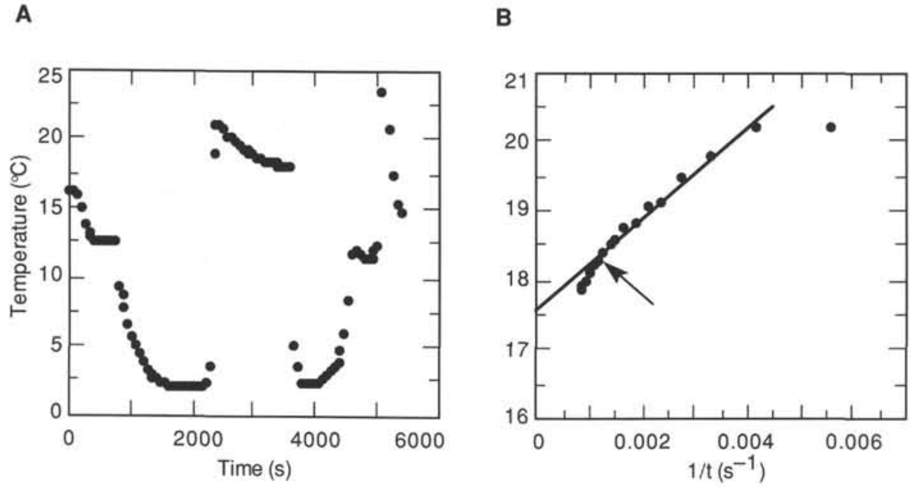

Figure 53. Temperature vs. time (**A**) and 1/t fit to data (**B**) at 187.1 mbsf in Hole 859B. Arrow marks departure (data "hook") from main trend at small 1/t time intervals (WSTP temperature probe only).

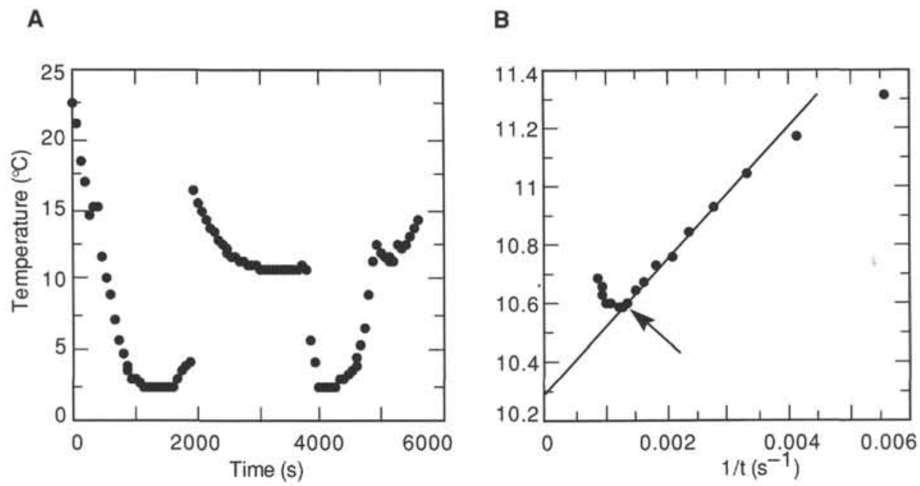

Figure 54. Temperature vs. time (**A**) and 1/t fit to data (**B**) at 216 mbsf in Hole 859B. Arrow marks departure (data "hook") from main trend at small 1/t time intervals (WSTP temperature probe only). The hook increases in importance down the hole from this point.

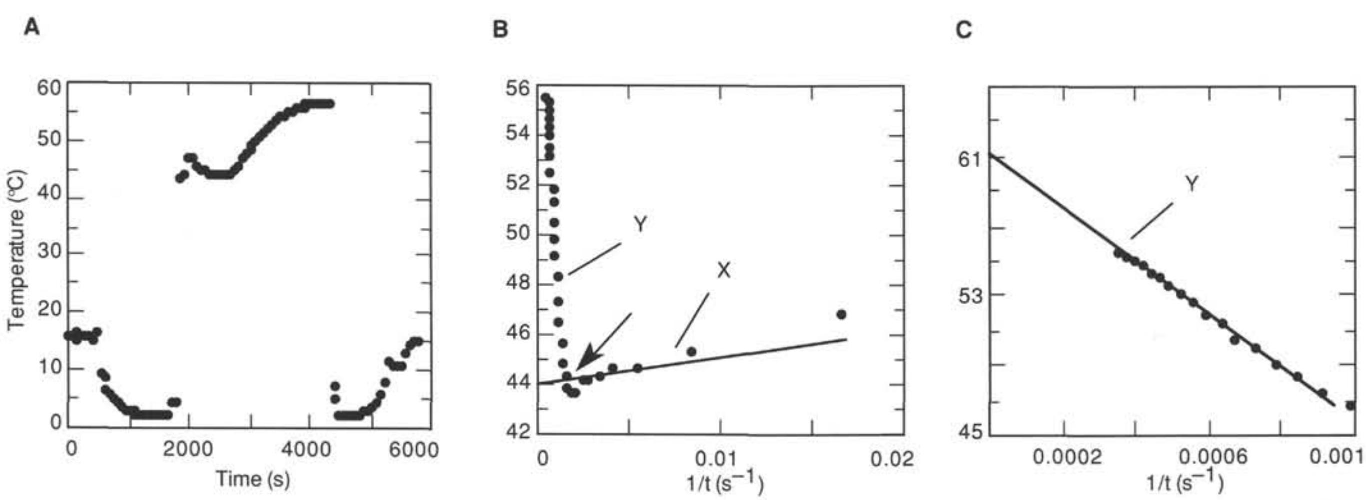

Figure 55. Temperature vs. time (**A**) and 1/t fit to data (**B**) and (**C**) at 245 mbsf in Hole 859B. Arrow marks departure (data "hook") from main trend at small 1/t time intervals (WSTP temperature probe only). **B.** Main trend (*X*) extrapolates to 43.6°C. **C.** Data hook (*Y*) extrapolates to 61.1°C.

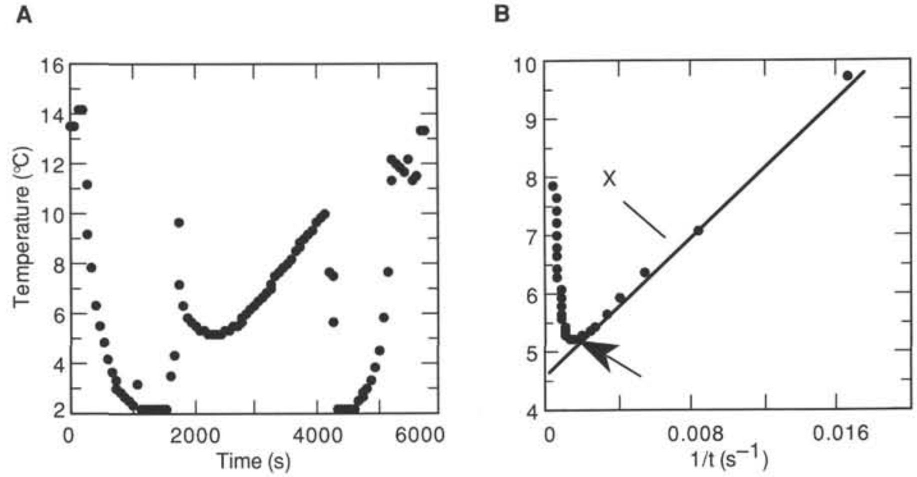

Figure 56. Temperature vs. time (**A**) and 1/t fit to data (**B**) at 254.6 mbsf in Hole 859B. Arrow marks departure (data "hook") from main trend at small 1/t time intervals (WSTP temperature probe only).

Data Reduction and Results from Site 859

We will combine Holes 859A and 859B and discuss each measurement in order of increasing depth below sea level. The results have been summarized in Table 22. The bottom-water temperature generally remained close to 2.2 ±0.04°C for most runs, except for when the tool was held below the mud line (when we recorded slightly higher values). For most deployments, the tool was left in the sediment for times exceeding 15 to 20 min, allowing sufficient time for extrapolation to equilibrium temperatures. In the case of Hole 859B measurements, the tool was left in the sediment for up to 30 min or more in the zone having the highest temperature gradients. While we initially used the shipboard WSTPFIT program, the complexity in the data in the deeper parts of Hole 859B forced us to abandon this approach, as the data warranted much closer examination. The 1/t approximation was used instead for extrapolation purposes as this allowed us to identify significant trends in the deeper runs at this site. We subsequently used the 1/t approach for the rest of the WSTP measurements at this site because (1) we wished to be consistent and (2) we found that the WSTPFIT program tended to be biased by the latter part of the equilibrium record, when the temperature from the main body of the tool appeared to have had sufficient time to migrate down the probe to perturb the readings in the region of the thermistor at the tip of the tool. Where possible, we give an error estimate based on the poorest reasonable fit through the data in 1/t space. In general, the older probe seems to be a little more noisy than the newer WSTP probe.

The main initial linear portion of the 1/t plot of the thermal equilibrium trend from the 49.0 mbsf probe measurement (Hole 859A) extrapolates to 16.68°C ±0.08°C (Fig. 49). Interestingly, there is a departure from the main linear trend (the data "hook") at long time intervals (lowest 1/t values). The data "hook" corresponds to a temperature perturbation that reaches the thermistor, at times generally exceeding 8 to 12 min. after penetration. In various forms and intensities, this "hook" is consistently developed in the data from most of the deployments we ran during both Holes 859A and 859B and we mark its departure from the main trend of the data by a small arrow in the figures. Looking back at the data displayed in the *Initial Reports* volume from Leg 131, Nankai Trough (Taira et al., 1991), where the same type of tools and 1/t approximation were used, we also find the same hook pattern commonly developed to various degrees. Thus, we conclude that this phenomenon is an inherent feature of the probe's behavior. If the two types of WSTP temperature tool completely penetrate the formation, the hook effect probably relates to the thermal lag in the larger diameter upper part of the probe. In general, these thermal lag effects in the tool result in small departures in temperature (<1.0°C) in the hook portion of the temperature record. In the case of the older temperature probe (Fig. 23 of the Explanatory Notes chapter, this volume), used in the more indurated formations where water sampling is no longer possible, the probe may not always penetrate the formation as deeply (possibly less than 10–14 cm in some hard formations). Indeed, in certain cases in the deep part of this hole (see discussion, this section), the hook may reflect the effect of conduction of borehole fluid temperatures down the relatively short stainless-steel tip. Where we propose this occurs, we observed substantial departures in the trend of the late temperature hook (>1°–2°C).

At 71.3 mbsf (Hole 859B), both the first and second penetrations of the newer WSTP tool give good fits when plotted vs. 1/t. The first penetration (Fig. 52) extrapolates to 16.45 ±0.04°C, while the second extrapolates to 16.16 ±0.06°C. The second penetration records a slightly cooler temperature, but this probably is the more disturbed reading. Thus, we will use the first penetration value of 16.45°C for our temperature profile.

At 98.5 mbsf (Hole 859A), the 1/t extrapolation (Fig. 50) indicates a temperature of 19.63 ±0.05°C. Similarly, the deployment of the older tool at 126.2 mbsf (Hole 859A) extrapolates (with some noise) to a temperature of 19.81 ±0.07°C (Fig. 51). A possibility exists that the tool was physically disturbed, particularly at the point marked by the arrow in Figure 51. The quality of the data from the older tool at 187.1 mbsf (Hole 859B) is noisy, but we can a make a reasonable extrapolation using 8 min of data to a temperature of 17.3 ±0.1°C (Fig. 53). The deployment of the older tool at 216.0 mbsf (Hole 859B) gives a less noisy record and nice 1/t fit for 9 min of data that extrapolates to 10.29 ±0.04°C. The data "hook" in this run at low 1/t values is particularly pronounced, and we found that the size of this hook increased dramatically during the next two runs.

At 245.0 mbsf (Hole 859B), the old temperature probe recorded a fairly good heat spike and temperature decay over 10 min. Subsequently, the temperature rose again before coming close to equilibrium at approximately 57°C (Fig. 55A). Even without any fitting of the data, the general temperature range of this run, between 42°and 57°C, obviously was considerably greater than the previous temperature of 10.29°C observed only 29 m above. As this is one of the most significant temperature observations at this site, however, the meaning of the dip and subsequent marked rise in temperature in the recording does concern us. If the probe failed to penetrate the formation, it is difficult to imagine why the borehole fluid should continue to cool for 10 min (in the confirmed absence of any circulation of the borehole fluid) and then subsequently warm. Consequently, we reject this as a possibility. Further investigations revealed that there may have been some tool disturbance in the 2000- to 2500-s time interval (Fig. 55A) that resulted from an extremely slow rotation (<1–2 rpm) of the drill string (which was stopped as soon as it was noticed). Thus, a hypothesis might be that the dip in the temperature relates to penetration of cool borehole fluid around the probe that stopped when drill rotation ceased (at 2500 s). The subsequent rise in temperature might then relate to warming of the probe tip by the surrounding formation. If this scenario is correct, the formation temperature probably was given by the extrapolation of the tail of the temperature data to 61.2 ±0.3°C (*Y* in Figs. 55B and 55C). There are two reasons, however, why we do not currently think this model is correct: first, the general form of the data at 245 mbsf is highly analogous to the readings of the deployments made immediately before and after, and in these cases, the deployments were normal in every respect that we can determine (see Figs. 54 and 56). Second, if this cool water penetration occurred, why does the 1/t fit of the main initial trend (*X* in Fig. 55B) remain relatively good (albeit with some minor noise) over a period of at least 7 to 8 min?

If we instead use a 1/t fit to the early 8 min of data after probe insertion (the first 2 min do not normally fall on the theoretical trend), we obtain a formation temperature of 43.6 ±0.2°C (*X* in Fig. 55B). Following on from the previous assessments of the implication of the late data hooks, the pronounced data hook in this run (*Y* in Fig. 55C) would then imply that a warm thermal anomaly, originating higher up the tool, reached the tip of the temperature probe approximately 10 min after insertion. This tool anomaly is normally small (< 1°C). However, in this deployment the hook anomaly exceeds 10°C. Thus, we need an extra source of heat to warm the upper part of the tool. We propose that the probe tip did not penetrate the formation to a great extent (10–14 cm) during this deployment and that it felt a "warm" borehole fluid influence after about 10 min. If this scenario is correct, the borehole fluid must have become considerably warmer (>61.2 ± 0.3°C) than the rock immediately surrounding the probe tip by the end of this run.

The general form of the 1/t fit at 245 mbsf is repeated for the subsequent deployment at 254.6 mbsf (Hole 859B), with a dip and subsequent rise in the temperature data (Fig. 56). The main trend, however, only extrapolates to 4.63 ±0.07°C (*X* in Fig. 56), which is a considerable difference in temperatures at a separation of only 10 m from the deployment at 245 mbsf! As far as we can ascertain, the temperature spike and initial decay look good and no unusual activity (such as tool disturbance or circulation of cool borehole fluid) took place during the run. We also have at least 9 min of data on the main trend that fit the linear 1/t extrapolation well. Thus, we are forced to propose that this is recording a real formation temperature, despite the apparent extreme temperature gradients in the formation that this would entail. The hook at the low 1/t values is pronounced (>3°C), again suggesting to us shallow penetration of the formation by the probe, and that the borehole fluid was considerably warmer than the local formation temperatures at this depth.

The last deployment was at 274.0 mbsf (Hole 859B). A considerable overpull was necessary to extract the tool and thus penetration of the formation was definitely achieved. The 1/t extrapolation only fits 5 to 6 min of data, however, and we suspect that either there was only a partial penetration or that some cracking of the formation occurred. Note also that its general form is different from the preceding three readings, which suggests to us that different processes were operating during its period of insertion. This data point suggests a formation temperature in the region of 16.8 ±0.3°C (*X*, Fig. 57B), but may not be well constrained. We include it here because it gives us a general constraint on the ambient temperature at this depth. Given the very large temperature gradients in this hole, even this poor constraint is useful. With some oscillations the hook in the data extrapolates toward approximately 22.5°C (Fig. 57C).

The combined temperature profile for Holes 859A and 859B has been plotted in Figure 58. As this figure clearly shows, an extremely disturbed temperature profile appears at this site. The main features of this temperature profile also can be observed, to a less dramatic extent, in the results of the logging undertaken several days later (see Wireline Measurements section, this chapter). We have not attempted a heat-flow estimate based on a conductive model because we see little evidence that conductive heat flow is the dominant mode of heat transport in this hole. We can divide the profile into three general sections.

Upper Section (0–226 mbsf)

In the upper section, we see a rapid temperature increase from the bottom-water temperature of 2.2° to approximately 16.6°C at 45.0 mbsf, a temperature gradient of approximately 320°C/km. The temperature then increases more slowly to approximately 19.7°C at 126 mbsf. A small temperature gradient reversal appears between 49 and 71 mbsf.

The predicted upper limit of the thermal stability of the gas hydrate is also shown in Figure 58, and is given by $\ln P = 46.74 - 10748/T$, where P is pressure (kPa), and T is degrees Kelvin. Much of the top of the hole appears to be in the stability field for hydrate (Claypool, pers. com., 1991). The temperature just intersects the upper temperature stability boundary of the gas hydrate field between 100 and 130 mbsf. The location of the BSR on the seismic reflection sections thus should correspond to a depth of 100 mbsf where the hydrate first breaks down (Fig. 58).

The steep upper temperature profile between 0 and 45 mbsf appears consistent with either recent removal of sediment from the top of the wedge or the upward advection of warm fluid. Thermal blanketing of the wedge by a unit having a very low conductivity (like a gas hydrate) in the region between 0 and 45 mbsf is also possible, but no clear evidence exists for significant concentrations of hydrate in this interval (see Inorganic Geochemistry section, this chapter).

Large Thermal Minimum (220–260 mbsf)

In the interval between 126.2 and 216 mbsf, a broad and substantial temperature inversion of approximately 9.5°C occurs from 19.8°C at 120 mbsf to 10.3°C at 216.0 mbsf (a temperature gradient of –90°C/km). Below the single, very warm temperature reading at 245 mbsf, the temperature decreases still further to 4.6°C at 254 mbsf before apparently increasing again. Downhole temperature logging (see Wireline Measurements section, this chapter) confirms that (apart from the local region of a single high temperature reading at 245 mbsf) a broad temperature minimum appears to be centered in the region between 120 and 254 mbsf.

The simplest explanation for this temperature minimum is the relatively recent lateral influx of cold water into the region between 200 and 260 mbsf (Figs. 58 and 59). This 60-m region broadly corresponds to a major break in many geological, physical, and geochemical parameters. For example, logging also revealed the sonic velocity to be substantially reduced in this part of the section (see Wireline Measurements section, this chapter). We suspect this is a major zone of fracturing (and faulting?) and enhanced fracture permeability (Fig. 59) that corresponds to the boundary between the domain of broken formation below and a

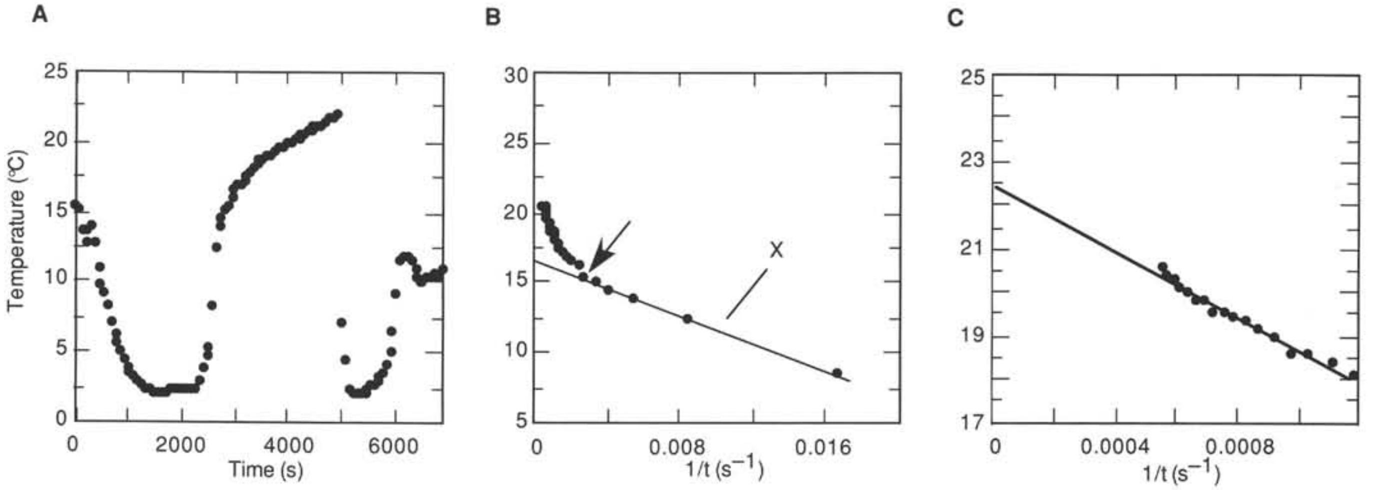

Figure 57. Temperature vs. time (**A**) and 1/t fit to data (**B**) at 274 mbsf in Hole 859B. Arrow marks departure (data "hook") from main trend at small 1/t time intervals (WSTP temperature probe only).

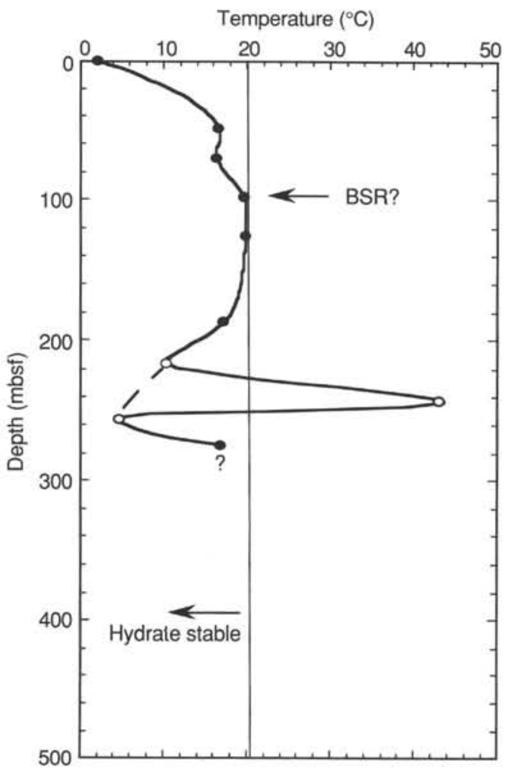

Figure 58. Temperature vs. depth for Holes 859A and 859B. The upper temperature of the gas hydrate stability field is shown (G.E. Claypool, pers. comm., 1992). Estimated position of upper BSR also is shown. The gas hydrate then becomes potentially stable again below 140 mbsf, and the potential exists for a second BSR at close to 300 mbsf. Open circles denote three anomalous temperature readings around the hot jet.

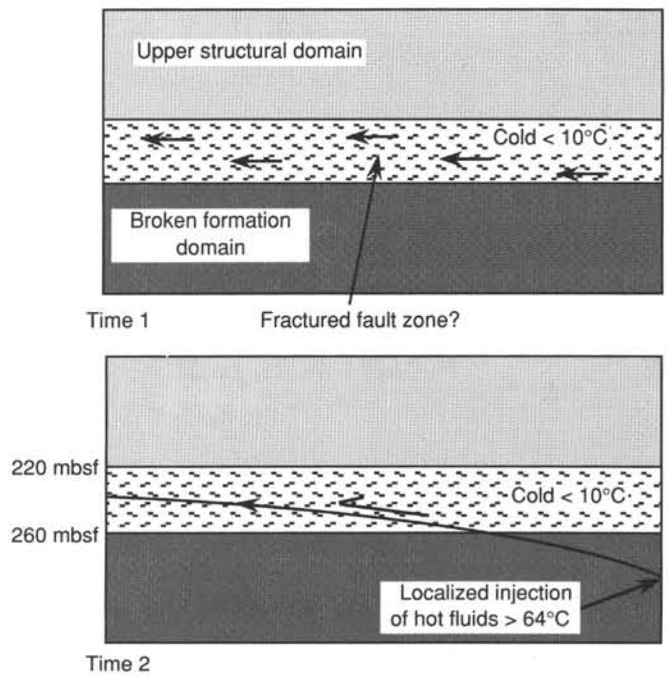

Figure 59. Schematic model of the thermal history of the faulted region between approximately 200 and 300 mbsf. In the fairly recent past (Time 1), cold water (perhaps as cold as 4°C) may have laterally migrated along the fractured region (probably fault related) that lies between approximately 220 and 260 mbsf. This created the major temperature minimum and inversion seen in Figure 58. Very recently (Time 2), localized injection of >61°C fluid into the fractured region near 245 mbsf caused a pronounced temperature spike that appears to affect a region less than 10 to 20 m in vertical thickness. It seems likely this thermal event is coupled to the reactivation of the structure by a thrust that intersects a source of hot fluids deep in the wedge (and possibly the oceanic basement).

different structural domain above (see Structural Geology section, this chapter). That the coldest portion of the thermal minimum is as low as 4.6°C is surprising. The origin of the cold water must be near the surface, but the geochemistry is confusing and cannot substantiate this. This thermal minimum corresponds to a similar, though less substantial, minimum on the temperature records of the wireline logs (see Wireline Measurements section, this chapter) and does appear to be a real feature.

Hot Jet (245.0 mbsf)

A very hot and channelized influx of fluid appears to intersect the borehole near 245.0 mbsf. If our preferred assessment of the temperature reading at 245 mbsf is correct, the local wall temperature of the conduit is 43°C. However, the temperature of the fluid influx into the borehole probably exceeded this. For example, extrapolation of the hook in the data at 245.0 mbsf (*Y* in Fig. 55) suggests that the borehole temperature exceeded 61°C at the time of measurement because heat would have been lost to the surrounding cool sediments around the buried shaft of the probe (Fig. 60). Heating of the bottom of the borehole to above 61°C in the interval between the cessation of pumping (immediately prior to probe insertion) and the end of the probe run some 40 min later suggests a rapid influx of hot (>61°C) fluid from a local conduit. The intersection of the hot jet with the borehole is probably within a few meters of the probe tip because it would be difficult to inject significant quantities of hot water downward into the sealed base of the borehole (Fig. 60). The in-situ rock temperature measurements below and above this region recorded no sign of this hot jet of fluid (Fig. 61). The most recent phase of hot fluid influx thus must be very young (post cold water influx), because the effects are very localized and it is difficult to imagine a temperature gradient of 40°C over 10 m being maintained as a steady state phenomenon (Figs. 58 and 59).

The estimated high temperature of the fluids in the hot jet suggests that their origin is deep in the wedge. This is consistent with the results of the interstitial water and gas analyses (see Inorganic Geochemistry and Organic Geochemistry sections, this chapter), which indicate that the fluids (containing relatively abundant hydrocarbons) at this level had seen oceanic basement at deep levels of the accretionary system and temperatures in excess of 80° to 100°C.

For completeness, we have included in Figure 61 estimates of the temperatures to which the various data hooks extrapolate (obtained by a simple linear extrapolation in the 1/t data). We can see a significant pattern. The extrapolated data hooks give temperature estimates that are consistently close (within a degree) to the determined wall rock temperature in the region above 245.0 mbsf. Below 245.0 mbsf, the extrapolated hooks indicate significantly higher temperatures. We propose that a source of heat above the base of the hole maintains the borehole temperatures well above the ambient rock temperatures (immediately below the base of the hole) and that the source of heat is the hot jet at 245.0 mbsf. The hot jet must have continued to be active for at least 12 hr after being first intersected. Logging conducted several days later suggests the activity of the hot jet had waned somewhat by this time, but the effects of both it and the surrounding broad cold-temperature region are still clearly seen (see Wireline Measurements section, this chapter).

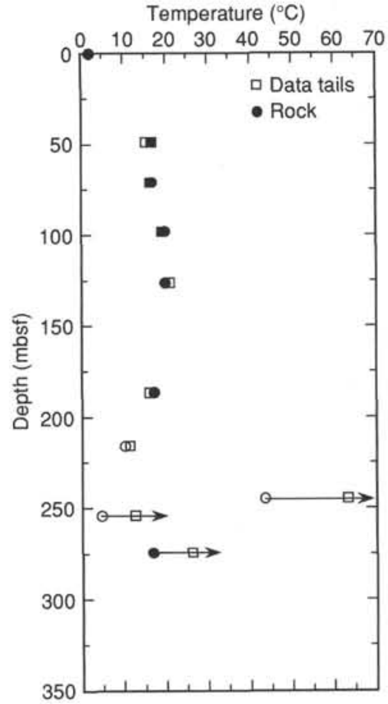

Figure 61. Minimum departure of the borehole temperature from the ambient rock temperature as estimated from the data hook at low 1/t values. Above the hot jet at 245 mbsf, the borehole and ambient temperatures are within a few degrees. Below the hot jet, the borehole fluids have been substantially warmed.

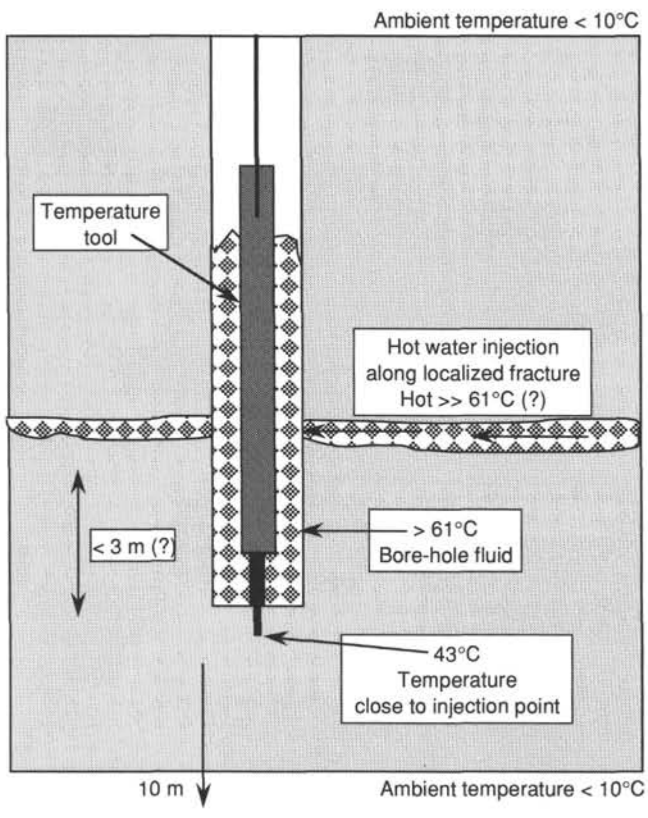

Figure 60. Estimated local temperature environment that existed near the hot jet at the end of the tool deployment at 245 mbsf in Hole 859B (see Fig. 55).

Summary

In summary, the temperature profile for Site 859 is extremely nonlinear and suggests the recent lateral movement of both cool and hot fluids though a relatively narrow region of the wedge. The injection of the cool fluid produced a broad pronounced thermal minimum and a temperature inversion of up to 15°C. It must pre-date the hydrothermal event associated with the hot jet, and its substantial magnitude suggests it may have been a moderately long-lived circulation feature. Presumably, the recent hot jet is currently distrupting this earlier "cool" fluid-flow regime.

Hot fluid (>61°C) has been recently injected into the center of this region of cold fluid influx (probably along a recent thrust that roots deep in the wedge). The close spatial and temporal juxtaposition of the two fluid migration events results in temperature gradients that exceed 40°C/10 m. This hot jet may be connected to processes operating deep in the subduction system to the east of the site, or may form part of the hydrothermal system operating in the oceanic spreading center (the axis of which is less than 4–6 km to the west).

The expected base of stability of the gas hydrate, and the level of the BSR, just about match the observed temperature profile. However, heat-flow estimates, based on conductive models of heat transfer that use the BSR to estimate the temperature profile, are not particularly relevant in the context of the vigorous hydrogeologic system in this particular area of the wedge.

WIRELINE MEASUREMENTS

Introduction

The primary objective of wireline measurements at this site was the measurement of in-situ properties of rocks comprising the toe of the accretionary wedge along the lower trench slope. Of additional interest were the physical properties of the gas hydrate zone that overlies a BSR observed in the site-survey seismic profile. The lack of hydrate in the recovered cores, presumably due to drilling disturbance, allowed for no direct characterization of its properties. Downhole measurements at this site complemented core observations for both characterization of the hydrate properties and distinction of the lithologic units.

Five tool strings were deployed in Hole 859B (see Operations section, this chapter). Separate runs of the geophysical and sonic tool strings were followed by the FMS. A vertical seismic profile (VSP) using the well seismic tool (WST) was attempted to examine the seismic character of the BSR and to correlate structural and stratigraphic boundaries with the seismic stratigraphy surrounding the borehole. The geochemical tool string was the fifth and last run of the logging tools. The Lamont-Doherty temperature tool (TLT) was run both with the WST and on the geochemical tool string.

Quality of Logs

The quality of many of the logs at Site 859 was significantly degraded by the size and rugosity of the borehole, which, due to washouts, was exceptionally large. The caliper log shows borehole diameters greater than the 17.2 in. (43.7 cm) maximum range of the caliper for most of the interval from 70 to 225 mbsf, and varying around 14 in. (36 cm) below 225 mbsf. The gamma ray, density, porosity, and geochemical tools are particularly susceptible to adverse effects from large hole diameter. The density tool, which is excentered, has an arm on one side that presses the tool against the borehole wall. This arm can only work effectively if it reaches the far borehole wall. In Hole 859B, the density log was severely degraded because of poor contact of the tool with the borehole wall. Corrections to rectify portions of this log may be possible, but we have disregarded it in our initial interpretation. The gamma-ray log also was highly degraded because of hole size and rugosity, so that its use has been limited to depth correlation among the logs. The geochemical tool string appears to provide useful information; however, it also has probably been somewhat degraded by the large hole diameter. The sonic logs, particularly the near-receiver sonic log, and the resistivity logs appear to provide continuous and consistent results and seem largely unaffected by the hole diameter. Some cycle skips were observed in the sonic log, particularly the far-receiver sonic log, but these can be identified and did not significantly hinder interpretation.

Establishing consistent depths for each of the logs was accomplished by correlating the gamma-ray logs. The absolute depth for all logs was fixed by setting the gamma-ray signal associated with the base of the drill string during the first log run (the geophysical tool string) to the depth of pipe (40.6 mbsf) provided by the driller.

The FMS images have been degraded by the large hole diameter and borehole rugosity. The pads of this tool extend to touch the borehole wall at four points, accommodating a hole having a diameter of 16 in. (40.6 cm). The bidirectional caliper log, which records the opening of the pads of the FMS tool, shows that the borehole is typically highly elliptical with the long axis usually greater than 16.0 in. (40.6 cm), and the short axis usually 11.0 in. (27.9 cm) or greater. Thus, we expect that only two or three pads were touching the borehole wall at most times. The other one or two pads were sensing only the borehole fluid. In several places in the shallow section, the pads oriented roughly east and west are devoid of detail, suggesting that they were sensing only borehole fluid, while the other two show small details that we suspect are real features of the borehole wall. Borehole rugosity has the effect of varying the response of a single pad as it moves over the rough surface, occasionally making and then losing contact with the borehole wall. We can see evidence of this effect in sections of the data.

The planned VSP was the least successful of the downhole measurements due to the irregularity and large diameter of the hole. The WST could only be clamped to the oversized hole at four depths, all deeper than 263 mbsf. At all other planned stations, the WST arm would not extend far enough even to hold the tool in place when cable tension was released, much less clamp it to the wall. When the tool was free in the borehole, the noise level overpowered the direct arrivals from the seismic source. Because of the small number and irregular spacing of the observation stations, the experiment did not provide the data necessary for a VSP, so the direct arrivals from the few available stations are useful only as a check-shot survey.

Two successful temperature logs were acquired in Hole 859B. Two factors affect temperature observations: (1) the response time of the temperature sensor and (2) the degree to which the temperature of borehole fluid shortly after drilling indicates the equilibrium geotherm.

The TLT normally records data from a fast-response temperature probe, a slow-response temperature probe, and a pressure sensor. The TLT used at this site, a back-up tool used because the primary tool had leaked, did not have a fast-response temperature sensor. The slow-response sensor responds to temperature change gradually over several minutes, and therefore does not record correct temperatures when moving quickly through a temperature gradient. When the TLT was attached to the WST, we occupied a series of temperature stations. The TLT on the geochemical tool string was run up the hole at 600 ft/hr (183 m/hr).

The circulation of cold seawater in the borehole during drilling lowers the temperature of the surrounding formations. This change decays slowly, over a period of weeks to years. Measuring the temperature of the borehole fluids a few days after drilling has stopped will likely record temperatures lower than the pre-drilling temperature at the bottom of the hole, and higher than the pre-drilling temperature at the top of the hole. If careful measurements are conducted in a borehole at several different times after fluid circulation is stopped, it is possible to estimate the equilibrium geotherm. We do not have adequate measurements in Hole 859B to estimate in more than a general way. However, the temperature log data do provide some constraint on the pre-drilling subsurface geotherm, particularly in the deeper parts of the hole where no other temperature measurements are available.

Logging Results

Logging Units

We have divided the logged interval in Hole 859B into six logging Units, largely on the basis of the sonic velocity, resistivity, and porosity logs (Fig. 62). The elemental yield logs from the geochemical tools were also evaluated for lithologic changes downhole. These logs were chosen because they were the least degraded by the large hole diameter. The logged interval (40.6–

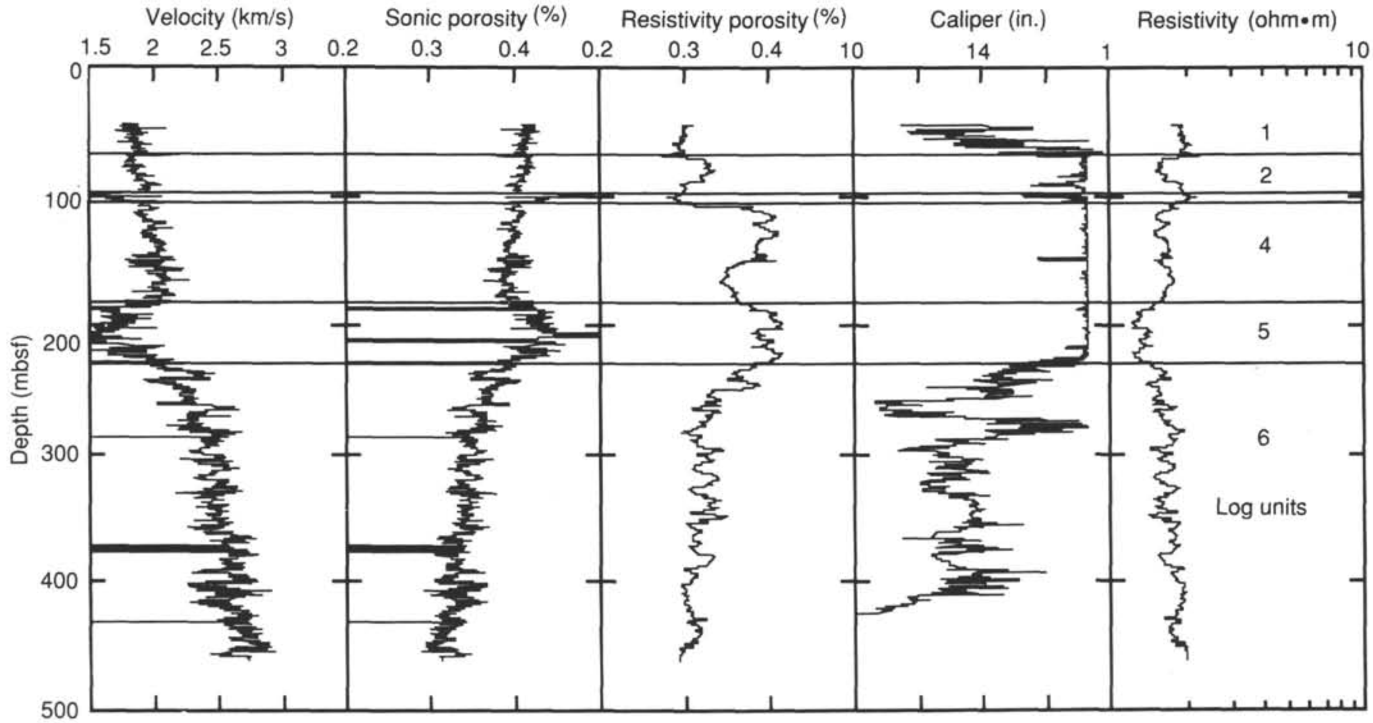

Figure 62. Log units in Hole 859B based on observations of near receiver velocity, porosities derived from sonic and resistivity logs, the caliper on the lithodensity tool, and the deep-resistivity log.

unconsolidated silts and clays at the top of the unit, and claystones and siltstones below 235.3 mbsf.

Log Unit 1 (41.0 [base of pipe]–67.0 mbsf)

The interval is characterized by uniform velocity (mean 1.85 km/s) and resistivity (4 ohm-m). The shallow resistivity values are slightly lower than the medium and deep resistivities, which perhaps indicates formation invasion by lower resistivity drilling fluid. Porosities determined from sonic and resistivity measurements are 42% and 36%, respectively. These values are anomalously low for shallowly buried, fine-grained clastic sediments.

Log Unit 2 (67.0–96.5 mbsf)

The interval is characterized by increasing velocity (1.8 km/s at the top to 1.95 km/s at the bottom) and increasing resistivity (3 ohm-m at the top to 4 ohm-m at the bottom). A small positive baseline shift in resistivity and perhaps in velocity occurs at 84 mbsf. At the top of log Unit 2 is a 1-m-thick layer of higher velocity (2.2 km/s), higher resistivity, and lower porosity. This thin interval appears to correspond to a more lithified layer.

Log Unit 3 (96.5–105.0 mbsf)

This 8.5-m-thick unit is distinguished by significantly lower velocity and higher resistivity (Fig. 63). In the lower half of the unit, velocity decreases to 1.6 km/s, while in the upper half of the unit, cycle skipping in the sonic log bounded by low-velocity values suggests the presence of a highly attenuating, low-velocity region.

Log Unit 4 (105.0–183.0 mbsf)

This interval is characterized by gradually increasing velocity (1.95 km/s at the top to 2.1 km/s at the bottom) and nearly uniform resistivity (3 ohm-m). The shallow resistivity value is slightly lower than the medium and deep resistivities, as in overlying units. An anomalous interval is seen from 143 to 156 mbsf with lower velocity and resistivity. Porosities calculated from the resistivity and velocity logs are about 39% in this interval. Hole diameter is at the 17.2 in. (43.7 cm) limit of the caliper log for the bottom half of Unit 4, suggesting that these sediments were easily washed out.

Log Unit 5 (183.0–230.0 mbsf)

This interval is distinguished by highly variable and relatively low velocities (apparently as low as 1.5 km/s) and low resistivities (as low as 2 ohm-m). While some of the low velocities are undoubtedly cycle skips, the velocity over the interval declines by at least 0.3 km/s. Porosity calculated from the resistivity and velocity logs increases to about 45% in this interval. Velocity and resistivity are lowest in the middle of the unit and vary upward to match the values of the adjacent units above and below. Hole diameter is at the 17.2 in. (43.7 cm) limit of the caliper log for most of Unit 5. The bottom of this unit corresponds to the "transition" zone between lithologic Subunits IIA and IIB (see Lithostratigraphy section, this chapter), which marks the change from unlithified above to lithified sediments below.

Log Unit 6 (230.0–458.0 mbsf [end of log run])

This interval is characterized by remarkably smoothly varying velocity and resistivity responses. A gradual increase of velocity occurs with depth (2.2 km/s at the top to 2.8 km/s at the bottom). The resistivity varies from 3 ohm-m at the top to 4 ohm-m at the bottom. Within this interval, the shallow resistivity value is roughly equal to or slightly greater than the medium and deep resistivity values. This suggests that there has been less drilling fluid invasion of the formation than in the upper units.

We identified three subunits of Unit 6 based on the velocity log. These are Subunit 6A (230.0–262.5 mbsf), Subunit 6B (262.5–363.0 mbsf), and Subunit 6C (363.0 mbsf to the bottom of the logged interval). Their boundaries lie where slight baseline increases in velocity are found in the overall gentle velocity increase. The porosity estimates calculated using the sonic and resistivity observations average about 30% in Unit 6. From 412

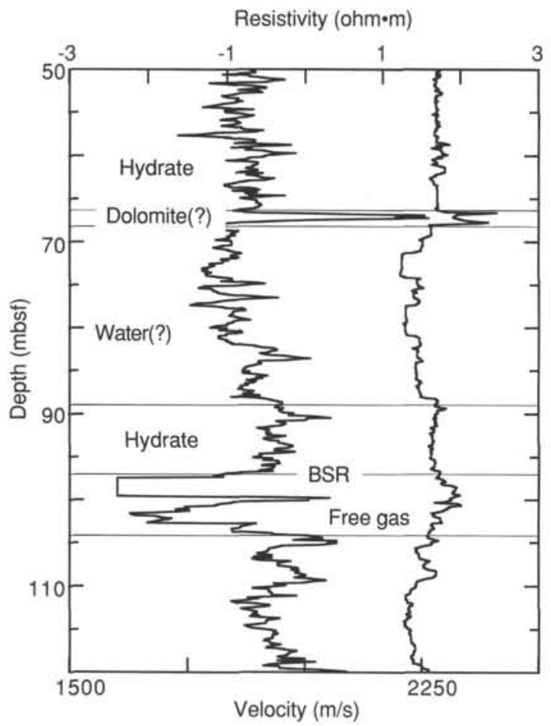

Figure 63. Resistivity (right) and velocity (left) logs through part of the zone of hydrate stability and the interface interpreted to produce the BSR. The BSR is thought to be a reflection off the contact at 97 mbsf between rocks containing hydrate and rocks containing free gas. The reflection is amplified by constructive interference with the reflection from the contact at 104 mbsf between rocks saturated with free gas and rocks containing water(?). Hydrate zones are characterized by slightly higher velocity and resistivity relative to water-saturated zones (Matthews and von Huene, 1985). The free gas zone is characterized by much lower velocity and higher resistivity than the water-saturated zones.

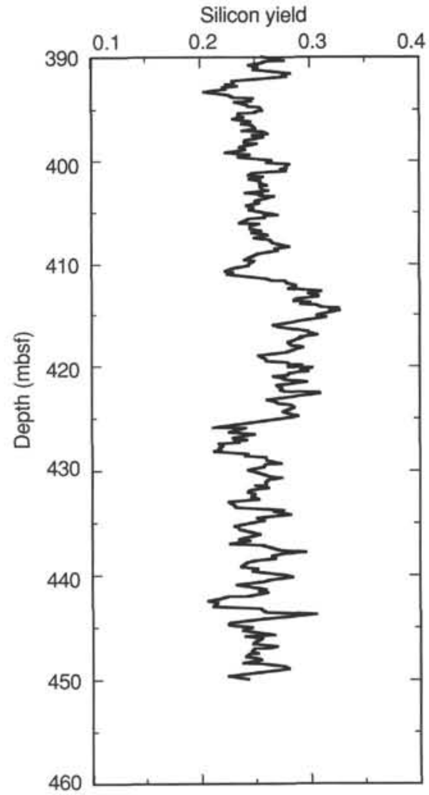

Figure 64. Silicon yield vs. depth for an interval within log Unit 6 showing increased silicon between about 412 and 426 mbsf.

to 426 mbsf, the silicon yield increases significantly (Fig. 64). Increased quartz content was noted in smear-slide analyses over this interval (see Lithostratigraphy section, this chapter). The velocity at the top of the high-silicon interval is relatively low (1.5 km/s); it increases to 1.9 km/s at the bottom of the interval. Within the high silicon interval, the velocity log has shorter period log variations than the data from intervals above and below.

Gas Hydrates and the Bottom-simulating Reflector

The gas hydrate layer produces a modest, but detectable, indication of its presence in two of the logs recorded. The base of the hydrate layer is marked by a prominent BSR that is characterized as a phase-reversed reflection on the seismic reflection section and indicates a decrease in seismic velocity or density. We correlate the BSR on the two sonic logs with a thin marked decrease in the velocity at a depth of 97 mbsf that may be produced by the presence of free methane at the base of the hydrate, as inferred in other areas (Miller et al., 1990). The velocity in a thin zone from 97 to 105 mbsf decreases from about 1.95 km/s to between 1.65 and 1.85 km/s. This zone is of sufficient thickness and velocity contrast to produce a strong seismic reflection. This is the largest velocity variation within the range of possible depths of the BSR and corresponds well with the expected depth to the base of the hydrate stability field estimated from the temperature-depth profile (see WSTP-ADARA Temperature Measurement section, this chapter). Cycle skipping within this zone, which may have been caused by poor sound transmission through this interval, produced several erroneous values. However, the thickness of this interval remains well defined even with the incorrect values removed. The resistivity log within the interval shows a corresponding increase in resistance that would be expected in the presence of a free gas layer.

The logs show indications of the presence of methane hydrate within the sediment above the BSR. Sonic and resistivity logs show higher resistivity and velocity in two intervals, between 88 and 97 mbsf and between 50 (the top of the logged interval for the sonic log run) and 68 mbsf (Fig. 63). We interpret this as an indication of an increase in the quantity of gas hydrate in the pore spaces. The small increase in velocity, roughly 0.1 km/s relative to the region between the two intervals and below the free gas anomaly, does not allow for large quantities of hydrate to be present in these sediments. We used the physical properties for hydrates reported by Matthews and von Huene (1985) to estimate that there is about 10% hydrate in the pore spaces of the rocks in the two hydrate regions. This is consistent with the interstitial water observations (Fig. 43), which indicated that the pore waters between 50 and 68 mbsf are a mix of about 5% to 15% freshwater (from hydrate melting) with seawater (see Inorganic Geochemistry section, this chapter). One interstitial water sample showing 25% hydrate saturation (Fig. 43) was taken above the logged interval; thus, no direct comparison can be made. The interval between 68 and 88 mbsf shows lower seismic velocity and resistivity and has been interpreted as a water-saturated interval having little or no hydrate (Fig. 63). Interstitial water samples in this interval (Fig. 43) show normal salinity, indicating that no hydrate melted as the cores were recovered.

Hole Ellipticity

At most depths in Hole 859B, the hole is elliptical rather than circular. The orientation of the long axis of the ellipse at each depth can be obtained because the FMS tends to orient itself in an elliptical hole so that one pair of its four pads points in the long-axis direction, and the tool records the two pad caliper readings and the azimuth of the pads. Thus, the pad that is most extended generally points along the azimuth of the long axis of the ellipse. Data generated from one of the FMS runs (Fig. 65) show that the long axis of the elliptical hole is oriented generally east-west for most of the hole. An interval occurs from approximately 150 to 230 mbsf in which the long axis of the ellipse is oriented roughly northeast-southwest. Both of these orientations are closer to the dip direction of the accretionary wedge than to its strike. We are not clear about how to interpret these results. If this ellipticity is the result of stress-related borehole breakouts, then it suggests that the direction of maximum compressional stress is parallel to the strike of the accretionary wedge. This would mean that the sediments in the wedge are currently in a state of downdip extensional stress. An alternative explanation for the ellipticity is that oriented weaknesses lie within the sediments at Site 859 that tend to cause the rock to wash out preferentially in certain directions. We do not know what weakness orientations would be expected to produce the observed pattern of washout.

Check-shot Survey

Two-way traveltimes were obtained (by doubling the observed one-way traveltimes) at four depths in Hole 859B (Fig. 66) where the WST could be clamped in the borehole. These range in depth from 263 to 460 mbsf. The two-way traveltime to the bottom of the hole is 4.212 s. The well is 11 m deeper than the deepest seismic observation. If a correction of 4 ms (based on velocity of 2800 m/s for 11 m) is added, the well is 4.216 s deep (Fig. 67). We were substantially short of reaching the dipping reflectors interpreted to be subducting oceanic crust.

Downhole Temperature Measurements

The TLT tool attached to the WST and geochemical tools recorded temperatures in the borehole for approximately 24 and 30 hr, respectively, after fluid circulation ceased in the borehole (Fig. 68). The TLT recorded pressure and time along with temperature, but no record of depth was performed. The depth log recorded by the geochemical logging string was synchronized with the TLT times to construct a depth-temperature record. This was done by synchronizing both the TLT and geochemical tools at the bottom of the borehole and then determining a depth/pressure table. This table was then used to assign depths to the record

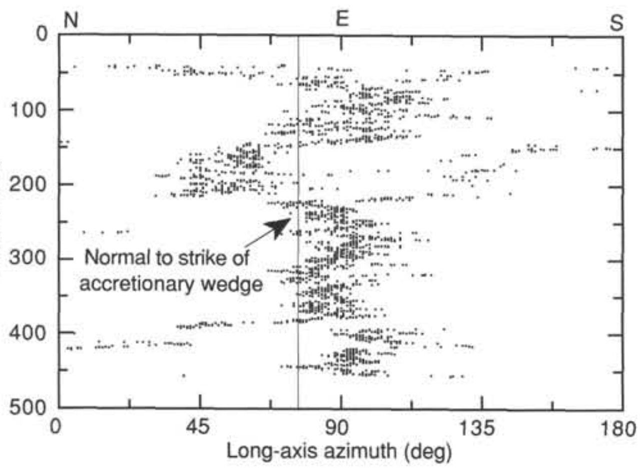

Figure 65. Direction of the long axis of the borehole as a function of depth. Note that the long axis is generally oriented east-west, normal to the strike of the accretionary wedge.

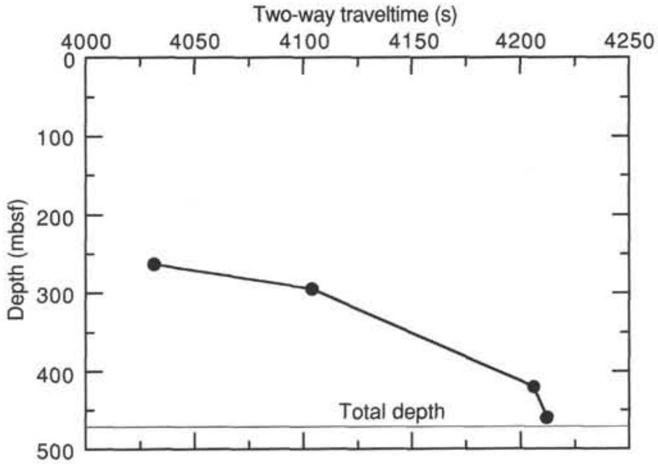

Figure 66. Two-way traveltime vs. depth data obtained during the check-shot survey.

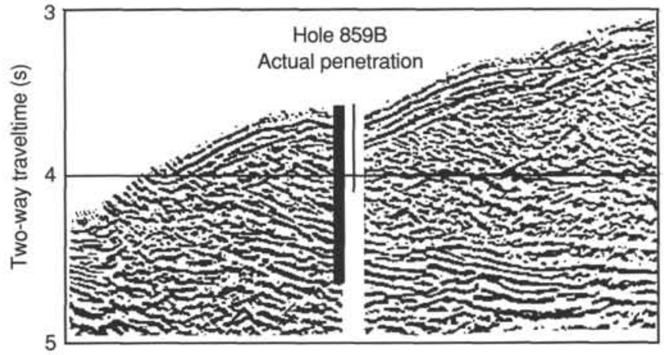

Figure 67. Seismic profile through Site 859 showing the depth of penetration (471 mbsf and 4.216 s) of Hole 859B. The data were obtained during the check-shot survey. Note that 250 mbsf is at 4.0 s. The vertical black bar on the seismic section to the left of the cut indicates the planned penetration.

of pressure from the TLT. This proved to be more accurate than using the pressure record and a constant density for borehole fluid to estimate depth, as was indicated by noticeable curvature in the depth/pressure profile.

The individual stations of the WST run were examined to determine the equilibrium temperature of the borehole fluid at a series of depths at approximately 25-m intervals (Fig. 68). The equilibrium temperature at each of these stations was determined by fitting exponential decay curves to observed temperature measurement series and by deriving the final decay temperature. Figure 69 shows one example of excellent agreement between fitted points and observed data. Comparison of the initial and final temperatures at each station (Fig. 68) shows the temperature of the tool may be more than 6°C greater than equilibrium. We attribute this to the thermal inertia of the tool and fluid that may be entrained with the tool as it is moved up the borehole to each station. These data also suggest that the downward logging run produced results that were considerably lower throughout most of the borehole than the equilibrium temperatures and therefore temperature data from the downgoing runs were not considered. Comparison of the final temperature at each station and with the later run on the geochemical tool (Fig. 70) shows that the final temperatures decay by varying amounts in such a way as to diminish the variations along the borehole. However, a large fluctuation in borehole temperatures from the steep ~95°C/km gradient was observed at approximately 200 mbsf, and a moderate

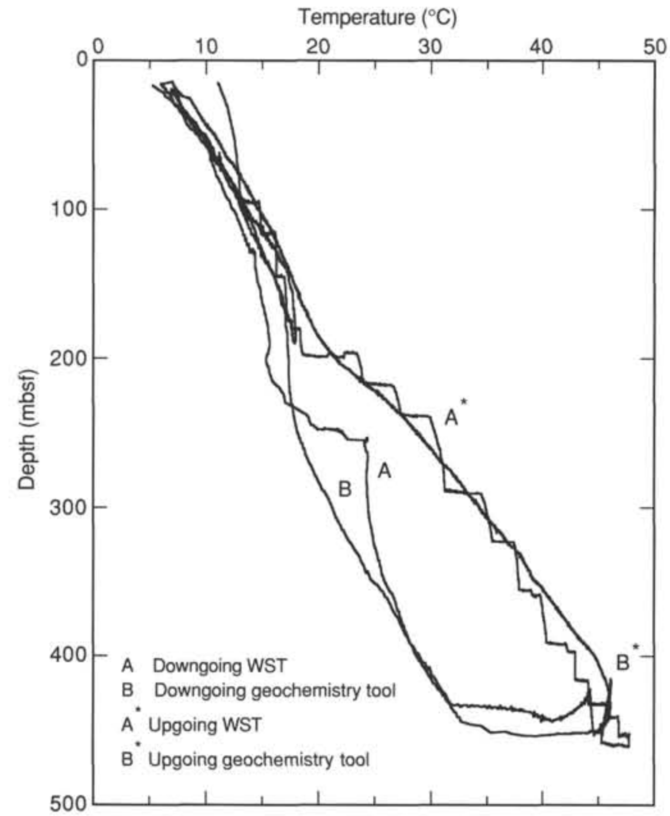

Figure 68. Temperature vs. depth recorded by the TLT during the WST check-shot survey. The tool recorded lower temperatures while it was being lowered than when it was raised. The tool was held stationary at a series of depths for periods of 8 to 15 min during which temperatures were recorded.

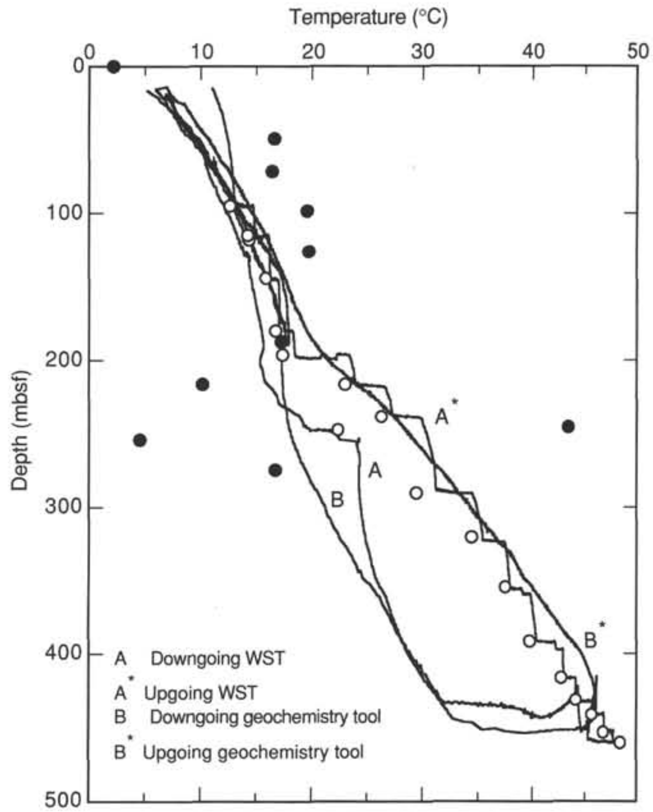

Figure 70. Compilation of temperature measurements made in Hole 859B. The lines indicate data from the TLT deployed on the WST and the geochemical tool string. The open circles represent equilibrium temperatures calculated at each of the stations observed during the WST run. The solid dots represent data from the WSTP temperature measurements.

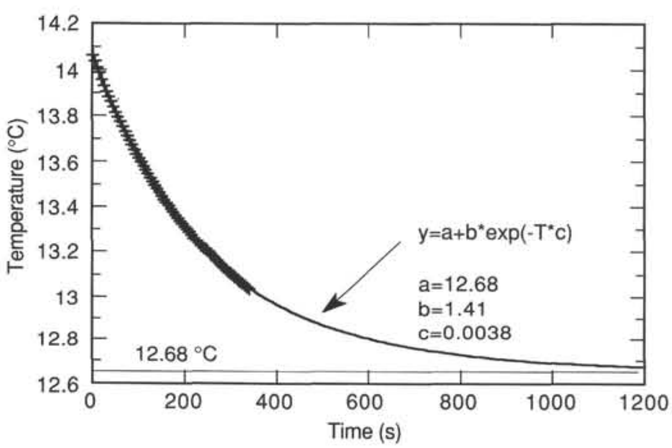

Figure 69. Temperature data and a best-fit thermal decay curve for a station at 95 mbsf, recorded during the check-shot survey. An exponential decay curve fits these data well and shows that the equilibrium temperature is 12.68°C.

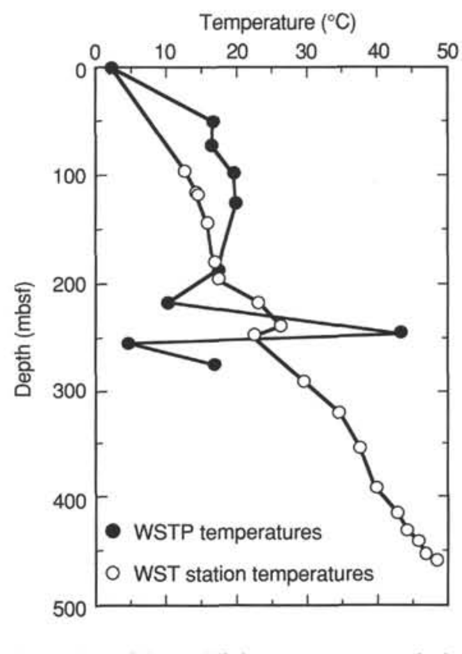

Figure 71. Comparison of the equilibrium temperatures calculated from stations observed using the TLT during the WST run with WSTP temperature observations. Note that both curves show a low-temperature anomaly between approximately 150 and 300 mbsf, and a more local high-temperature anomaly between about 210 and 250 mbsf. The response is more subdued in the TLT data than the WSTP data.

deviation at 250 to 320 mbsf, where temperatures are notably low. This profile agrees reasonably well in form but does not show formation temperature variations as extreme as those seen in the WSTP results (Figs. 70 and 71; also see WSTP-ADARA Temperature Measurements section, this chapter).

Comparison of data from the later TLT run, on the geochemical tool string, with the data from the earlier run was difficult as the stations of the WST run indicate that the initial temperatures at each depth are unequilibrated. Near the bottom of the borehole, temperatures are 2° to 3°C greater in the later run, which is most likely the result of warming following the termination of fluid circulation (Fig. 70). Between 200 and 300 mbsf, the borehole appears to have cooled between the two runs as a result of no fluid circulation from deeper in the well into these depths. The geochemical-run temperatures are thought to be somewhat less reliable than those of the stations as a result of the cooling effects described above.

FMS Images

The effects of hole size and rugosity, combined with the relative uniformity of the sedimentary rocks encountered in the borehole, resulted in a relatively featureless FMS image. Many apparently horizontal bands of high and low resistivity can be seen. We suspect that these may be artifacts of the gain application during processing because they are present on all four pads—including the pads that we suspect were only sensing the borehole fluid. If these bands are not artifacts, then we would conclude that most surfaces dip less than 2°. This conflicts with direct dip measurements in portions of the hole (see Structural Geology section, this chapter).

SUMMARY AND CONCLUSIONS

Drilling at Site 859 penetrated the toe region of an approximately 10-km-wide accretionary wedge at the leading edge of the South American forearc basement. For most of the following discussion, the relevant information can be extracted from the "Master Charts" for Holes 859A and 859B (Fig. 72), and no direct reference will be made to these two figures. Where necessary, reference will be made to individual diagrams and tables in the preceding sections. The purposes of this section is to summarize the most important scientific findings at Site 859 and to discuss their significance in light of the objectives outlined earlier in this site chapter.

The uppermost part of the rock column intersected is made up of clayey silts and silty clays of lithologic Unit I, which contains abundant radiolarians and diatoms of late Pleistocene age. Below 10 mbsf to a depth of 235 mbsf, uniform Pleistocene and upper Pliocene clayey silts and silty clays make up lithologic Subunit IIA. Lithologic Subunit IIB extends from 235 mbsf to terminal depth of Hole 859B at 476 mbsf and consists of upper Pliocene silty claystones and clayey siltstones. The boundary between Subunits IIA and IIB is defined by a transition zone between 216 and 235 mbsf and is not caused by a marked difference in sedimentary facies or mineralogical composition, but by a prominent discontinuity in the degree of lithification. The abundance of silt-sized unweathered feldspar and the occurrence of fresh detrital biotite indicate the absence of pronounced chemical weathering and along with the silt-sized quartz, these minerals are the contribution of glacial rock-flour to the sediment. The source of the sediment is the nearby Andean crystalline basement and the volcanic arc. The sediment is terrigenous, and perhaps the most marked feature of the rocks cored at Site 859 is their uniformity both in facies and mineralogical composition. Benthic foraminifers (e.g., *Uvigerina mantanensis, Ehrenbergina pupa, Bulimina mexicana*; see Biostratigraphy section, this chapter) indicate a middle to lower bathyal depth of deposition of the sediment cored at Site 859. This is compatible with deposition on young and therefore buoyant oceanic crust prior to offscraping and accretion. A new and surprising result of the biostratigraphic studies is the identification of a temperate to subtropical marine paleoenvironment during the late Pleistocene. Some evidence exists from radiolarian and foraminifer fauna for coastal upwelling both during the Pliocene and the Pleistocene.

According to the results of the biostratigraphic analysis, an upright and seemingly continuous stratigraphic section was intersected at Site 859. This is corroborated by the magnetostratigraphic data set, which suggests an upright suite of rocks having an age range from the Matuyama to the Gilbert chron. The apparent absence of biostratigraphic and magnetostratigraphic age inversions argues against the presence of thrusts with large displacement and associated heave. However, the lower limit of biostratigraphic resolution, especially in the Pliocene, is imposed by a duration of individual foraminifer zones of 1 m.y. or more (Zones N19 through N22), so that thrusts with vertical displacements of less than 50 to 100 m can remain undetected. In principle, the same holds true for the resolution limit of the magnetostratigraphic data. Here, the record is severely disrupted by poor core recovery and by remagnetization that accompanied deformation of the upper 80 mbsf. The thick (>400 m) Pliocene section found at Site 859 is most easily explained either as a result of imbrication by thrusting at a scale smaller than the lower limits of stratigraphic resolution, or as a result of pervasive, macroscopically ductile thickening. At least for the section below 200 mbsf, the available structural data indicate that the Pliocene silts and clays have suffered pervasive shearing and stratal disruption. This type of deformation in the toe region of the accretionary wedge is clearly different from the extreme localization of shearing and thrust displacement observed in the frontal regions of other accretionary wedges (e.g., Behrmann et al., 1988; Moore et al., 1990). It is probably more akin to that of "broken formations" (e.g., Aalto, 1982; Blake et al., 1982) without implying that deformation be dominantly by cataclastic mechanisms (Lucas and Moore, 1986). The flat-bedded formation between 80 and 200 mbsf lacks comparable fabrics and may be the basal part of a slope sediment cover, which also comprises the partly folded upper Pliocene and Pleistocene sections between the mud line and 70 mbsf. However, we advance this interpretation with caution as core recovery between 80 and 200 mbsf was fragmentary, and few structural data are available to test it.

High grain densities (average: 2.8 g/cm^3) are characteristic for the rocks cored at Site 859. This is in part a reflection of the low content of water-rich sheet silicates, especially smectite and the high content of quartz, feldspar, and detrital Mg/Fe-rich silicates, such as biotite, pyroxene, and hornblende. Porosities are low if compared with fine-grained rocks found in other forearcs that have been subjected to similar depths of burial (e.g., Mascle, Moore, et al. 1988; Taira, Hill, Firth, et al., 1991). Porosities near the mud line show a wide scatter, with an average at around 55%. These decrease downhole to values near 15% at 470 mbsf (see Fig. 45), with wet-water contents as low as 5%. It seems that the generally low porosities do not reflect cementation, but an unusually consolidated sediment. Two intervals have anomalously high porosity: one at 200 to 240 mbsf and a second at 380 to 420 mbsf. The first interval coincides with a zone of anomalously low sonic velocity in the downhole log (log Unit 5 in the Master Chart of Hole 859B), suggesting that this low-velocity zone may indeed be caused by high pore volume. Therefore, it is a zone of high fluid permeability and hosts some of the major perturbations in the thermal structure and the geochemical signature of interstitial fluids at Site 859.

Downhole temperatures, as measured in-situ with the WSTP tool (Fig. 58), show a decrease of temperatures toward this zone from 130 mbsf downward. Then, after a first minimum of just over 10°C at 216 mbsf, a sharp increase to 42°C occurs at 240 mbsf, followed by a second minimum of 4.6°C. The evaluation of the temperature data recorded at 240 mbsf shows that the borehole fluid at this depth was substantially hotter. This can only be reasonably explained by the injection of hot fluids into the borehole from an aquifer of limited stratigraphic thickness in the near

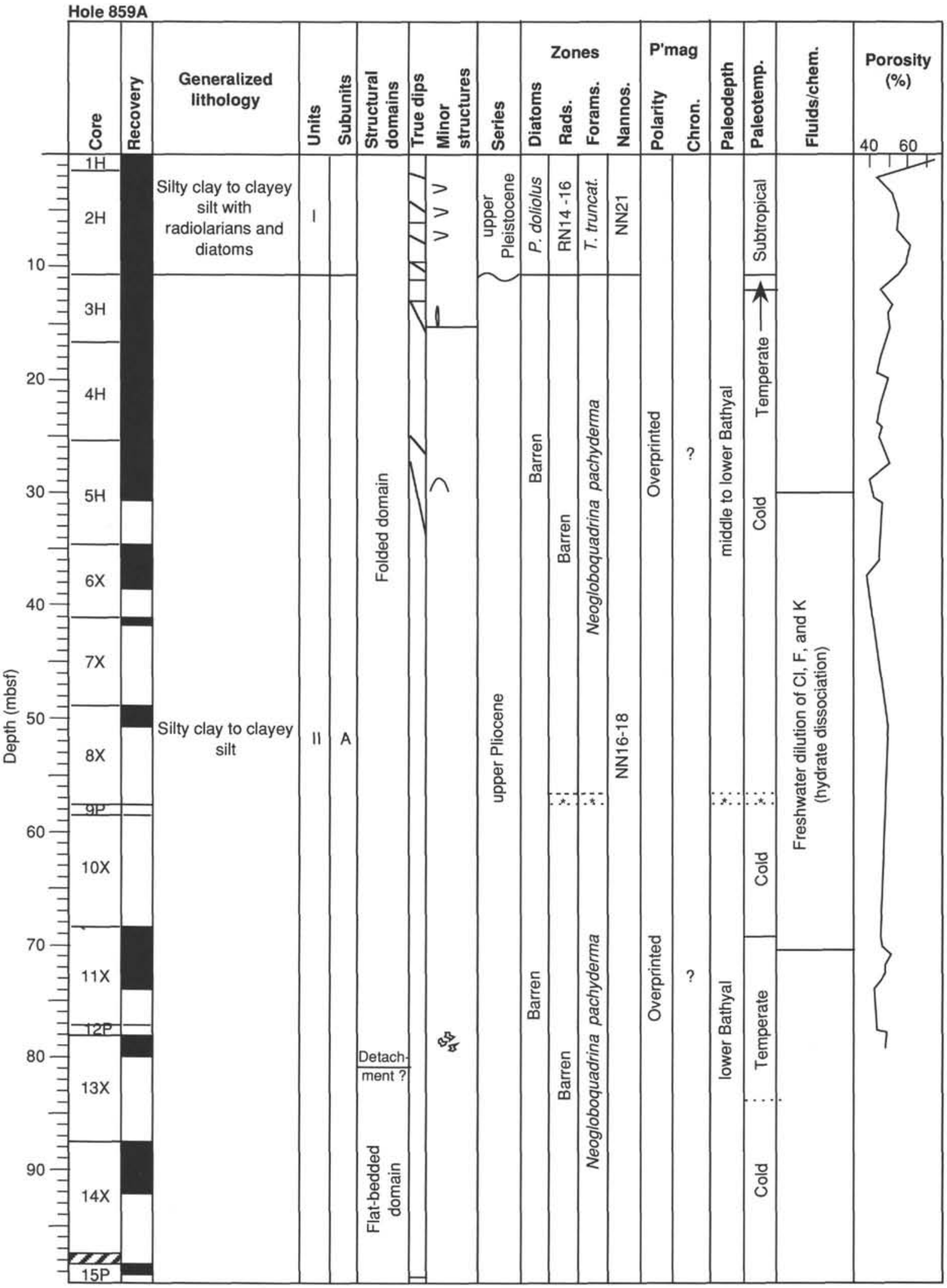

Figure 72. Master chart for Site 859.

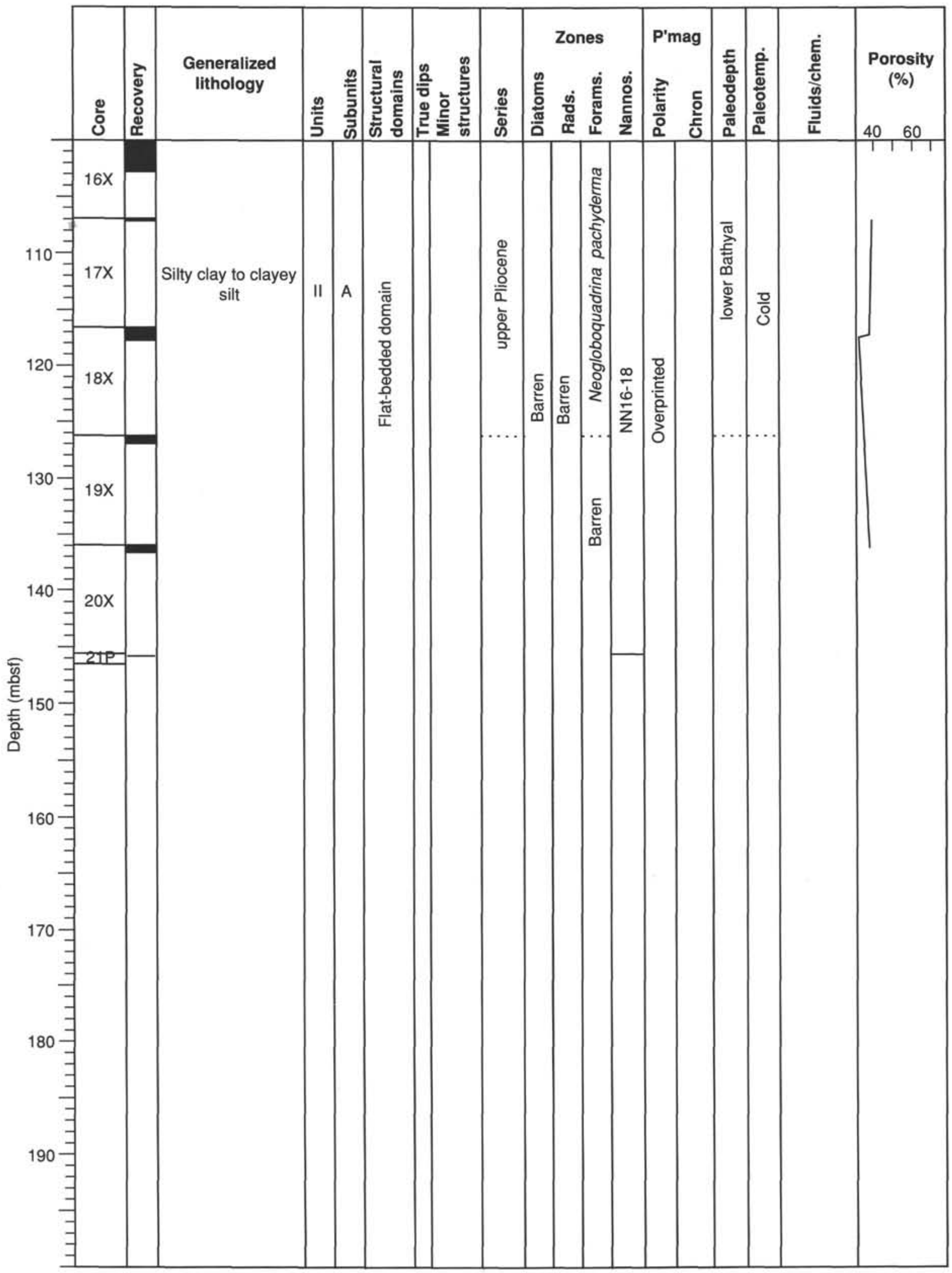

Folds: drawn in orientation observed in core
Clastic vein
Fault/ tectonic contact
Sedimentary breccia
Unless otherwise indicated, true-dips refer to bedding

Tropical radiolarian zones (After Sanfilippo et al., 1985)
RN16 = *Buccinosphaera invaginata*
RN15 = *Collosphaera tuberosa*
RN14 = *Amphirhopalum ypsilon*
B = Barren

RN13 = *Anthocyrtidium angulare*
RN12 = *Pterocanium prismatium*
RN11 = *Spongaster pentas*
RN10 = *Stichocorys peregrina*
* = Downhole reworking

Figure 72 (continued).

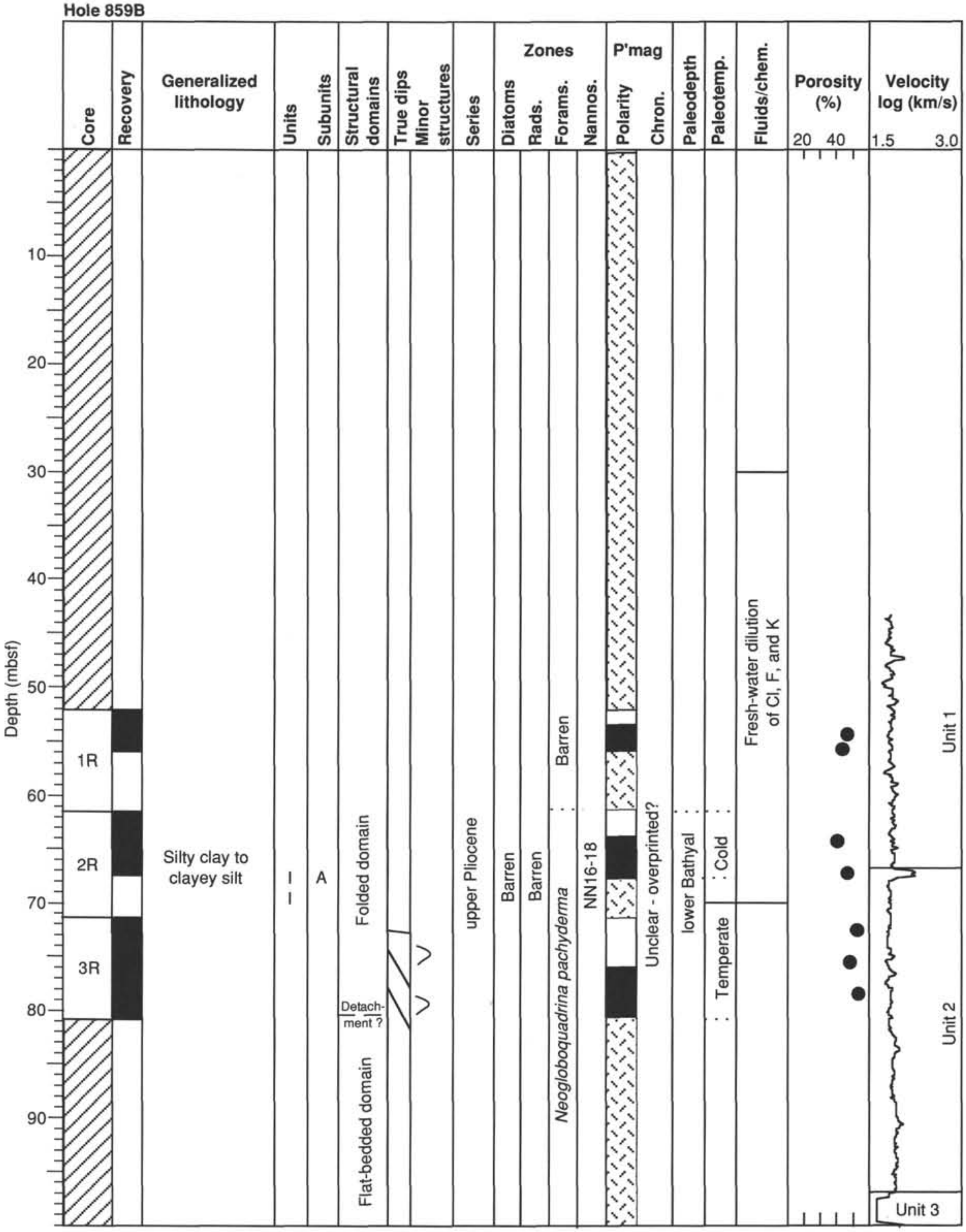

Figure 72 (continued).

vicinity (see Figs. 59 and 60). The evaluation of borehole temperatures from the downhole logging run (Fig. 71) confirms this general pattern; however, without reproducing the inversion of the thermal gradient between 130 and 220 mbsf. This difference is most likely the result of continuing upward flow of warm fluids through the borehole before and during the logging runs. In summary, the irregular downhole temperature profile documents lateral fluid flow through the toe of the accretionary wedge. The two-fold change between intervals of normal and inverted temperature gradients reflects a complex hydrological system in which a closely defined zone of channelized hot fluid flow (the "hot jet") is located in a much broader aquifer of moving cold

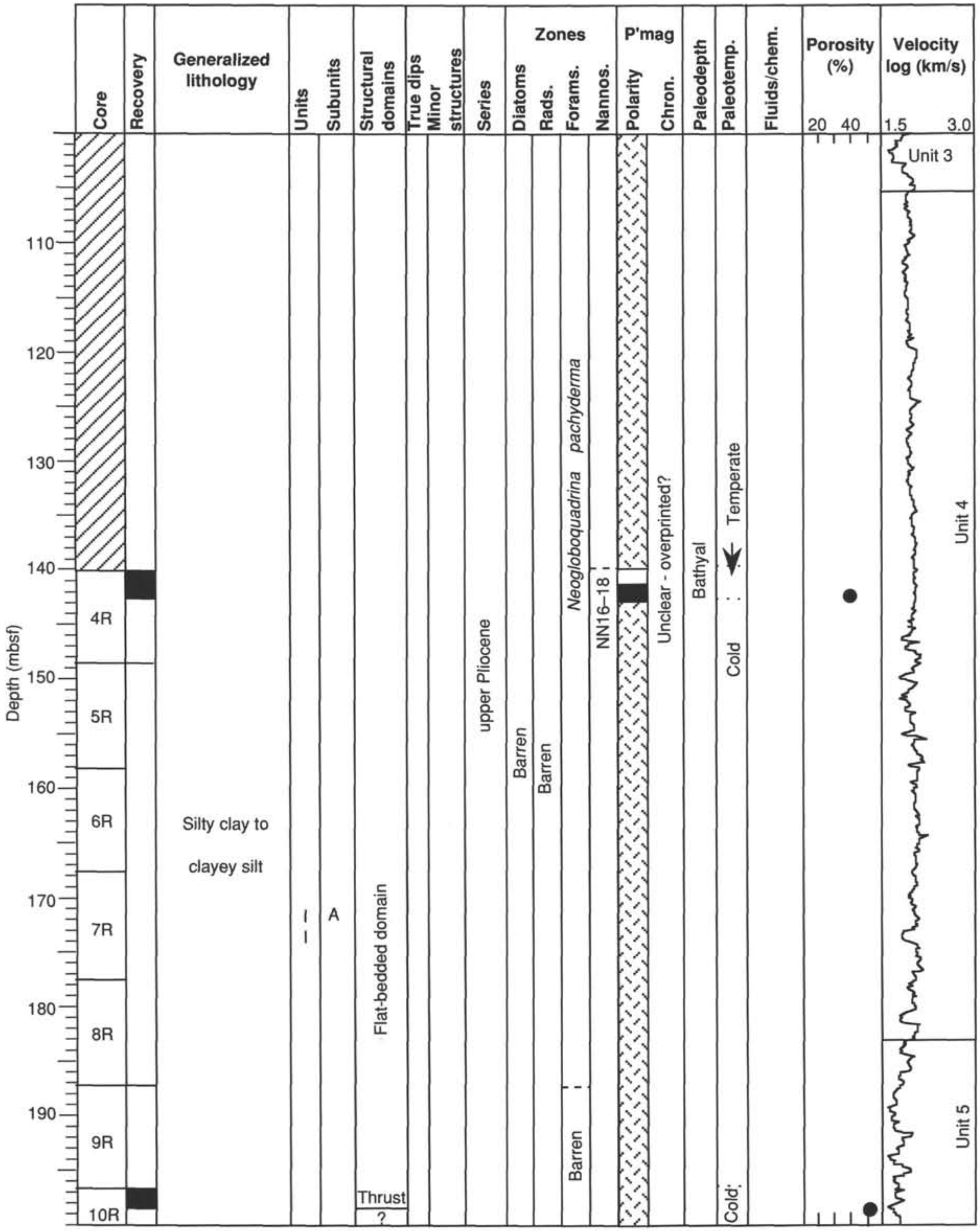

Figure 72 (continued).

water. The temperature profile found at Site 859 is most peculiar, and nothing comparable has been reported from an ODP drill hole into an accretionary wedge before (cf. Mascle, Moore, et al., 1988; Taira, Hill, Firth, et al., 1991).

The nature and compositions of the advecting fluids can be characterized through the chemical analysis of interstitial waters (see Fig. 43). Most of the fluids in the sediment column recovered show a Mg/Ca signature diagnostic of a reaction with basaltic basement, with vertical slow diffusion. However, there is a zone of anomalous Mg depletion and Ca enrichment between 220 and 280 mbsf, reflecting a sourcing of fluids in lithologic units deeper than those recovered. The zone also coincides with a minimum in alkalinity and with breaks in the contents of K and Si. These anomalies in the chemical composition of the interstitial water

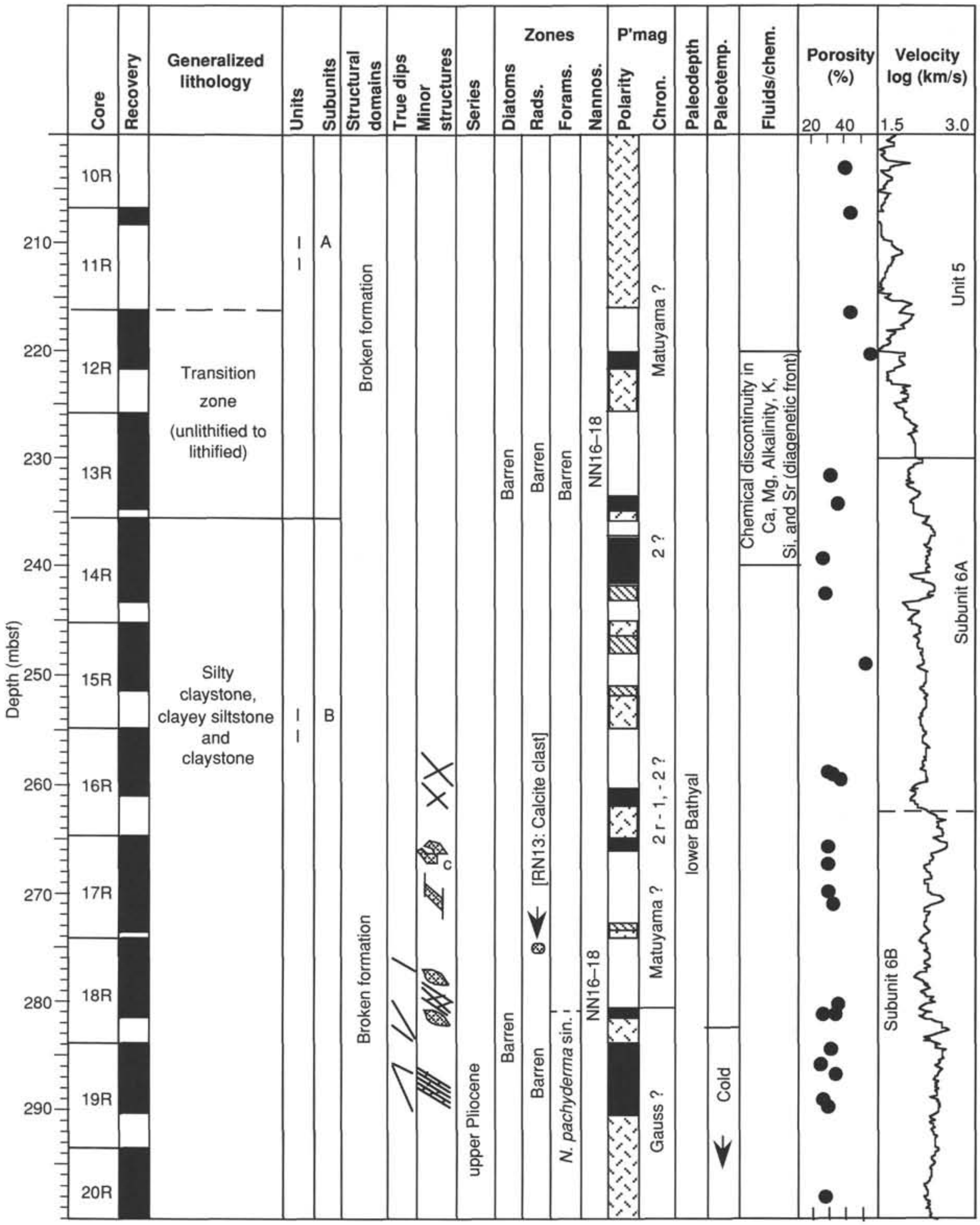

Figure 72 (continued).

provide evidence that long-term advection of fluids is occurring from deep parts of the accretionary wedge. The temperature anomaly associated with the "hot jet" is probably a transient, short-lived phenomenon, but the general process may be viewed adequately as a succession of many "hot-jet" events. More evidence for active defluidizing of the accretionary wedge through the lower part of the section at Site 859 is provided by the composition of gas trapped in the core liners on recovery. Whereas the gas found in the upper 200 mbsf is of microbial biogenic origin, a significant thermogenic gas component is evident from the analyses of the cores in the lower part of Hole 859B. As the content of solid organic carbon in the sediment is low, generally less than 0.5%, and a low degree of maturity exists, the thermogenic gas component must have migrated to its present

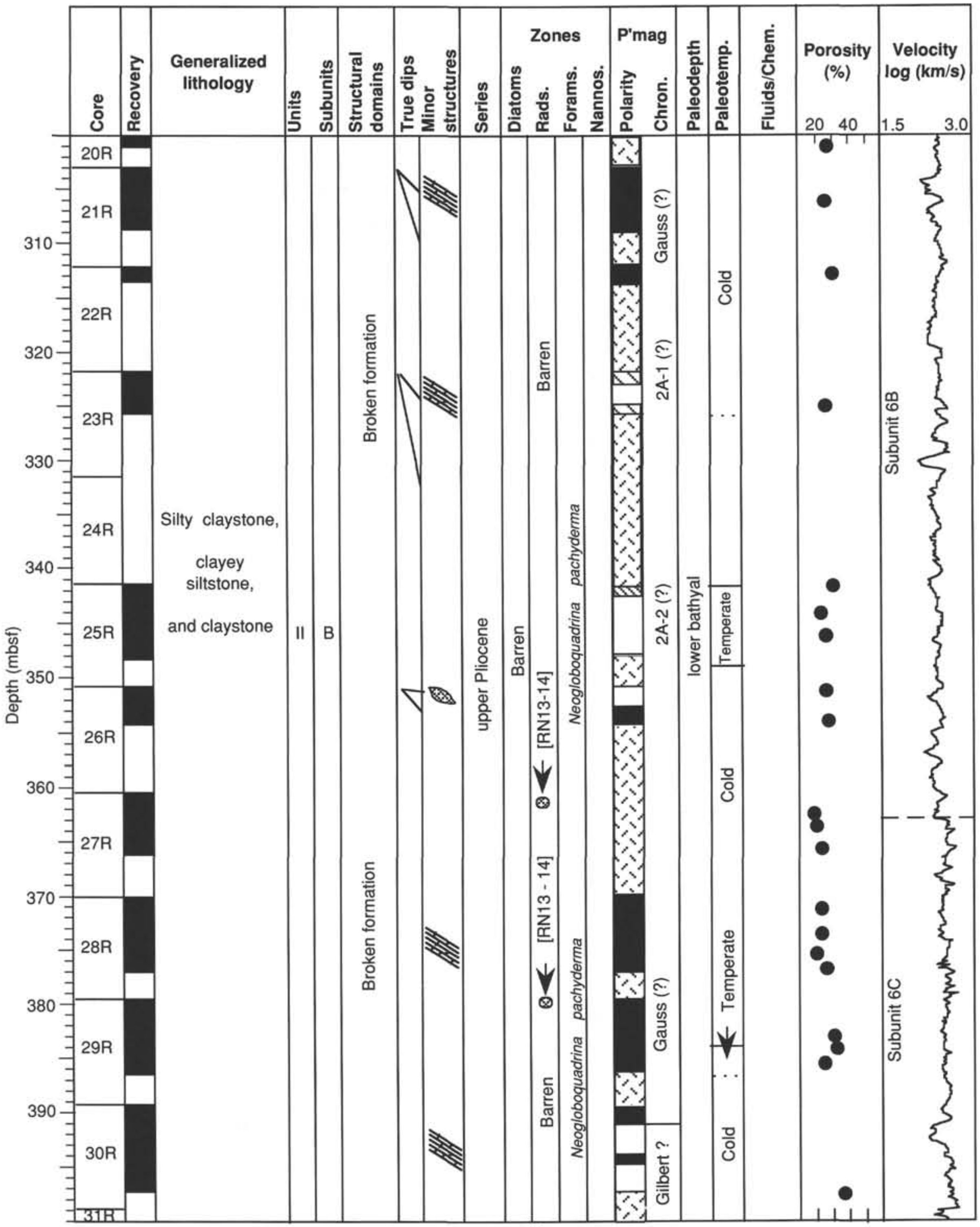

Folds: drawn in orientation observed in core

Clastic vein

Fault/tectonic contact

Broken formation: anastamosing shear surfaces
True dips here refer to shear surfaces and layering in broken formation.

Shear bands in silt/sand units

Fracture cleavages: true dips refer to cleavage orientation

Jointing

Cementation veins in sandstone

Breccia

c Calcite veins

Unless otherwise indicated, true-dips refer to bedding

Figure 72 (continued).

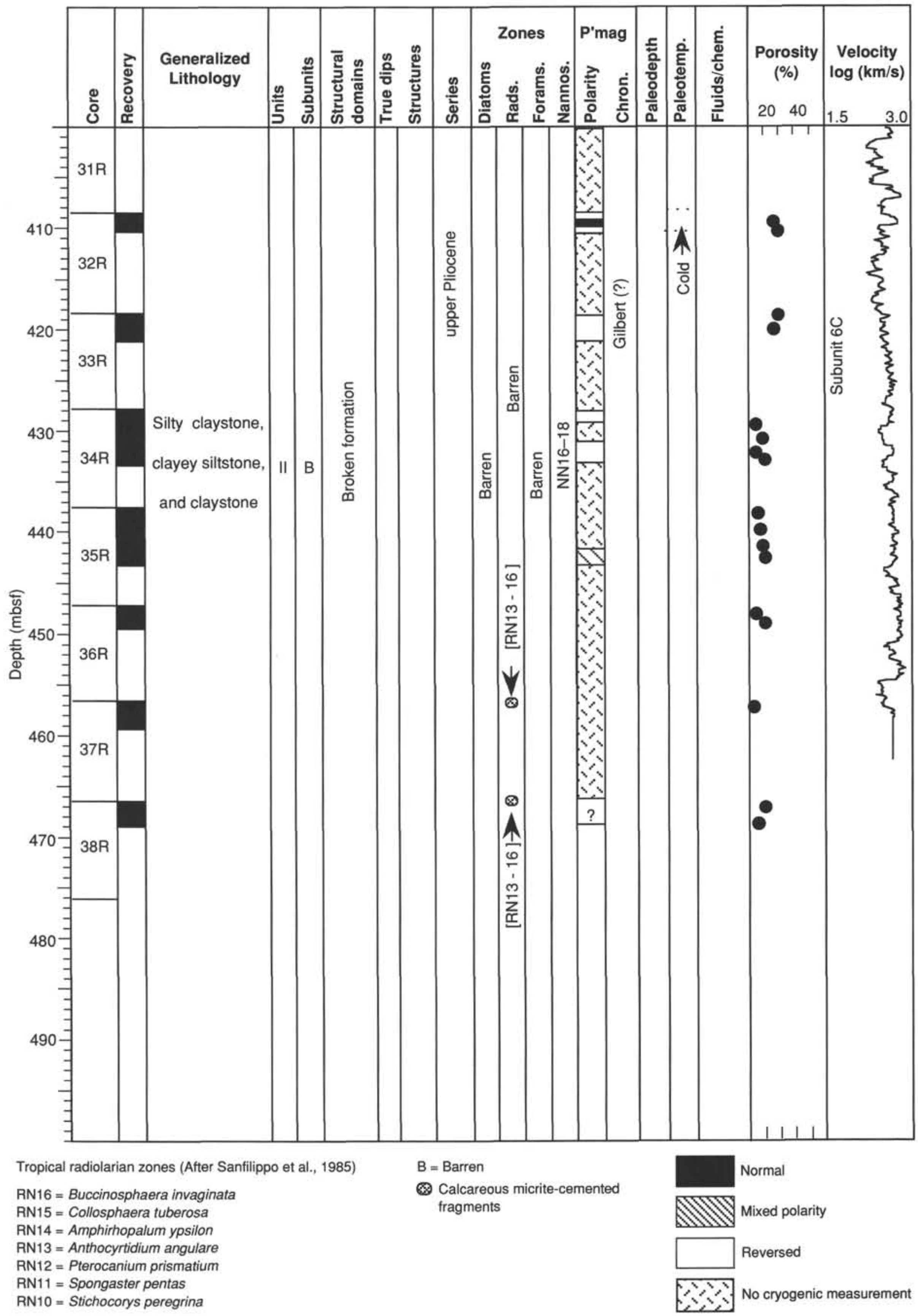

Figure 72 (continued).

position from deeper and presumably downdip positions in the subduction zone.

No gas hydrates were recovered at Site 859. However, strong evidence exists for the presence of gas hydrates in the sediment in situ from interstitial and WSTP water samples and downhole logging measurements. First, sharp and distinct salinity and chloride minima can be seen between 27 and 70 mbsf that have been interpreted as resulting from the dissociation of gas hydrates on or immediately before core recovery. If the difference between background and minimum chloride values observed reflect decomposition of gas hydrate in a sediment of 50% porosity, then about 25% of the pore space has been occupied by solid gas hydrate in situ. Analysis of the sonic velocity log shows a zone of relatively high velocity down to 97 mbsf, which can be interpreted to contain up to 10% gas hydrate. This is followed by a thin zone of distinctly lower velocity between 97 and 105 mbsf. This zone is thought to contain free methane. Supporting observational evidence for this comes from the fact that Core 141-859A-14X (basal depth 97.3 mbsf) contained large gas pockets and separations of core on retrieval. Although we did not recover the gas hydrates, this first-ever intentional penetration of a BSR was successful regarding the observations made on its physical and chemical state in situ.

REFERENCES

Aalto, K.R., 1982. The Franciscan Complex of northern California: sedimentation and tectonics. *In* Leggett, J.K. (Ed.), *Trench-forearc Geology*. Geol. Soc. Spec. Publ. London, 10:419–432.

Agar, S.M., 1990. The interaction of fluid flow and deformation during the progressive deformation of accreted sediments. *J. Geophys. Res.*, 95:9133–9147.

Agar, S.M., Prior, D.J., and Behrmann, J.H., 1989. A BSE investigation of the tectonic fabrics of some fine grained sediments: implications for deformation mechanisms and nomenclature. *Geology*, 17:901–904.

Barron, J.A., 1985. Miocene to Holocene planktic diatoms. *In* Bolli, H.M., Saunders, J.B., and Perch-Nielsen, K. (Eds.), *Plankton Stratigraphy:* Cambridge (Cambridge Univ. Press), 763–809.

Behrmann, J., Brown, K., Moore, J.C., Mascle, A., Taylor, E., Alvarez, F., Andreieff, P., Barnes, R., Beck, C., Blanc, G., Clark, M., Dolan, J.F., Fisher, A., Gieskes, J., Hounslow, M.W., McLellan, P., Moran, K., Ogawa, Y., Sakai, T., Schoonmaker, J., Vrolijk, P., Wilkens, R.H., Williams, C.F., 1988. Evolution of structures and fabrics in the Barbados Accretionary Prism: insights from Leg 110 of the Ocean Drilling Program. *J. Struct. Geol.*, 10:577–591.

Berggren, W.A., Kent, D.V., Flynn, J.J., and Van Couvering, J.A., 1985a. Cenozoic geochronology. *Geol. Soc. Am. Bull.*, 96:1407–1418.

Berggren, W.A., Kent, D.V., and Van Couvering, J.A., 1985b. The Neogene: Part 2. Neogene geochronology and chronostratigraphy. *In* Snelling, N.J. (Ed.), *The Chronology of the Geological Record.* Geol. Soc. London Mem., 10:211–260.

Blake, M.C., Jayko, A.S., and Howell, D.G., 1982. Sedimentation, metamorphism and tectonic accretion of the Franciscan assemblage of northern California. *In* Leggett, J.K. (Ed.), *Trench-forearc Geology.* Geol. Soc. Spec. Publ. London, 10:433–438.

Byrne, T., 1984. Structural geology of melange terranes in the Ghost Rocks Formation. *In* Raymond, L. (Ed.), *Melanges: Their Origin and Significance.* Spec. Pap.—Geol. Soc. Am., 198:21–51.

Byrne, T., Maltman, A.J., Lallement, S., Karig, D.E., Soh, W., and Stephenson, E., in press. Deformation and fluid flow in the Nankai Accretory Prism, Japan. *In* Hill, I., Taira, A., et al., *Proc. ODP., Sci. Results,* 131: College Station, TX (Ocean Drilling Program).

Cande, S.C., Leslie, R.B., Parra, J.C., and Hobart, M., 1987. Interaction between the Chile Ridge and Chile Trench: geophysical and geothermal evidence. *J. Geophys. Res.*, 92:495–520.

Caulet, J.-P., Vénec-Peyré, M.-T., Vergnaud-Grazzini, C., and Nigrini, C., in press. Variation of Somalian upwelling during the last 160 KYR: radiolarian and foraminifera records in Core MD 85674. *In Evolution of Upwelling Since the Miocene.* Geol. Soc. Spec. Publ. London.

Chase, C.G., 1978. Plate kinematics: the Americas, East Africa, and the rest of the world. *Earth Planet. Sci. Lett.*, 37:355–368.

Claypool, G.E., and Kaplan, I.R., 1974. The origin and distribution of methane in marine sediments. *In* Kaplan, I.R. (Ed.), *Natural Gases in Marine Sediments:* New York (Plenum Press), 99–139.

Cobbold, P., and Quinquis, H., 1980. Development of sheath folds in shear regimes. *J. Struct. Geol.*, 2:119–126.

Cowan, D.S., 1974. Deformation and metamorphism of the Franciscan subduction zone complex northwest of Pachecho Pass, California. *Geol. Soc. Am. Bull.*, 85:1623–1634.

———, 1982. Deformation of partly dewatered and consolidated Franciscan sediments near Piedras Blancas Point, California. *In* Leggett, J.K. (Ed.), *Trench-Forearc Geology.* Geol. Soc. Spec. Publ. London, 10:439–458.

———, 1985. The origin of some common types of melange in the western Cordillera of North America. In Nasu, N., et al. (Eds.), Formation of *Active Ocean Margins:* Tokyo (Terra Sci. Publ.), 257–272.

Didyk, B.M., and Simoneit, B.R.T., 1989. Hydrothermal oil of Guaymas Basin and implications for petroleum formation mechanisms. *Nature,* 342:65–68.

Didyk, B.M., Simoneit, B.R.T., Brassell, S.C., and Eglinton, G., 1978. Organic geochemical indicators of palaeoenvironmental conditions of sedimentation. *Nature,* 272:216–222.

Emeis, K.-C., and Kvenvolden, K.A., 1986. Shipboard organic geochemistry on *JOIDES Resolution. ODP Tech. Note,* 7.

Farrington, J.W., Davis, A.C., Tarafa, M.E., McCaffery, M.A., Whelan, J.K., and Hunt, J.M., 1988. Bitumen molecular maturity parameters in the Ikpikpuk well, Alaskan North Slope. *Org. Geochem.*, 13:303–310.

Fitches, W.R., Cave, R., Craig, J., and Maltman, A.J., 1986. Early veins as evidence of detachment in the lower Palaeozoic rocks of the Welsh basin. *J. Struct. Geol.*, 8:607–620.

Hoffman, K.A., and Day, R., 1978. Separation of multi-component NRM: a general method. *Earth Planet. Sci. Lett.*, 40:433–438.

Karig, D.E., and Lundberg, N., 1990. Deformation bands from the toe of the Nankai Accretionary Prism. *J. Geophys. Res.*, 95:9099–9109.

Karlin, R., Lyle, M., and Ross Heath, G., 1987. Authigenic magnetite in suboxic marine sediments. *Nature,* 326:490–493.

Knipe, R.J., 1986a. Deformation mechanism path diagrams for sediments undergoing lithification. *In* Moore, J.C. (Ed.), *Structural Fabrics in Deep Sea Drilling Project Cores From Forearcs.* Mem. Geol. Soc. Am., 166:151–160.

———, 1986b. Faulting mechanisms in slope sediments: examples from Deep Sea Drilling Project cores. *In* Moore, J.C. (Ed.), *Structural Fabrics in Deep Sea Drilling Project Cores From Forearcs.* Mem. Geol. Soc. Am., 166:45–54.

———, 1986c. Microstructural evolution in vein arrays preserved in Deep Sea Drilling Project cores from the Japan Trench, Leg 57. *In* Moore, J.C. (Ed.), *Structural Fabrics in Deep Sea Drilling Project Cores From Forearcs.* Mem. Geol. Soc. Am., 166:75–88.

Kroenke, L.W., Berger, W.H., Janacek, T.R., et al., 1991. *Proc. ODP, Init. Repts.*, 130: College Station, TX (Ocean Drilling Program).

Kuustraa, V.A., Hammershaimb, E.C., Holder, G.D., and Sloan, E.D., 1983. *Handbook of Gas Hydrate, Properties and Occurrence:* Washington (U.S. Dept of Energy, Office of Scientific and Technical Information), Rep. DOE/MC/19239-1546.

Lazarus, D., 1990. Middle Miocene to Recent radiolarians from the Weddell Sea, Antarctica, ODP Leg 113. *In* Barker, P.F., Kennett, J.P., et al., *Proc. ODP, Sci. Results,* 113: College Station, TX (Ocean Drilling Program), 709–727.

Lazarus, D., 1992. Antarctic Neogene radiolarians from the Kerguelen Plateau, ODP Legs 119 and 120. *In* Wise, S. W., Jr., Schlich, R., et al., *Proc. ODP, Sci. Results,* 119: College Station, TX (Ocean Drilling Program), 785–810.

Lombari, G., and Boden, G., 1985. *Modern Radiolarian Global Distributions.* Spec. Publ. Cushman Found. Foraminiferal Res., 16A.

Lucas, S.E., and Moore, J.C., 1986. Cataclastic deformation in accretionary wedges: Deep Sea Drilling Project Leg 66, southern Mexico, and on-land examples from Barbados and Kodiak Islands. *In* Moore, J.C.

(Ed.), *Structural Fabric in Deep Sea Drilling Project Cores From Forearcs.* Mem. Geol. Soc. Am., 166:89–103.

Lundberg, N., and Moore, J.C., 1986. Macroscopic structural features in Deep Sea Drilling Project cores from forearc regions. *In* Moore, J.C. (Ed.), *Structural Fabrics in Deep Sea Drilling Project Cores From Forearcs.* Mem. Geol. Soc. Am., 166:13–44.

Maltman, A.J., Byrne, T., Karig, D.E., Lallement, S., Knipe, R.J., and Prior, D.J., in press. Deformation structure at ODP Site 808. *In* Hill, I., Taira, A., et al., *Proc. ODP. Sci. Results,* 131: College Station, TX (Ocean Drilling Program).

Mann, S., Frankel, R.B., and Blakemore, R.P., 1984. Structure, morphology and crystal growth of bacterial magnetite. *Nature,* 310:405–407.

Mascle, A., Moore, J.C., et al., 1988. *Proc. ODP, Init. Repts.,* 110: College Station, TX (Ocean Drilling Program), 1–603.

Matthews, M.A., and von Huene, R., 1985. Site 570 Methane Hydrate Zone: DSDP Leg 84. *In* von Huene, R., Aubouin, J., et al., *Init. Repts. DSDP,* 84: Washington (U.S. Govt. Printing Office), 773–790.

McCollum, D.W., 1975. Diatom stratigraphy of the southern ocean. *In* Hays, D.E., Frakes, L.A., et al., *Init. Repts. DSDP,* 28: Washington (U.S. Govt. Printing Office), 515–571.

McElhinny, M.W., 1973. *Palaeomagnetism and Plate Tectonics:* Cambridge, U.K. (Cambridge University Press).

Miller, J.J., Lee, M.W., and von Huene, R., 1990. An analysis of a seismic reflection from the base of a gas hydrate zone, offshore Peru. *AAPG Bull.,* 75:910–924.

Moore, G.F., Shipley, T.H., Stoffa, P.L., Karig, D.E., Taira, A., Kuramoto, S., Tokuyama, H., and Suyehiro, K., 1990. Structure of the Nankai Trough accretionary zone from multichannel seismic reflection data. *J. Geophys. Res.,* 95:8753–8765.

Morley, J.J., 1980. Analysis of the abundance variations of the subspecies of Cycladophora davisiana. *Mar. Micropaleontol.,* 5:205–214.

Nigrini, C., and Caulet, J.P., in press. Late Neogene radiolarian assemblages characteristic of Indo-Pacific areas of upwelling. *Micropaleontology.*

Nigrini, C.A., 1970. Radiolarian assemblages in the North Pacific and their application to a study of Quaternary sediments in Core V20-130. *Mem. Geol. Soc. Am.,* 126:139–175.

Pickering, K., Agar, S.M., and Ogawa, Y., 1988. Genesis and deformation of mud injections containing chaotic basalt-limestone-chert associations: examples from the southwest Japan forearc. Geology, 16:881–885.

Prior, D.J., and Behrmann, J.H., 1990. Thrust related mudstone fabrics from the Barbados forearc: a back-scattered SEM study. *J. Geophys. Res.,* 95:9055–9067.

Ramsay, J.G., 1967. *Folding and Fracturing of Rocks.* New York (McGraw-Hill).

Raymond, L., 1984. *Melanges: Their Origin and Significance.* Spec. Pap. Geol Soc. Am., 198.

Ruddiman, F.W., Cameron, D., and Clement, M.B., 1987. Sediment disturbance and correlation of offset holes drilled with the hydraulic piston corer. *In* Ruddiman, W.F., Kidd., R.B., Thomas, E., et al., *Init. Repts. DSDP,* 94: Washington (U.S. Govt. Printing Office), 615–634.

Sanfilippo, A., Westberg-Smith, M.J., and Riedel, W., 1985. Cenozoic radiolaria. *In* Bolli, H.M., Saunders, J.B., and Perch-Nielsen, K. (Eds.), *Plankton Stratigraphy:* Cambridge (Cambridge University Press), 631–712.

Shipboard Scientific Party, 1982. Guaymas Basin: Sites 477, 478, and 481. *In* Curray, J.R., Moore, D.G., et al., *Init. Repts. DSDP,* 64 (Pt. 1): Washington (U.S. Govt. Printing Office), 210–415.

Simoneit, B.R.T., 1977. Diterpenoid compounds and other lipids in deep-sea sediments and their geochemical significance. *Geochim. Cosmochim. Acta,* 41:463–476.

_______, 1978. The organic chemistry of marine sediments. *In* Riley, J.F., and Chester, R. (Eds.), *Chemical Oceanography* (2nd ed.) (Vol. 7): New York (Academic Press), 233–311.

Simoneit, B.R.T., Brenner, S., Peters, K.E., and Kaplan, I.R., 1981. Thermal alteration of Cretaceous black shale by basaltic intrusions in the eastern Atlantic. II: effects on bitumen and kerogen. *Geochim. Cosmochim. Acta,* 45:1581–1602.

Srinivasan, M.S., and Kennett, J.P., 1981. A review of Neogene planktonic foraminiferal biostratigraphy: applications in the equatorial and South Pacific. *Spec. Publ.—Soc. Econ. Paleontol. Mineral.,* 32:395–432.

Suess, E., von Huene, R., et al., 1988. *Proc. ODP, Init. Repts.,* 112: College Station, TX (Ocean Drilling Program).

Taira, A., Hill, I., Firth, J.V., et al., 1991. *Proc. ODP, Init. Repts.,* 131: College Station, TX (Ocean Drilling Program).

Takahashi, K., 1987. Radiolarian flux and seasonality: climatic and El Nino response in the subarctic Pacific, 1982–1984. *Global Biogeochem. Cycles,* 1:213–231.

Tarduno, J.A., Mayer, L.A., Musgrave, R., and Shipboard Scientific Party, 1991. High-resolution, whole-core magnetic susceptibility data from Leg 130, Ontong Java Plateau. *In* Kroenke, L.W., Berger, W.H., Janacek, T.R., et al., 1991. *Proc. ODP, Init. Repts.,* 130: College Station, TX (Ocean Drilling Program), 541–548.

von Huene, R., and Scholl, D.W., 1991. Observations at convergent margins concerning sediment subduction and subduction erosion, and the growth of continental crust. *Rev. Geophys.,* 29:279–316.

Ms 141IR-106

NOTE: For all sites drilled, core-description forms ("barrel sheets") and core photographs have been reproduced on coated paper and can be found in Section 3, beginning on page 449. Forms containing smear-slide data can be found in Section 4, beginning on page 665.

Hole 859B: Resistivity-Velocity-Natural Gamma Ray Log Summary

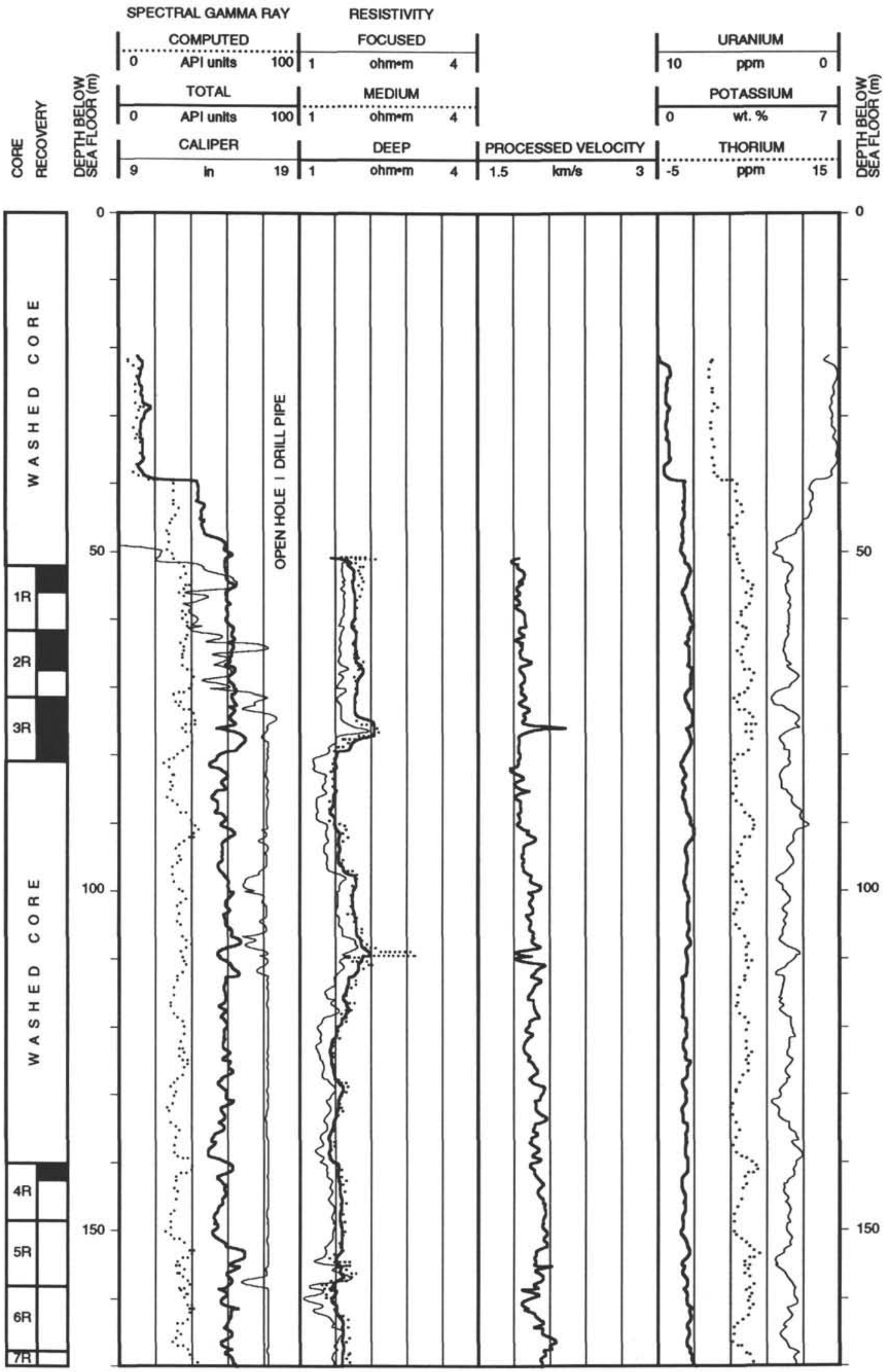

Hole 859B: Resistivity-Velocity-Natural Gamma Ray Log Summary (continued)

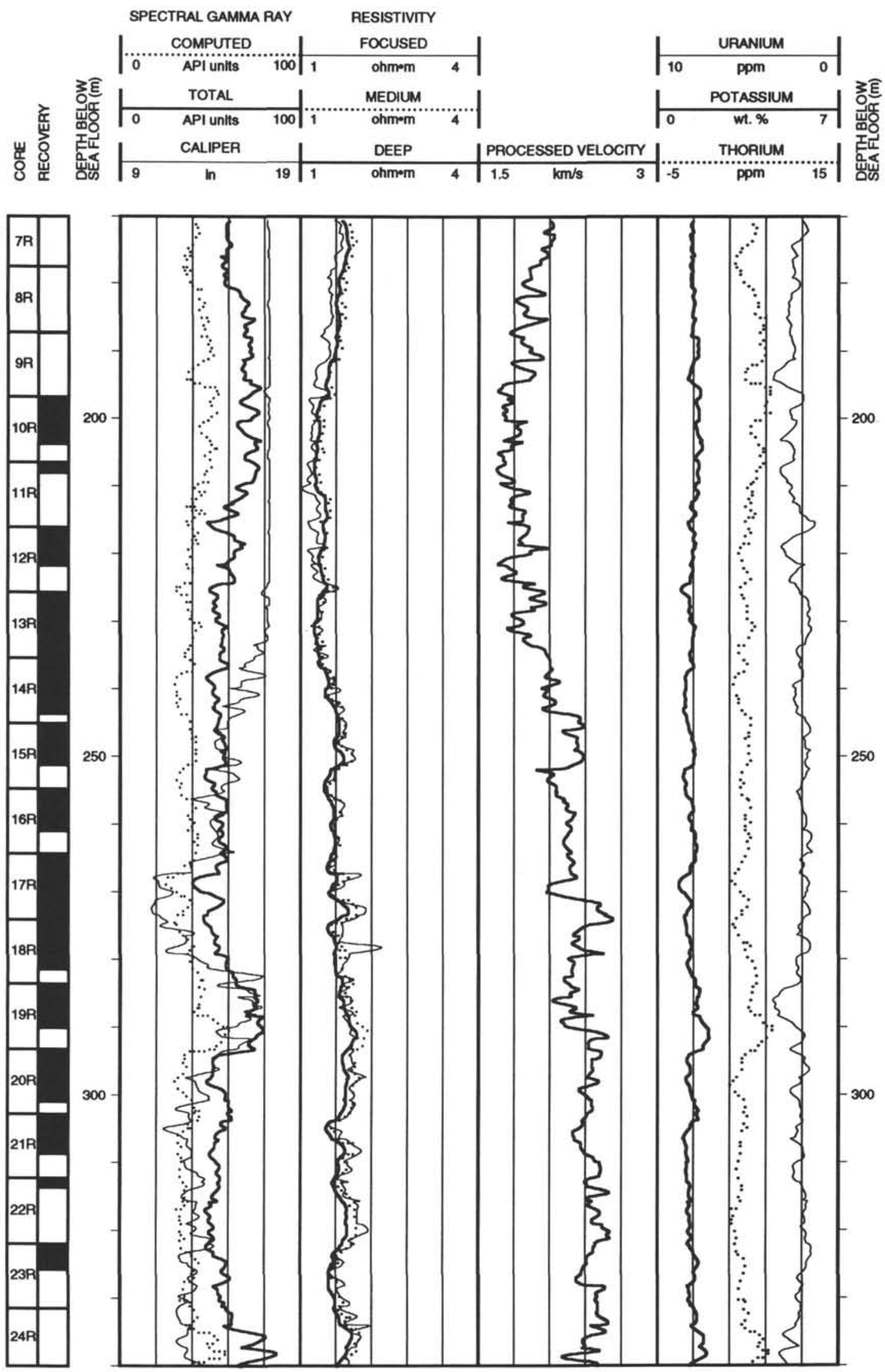

Hole 859B: Resistivity-Velocity-Natural Gamma Ray Log Summary (continued)

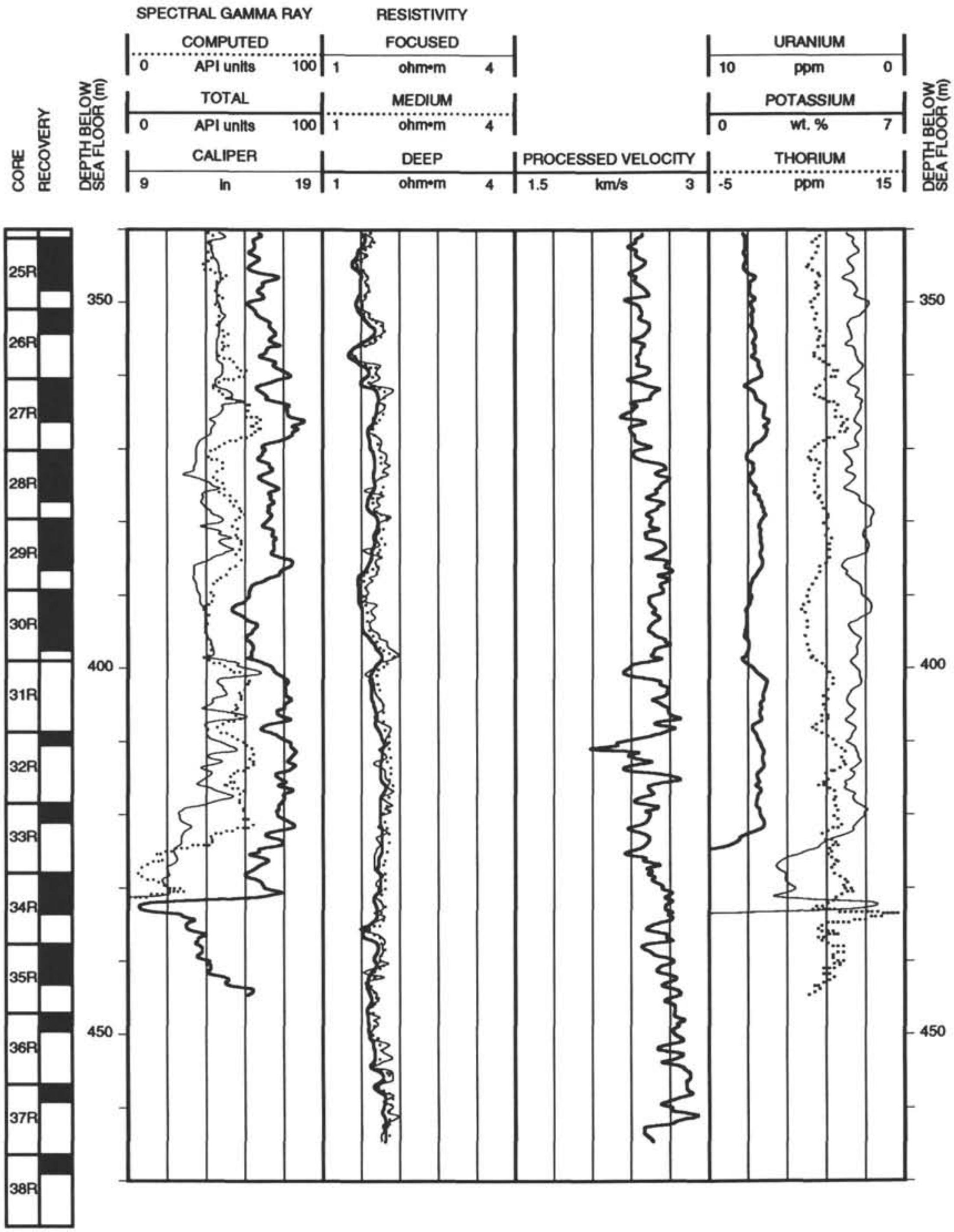

Hole 859B: Density-Natural Gamma Ray Log Summary

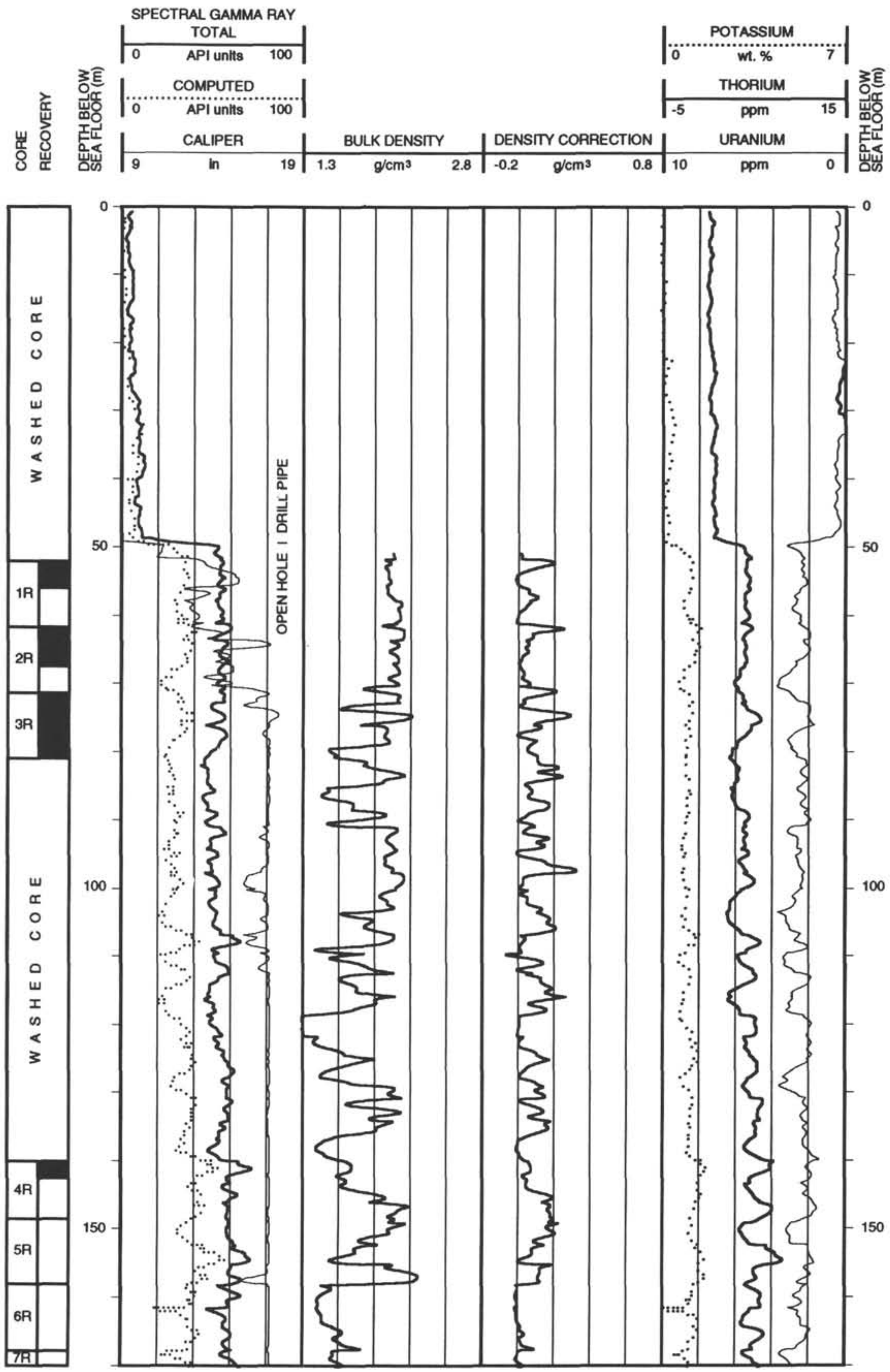

Hole 859B: Density-Natural Gamma Ray Log Summary (continued)

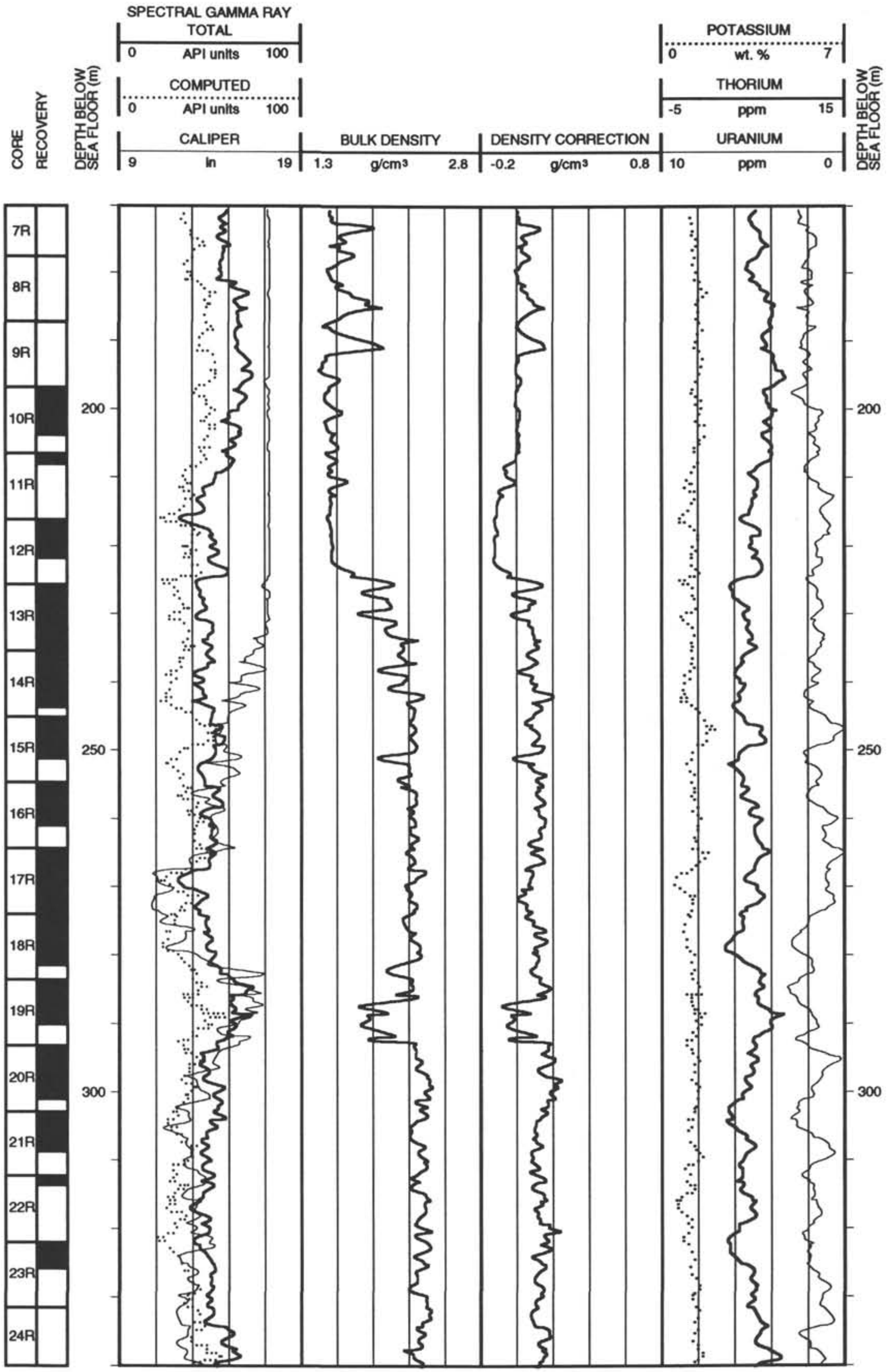

Hole 859B: Density-Natural Gamma Ray Log Summary (continued)

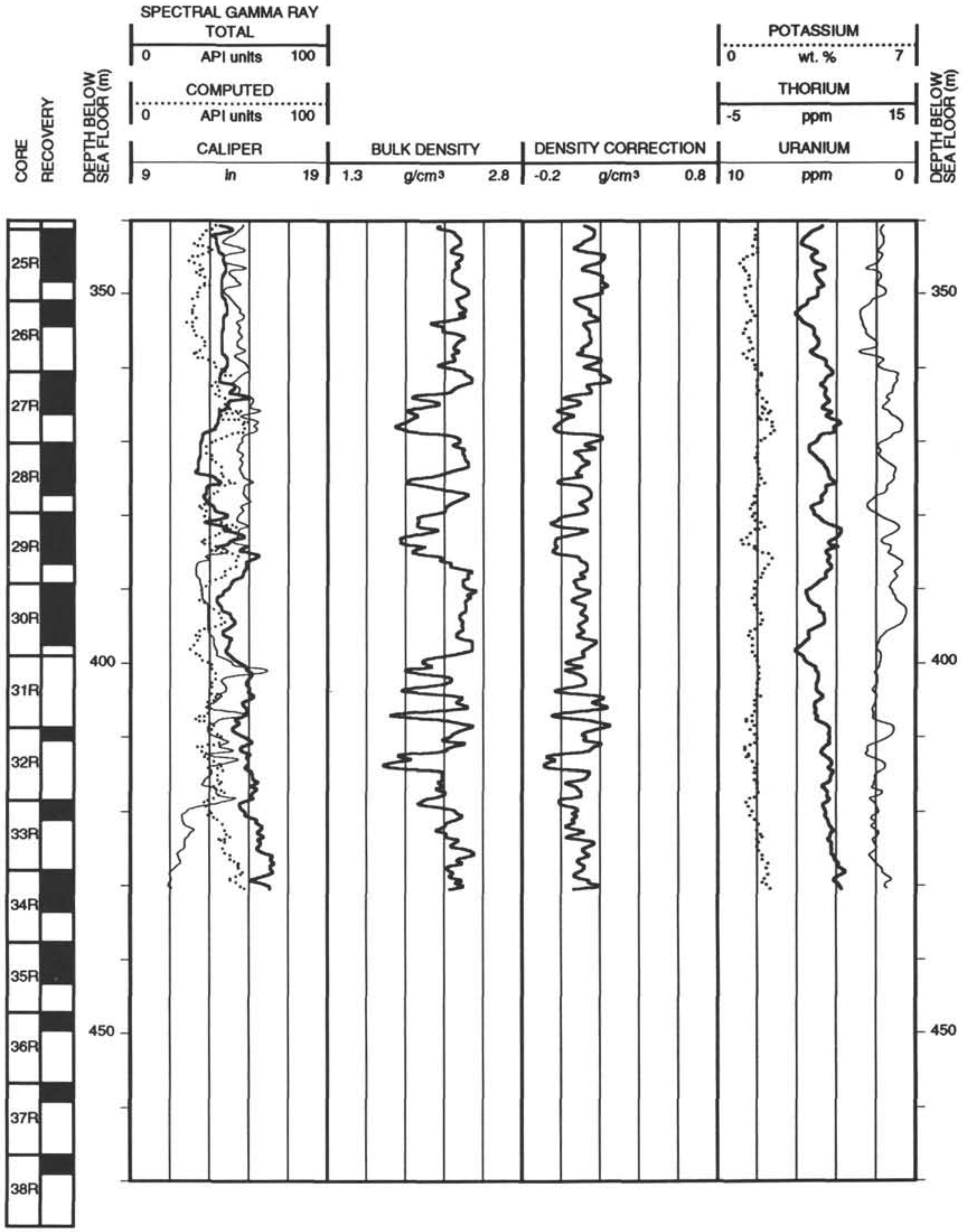

Hole 859B: Geochemical Log Summary

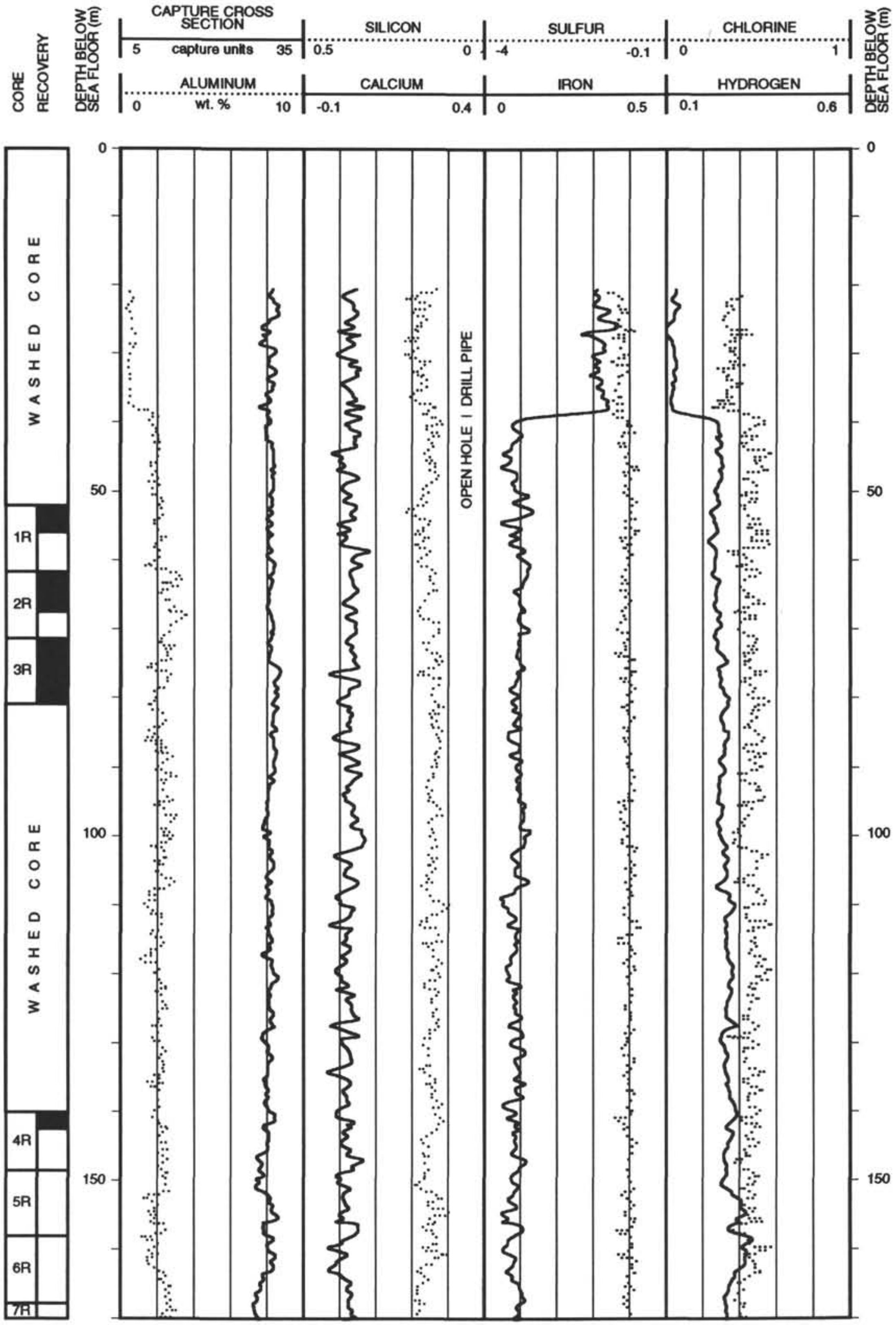

Hole 859B: Geochemical Log Summary (continued)

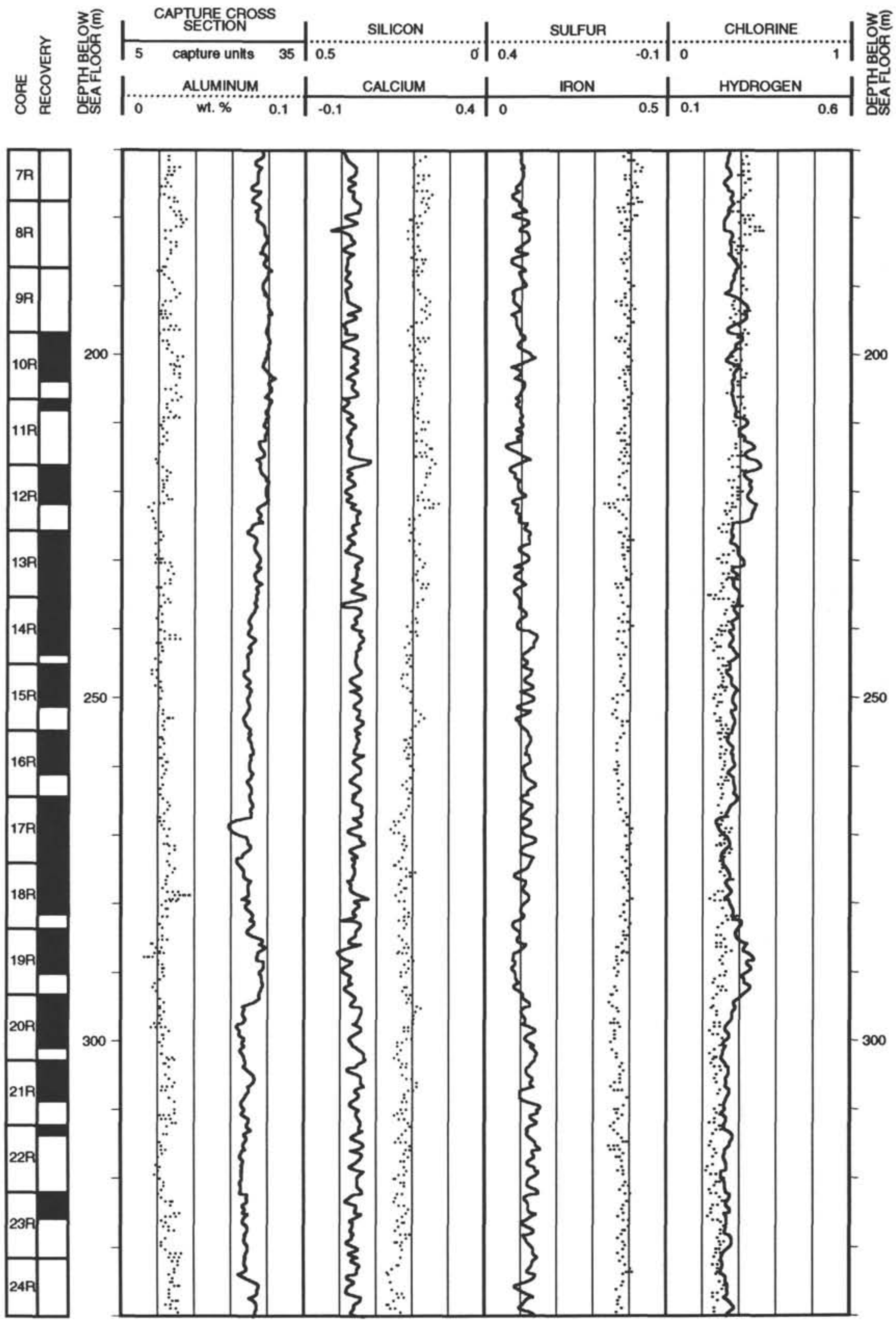

Hole 859B: Geochemical Log Summary (continued)